ISSN 2079-1372 ***DOI: 10.31891/2079-1372***

THE INTERNATIONAL SCIENTIFIC JOURNAL

PROBLEMS OF TRIBOLOGY

Volume 31 ***No 3/121-2026***

МІЖНАРОДНИЙ НАУКОВИЙ ЖУРНАЛ

ПРОБЛЕМИ ТРИБОЛОГІЇ

PROBLEMS OF TRIBOLOGY

INTERNATIONAL SCIENTIFIC JOURNAL

Published since 1996, four time a year

Volume 31 No 3/121-2026

Establishers:

Khmelnytskyi National University (Ukraine)
Lublin University of Technology (Poland)

Associated establisher:
Vytautas Magnus University (Lithuania)

Editors:

O. Dykha (Ukraine), **M. Pashechko** (Poland), **J. Padgurskas** (Lithuania)

Editorial board:

V. Aulin (Ukraine),
N. Brunetiere (France),
V. Voitov (Ukraine),
V. Vynar (Ukraine),
E. Ciulli (Italy),
V. Dvoruk (Ukraine),
A. Zagorulko (Ukraine),
O. Mikosianchyk (Ukraine),
R. Mnatsakanov (Ukraine),
J. Musial (Poland),
O. Milanenko (Ukraine),
V. Oleksandrenko (Ukraine),
V. Savulyak (Ukraine),
M. Stechyshyn (Ukraine),
T. Al-Quraan (Jordan),
H. Zhang (Chine)

Executive secretary: O. Dytynuik

Editorial board address:
International scientific journal "Problems of Tribology",
Khmelnytskyi National University,
Instytutska str. 11, Khmelnytskyi, 29016, Ukraine
phone +380975546925

Indexed: CrossRef, DOAJ, Ulrichsweb, ASCI, Google Scholar, Index Copernicus

E-mail: tribology@khmnu.edu.ua

Internet: https://tribology.khmnu.edu.ua/

ПРОБЛЕМИ ТРИБОЛОГІЇ

МІЖНАРОДНИЙ НАУКОВИЙ ЖУРНАЛ

Видається з 1996 р. ***Виходить 4 рази на рік***

Том 31 **№ 3/121-2026**

Співзасновники:
Хмельницький національний університет (Україна)
Університет Люблінська Політехніка (Польща)

Асоційований співзасновник:

Університет Вітовта Великого (Литва)

Редактори:

О. Диха (Хмельницький, Україна), М. Пашечко (Польща), Ю. Падгурскас (Литва)

Редакційна колегія:

В. Аулін (Україна),
Н. Брюнетьєр (Франція),
В. Войтов (Україна),
В. Винар (Україна),
Е. Чіуллі (Італія),
В. Дворук (Україна),
А. Загорулько (Україна),
О. Мікосянчик (Україна),
Р. Мнацаканов (Україна),
Я. Мушял (Польща),
О. Міланенко (Україна),
В. Олександренко (Україна),
В. Савуляк (Україна),
М. Стечишин (Україна),
Т. Аль-Коран (Йорданія),
Х. Чжан (Китай)

Відповідальний секретар: О.П. Дитинюк

Адреса редакції:
Україна, 29016, м. Хмельницький, вул. Інститутська 11, к. 4-401
Хмельницький національний університет, редакція журналу “Проблеми трибології”

тел. +380975546925, **E-mail**: tribology@khmnu.edu.ua

Internet: https://tribology.khmnu.edu.ua/

Зареєстровано Міністерством юстиції України
Свідоцтво про держреєстрацію друкованого ЗМІ: Серія КВ № 1917 від 14.03. 1996 р.
(перереєстрація № 24271-14111ПР від 22.10.2019 року)

Входить до переліку наукових фахових видань України
(Наказ Міністерства освіти і науки України № 612/07.05.19. Категорія Б)

Індексується в МНБ: CrossRef, DOAJ, Ulrichsweb, ASCI, Google Scholar, Index Copernicus

Рекомендовано до друку рішенням вченої ради ХНУ, протокол № 3 від 24.09.2026 р.

© Редакція журналу “Проблеми трибології (Problems of Tribology)”, 2026

ISSN 2079-1372 Problems of Tribology, V. 31, No 3/121-2026

Problems of Tribology
Website: http://tribology.khnu.km.ua/index.php/ProbTrib
E-mail: tribosenator@gmail.com

CONTENTS

***ISSN 2079-1372 Problems of Tribology**, V. 31, No 3/121-2026*

Problems of Tribology

Website: http://tribology.khnu.km.ua/index.php/ProbTrib

E-mail: tribosenator@gmail.com

ЗМІСТ

*ISSN 2079-1372 **Problems of Tribology**, V. 31, No 3/121-2026, 6-12*

Problems of Tribology
Website: http://tribology.khnu.km.ua/index.php/ProbTrib
E-mail: tribosenator@gmail.com

DOI: https://doi.org/10.31891/2079-1372-2026-121-3-6-12

Implementation of the process of forming regular micro-reliefs on the working surfaces of connecting rod bearings

V.O. Dzyura0000-0002-1801-2419, **T.R. Dzhyvak**0009-0008-9170-2126

Ternopil Ivan Puluy National Technical University, Ukraine
E-mail: volodymyrdzyura@gmail.com

Received: 20 June 2026: Revised 10 July 2026: Accept: 22 July 2026

Abstract

The article presents the results of designing a technological operation for the formation of a Type II regular mesh micro-relief with triangular grooves, performed using a vibration-free method in a single pass on the inner cylindrical surface of connecting rod bearings. The technological operation is implemented utilizing a specially designed tool by machining a pair of connecting rod bearings within a split holding fixture. The connecting rod body for the specified bearing size was used as the holding fixture. The required depth of the micro-relief grooves is achieved through a dimensional analysis of the developed special tool designed for the plastic deformation of the connecting rod bearing surface. Relative micro-relief areas of 14.9% and 28.5% were obtained by determining the appropriate feed rate and tool rotational speed. Experimental samples of connecting rod bearings for a Volvo V50 1.6 HDI vehicle, with the geometric parameters D_{ring} = 47.0 mm and B_{ring} = 16.9 mm, were produced with the formed regular micro-relief. The process was executed at an axial tool feed rate of f_{in} = 19.43 mm/rev (for the 28.5% area) and f_{in} = 39.56 mm/rev for the 14.9% area, utilizing a HAAS VF-B/40HE CNC vertical milling machine. It has been established that this technological operation can be performed either during the finishing stage of machining the copper-lead base of the bearing (which has a thickness of 250–400 μm) immediately prior to the application of protective metal layers of nickel, copper, and/or composite materials, or after the application of the protective coating. The creation of a regular micro-relief ensures high operational reliability, enhanced durability, and the stable performance of both the connecting rod bearings and the internal combustion engine as a whole.

Keywords: connecting rod bearings, technology, tool, parameters, formation modes, regular micro-relief

Introduction

Modern internal combustion engines (ICEs) are highly sophisticated mechanisms that convert thermal energy into mechanical energy. However, as their design becomes more complex, there is a noticeable trend towards a reduction in their operational lifespan. In contrast to the durable engines of previous decades, modern turbocharged engines (particularly low-displacement gasoline units subjected to high thermal loads) frequently exhaust their service life before reaching a mileage of 150,000 km. Stringent environmental standards also exert a negative impact on engine durability: in an effort to minimize toxic emissions and optimize combustion, manufacturers increase the compression ratio of the fuel-air mixture, thereby imposing additional loads on engine components. The scientific literature has already addressed a range of issues concerning the reliability, performance characteristics, and durability of ICE components [1]. To gain a profound understanding of the physical and mechanical processes occurring within friction zones, it is essential to systematically investigate the impact of operating conditions on the overall service life of the engine [2]. Consequently, the systematization and analysis of operational damage in automotive plain bearings (connecting rod bearings) remains a highly relevant objective in modern mechanical engineering [3–6]. Connecting rod bearings are among the most heavily loaded components of an ICE. Operating as plain bearings, they function under conditions of extreme temperatures and high specific pressures. Given that their working surfaces are continuously subjected to friction, the optimization of tribological conditions is a fundamental prerequisite for ensuring the reliable and uninterrupted operation of the engine.

Copyright © 2026 V.O. Dzyura, T.R. Dzhyvak. This is an open access article distributed under the Creative Commons Attribution License, which permits unrestricted use, distribution, and reproduction in any medium, provided the original work is properly cited.

Literature review

The mounting conditions and stiffness parameters of automotive plain bearings (particularly connecting rod bearings), which are among the most critical components of internal combustion engines (ICEs), are determining factors in the formation of their stress-strain state during operation. Based on the simulation of the technological operations of forming and fitting, the patterns of residual stress generation and their correlation with cyclic operational deformations induced by piston kinematics have been established [7, 8]. Furthermore, distinctions between hydrodynamic and elastohydrodynamic lubrication regimes have been identified, and the direct influence of bearing mounting parameters on the spatial distribution of hydrodynamic pressure has been demonstrated. Under normal operating conditions of modern ICEs, the thickness of the hydrodynamic lubricating film in plain bearings varies within the range of 1–20 μm (0.001–0.02 mm) [9–12].

At high rotational speeds and optimal lubricant viscosity, the film thickness can reach 15–20 μm, whereas at low speeds under increased load conditions, it is reduced to a few micrometers. A decrease in the lubricating film thickness to below 1 μm induces partial direct contact between the mating surfaces of the friction pair, leading to their intensive wear. An analysis of the causes of connecting rod bearing failures indicates that, under significant loads, insufficient lubrication of the contact zone is one of the primary reasons for their breakdown. This results in a shift in interaction regimes, causing a transition from Zone II (semi-fluid friction) to Zone I (boundary friction). Consequently, the formation and maintenance of a stable lubricating film is a priority objective for normalizing operating conditions and achieving the designed service life of the friction pair. An effective technological solution to this problem is the application of micro-grooved bearings (MGBs) – plain bearings with circumferential micro-grooves machined on their working surfaces [13, 14].

Compared to conventional non-profiled bearings (NPBs), MGBs are distinguished by a number of significant operational advantages. Specifically, they demonstrate enhanced resistance to seizure (scuffing) and fatigue failure, provide a lower operating temperature regime under high loads, and are characterized by improved starting properties at low temperatures [15, 16].

The formation of a regular micro-relief on the working surfaces of the bearings is objectively accompanied by a partial reduction in their relative load-bearing area. However, according to static calculations [17], the application of micro-grooves does not lead to a decrease in the load-carrying capacity of the bearing. Highly indicative are the results of studies investigating the operating time to seizure under conditions of an artificial interruption of the lubricant supply [17]. Unlike standard bearings, where premature seizure was recorded in three out of five test samples, the bearings with a micro-relief functioned stably for an extended period without any signs of critical failure. Such operational performance convincingly confirms the high capacity of micro-grooved bearings to accumulate and retain lubricant within the contact zone of the friction pair.

To prevent the occurrence of operational defects, it is proposed to form a regular micro-relief on the working surfaces of the connecting rod bearings. This technological solution contributes to increasing the temperature threshold for the onset of seizure between the contacting surfaces in the «bearing–journal» tribological pair [18]. Previous studies have demonstrated that the application of a micro-relief on cylindrical surfaces with the following parameters: relative area of the micro-relief F_n = 25–45%, groove inclination angle γ = 25–32°, and groove depth h_k = 22–27 μm, guarantees the formation of a lubricating film with a thickness of 3–3.5 μm [19].

The high effectiveness of forming regular micro-asperities to optimize the performance characteristics of friction surfaces is further corroborated by the research findings of other authors [20–22]. In light of this, the development of a technological process for applying a regular micro-relief to the working surfaces of connecting rod bearings emerges as a highly relevant scientific and applied objective in modern automotive engineering. The successful resolution of this task will enable a substantial increase in the overall service life of internal combustion engines.

The aim of this work is to develop and implement a technological process for forming a Type II regular micro-relief on the working surfaces of connecting rod bearings using a vibration-free plastic deformation method. The study also aims to determine the technological parameters required to obtain specified relative micro-relief areas and to experimentally validate the proposed process on connecting rod bearings of an internal combustion engine.

Research materials and methodology

The design of the technological operation for forming a regular micro-relief was carried out using a specially developed tool. These micro-reliefs are formed on the inner surface of the connecting rod bearings of a Volvo V50 1.6 HDI vehicle with the following geometric parameters: D_{ring} = 47.0 mm; B_{ring} = 16.9 mm, during their machining in a holding fixture (Fig. 1).

To calculate the relative area of the micro-relief, equation (1) was utilized, which allows for establishing the relationship between the area of the micro-relief grooves and the forming parameters.

$$F_a = \frac{\dfrac{2B_{ring} \cdot n_{in} \cdot b_g}{\pi D_{ring} tg(\gamma_{c.g}/2)} \sqrt{(\pi D_{ring})^2 + (\pi D_{ring} tg(\gamma_{c.g}/2))^2} - \dfrac{n_{c.g.tot} \cdot b_g^2 \cdot \sin(\gamma_{c.g})}{\sin^2(2\gamma_{c.g})}}{\pi \cdot D_{ring} \cdot B_{ring}} \tag{1}$$

where B_{ring} – width of the connecting rod bearing, mm;
D_{ring} – diameter of the inner cylindrical surface of the connecting rod bearing, mm;
n_{in} – number of deforming elements involved in the formation of the micro-relief, units;
b_g – width of the micro-relief groove, mm;
$\gamma_{c.g.}$ – angle between the micro-relief grooves, deg;
$n_{c.g.tot}$ – total number of groove intersections, units.

Taking into account the geometric parameters of the connecting rod bearings, a schematic layout of the regular micro-reliefs was developed with two values of the relative micro-relief area: 28.5% and 14.9% (Fig. 1).

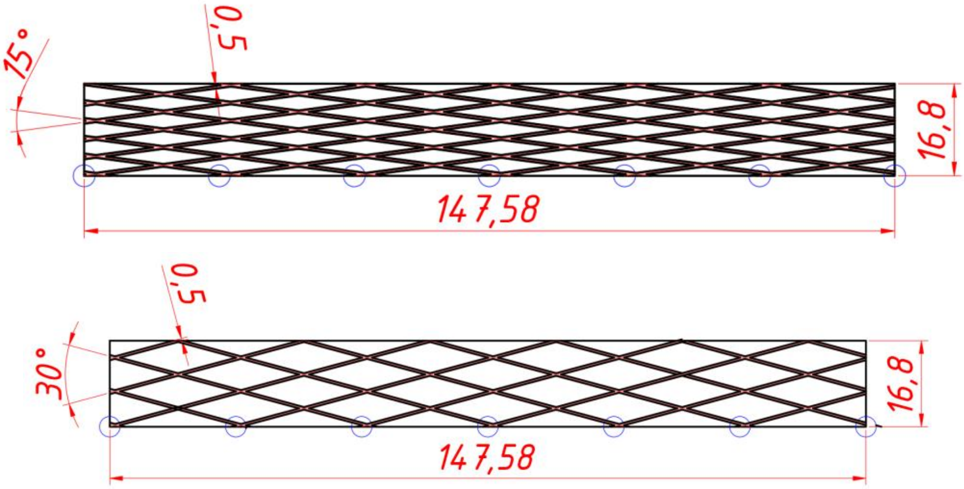

Fig. 1. Unfolded view of two pairs of Volvo V50 1.6 HDI connecting rod bearings for the formation of regular micro-reliefs with a relative micro-relief area of 28.5% and 14.9%

In this case, the axial feed of the tool f_{in} is determined from equation (2).

$$f_{in} = \pi D_{ring} tg(\gamma_{c.g}/2) \tag{2}$$

Thus, the feed rate required to achieve a relative micro-relief area of 28.5% is f_{in} = 19.43 mm/rev, whereas for an area of 14.9%, it is f_{in} = 39.56 mm/rev. The calculations were performed taking into account that the deforming elements form a groove with a width of 0.5 mm.

The formation of a regular micro-relief on the working surfaces via plastic deformation significantly reduces the height of surface micro-asperities, particularly those involved in contact interaction during the initiation of the adhesive seizure process. The generation of the regular micro-relief on the working surface must be carried out during the finishing stage of machining the copper-lead base of the bearing, which has a thickness of 250–400 µm. Only after the regular micro-relief has been formed should the protective metal layers of nickel, copper, or composite materials be applied. A dimensional analysis [24] of the tool design was conducted using the method of complete interchangeability by solving the inverse problem of the dimensional chain. Based on the performed calculations, the nominal dimensions and tolerance zones of the tool's closing link were determined, taking into account the elastic and elasto-plastic deformation of the surface layer material. The proposed tool design (Fig. 2) provides the capability for the continuous adjustment of the protrusion height of the deforming elements within a range of 47–48 mm.

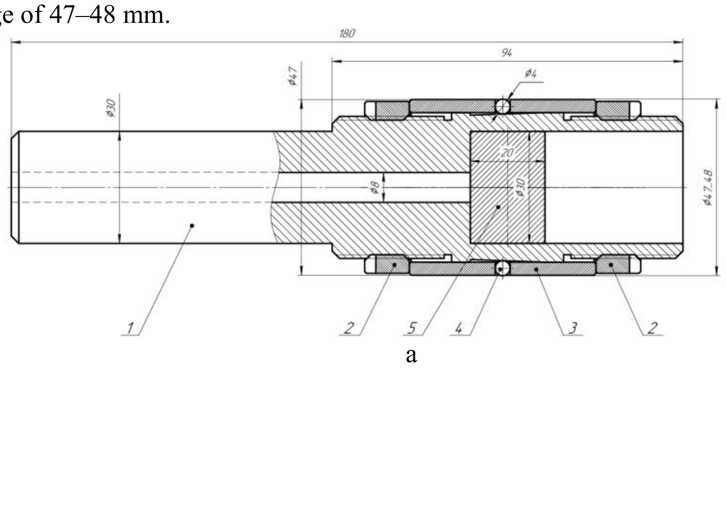

a

b

Fig. 2. Tool for forming a regular micro-relief on the inner surface of connecting rod bearings: a – drawing; b – actual view 1 – tool body; 2 – front and rear nuts; 3 – cage; 4 – deforming elements; 5 – magnet

The application of the developed tool enables the formation of surfaces with an optimal relative micro-relief area, thereby enhancing the oil retention capacity and operational reliability of internal combustion engine connecting rod bearings.

Adjusting the protrusion height of the deforming elements allows them to penetrate the surface of the connecting rod bearings to various depths, consequently forming grooves of varying widths.

It was decided to use the base of the connecting rod for these bearings as the technological tooling (the holding fixture), since its internal mounting diameter is precisely fitted to the outer diameter of the connecting rod bearings (Fig. 3). The fixture possesses sufficient stiffness to ensure the plastic deformation of the bearing surface.

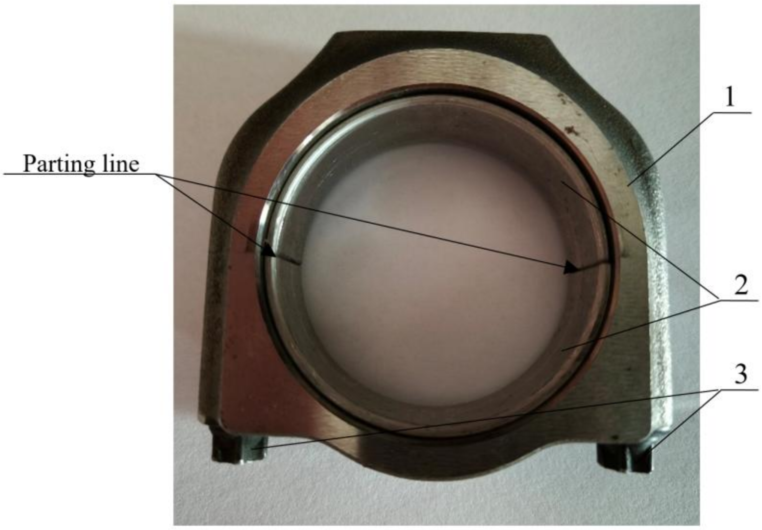

Fig. 3. Split holding fixture for the formation of regular micro-reliefs on the working surfaces of connecting rod bearings: 1 – fixture body; 2 – connecting rod bearings; 3 – fastening elements

The process of forming the micro-relief grooves was performed on a HAAS VF-B/40HE CNC vertical milling machine. The regular micro-reliefs obtained on the working surfaces of the connecting rod bearings are shown in Fig. 4.

a) b)

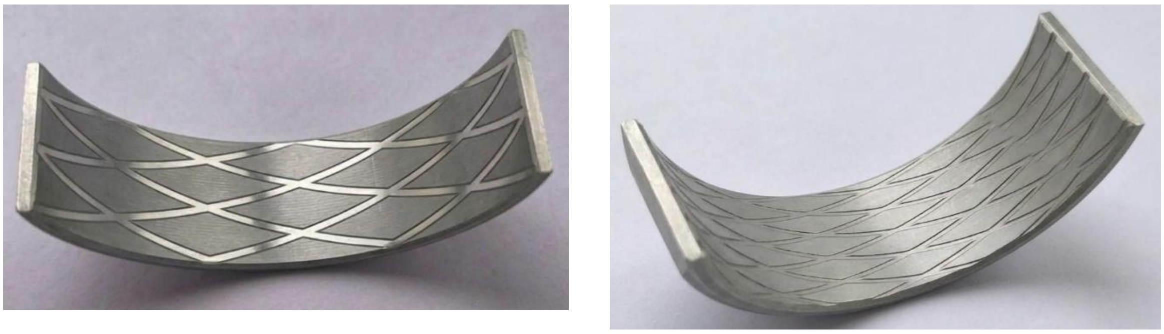

c) d)

Fig. 4. Internal combustion engine connecting rod bearings: a – without the formation of a regular micro-relief; b – with the formation of a regular micro-relief using a Ø3.5 mm deforming element and a relative micro-relief area of 14.9%; c – with the formation of a regular micro-relief using a Ø4.0 mm deforming element and a relative micro-relief area of 14.9%; d – with the formation of a regular micro-relief using a Ø3.5 mm deforming element and a relative micro-relief area of 28.5%

The depth of the grooves in the formed micro-relief is related to their width, as the grooves are formed by a spherical deforming element. Therefore, by varying the diameter of the deforming element and positioning it on different parts of the tool's conical surface, grooves can be formed within a relatively narrow yet sufficient range of geometric parameters. An increase in the diameter of the deforming element widens the groove but reduces its depth, and conversely, a decrease in the deforming element's diameter narrows the groove and increases its depth. Altering the diameter of the deforming element changes not only the groove parameters but also the physics of the interaction between the contacting surfaces. A smaller diameter of the deforming element results in a smaller contact area, which consequently increases the specific pressures within the contact zone.

This groove shape in the formed micro-relief correlates with the optimal groove design for plain bearings, which feature a "herringbone" geometry that ensures a guaranteed level of lubricant in the friction zone [25]. The eccentricity ratio, number of grooves, spiral angle, groove width ratio, and groove depth are selected as the key factors for designing a spiral-groove plain bearing. Under normal operating conditions, the heat generated by friction is dissipated and absorbed by the engine housing; wear debris is minimal and is continuously removed by the lubricant circulating within the friction zone.

Although the groove formation operation demonstrated excellent results regarding the shape of the formed micro-relief grooves, this process leads to the destruction of the antifriction coating and the formation of material pile-ups at the edges of the created grooves, which can negatively affect operational performance. Therefore, the process of forming the regular micro-relief grooves should be carried out prior to the application of the antifriction coating.

Conclusions

A technological operation was developed for the formation of Type II regular micro-reliefs on the inner cylindrical surfaces of a pair of connecting rod bearings by machining in a split holding fixture using a vibration-free method in a single pass. To implement the process of forming the regular micro-relief (RMR) on the working surfaces of Volvo V50 1.6 HDI connecting rod bearings, a special tool was designed and manufactured based on dimensional analysis. The operating parameters of the tool were calculated in accordance with the required value of the relative micro-relief area to be achieved. The implementation of this operation made it possible to form the designed regular micro-relief with the specified geometric parameters.

References

1. Taylor, C. M. (1998). Automobile engine tribology–design considerations for efficiency and durability. *Wear*, *221*(1), 1–8. https://doi.org/10.1016/S0043-1648(98)00253-1

2. Aulin, V., Lysenko, S., Hrynkiv, A., Liashuk, O., Hupka, A., & Livitskyi, O. (2022). Parameters of the lubrication process during operational wear of the crankshaft bearings of automobile engines. *Problems of Tribology*, *27*(4), 69–81. https://doi.org/10.31891/2079-1372-2022-106-4-69-81

3. Santos, N. D. S. A., Roso, V. R., & Faria, M. T. C. (2020). Review of engine journal bearing tribology in start-stop applications. *Engineering Failure Analysis*, *108*, Article 104344. https://doi.org/10.1016/j.engfailanal.2019.104344

4. Tala-Ighil, N., Fillon, M., & Maspeyrot, P. (2011). Effect of textured area on the performances of a hydrodynamic journal bearing. *Tribology International*, *44*(3), 211–219. https://doi.org/10.1016/j.triboint.2010.10.003

5. Tomoko, H., Naomi, Y., Shingo, S., Noriaki, H., Takashi, M., & Hiroshi, Y. (2009). Optimization of groove dimensions in herringbone-grooved journal bearings for improved repeatable run-out characteristics. *Tribology International*, *42*(5), 675–681. https://doi.org/10.1016/j.triboint.2008.09.006

6. Ashihara, K., & Hashimoto, H. (2010). Theoretical modeling for microgrooved journal bearings under mixed lubrication. *Journal of Tribology*, *132*(4), Article 041501. https://doi.org/10.1115/1.4002214

7. Thomazi, C., Pérez, M., & Syngellakis, S. (2005, November 6–11). *Two dimensional analysis of precision insert bearing interference fit* [Paper presentation]. 18th International Congress of Mechanical Engineering (COBEM), Ouro Preto, Brazil. https://abcm.org.br/anais/cobem/2005/PDF/COBEM2005-0923.pdf

8. Syngellakis, S., & Burke-Veliz, A. (2012). Residual and cyclic stresses in automotive plain bearings. *WIT Transactions on Engineering Sciences*, *76*, 189–200. https://www.witpress.com/elibrary/wit-transactions-on-engineering-sciences/76/23772

9. Yang, B., Shi, F., Fisher, J. B., & Wilson, Q. A. (2019). *Journal bearings with surface features for improved bearing oil supply* (U.S. Patent No. 10,233,970). U.S. Patent and Trademark Office. https://patents.google.com/patent/US10233970B2

10. Avan, E. Y., Spencer, A., Dwyer-Joyce, R. S., Almqvist, A., & Larsson, R. (2012). Experimental and numerical investigations of oil film formation and friction in a piston ring–liner contact. *Proceedings of the Institution of Mechanical Engineers, Part J: Journal of Engineering Tribology*, *227*(2), 126–140. https://doi.org/10.1177/1350650112464706

11. Wei, S. J., Wang, J. R., Cui, J., Song, S. S., Li, H. C., & Fu, J. F. (2022). Online monitoring of oil film thickness of journal bearing in aviation fuel gear pump. *Measurement*, *204*, Article 112050. https://doi.org/10.1016/j.measurement.2022.112050

12. Zhang, Y., Wang, W., Zhang, S., et al. (2016). Optical analysis of ball-on-ring mode test rig for oil film thickness measurement. *Friction*, *4*(4), 324–334. https://doi.org/10.1007/s40544-016-0127-5

13. Hashizume, K., et al. (1995). Performance of microgrooved bearings in automotive engines. Part 1 [In Japanese with English summary]. *Proceedings of the Society of Automotive Engineers of Japan*, No. 9539752. https://doi.org/10.2474/trol.3.304

14. Kumada, Y., Hashizume, K., & Kimura, Y. (1996). Performance of microgrooved bearings in automotive engines. Part 2 [In Japanese with English summary]. *Proceedings of the Society of Automotive Engineers of Japan*, No. 9633900.

15. Laguna-Camacho, J. R., Sánchez-Yáñez, S. M., Juárez-Morales, G., Cruz-Orduña, M. I., Ramos-González, L. M., Cortez-Domínguez, C., … Calderón-Sánchez, J. (2020). A wear analysis carried on connecting rod bearings from internal combustion engines. *IntechOpen*. https://doi.org/10.5772/intechopen.89263

16. Yin, J., Zhang, R., Lyu, B., & Meng, X. (2024). Temperature evolution prediction of engine big-end bearing by tribo-dynamics modeling and wireless measurement verification. *Tribology International*, *194*, Article 109548. https://doi.org/10.1016/j.triboint.2024.109548

17. Kato, T., & Obara, S. (1996). Improvement in dynamic characteristics of circular journal bearings by means of longitudinal microgrooves. *Tribology Transactions*, *39*(2), 462–468. https://doi.org/10.1080/10402009608983553

18. Adatepe, H., Bıyıklıoglu, A., & Sofuoglu, H. (2013). An investigation of tribological behaviors of dynamically loaded non-grooved and micro-grooved journal bearings. *Tribology International*, *58*, 103–110. (Зазначено лише том). https://doi.org/10.1016/j.triboint.2012.09.009

19. Karimaei, H., & Chamani, H. (2009). Study of cavitation and wear damages in conrod big end bearing of a heavy duty diesel engine by using elasto-hydrodynamic method. *Proceedings of the ASME Internal Combustion Engine Division Fall Technical Conference 2009*. https://doi.org/10.1115/ICEF2009-14091

20. Galda, L., Pawlus, P., & Sep, J. (2009). Dimples shape and distribution effect on characteristics of Stribeck curve. *Tribology International*, *42*(10), 1505. https://doi.org/10.1016/j.triboint.2009.06.001

21. Galda, L., Dzierwa, A., Sep, J., & Pawlus, P. (2009). The effect of oil pockets shape and distribution on seizure resistance in lubricated sliding. *Tribology Letters*, *37*(2), 301–311. https://doi.org/10.1007/s11249-009-9522-7

22. Pawlus, P., Koszela, W., & Reizer, R. (2022). Surface texturing of cylinder liners: A review. *Materials*, *15*(23), Article 8629. https://doi.org/10.3390/ma15238629

23. Wos, S., Koszela, W., & Pawlus, P. (2020). Comparing tribological effects of various chevron-based surface textures under lubricated unidirectional sliding. *Tribology International*, *146*, Article 106205. https://doi.org/10.1016/j.triboint.2020.106205

24. Dzyura, V., Dzhyvak, T., & Kyryk, S. (2026). Design of a tool for forming regular microreliefs on the working surfaces of connecting rod inserts. *Herald of Khmelnytskyi National University. Technical Sciences*, *365*(3), 181–186. https://doi.org/10.31891/2307-5732-2026-365-27

25. Zhang, G., Tang, S., Zheng, Y., He, J., Cui, H., & Liu, Y. (2023). Numerical and experimental investigation on the performances of a liquid metal bearing with spiral groove structures. *Tribology International*, *185*, Article 108526. https://doi.org/10.1016/j.triboint.2023.108526

Дзюра В.О., Дживак Т.Р. Реалізація процесу формування регулярних мікрорельєфів на робочих поверхнях шатунних підшипників

В статті наведено результати проектування технологічної операції формування регулярного сітчастого мікрорельєфу II типу із канавками трикутної форми безвібраційним способом за один робочий хід на внутрішній циліндричній поверхні шатунних вкладишів. Технологічну операцію реалізовано з використання спеціально розробленого інструменту обробкою в розбірній обоймі пари шатунних вкладишів. В якості обоми використано корпус шатуна для даного типорозміру шатунних вкладишів. Необхідну глибину канавок мікрорельєфу реалізовано за рахунок розмірного аналізу конструкції спроектованого спеціального інструменту для пластичного деформування поверхні шатунного вкладиша. Відносну площу мікрорельєфу у 14,9% та 28,5% досягнуто визначенням відповідної величини подачі та частоти обертання інструменту. Отримано дослідні зразки шатунних вкладишів для автомобіля Volvo V50 1.6 HDI та параметрами D_{ring} = 47,0 mm; B_{ring} = 16,9 mm із сформованим регулярним мікрорельєфом. Процес реалізовано при осьовій подачі інструменту складає f_{in} = 19,43 мм/об, а для площі 14,9% – f_{in} = 39,56 мм/об на вертикально-фрезерному верстаті з ЧПК HAAS VF-B/40HE. Встановлено, що дану технологічну операцію можна виконувати як на стадії фінішної обробки мідно-свинцевої основи вкладиша, товщина якої становить 250-400 мкм, безпосередньо перед нанесенням захисних металевих шарів нікелю, міді та/або композитних матеріалів так і після нанесення захисного покриття. Створення регулярного мікрорельєфу забезпечуючи високу експлуатаційну надійність, довговічність та стабільну роботу шатунних вкладишів і двигуна внутрішнього згоряння в цілому.

Ключові слова: шатунні вкладиші, технологія, інструмент, параметри, режими формування, регулярний мікрорельєф

ISSN 2079-1372 Problems of Tribology, V. 31, No 3/121-2026, 13-18

Problems of Tribology
Website: http://tribology.khnu.km.ua/index.php/ProbTrib
E-mail: tribosenator@gmail.com

DOI: https://doi.org/10.31891/2079-1372-2026-121-3-13-18

Transformation of groove area distribution non-uniformity in partially regular microrelief of the rotational type with increasing axial pitch

I.B. Zinchenko[1] 0009-0007-6504-939X, **A.M. Savchuk**[2] 0000-0001-5460-4879, **V.Y. Fediv**[1] 0009-0009-2067-1120, **O.Y. Kruk**[1] 0000-0001-6431-1287

[1]*Ternopil Ivan Puluy National Technical University, Ukraine*
[2]*National transport university*
E-mail: volodymyrdzyura@gmail.com

Received: 25 June 2026: Revised 12 July 2026: Accept: 25 July 2026

Abstract

The transformation of the groove shape in a rotary-type regular micro-relief with varying degrees of groove loop overlap, simulated by an increase in the rotary tool feed rate, is considered. A search was conducted to find the optimal groove shape for partially regular micro-reliefs formed by the rotary method, subject to ensuring the optimal value of the planar heterogeneity coefficient of the groove area distribution. Graphs illustrating the planar heterogeneity of the groove area distribution were constructed for groove shapes formed at tool feed rates of f_g = 2, 2.5, and 3.5 mm/s. It was established that as the longitudinal spindle feed rate increases, the planar heterogeneity coefficient of the groove area distribution, k_g, decreases in both the axial direction and the direction perpendicular to it. Concurrently, the parameters R_{Xmax} and R_{Xaver} increase, whereas R_{Ymax} and R_{Yaver} decrease. The relative area of the micro-relief also decreases as a result. Thus, it is proven that increasing the tool feed rate at a constant rotational speed leads to an increase in the heterogeneity of the groove area distribution for a partially regular micro-relief formed by the rotary method. Optimization of the micro-relief creates a favorable profile of compressive residual stresses, preventing the propagation of microcracks. As the tool feed rate increases, the number of groove intersections decreases from 4 to 2, and the shape itself becomes elongated in the axial direction. Correspondingly, the planar heterogeneity coefficients k_{gX} decrease from 0.69 to 0.48, and k_{gY} decrease from 0.71 to 0.6. The overall relative area of the micro-relief, F_n, drops sharply from 68.48% to 45.9%, which is a critical parameter for determining the load-bearing capacity of the component surfaces.

Keywords: regular micro-reliefs; grooves; planar heterogeneity; area distribution; coefficient; quantitative assessment; parameters

Introduction

Enhancing the operational characteristics of the working surfaces of machine components through technological methods is a highly relevant objective for researchers in the field of surface engineering. In this context, novel types of surface structures capable of providing the required level of operational properties over a specified service period are being investigated. One of the effective approaches to achieving such properties is surface regularization. It involves the creation of asperities with a predetermined shape, dimensions, and spatial arrangement, which contributes to the improvement of the physical and mechanical characteristics of the surface. The primary purpose of regularization is to reduce the proportion of random asperities with uncontrolled shapes and sizes. The fraction of ordered micro-asperities is characterized by the relative area of the micro-relief, which is defined as the ratio of the area of the regular micro-asperities to the total area of the surface on which they are formed. It is this specific parameter that significantly influences the operational properties of the surface, and its optimal value is determined taking into account specific operating conditions. In this regard, investigating the features of new types of regular and partially regular micro-reliefs represents a crucial stage in the search for rational forms of regular micro-asperities capable of ensuring the specified operational characteristics for the working surfaces of machine components.

Literature review

Copyright © 2026 I.B. Zinchenko, A.M. Savchuk, V.Y. Fediv, O.Y. Kruk. This is an open access article distributed under the Creative Commons Attribution License, which permits unrestricted use, distribution, and reproduction in any medium, provided the original work is properly cited.

The creation of new types of regular and partially regular micro-reliefs opens up new possibilities for ensuring enhanced operational properties of the working surfaces of machine components. Traditional micro-relief groove shapes–triangular and sinusoidal–although providing a high degree of micro-relief regularity, still remain difficult to form on general-purpose machine tools. This is associated with the challenge of ensuring the regularity of the micro-relief grooves, which is particularly evident on long surface sections. Furthermore, the mechanisms that provide a periodic groove profile with a specific amplitude and a symmetrical arrangement of the groove elements necessitate special tooling and require additional balancing, which consequently complicates the design of the respective equipment.

Working surfaces in the form of cycloidal curves are widely used in cycloidal drives [1], which are employed as actuators in industrial robots, machine tools, aerospace, and other industrial sectors. These transmissions provide a high gear ratio, low weight, compact dimensions, high precision, and impact resistance [2, 3].

As is known, the primary parameter determining the operational properties of a surface with a regular micro-relief–specifically, the coefficient of mutual friction–is the relative area of the micro-relief, which depends on the total area of the micro-relief grooves [4].

While the area of micro-relief grooves of standard shapes and their intersections can be relatively easily determined analytically [5, 6], calculating the area for complex groove shapes remains an unresolved task.

From the perspective of creating various types of micro-reliefs using a rotary tool, the study [7] is of particular interest. The authors developed a mathematical model of the tool's kinematics and the resulting micro-relief profiles formed by it, depending on its operating parameters. It has been demonstrated that face milling allows for the formation of partially regular micro-reliefs featuring various groove shapes and spatial arrangements–specifically, parallel grooves and grooves offset by a fraction of the pitch. Additionally, a 2-DOF (degrees of freedom) vibration platform was developed to provide oscillation along the feed and cross-feed directions during the micro-milling process.

The study [8] investigates the characteristics of forming trochoidal and elliptical grooves. Trochoidal and elliptical modified trochoidal tool trajectories were analyzed, along with the distance between loops, overlap, feed rate, and spindle speed. The proposed method for forming a micro-relief with such groove shapes allows for the optimization of the tool trajectory in order to reduce surface roughness.

The formation of trochoidal micro-relief grooves ensures enhanced operational parameters of the surface, specifically its microhardness [9], which can be increased by 60% relative to the initial value. This machining method yields lower surface roughness parameters compared to conventional milling.

The positive impact on the uniformity of the distribution of surface micro-asperities during machining with a rotary tool utilizing spherical deforming elements is presented in [10]. It has been proven that a radical improvement in the degree of surface isotropy–specifically, an increase of over 80% – could be achieved by employing tools that, in addition to the primary burnishing feed motion, feature an additional rotational movement of the burnishing head (equipped with a greater number of burnishing balls or rollers).

The aim of this work is to determine the variation in the heterogeneity of the groove area distribution for a rotary-type partially regular micro-relief with an increase in the axial pitch, as well as to identify the optimal groove shape of a partially regular micro-relief formed by a rotary method, for which the value of the groove area distribution uniformity coefficient is as close to the optimum as possible, i.e., to 1.

Research materials and methodology

An increase in the productivity of forming partially regular micro-reliefs is associated with an increase in the feed rate of the deforming tool f. Increasing the feed rate while maintaining a constant tool rotational speed leads to a change in the groove shape of the partially regular micro-relief formed by the rotary method. Altering the micro-relief groove shape results in a redistribution of microhardness in the vicinity of the groove, which significantly affects the uniformity of the groove distribution across the plane where the micro-relief is formed. Thus, the uniformity of the groove area distribution across the plane leads to a uniform distribution of surface microhardness. With a dense arrangement of grooves, corresponding to low feed rate values, the plastic deformation zones from adjacent indenter passes overlap. This leads to the formation of a continuous or more uniformly hardened layer with increased microhardness. When the loops are stretched, corresponding to high feed rate values, the hardening becomes local (only within the zone of the grooves themselves), while areas with the initial hardness remain between them.

Plastic deformation generates beneficial compressive residual stresses in the surface layer. Modifying the shape of the groove mesh allows for the formation of a specific framework of compressive stresses. The optimal loop density creates a favorable stress distribution profile that prevents the initiation and propagation of microcracks.

There is an optimal value for the relative groove area (typically within the range of 25–40%, depending on operating conditions). Deviations from the optimal trajectory shape (excessive overlap or, conversely, an excessively sparse mesh) lead to a reduction in wear resistance due to decreased load-bearing capacity or insufficient lubrication, respectively.

As is evident, an increase in the feed rate results in a decrease in the number of micro-relief groove intersections. In Fig. 1a, the number of intersections is 4; in Fig. 1b, it is 3; and in Fig. 1c, it is 2. The number of groove intersections and the distance between them, l_d (Fig. 1), constitute some of the most critical parameters determining the surface topology. At the intersection points of the tool trajectories, specific nodes are formed where the material is subjected to a dual deforming impact. This creates distinct conditions that differ significantly from areas featuring isolated grooves. At the groove intersection points, the indenter passes twice, which leads to more intensive plastic deformation. Consequently, at the intersection nodes, the microhardness of the material reaches its maximum values, and the depth of the hardened layer is the greatest compared to other regions of the surface. If the number of intersections is excessively high (indicating a very dense mesh), the repeated plastic deformation of the same metal micro-volumes can lead to the exhaustion of its plasticity – a phenomenon known as over-work hardening. This causes the formation of microcracks, the flaking of the surface layer, and a sharp reduction in fatigue strength.

To determine the variation in the uniformity parameters of the groove area distribution on the plane where the partially regular micro-relief is formed, we will simulate an increase in the tool's traverse speed – that is, an increase in its feed rate – which will result in a corresponding increase in the axial pitch T_g of the micro-relief grooves. The formed grooves possess an identical amplitude value, A_g, but differ in their axial groove pitch values, T_g. The coordinate grid in the figure is specified in millimeters (Fig. 1).

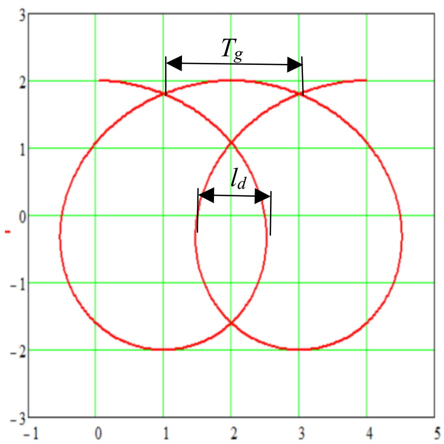

a

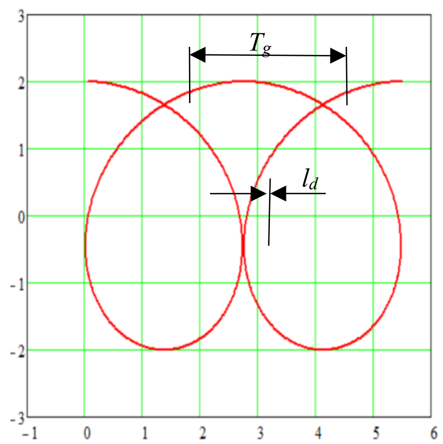

b

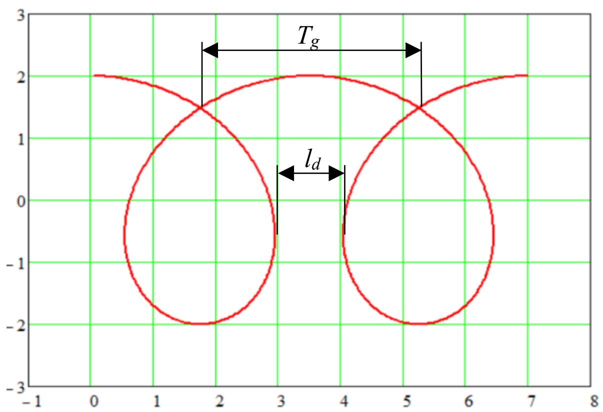

c

Fig. 1. Transformation of the groove centerline trajectory of a rotary-type regular micro-relief with an increase in feed rate: a – f_g = 2 mm/s; b – f_g = 2.75 mm/s; c – f_g = 3.5 mm/s.

The essence of the method for determining the planar heterogeneity of the groove area distribution in regular or partially regular micro-reliefs is described in detail in [11]. This method allows for determining the optimal mutual arrangement of the micro-relief grooves, at which their area will be distributed most uniformly. This will ensure consistent operational properties of the surface with a regular micro-relief across any of its regions.

The method for determining the planar heterogeneity of the groove area distribution involves determining several parameters, specifically the planar heterogeneity coefficient k_g, and the parameters R_{max} and R_{aver}.

The heterogeneity coefficient k_g is defined as the ratio of the average value R_{aver} to the maximum groove height R_{max}.

$$k_g = \frac{R_{aver}}{R_{\max}} \tag{1}$$

The value of this coefficient is determined in the axial or transverse directions. Under the condition of a completely uniform distribution of the groove area, the value of the coefficient will be 1. The degree of proximity to this value reflects the level of uniformity of the groove area distribution in the selected direction.

The average value of the groove cross-section is determined by the formula:

$$R_{aver} = \frac{\sum_{i=1}^{n} h_{gi}}{n} \tag{2}$$

where h_{Ygi} (h_{Xgi}) – height of the i-th segment on the corresponding planar heterogeneity graph, mm.

The calculated height values h_{Ygi} are determined within the axial pitch T_g for the axial planar heterogeneity graph, whereas the height values h_{Xgi} are determined within the transverse pitch of magnitude $2A_g$+b_g for the transverse planar heterogeneity graphs. The value A_g corresponds to the groove amplitude, and b_g to its width.

For comparison, we will simulate the groove shape of a rotary micro-relief during its transformation as the feed rate increases. The parameters of the micro-relief groove are as follows: R_g = 2 mm; n_g = 1 rev/s, and groove width b_g= 0.5 mm.

To determine the main parameters of the uniformity of the groove area distribution, it is necessary to construct graphs of their planar distribution (Fig. 2).

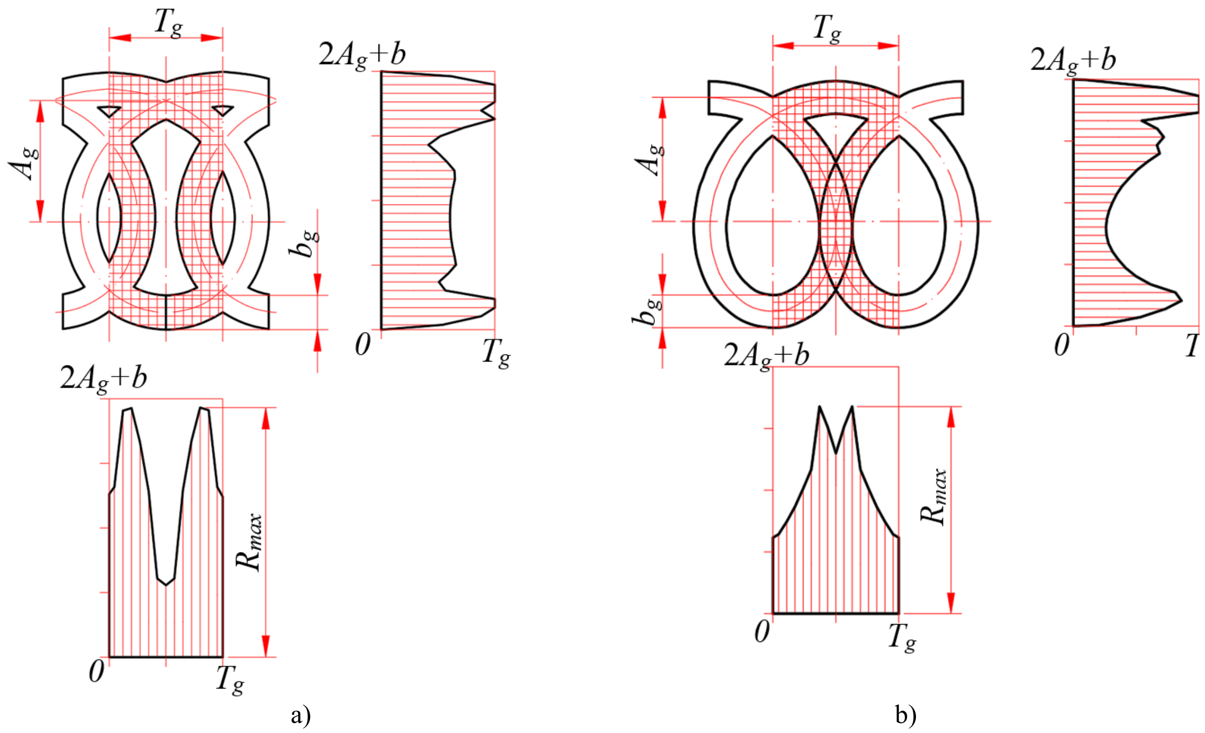

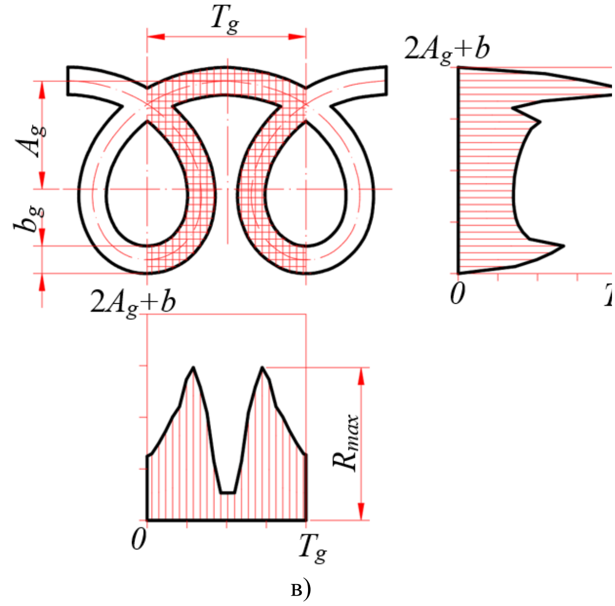

Fig. 2. Graphs of planar heterogeneity of the groove surface area distribution of a rotary-type partially regular micro-relief, obtained for a feed rate: а – f_g =2 mm/s; б – f_g =2,75 mm/s; в – f_g=3,5 mm/s

The results of determining the parameters of the graphs of planar heterogeneity of their area distribution, obtained by increasing the axial pitch through an increased tool feed rate, are presented in Table 1.

As is evident from Table 1, the coefficients of planar heterogeneity of the groove area distribution decrease with an increase in the tool feed rate and the axial groove pitch.

Table 1

Values of parameters and coefficients of planar heterogeneity for grooves of a rotary-type partially regular micro-relief

Measurement parameters	Feed rate		
	f_g =2 mm/s	f_g =2,75 mm/s	f_g=3,5 mm/s
R_{Xmax}	1,71	1,99	2,97
R_{Xaver}	1,18	1,08	1,41
k_{gX}	**0,69**	**0,54**	**0,48**
R_{Ymax}	3,76	3,26	2,86
R_{Yaver}	2,66	2,11	1,72
k_{gY}	**0,71**	**0,65**	**0,6**
F_n, %	68,48	54,33	45,9

Moreover, this decrease occurs both along the axial line of the groove and in the perpendicular direction. This indicates that, despite the groove amplitude remaining constant at 0.5 mm, the heterogeneity coefficient of the groove area distribution along the Y-axis, k_{gX}, decreased from 0.69 to 0.48. At the same time, the increase in the tool feed rate led to an increase in the axial groove pitch. As a result, its shape stretched in the axial direction, which also led to a decrease in the uniformity coefficient of the groove area distribution, k_{gY}, from 0.71 to 0.6. Accordingly, the relative area of the micro-relief, F_n, also decreased from 68.48% to 45.9%.

Conclusions

Based on the text of the provided article, the following conclusions can be formulated:

With an increase in the feed rate of the rotary tool (from 2 to 3.5 mm/s) at a constant rotational speed, the heterogeneity of the groove area distribution for the partially regular micro-relief formed by the rotary method increases.

As the longitudinal spindle feed rate increases, with a corresponding increase in the axial groove pitch, the coefficients of planar heterogeneity of the groove area distribution decrease both in the perpendicular direction, k_{gX}, from 0.69 to 0.48, and in the axial direction, k_{gY}, from 0.71 to 0.6. The increase in the tool feed rate affects the uniformity parameters of the groove area distribution; specifically, R_{Xmax} increases from 1.71 to 2.97, and R_{Xaver} grows from 1.18 to 1.41. Conversely, R_{Ymax} decreases from 3.76 to 2.86, and R_{Yaver} decreases from 2.66 to 1.72.

An increase in the feed rate from f_g = 2 to 3.5 mm/s leads to a reduction in the number of micro-relief groove intersections from 4 to 2. However, this simultaneously causes the groove shape to stretch in the axial direction, which results in a substantial decrease in the overall relative area of the micro-relief, F_n, from 68.48% to 45.9%.

References

1. Li, X.; Tang, L.; He, H.; Sun, L. Design and Load Distribution Analysis of the Mismatched Cycloid-Pin Gear Pair in RV Speed Reducers. Machines 2022, 10, 672. https://doi.org/10.3390/ machines10080672

2. Wang, H.; Shi, Z.-Y.; Yu, B.; Xu, H. Transmission Performance Analysis of RV Reducers Influenced by Profile Modification and Load. *Appl. Sci.* **2019**, *9*, 4099. https://doi.org/10.3390/app9194099

3. Zhang, T.; Li, X.; Wang, Y.; Sun, L. A Semi-Analytical Load Distribution Model for Cycloid Drives with Tooth Profile and Longitudinal Modifications. *Appl. Sci.* **2020**, *10*, 4859. https://doi.org/10.3390/app10144859

4. Zhan X, Yi P, Liu Y, Xiao P, Zhu X, Ma J. Effects of single- and multi-shape laser-textured surfaces on tribological properties under dry friction. Proceedings of the Institution of Mechanical Engineers, Part C: Journal of Mechanical Engineering Science. 2020;234(7):1382-1392. doi:10.1177/0954406219892294

5. Dzyura, V., Maruschak, P., Kozbur, H., Kryvyi, P., and Prentkovskis, O. Determining Optimal Parameters of Grooves of Partially Regular Microrelief Formed on End Faces of Rotary Bodies. ASTM International. Smart Sustain. Manuf. Syst.. January 2021; 5(1): 18–29. https://doi.org/10.1520/SSMS20200057

6. Dzyura, V.; Maruschak, P.; Prentkovskis, O. Determining Optimal Parameters of Regular Microrelief Formed on the End Surfaces of Rotary Bodies. *Algorithms* 2021, *14*, 46. https://doi.org/10.3390/a14020046

7. Song, B.; Zhang, D.; Jing, X.; Ren, Y.; Chen, Y.; Li, H. Theoretical and Experimental Investigation of Surface Textures in Vibration-Assisted Micro Milling. Micromachines 2024, 15, 139. https://doi.org/10.3390/ mi15010139

8. Zsolt Kovács, Gábor Kónya, Balázs Markó, György Póka. Experimental and theoretical investigation of the influence of tool paths and burnishing parameters on the quality of the burnished surface by magnetic assisted ball burnishing. Results in Engineering. Volume 27. 2025. 105779. https://doi.org/10.1016/j.rineng.2025.105779

9. Zsolt F. Kovács, Zsolt J. Viharos, János Kodácsy. Surface flatness and roughness evolution after magnetic assisted ball burnishing of magnetizable and non-magnetizable materials. Measurement. Volume 158. 2020. 107750. https://doi.org/10.1016/j.measurement.2020.107750

10. Grochała, D.; Grzejda, R.; Józwik, J.; Siemi ̨ atkowski, Z. Improving the Degree of Surface Isotropy of Parts Manufactured Using Hybrid Machining Processes. Coatings 2025, 15, 461. https://doi.org/ 10.3390/coatings15040461

11. Dzyura, V.; Maruschak, P.; Bytsa, R.; Zinchenko, I. Planar Non Uniformity of Regular and Partially Regular Microreliefs and Method for Its Evaluation. Eng 2025, 6, 314. https://doi.org/10.3390/ eng6110314

Зінченко І.Б., Савчук А.М., Федів В.Я., Крук О.Ю. Трансформація неоднорідності розподілу площі канавок частково регулярного мікрорельєфу ротаційного типу зі збільшенням осьового кроку

Розглянуто трансформації форми канавок ротаційного РМР із різним ступенем перекриття витків канавки, яке змодельовано збільшенням швидкості подачі ротаційного інструменту. Проведено пошук оптимальної форми канавок частково регулярних мікрорельєфів сформованих ротаційним способом, за умови забезпечення оптимального значення коефіцієнта площинної нерівномірності розподілу площі канавок. Побудовано графіки площинної нерівномірності розподілу площі канавок для форм канавок сформованих при подачі інструменту f_g = 2, 2,5 та 3,5 мм/с. Встановлено, що із зростанням величини повздовжньої подачі шпинделя коефіцієнт площинної нерівномірності розподілу площі канавок k_g зменшується як в осьовому так і в перпендикулярному до нього напрямку. При цьому параметри R_{Xmax} та R_{Xaver} зростають, а R_{Ymax} та R_{Yaver} зменшуються. Відносна площа мікрорельєфу при цьому також зменшується. Таким чином доведено, що при збільшенні швидкості подачі інструменту при незмінній частоті обертання нерівномірність розподілу площі канавок частково регулярного мікрорельєфу, сформованого ротаційним способом збільшується.

Ключові слова: регулярні мікрорельєфи; канавки; площинна неоднорідність; розподіл площин; коефіцієнт; кількісна оцінка; параметри

ISSN 2079-1372 Problems of Tribology, V. 31, No 3/121-2026, 19-26

Problems of Tribology

Website: http://tribology.khnu.km.ua/index.php/ProbTrib
E-mail: tribosenator@gmail.com

DOI: https://doi.org/10.31891/2079-1372-2026-121-3-19-26

Numerical Rheological Modeling of Thin Lubricating Oil Films Considering Polymolecular Adsorption and ZDDP

I. Drach0000-0003-0590-9814, **M. Dykha** 0000-0002-6075-1549, **D. Tovstiuk**

Khmelnytskyi National University, Ukraine
E-mail: drachil@khmnu.edu.ua

Received: 30 June 2026: Revised 18 July 2026: Accept: 30 July 2026

Abstract

A numerical rheological model of a thin lubricating oil film was developed and verified to account for polymolecular adsorption, pseudo-solid adsorption layers, and the influence of zinc dialkyldithiophosphate (ZDDP) on the rheological properties of the lubricating film. The model adapts the concept of the Polanyi adsorption potential to describe the viscosity distribution across the film thickness, incorporating pseudo-solid adsorption layers adjacent to both friction surfaces, while the effective viscosity is determined by harmonic averaging with numerical integration performed using the trapezoidal rule (n = 200) implemented in Microsoft Excel. Shear-thinning of the bulk lubricant is described by the Carreau–Yasuda model. Model parameters were identified by fitting calculated friction coefficients to experimental data obtained for base oil I-20A and oils containing 1.25 and 2.5 wt% ZDDP. The identified adsorption layer parameters increased systematically with ZDDP concentration: surface viscosity μ_s rose from 0.14 to 1.68 Pa·s, the characteristic decay length l_h from 2.1 to 4.6 nm, and the optimum pseudo-solid layer thickness h_s from 0.8 to 1.9 nm. The average relative deviation between calculated and experimental friction coefficients was 6.9–10.2%. The calculated pressure corresponding to the minimum friction coefficient shifted from approximately 5 MPa for the base oil to about 8 MPa for ZDDP-containing oils, indicating an expansion of the hydrodynamic lubrication regime. The developed model represents a novel numerical approach that combines polymolecular adsorption, pseudo-solid adsorption layers and non-Newtonian lubricant behaviour for thin-film lubrication, suggesting that—beyond tribochemical processes—an increase in the effective viscosity of the polymolecular adsorption layer makes a significant contribution to friction reduction in the mixed lubrication regime. The proposed Excel-based methodology enables identification of model parameters and comparative prediction of lubricant tribological performance without specialized numerical software, and may be used as an engineering tool for assessing the influence of ZDDP concentration on the tribological performance of lubricating oils for plain bearings.

Keywords: thin-film lubrication, polymolecular adsorption, ZDDP, pseudo-solid adsorption layer, effective viscosity, rheological modeling, friction coefficient.

Introduction

Current developments in internal combustion engines are focused on improving energy efficiency, reducing fuel consumption, and lowering exhaust emissions. One of the principal approaches to achieving these objectives is the use of low-viscosity engine oils, with a transition from conventional SAE 40–50 grades to SAE 0W-16 and even lower viscosity grades. However, reducing the bulk viscosity of the lubricant (μ_0) inevitably decreases the thickness of the hydrodynamic lubricating film and expands the mixed lubrication regime in heavily loaded tribological contacts, particularly in connecting-rod and main journal bearings, where contact pressures may reach 10–20 MPa [1, 2].

When the lubricant film thickness decreases to the submicrometre and nanometre scales, the rheological behaviour of the lubricant may differ significantly from its bulk properties. Experimental studies based on the surface forces apparatus (SFA) and molecular dynamics simulations have demonstrated that, when the separation between solid surfaces becomes smaller than approximately six to seven molecular layers, the apparent viscosity of the confined lubricant increases by several orders of magnitude and the lubricant may exhibit pseudo-solid behaviour [3, 4]. This phenomenon, commonly referred to as confinement-induced non-Newtonian behaviour, is

Copyright © 2026 I. Drach, M. Dykha, D. Tovstiuk. This is an open access article distributed under the Creative Commons Attribution License, which permits unrestricted use, distribution, and reproduction in any medium, provided the original work is properly cited.

generally attributed to the molecular ordering of the lubricant under adsorption forces and to the restricted molecular mobility normal to the solid surfaces.

Zinc dialkyldithiophosphate (ZDDP) is one of the most widely used anti-wear additives in modern engine oils. Its effectiveness has traditionally been attributed to the formation of protective tribochemical phosphate-based films on metallic surfaces during sliding contact [5, 6]. However, several experimental studies have reported a noticeable reduction in friction at the early stages of loading or under mixed lubrication conditions, where tribofilms are not yet fully developed [7]. These observations suggest that, in addition to tribochemical reactions, other physical mechanisms associated with changes in the structure and rheological properties of the adsorption layer may contribute to friction reduction.

Despite considerable progress in thin-film lubrication research, no engineering model is currently available that simultaneously accounts for polymolecular adsorption, the formation of pseudo-solid adsorption layers, the non-Newtonian rheology of the lubricant, and the influence of ZDDP on the rheological behaviour of thin lubricating films. Addressing this gap is essential for predicting the tribological performance of modern low-viscosity engine oils operating under mixed lubrication conditions.

The aim of this study is to develop and verify a numerical rheological model of a thin lubricating oil film based on the concept of polymolecular adsorption, incorporating pseudo-solid adsorption layers and non-Newtonian lubricant behaviour, and to validate the proposed model using experimental friction data obtained for the base oil I-20A and oils containing different concentrations of ZDDP. The numerical implementation was developed in Microsoft Excel to provide an engineering-oriented methodology suitable for practical tribological analysis without specialized computational software.

Literature review

Classical elastohydrodynamic lubrication (EHL) theory, developed by Dowson and Higginson [8], assumes that the lubricant viscosity is uniformly distributed across the film thickness. This assumption provides satisfactory accuracy for conventional hydrodynamic contacts; however, its applicability decreases as the lubricant film thickness approaches the submicrometre and nanometre scales. Experimental investigations using surface forces apparatus (SFA) techniques and nanoscale rheological measurements have demonstrated a pronounced increase in the apparent viscosity of lubricants confined between closely spaced solid surfaces [3, 4, 9]. These findings indicate that the rheological behaviour of thin lubricating films differs substantially from that of the bulk lubricant and cannot be adequately described by conventional EHL models. Several approaches have been proposed to account for viscosity inhomogeneity within thin lubricating films. Tichy [10] introduced a surface-layer model based on a stepwise increase in viscosity adjacent to the solid surface, whereas Ono [11] developed a modified Reynolds equation for lubrication with a highly viscous boundary layer. These models improved the description of thin-film flow; however, they do not consider polymolecular adsorption, the symmetric formation of adsorption layers on both friction surfaces, or the influence of lubricant additives on the rheological properties of the adsorption layer. The concept of the Polanyi adsorption potential [12] provides a theoretical framework for describing polymolecular adsorption on solid surfaces. Although this concept has been widely applied to adsorption phenomena in gases and porous materials, its adaptation to thin-film lubrication offers a physically justified basis for modelling the continuous variation of lubricant viscosity within the adsorption layer. Such an approach makes it possible to represent the gradual transition from highly structured near-surface regions to the bulk lubricant instead of assuming an abrupt change in material properties. Most contemporary studies devoted to zinc dialkyldithiophosphate (ZDDP) focus on the mechanisms of tribofilm formation and their influence on friction and wear [5–7, 14]. Correlations between tribofilm morphology, chemical composition, adhesion properties, and tribological performance have been extensively investigated. However, considerably less attention has been paid to the possible contribution of adsorption-induced changes in lubricant rheology to friction reduction under mixed lubrication conditions. Recent studies of confined lubricants and boundary films [13, 15, 16] indicate that molecular ordering and non-Newtonian behaviour may significantly influence friction, although these effects have rarely been incorporated into engineering lubrication models.

Therefore, the available literature indicates the absence of an engineering-oriented model that simultaneously considers polymolecular adsorption, the formation of pseudo-solid adsorption layers on both friction surfaces, the non-Newtonian rheology of the lubricant, and the influence of ZDDP on the rheological properties of thin lubricating films. Developing such a model is expected to improve the physical interpretation of friction processes in the mixed lubrication regime and provide a practical numerical tool for analysing the tribological performance of modern low-viscosity engine oils.

Problem statement

Existing thin-film lubrication models primarily describe the lubricant either as a homogeneous Newtonian continuum or by introducing simplified high-viscosity boundary layers with prescribed properties. Although such approaches improve the prediction of lubrication performance under certain operating conditions, they do not simultaneously account for polymolecular adsorption, the gradual variation of viscosity across the lubricant film, non-Newtonian shear-thinning behaviour, and the influence of anti-wear additives on the rheological properties of the adsorption layer.

Experimental observations reported in the literature indicate that lubricant molecules confined within nanometre-scale films exhibit pronounced structural ordering, resulting in a substantial increase in apparent viscosity and the formation of highly structured adsorption layers adjacent to solid surfaces. At the same time, ZDDP additives are known not only to promote tribochemical film formation but also to modify intermolecular interactions within the lubricant. These observations suggest that changes in the rheological properties of the adsorption layer may contribute to friction reduction under mixed lubrication conditions. Based on these considerations, the lubricating film is represented as a heterogeneous medium consisting of a bulk lubricant region and adsorption layers formed on both friction surfaces. The viscosity within the adsorption layer is assumed to vary continuously according to a function derived from the concept of the Polanyi adsorption potential, while the near-surface regions are represented by pseudo-solid adsorption layers characterized by restricted molecular mobility. The rheological behaviour of the bulk lubricant is described using the Carreau–Yasuda model to account for shear-thinning effects. The objective of the proposed model is to establish a physically justified relationship between the rheological characteristics of the adsorption layer and the experimentally observed friction behaviour of lubricants with different ZDDP concentrations. The model is intended to provide an engineering-oriented numerical framework suitable for parameter identification and comparative analysis of lubricating oils operating under mixed lubrication conditions.

Theoretical Model and Numerical Calculation Methodology

To describe the friction processes in the mixed lubrication zone, the lubricating film is regarded as a non-uniform medium consisting of bulk oil and near-surface adsorption layers formed on both friction surfaces. It is assumed that, as a result of polymolecular adsorption, the viscosity of the lubricant varies continuously across the film thickness. In the immediate vicinity of the surfaces, a pseudo-solid adsorption layer is formed in which the mobility of molecules is substantially restricted. The rheological properties of the bulk oil are described by the Carreau–Yasuda model, whereas the viscosity distribution in the adsorption layer is determined by the adapted concept of the Polanyi adsorption potential [12].

It is assumed that the change in viscosity is of a continuous nature and is determined by the degree of structuring of the lubricant molecules in the adsorption layer. For the mathematical description of this process, an exponential dependence is used, which reflects the gradual decrease in the influence of the surface with increasing distance from it:

$$\mu(\zeta) = \mu_s + (\mu_0 - \mu_s) \cdot \left[1 - \exp\left(-\frac{\zeta}{l_h}\right)\right], \tag{1}$$

where ζ is the distance from the current point in the film to the nearest surface; μ_0 is the dynamic viscosity of the bulk oil; μ_s is the viscosity of the adsorption layer near the surface; l_h is the characteristic decay length of the adsorption potential.

At $\zeta = 0$, the viscosity equals μ_s. At $\zeta >> l_h$, the viscosity approaches the bulk value μ_0. The parameter l_h is physically interpreted as the thickness of the zone in which surface adsorption forces significantly affect the mobility of lubricant molecules. For low-molecular-weight hydrocarbon oils, l_h is 1–3 nm, whereas for oils with complex additive packages this value may reach 5–10 nm [3, 13].

For a symmetric contact with identical adsorption layers on both surfaces, the distance ζ is determined as

$$\zeta(z)=\min(z-h_s,\ h-h_s-z), \tag{2}$$

where z is the coordinate in the direction normal to the surface, measured from the lower boundary of the pseudo-solid layer; h is the total thickness of the lubricating film; h_s is the thickness of the pseudo-solid adsorption layer on each surface.

The effective thickness of the fluid film, in which hydrodynamic flow occurs, is

$$h_r=h-2h_s. \tag{3}$$

The friction force is determined by shear in the fluid part:

$$F_t = \overline{\mu} \cdot A \cdot \frac{u}{h - 2h_s},$$

where A is the contact area; u is the relative sliding velocity; $\overline{\mu}$ is the effective viscosity of the film.

The optimal thickness of the pseudo-solid layer is determined from the condition of minimum friction force:

$$\frac{dF_t}{dh_s} = 0 \cdot$$

This criterion reflects the competition between two opposing trends: on the one hand, an increase in h_s reduces the effective thickness of the fluid film, which at constant $\overline{\mu}$ leads to an increase in the velocity gradient and friction force; on the other hand, pseudo-solid layers increase the effective viscosity $\overline{\mu}$ due to high-viscosity adsorption layers and enhance the hydrodynamic lifting force, which promotes an increase in h and a reduction in the velocity gradient.

The effective viscosity of the lubricating film is determined by harmonic averaging of the local viscosity over the thickness of the fluid part:

$$\overline{\mu} = \frac{h - 2h_s}{\int_{h_s}^{h-h_s} \frac{dz}{\mu(z)}} \cdot \tag{4}$$

Harmonic averaging is employed because individual layers of the lubricant material act as elements connected in series that resist shear deformation. This approach is widely used for multilayer media with a non-uniform distribution of rheological properties.

For a symmetric contact with the viscosity profile (1), the integral in the denominator of (4) is calculated analytically:

$$\int_{h_s}^{h-h_s} \frac{dz}{\mu(z)} = \frac{2l_h}{\mu_0} \cdot \ln\left\{\frac{\mu_0 \cdot \exp\left(\frac{h-2h_s}{2l_h}\right) - \mu_0 + \mu_s}{\mu_s}\right\}. \tag{5}$$

In the general case, when the adsorption potentials from both surfaces overlap or the contact conditions are asymmetric, the integral is computed numerically.

Accounting for Non-Newtonian Behaviour. The rheological properties of the bulk oil are described by the Carreau–Yasuda model [17]:

$$\mu_0(\dot{\gamma}) = \mu_\infty + (\mu_0 - \mu_\infty) \cdot \left[1 + (\lambda\dot{\gamma})^\alpha\right]^{\frac{n-1}{\alpha}}, \tag{6}$$

where $\dot{\gamma} = u/h_r$ is the average shear rate in the fluid part of the film; λ is the relaxation time; a is the transition parameter; n is the power-law index; μ_∞ is the limiting viscosity at high shear rates. At low shear rates the model reduces to the Newtonian flow law, whereas at high shear rates it describes shear thinning of the lubricant.

The numerical implementation of the model was performed in the Microsoft Excel environment. Integration of the viscosity distribution across the thickness of the lubricating film was carried out using the trapezoidal method with n=200 nodes, which ensured convergence of the results. The model parameters (μ_s, l_h, h_s) were determined by minimising the root-mean-square deviation between the experimental and calculated values of the friction coefficient.

The parameters subject to identification include:

μ_s – viscosity of the adsorption layer near the surface;

l_h – characteristic decay length of the adsorption potential;

h_s – thickness of the pseudo-solid adsorption layer.

The other parameters (μ_0, λ, α, n, μ_∞) were taken in accordance with the experimental conditions and literature data for base oil I-20A.

Results of Numerical Modeling and Model Verification

The model parameters μ_s, l_h and the optimal thickness of the pseudo-solid layer $h_{s,\text{opt}}$ were identified by approximating the calculated values of the friction coefficient to the experimental data for base oil I-20A and oils containing 1.25 and 2.5 wt.% ZDDP using the least-squares method. The optimisation was carried out by the method of successive approximations in Microsoft Excel, using as the objective function the minimum of the sum of squared deviations between the calculated and experimental values of the friction coefficient. The identification results are presented in Table 1.

Table 1

Model parameters for the investigated oils

Parameter	Base oil I-20A (0% ZDDP)	1.25 % ZDDP	2.5 % ZDDP
μ_s, Pa·s	0.14	0.98	1.68
μ_s/μ_0	5.0	35.0	60.0
l_h, nm	2.1	3.8	4.6
$h_{s,\mathrm{opt}}$ nm	0.8	1.4	1.9

Although the identified surface viscosity is one to two orders of magnitude higher than the bulk viscosity, this parameter characterizes the rheological response of the highly structured adsorption layer rather than the bulk lubricant and therefore should not be interpreted as the viscosity of the liquid phase.

With increasing ZDDP concentration, a systematic increase in surface viscosity μ_s, characteristic decay length l_h, and optimal thickness of the pseudo-solid adsorption layer h_s is observed.

Calculation of the $\mu(\zeta)$ profile using equation (1) at a fixed bulk viscosity of $\mu_0 = 0.028$ Pa·s showed that for base oil I-20A with the fitted parameters $\mu_s = 0.14$ Pa·s and $l_h = 2.1$ nm, the viscosity reaches 95% of the bulk value at a distance of $\zeta \approx 6$ nm from the surface. For oils with ZDDP, the transition zone expands: at $\mu_s = 0.98$ Pa·s and $l_h = 3.8$ nm (1.25% ZDDP) and $\mu_s = 1.68$ Pa·s and $l_h = 4.6$ nm (2.5% ZDDP), the viscosity approaches μ_0 only at a distance of 15–20 nm. This indicates the formation of a thicker and denser polymolecular adsorption layer upon the introduction of ZDDP, which is consistent with data on the formation of phosphate adsorption complexes on iron surfaces [5, 13].

Figure 1 presents a comparison of the experimental and calculated dependences of the friction coefficient on contact pressure.

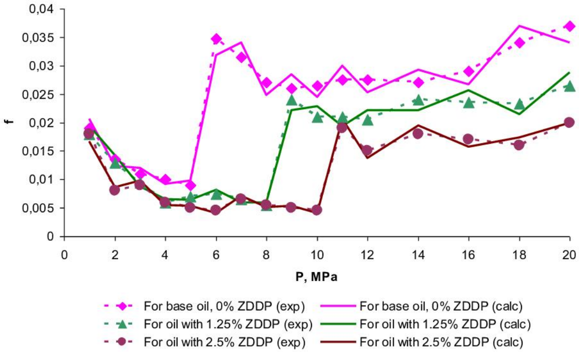

Fig. 1. Dependence of the friction coefficient on contact pressure for base oil and oils with various ZDDP concentrations

For all investigated oils, the model correctly reproduces the shape of the curves, the position of the friction coefficient minimum, and the character of the transition between lubrication regimes.

The average relative deviation between calculated and experimental values was 10.2% for the base oil, 7.8% for the oil with 1.25% ZDDP, and 6.9% for the oil with 2.5% ZDDP.

Based on the experimental and calculated f(P) curves, the characteristic points of the Stribeck diagram have been determined (Table 2). The data are presented as calculated examples typical for similar tribosystems.

The pressure corresponding to the minimum friction coefficient shifts towards higher values for oils containing ZDDP. The hydrodynamic lubrication range, defined as the interval from the minimum to the onset of the sharp increase in friction, expands upon introduction of the additive. The relative expansion of the hydrodynamic lubrication range is approximately 60% for 1.25% ZDDP and 100% for 2.5% ZDDP compared with the base oil.

For the oil with 2.5% ZDDP, the friction minimum is flatter (a plateau in the range of 6–10 MPa), indicating an extended zone of stable hydrodynamic lubrication due to the formation of a thick adsorption–tribochemical layer with enhanced load-carrying capacity.

Table 2

Characteristic points of the Stribeck diagram

Parameter	Base oil I-20A (0% ZDDP)	1.25 % ZDDP	2.5 % ZDDP
P_1 (minimum f), MPa	4–6	6–10	6–10
$f_{\min}$	0.008–0.010	0.005–0.007	0.004–0.006
P_2 (start of f increase), MPa	5–7	8–10	9–12
P_3 (boundary regime plateau), MPa	9–12	12–16	14–18

The obtained parameters demonstrate a monotonic increase with growing ZDDP concentration. The most substantial growth is observed for surface viscosity μ_s: the ratio μ_s/μ_0 changes from 5.0 for the base oil to 35.0 and 60.0 for oils with ZDDP. This indicates enhanced structuring of the lubricant material in near-surface layers upon introduction of the antiwear additive.

To generalise the results of numerical modelling, dependences of the effective viscosity of the lubricating film on its thickness have been constructed for the base oil and oils with various ZDDP concentrations (Fig. 2). The calculated dependences show that at a film thickness $h < 0.3$ μm, the effective viscosity of oils with ZDDP exceeds the corresponding value for the base oil by a factor of 2–4. As the film thickness increases, this effect gradually decreases: at $h > 1$ μm the difference is only 5–10%, and at $h > 2$ μm all curves practically coincide with the bulk viscosity of the oil $\mu_0 = 0.028$ Pa·s. The obtained results indicate that adsorption effects are decisive at a lubricating film thickness of less than approximately 0.3 μm for the base oil and 0.6–0.8 μm for oils with ZDDP.

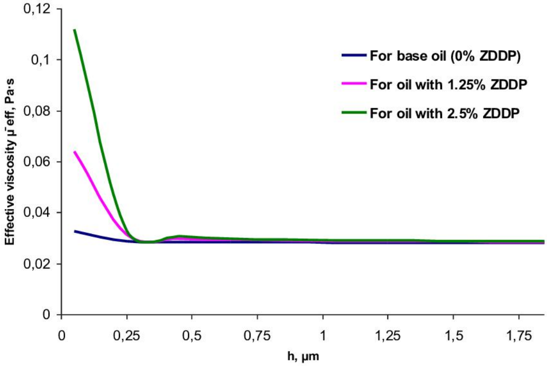

Fig. 2. Calculated dependence of the effective viscosity on the lubricating film thickness for the base oil and oils containing different ZDDP concentrations

A parametric analysis has been conducted of the influence of the characteristic length of the adsorption layer (l_h) and the surface viscosity (μ_s) on the effective viscosity of the lubricating film and the friction coefficient. At a lubricating film thickness of $h = 0.5$ μm, an increase in l_h from 1.0 to 6.0 nm at a fixed value of $\mu_s = 0.98$ Pa·s leads to an increase in the effective viscosity from 0.033 to 0.061 Pa·s. At $h = 5$ μm the influence of this parameter decreases substantially: the effective viscosity exceeds the bulk viscosity μ_0 by only 1.8% and 28.6%, respectively. Thus, the sensitivity of the model to the parameter l_h is greatest in the mixed lubrication region ($0.1 < h < 1.0$ μm), where adsorption phenomena determine the rheological properties of the lubricating film.

A sensitivity analysis performed using normalised partial derivatives at the operating point ($P = 8$ MPa, ZDDP concentration 1.25 wt.%) showed that the surface viscosity μ_s (normalised sensitivity coefficient –0.65) and the characteristic length of the adsorption layer l_h (–0.48) have the greatest influence on the friction coefficient, whereas the influence of the bulk viscosity μ_0 is less pronounced (–0.28). The obtained results indicate that the tribotechnical characteristics of the oil under thin-film mixed lubrication conditions are determined to a considerable extent by the structural-rheological properties of the adsorption layer, and not solely by the viscosity of the base oil.

The average relative deviation between calculated and experimental values of the friction coefficient was 6.9–10.2%. The largest deviations were observed in the region of transition from mixed to hydrodynamic lubrication regime, which may be associated with the simplified assumptions of the model regarding the properties of the adsorption layer.

The proposed model is based on a one-dimensional description of viscosity distribution and does not account for local temperature non-uniformities, elastic deformation of surfaces, and the kinetics of tribochemical growth of ZDDP films. The obtained results should be regarded as a description of the rheological contribution of polymolecular adsorption to the change in the friction coefficient. Further development of the model may be associated with accounting for elastohydrodynamic effects, temperature dependence of adsorption layer parameters, and tribochemical kinetics of protective film formation.

Conclusions

1. A numerical rheological model of a thin lubricating oil film has been developed based on the concept of polymolecular adsorption. The model combines a continuous viscosity distribution within the adsorption layer, pseudo-solid adsorption layers adjacent to both friction surfaces, and the non-Newtonian rheology of the bulk lubricant described by the Carreau–Yasuda model.

2. The proposed methodology enables identification of the adsorption-layer parameters from experimental friction data. The identified parameters demonstrate a systematic increase with increasing ZDDP concentration, indicating enhanced molecular structuring of the lubricant in the near-surface region.

3. Comparison between calculated and experimental friction coefficients confirmed that the proposed model adequately reproduces the characteristic shape of the friction–pressure relationship over the investigated range of contact pressures. The obtained agreement indicates that the model captures the principal rheological features governing friction under mixed lubrication conditions.

4. The obtained results suggest that, in addition to the well-established tribochemical action of ZDDP, adsorption-induced changes in the rheological properties of the lubricating film may contribute to friction reduction. The proposed model therefore provides a complementary physical interpretation of the influence of anti-wear additives on tribological behaviour.

5. The developed numerical approach is implemented in Microsoft Excel and does not require specialized computational software. Owing to its engineering-oriented formulation, the model may be applied for comparative evaluation of lubricant formulations, identification of adsorption-layer parameters, and preliminary prediction of tribological performance in plain bearings operating under mixed lubrication conditions.

Future work will focus on incorporating elastohydrodynamic effects, temperature-dependent rheological properties, and tribochemical film growth kinetics to extend the applicability of the proposed model to a wider range of operating conditions.

References

1. Zhmud B., Coen A., Zitouni K. Fuel Economy Engine Oils: Scientific Rationale and Controversies. BIZOL Technical Bulletin, 2024. URL : https://bizol.com/blog/fuel-economy-engine-oils-scientific-rationale-and-controversies/

2. Low Viscosity Engine Lubricant. North American Council for Freight Efficiency (NACFE), Confidence Report, 2016. URL : https://nacfe.org/wp-content/uploads/2018/07/low-viscosity-lubricants-confidence-report.pdf

3. Hu W., Granick S. Viscoelastic dynamics of confined polymer melts. Macromolecules, 1998, vol. 31, no. 13, pp. 4656–4663. https://doi.org/10.1126/science.258.5086.1339

4. Klein J., Kumacheva E. Confinement-induced phase transitions in simple liquids. Science, 1995, vol. 269, no. 5225, pp. 816–819. https://doi.org/10.1126/science.269.5225.816

5. Rydel J.J., Pagkalis K., Kadiric A., Rivera-Diaz-del-Castillo P.E.J. The correlation between ZDDP tribofilm morphology and the microstructure of steel. Tribology International, 2017, vol. 113, pp. 13–25. URI: https://eprints.lancs.ac.uk/id/eprint/126510

6. Dawczyk J., Morgan N., Russo J., Spikes H. Film Thickness and Friction of ZDDP Tribofilms. Tribology Letters, 2019, vol. 67 (2). https://doi.org/10.1007/s11249-019-1148-9

7. Zhang Y., Zhao Y., Ma R., Zhao J., Li W., Li, X M, Liu H-C. Characteristics of tribofilm growth and interfacial friction of DPP and ZDDP anti-wear additives at different temperatures. Tribology International, 2024, vol. 204, 110501. https://doi.org/10.1016/j.triboint.2024.110501

8. Greenwood J.A. Elastohydrodynamic Lubrication. Lubricants. 2020; 8(5):51. https://doi.org/10.3390/lubricants8050051

9. Zhang X., Han, M., Espinosa-Marzal R. Thin-Film Rheology and Tribology of Imidazolium Ionic Liquids. ACS Applied Materials & Interfaces. 2023. 15(38). https://doi.org/10.1021/acsami.3c10018

10. Tichy J.A. A surface layer model for thin film lubrication. Tribology Transactions, 1995, Vol. 38, 3. P. 577–585. https://doi.org/10.1080/10402009508983445

11. Ono K. Modified Reynolds Equations for Thin Film Lubrication with Saturated High-Viscosity Surface Layer and Lubrication Analysis of Tapered Pad Bearing. Tribology Online, 2022, vol. 17, no. 3, pp. 207–215. https://doi.org/10.2474/trol.17.207

12. Polanyi M. The Potential Theory of Adsorption. Science. 141, 1010-1013 (1963). https://doi.org/10.1126/science.141.3585.1010

13. Abouhadid F., Lai V-V., Morgado N., Mazuyer D., Cayer-Barrioz J. Effect of Surface Chemistry on the Squeeze-Thin Film and Friction of Boundary Films. Langmuir, 2024, vol. 40(10). https://doi.org/10.1021/acs.langmuir.3c03409

14. Sato K., Watanabe S., Sasaki S. High Friction Mechanism of ZDDP Tribofilm Based on in situ AFM Observation of Nano-Friction and Adhesion Properties. Tribology Letters, 2022, vol. 70(3). https://doi.org/10.1007/s11249-022-01635-x

15. Shahrivar K., Ortigosa-Moya E., Hidalgo-Alvarez R., de Vicente J. Isoviscous elastohydrodynamic lubrication of inelastic non-Newtonian fluids. Tribology International, 2019, vol. 140. https://doi.org/10.1016/j.triboint.2019.03.065

16. Gao H., Müser M. On the Shear-Thinning of Alkanes. Tribology Letters, 2023, vol. 72(1). https://doi.org/10.1007/s11249-023-01813-5

17. Yasuda K., Armstrong R.C., Cohen R.E. Shear flow behavior of concentrated solutions of linear and star branched polystyrenes. Rheologica Acta, 1981, vol. 20, pp. 163–178. https://doi.org/10.1007/BF01513059

Драч І., Диха М., Товстюк Д. Чисельне реологічне моделювання тонкого шару моторної оливи з урахуванням полімолекулярної адсорбції та впливу ZDDP

Розроблено та верифіковано чисельну реологічну модель тонкого шару моторної оливи з урахуванням полімолекулярної адсорбції, псевдотвердих адсорбційних шарів і впливу протизносної присадки ZDDP на реологічні властивості змазувального шару. Для опису розподілу в'язкості в товщині змазувального шару адаптовано реологічну модель, побудовану на основі концепції адсорбційного потенціалу Полані. До моделі введено псевдотверді адсорбційні шари на обох поверхнях тертя, а ефективну в'язкість визначено методом гармонійного усереднення з чисельним інтегруванням методом трапецій (n = 200), реалізованим у Microsoft Excel. Неньютонівське зрідження мастила враховано за моделлю Карро–Ясуди. Параметри моделі визначали шляхом узгодження розрахункових і експериментальних значень коефіцієнта тертя для базової оливи І-20А та олив із вмістом ZDDP 1,25 і 2,5 мас. %. Встановлено зростання параметрів адсорбційного шару зі збільшенням концентрації ZDDP: в'язкість приповерхневого шару μ_s збільшилася від 0,14 до 1,68 Па·с, характерна довжина спаду l_h – від 2,1 до 4,6 нм, а оптимальна товщина псевдотвердого шару h_s – від 0,8 до 1,9 нм. Середнє відносне відхилення між розрахунковими та експериментальними значеннями коефіцієнта тертя становило 6,9–10,2 %, що підтверджує задовільну узгодженість моделі з експериментальними даними. Розрахунковий тиск, що відповідає мінімуму коефіцієнта тертя, зміщується приблизно з 5 МПа для базової оливи до близько 8 МПа для олив із ZDDP, що свідчить про розширення області гідродинамічного мащення. Наукова новизна. Розроблена чисельна реологічна модель тонкого змазувального шару є новим числовим підходом, що поєднує полімолекулярну адсорбцію, концепцію псевдотвердих адсорбційних шарів і неньютонівську реологію мастила. Отримані результати свідчать, що поряд із трибохімічними процесами істотний внесок у зниження тертя в зоні змішаного мащення може забезпечувати підвищення ефективної в'язкості полімолекулярного адсорбційного шару. Запропонована методика, реалізована в середовищі Microsoft Excel, дає змогу ідентифікувати параметри моделі та прогнозувати триботехнічні характеристики мастильних матеріалів без використання спеціалізованого програмного забезпечення. Розроблений підхід може бути використаний для інженерного оцінювання впливу концентрації ZDDP на триботехнічні властивості моторних олив для підшипників ковзання.

Ключові слова: тонкошарове мащення, полімолекулярна адсорбція, ZDDP, псевдотвердий адсорбційний шар, ефективна в'язкість, реологічне моделювання, коефіцієнт тертя.

ISSN 2079-1372 Problems of Tribology, V. 31, No 3/121-2026, 27-35

Problems of Tribology

Website: http://tribology.khnu.km.ua/index.php/ProbTrib
E-mail: tribosenator@gmail.com

DOI: https://doi.org/10.31891/2079-1372-2026-121-3-27-35

Dynamics of a Journal Bearing During Sudden Rotor Stoppage Considering Inertial Properties and Pressure-Dependent Lubricant Viscosity

D.D. Marchenko* 0000-0002-0808-2923 **, K.S. Matvyeyeva** 0000-0003-0974-3022

**Mykolayiv National Agrarian University, Mykolayiv, Ukraine*
E-mail: marchenkodd@mnau.edu.ua

Received: 03 July 2026: Revised 28 July 2026: Accept: 05 August 2026

Abstract

The dynamic behavior of a journal bearing during sudden rotor stoppage is investigated using a mathematical model that accounts for the inertial properties of the rotor and the pressure dependence of lubricant viscosity. The lubricant viscosity is described by the Barus law, and the pressure distribution in the lubricant film is determined from the Reynolds equation for one-dimensional flow with variable viscosity. The resultant hydrodynamic force is incorporated into the second-order equation of motion of the rotor–bearing system. A sinusoidal half-wave is used to represent the external impact load, and the resulting nonlinear differential equation is solved numerically. The transient variation of lubricant-film thickness and maximum lubricant-film pressure is analyzed during the impact and after removal of the load. For the investigated conditions, the maximum pressure in the lubricant film reaches approximately 74 MPa and subsequently decreases to low-amplitude oscillations around a mean value of about 14 MPa. The lubricant-film thickness remains sufficient to preserve film integrity throughout the considered transient process. Comparison with the approximate approach shows that the latter overestimates the displacement, velocity, and pressure responses. The proposed model can be used to assess the dynamic behavior and impact resistance of journal bearings under sudden rotor stoppage and impact loading

Keywords: journal bearing, sudden rotor stoppage, impact loading, rotor inertia, lubricant viscosity, pressure dependence, lubricant film, dynamic analysis, impact resistance.

Introduction

Rapid stoppage of rotating machinery can generate transient impact loads in journal bearings and cause a substantial reduction in the hydrodynamic load-carrying capacity of the lubricant film. The resulting transient motion of the rotor relative to the bearing may lead to a significant decrease in lubricant-film thickness and a corresponding increase in pressure within the lubricating layer. Therefore, the dynamic behavior of journal bearings during sudden rotor stoppage is an important factor in assessing their reliability and resistance to impact loading. The analysis of transient processes in journal bearings traditionally relies on hydrodynamic lubrication theory based on the Reynolds equation. In many engineering calculations, the lubricant viscosity is assumed to be constant and the inertia of the rotor is neglected. Such assumptions simplify the governing equations but may limit the accuracy of the predicted transient response, particularly under relatively high impact loads.

An important factor affecting the dynamic characteristics of the lubricant film is the pressure dependence of lubricant viscosity. This effect can be described using the Barus relation, according to which lubricant viscosity increases with pressure. Accounting for this dependence makes it possible to obtain a more realistic description of the pressure distribution and load-carrying capacity of the lubricant film under transient conditions. The influence of lubricant viscosity on the impact resistance of journal bearings has been considered in previous studies, including approaches based on approximate solutions.

At the same time, the inertia of the rotor may play a significant role in the transient response of the rotor–bearing system. When rotor acceleration is neglected, the governing equation is reduced to a first-order nonlinear differential equation, whose numerical implementation may be associated with computational instability. Including the inertial force of the rotor leads to a second-order equation of motion that provides a direct description of the dynamic process and is convenient for numerical solution.

Copyright © 2026 D.D. Marchenko, K.S. Matvyeyeva. This is an open access article distributed under the Creative Commons Attribution License, which permits unrestricted use, distribution, and reproduction in any medium, provided the original work is properly cited.

Literature review

The performance of journal bearings is strongly influenced by lubricant properties, which affect the load-carrying capacity, minimum lubricant-film thickness, maximum pressure, and dynamic characteristics of the bearing [1]. These relationships provide a theoretical basis for determining the initial operating conditions of a journal bearing and remain widely used in engineering analysis.

The dynamic response of journal bearings under rapidly changing loads has subsequently attracted considerable attention. Transient behavior under dynamic and suddenly applied loads has been investigated, with particular attention to journal misalignment, lubricant-film thickness, maximum film pressure, and journal motion [2]. The dependence of lubricant viscosity on pressure has also been considered, and an approximate solution for the transient problem has been obtained [3]. These studies established the basis for assessing the influence of lubricant properties on the impact resistance of journal bearings.

More recent studies have significantly expanded the range of physical effects considered in transient journal-bearing models. An analytical solution for the dynamic forces generated by lubricated long journal bearings under dynamic loading has been developed. By analytically integrating the Reynolds equation using Sommerfeld variables, expressions for dynamic lubricant forces have been obtained and squeeze-film and hydrodynamic contributions have been separated, reducing the dependence on classical approximate solutions [4].

Particular attention in recent research has been given to the coupled dynamics of the rotor and bearing under nonstationary loading. A dynamic misalignment model coupled with rotor dynamics and transient mixed elastohydrodynamic lubrication has been proposed. The results demonstrated that dynamic misalignment can substantially influence the transient lubrication characteristics, particularly under nonstationary operating conditions. The model incorporated journal-center translation, surface roughness, cavitation, and elastic deformation of the bearing [5]. The influence of bearing deformation under impact loading has also been investigated. A transient mixed-lubrication model accounting for the coupled effects of journal misalignment and bearing viscoelastic deformation was developed in [6]. The results showed that the effects of deformation become particularly important at high rotational speeds, heavy loads, and rapidly changing impact loads, where neglecting the compliance of the bearing structure may lead to less realistic predictions of lubrication performance. For marine applications, the nonlinear tribo-dynamic behavior and transient stability of offset-halves journal bearings under sudden loading have been investigated [7]. The thermo-elasto-hydrodynamic model considered load amplitude, bearing geometry, and lubricant properties and demonstrated that these parameters significantly affect the transient response and stability of the bearing–rotor system. Recent research has also demonstrated the importance of considering thermal effects and time-varying operating conditions. A transient thermal elastohydrodynamic model of a journal-thrust coupled bearing subjected to time-varying loads was developed [8]. The study showed that the coupled thermal-pressure effects can significantly influence transient lubrication characteristics and therefore should not be neglected when analyzing bearings under realistic dynamic operating conditions. In addition, transient lubrication models are increasingly being coupled with wear and surface-contact phenomena. This development is associated with the fact that the operating conditions of journal bearings during start-up and other nonstationary regimes are accompanied by significant changes in the lubricant-film thickness, local contact conditions, and hydrodynamic pressure distribution. Under such conditions, the interaction between the bearing surfaces may become more pronounced, and the simultaneous consideration of lubrication, mechanical contact, and wear becomes important for a reliable assessment of bearing performance. A tribo-dynamic model of a hydrodynamic bearing–rotor system under start-up conditions has been developed, accounting for misalignment, wear, rotor imbalance, surface contact, and elastic deformation [9]. The results demonstrate that these factors are mutually coupled and may considerably affect the transient response of the bearing–rotor system. In particular, the interaction between transient lubrication and rotor dynamics becomes important during nonstationary operating regimes, when the journal position, lubricant-film characteristics, and mechanical loading change continuously with time. These approaches indicate that the analysis of journal bearings under transient conditions should consider not only the hydrodynamic pressure field but also the changes in contact and surface conditions associated with wear and deformation. The influence of piezoviscous effects on journal-bearing characteristics has also been investigated for different bearing configurations. The pressure dependence of lubricant viscosity becomes especially important in regimes characterized by high local pressures, because an increase in pressure leads to a corresponding increase in lubricant viscosity and therefore changes the hydrodynamic resistance and pressure distribution within the lubricant film. This effect may alter the load-carrying capacity of the bearing and influence the dynamic characteristics of the lubricated contact. Modern lubrication models incorporating piezoviscous behavior have therefore been used to obtain a more realistic description of pressure generation in the lubricant layer under elevated-pressure conditions [10]. The results indicate that pressure-dependent viscosity affects lubricant-film pressure, stiffness, damping, and friction characteristics. Consequently, the assumption of constant lubricant viscosity may lead to deviations in the predicted dynamic response of a journal bearing, particularly when the bearing operates under high transient loads. This confirms the relevance of incorporating pressure-dependent viscosity into mathematical models intended for the analysis of short-duration dynamic and impact processes.

Recent tribo-dynamic models have also incorporated additional coupled effects, including journal axial motion and misalignment, to describe complex transient behavior under dynamic loading [11]. Such approaches extend conventional two-dimensional descriptions of journal-bearing operation by considering additional degrees of freedom of the journal and the possibility of simultaneous translational and axial motion. Misalignment may modify the local lubricant-film geometry and produce a nonuniform pressure distribution along the bearing width, while axial motion may further alter the temporal evolution of the lubricant-film state. Accounting for these effects allows a more comprehensive representation of the actual transient behavior of bearing systems subjected to dynamic loading. The results of such studies demonstrate that the response of a lubricated bearing may depend on the coupling between the journal motion, bearing geometry, and lubrication conditions, which should be taken into account when developing more general rotor–bearing dynamic models.

Wear-related effects are also important for assessing the long-term performance of sliding bearings. In addition to the instantaneous hydrodynamic response, the reliability of a sliding bearing is determined by the ability of the friction surfaces to maintain their functional characteristics during repeated loading and sliding. Wear changes the geometry of the contacting surfaces and may consequently alter the lubricant-film thickness, contact pressure, and operating conditions of the tribosystem. A calculation-experimental approach based on contact pressure and sliding velocity has been proposed for predicting wear and evaluating the wear resistance of cylindrical sliding bearings [12]. Such approaches make it possible to relate the kinematic and loading parameters of the tribosystem to the evolution of wear and provide additional information for assessing bearing durability. Although wear is not directly considered in the present transient model, the results of these studies indicate that the evolution of the friction surfaces is an important factor in the long-term assessment of sliding-bearing performance and should be considered in further development of dynamic models.

The wear resistance of friction elements is also affected by the conditions of surface interaction and lubrication. The state of the surface layer, the characteristics of the contact interaction, and the availability of lubricant may determine the intensity of material removal and the stability of the friction process. Experimental investigations of surface plastic deformation have demonstrated that the technological conditions of surface treatment can significantly influence the wear resistance of friction tools and contacting surfaces [13]. These results are relevant to the analysis of sliding bearings because the functional characteristics of the mating surfaces are directly related to the ability of the lubricant film to separate the surfaces during operation. Therefore, consideration of the condition and wear resistance of the friction surfaces complements the hydrodynamic analysis and provides a more comprehensive basis for evaluating the reliability of tribological systems.

Transient tribo-dynamic analysis has also been coupled with wear modeling to evaluate the evolution of lubricant-film and wear characteristics during nonstationary operation. Such models make it possible to analyze the mutual influence of the changing lubricant-film state and the gradual modification of the friction surfaces during transient processes. The influence of acceleration mode, acceleration time, external load, lubricant viscosity, and operating time on the transient response has been analyzed [14]. The results demonstrate that the transient behavior of a bearing is determined not only by the instantaneous value of the external load but also by the manner in which the loading is introduced and by the duration of the transient regime. These findings are particularly relevant to start-up and other rapidly changing operating conditions, where the lubricant film does not immediately reach a steady state and the bearing response is governed by coupled dynamic and tribological processes. Recent studies have further considered viscosity variation in rough and non-conventional bearing configurations, demonstrating the influence of viscosity variation on pressure distribution and load-carrying capacity [15]. Consideration of variable lubricant viscosity allows the influence of pressure and other physical effects on the formation of the lubricant film to be described more accurately than in models based on the constant-viscosity assumption. At the same time, bearing surface roughness and deviations from conventional geometry may alter the local film profile and pressure field, thereby affecting the overall load-carrying behavior of the lubricated contact. These results further confirm that the rheological properties of the lubricant and the geometric characteristics of the bearing should be considered jointly when analyzing bearing operation under nonstationary and elevated-pressure conditions.

Despite these advances, the specific problem of sudden rotor stoppage in a journal bearing with simultaneous consideration of rotor inertia and pressure-dependent lubricant viscosity remains insufficiently investigated. Most recent models focus on misalignment, thermal effects, viscoelastic deformation, wear, or complex bearing geometries, whereas the combined influence of rotor inertial loading and piezoviscous effects during the short transient following sudden stoppage requires further study. In particular, the interaction between the rapidly changing motion of the journal and the pressure-dependent rheological response of the lubricant may substantially affect the evolution of the lubricant-film thickness and the maximum pressure during the impact event. This provides the motivation for the present work, which develops and numerically analyzes a dynamic model of a journal bearing during sudden rotor stoppage with pressure-dependent lubricant viscosity and rotor inertia.

Purpose

The purpose of this study is to develop and numerically investigate a mathematical model of the transient dynamics of a journal bearing during sudden rotor stoppage, taking into account the rotor inertial properties and the pressure dependence of lubricant viscosity. Particular attention is given to determining the transient variation of lubricant-film thickness and pressure during impact loading and after its removal, as well as to assessing the influence of the considered physical factors on the impact resistance and serviceability of the journal bearing.

Research methodology

The study is based on the hydrodynamic theory of lubrication and numerical analysis of the transient motion of a rotor–journal bearing system subjected to sudden rotor stoppage. An infinitely long journal bearing with a rigid bearing liner is considered. The lubricant viscosity is assumed to depend on pressure according to the Barus law:

$$\mu = \mu_0 e^{\alpha p},$$

where μ_0 – is the lubricant viscosity at atmospheric pressure, α – is the piezoviscosity coefficient, and p – is the local pressure in the lubricant film.

The pressure distribution in the lubricant film is determined from the one-dimensional Reynolds equation for a lubricant with variable viscosity. The equation is transformed from the linear coordinate to the angular coordinate of the journal, while the time-dependent lubricant-film thickness and the velocity of approach between the journal and bearing liner are taken into account. The resulting equation is integrated subject to the corresponding boundary conditions, yielding the pressure distribution in the lubricant film.

The resultant hydrodynamic force generated by the lubricant film is obtained by integrating the pressure distribution over the bearing surface. To describe the transient motion of the rotor, the inertial force of the rotor is included in the equation of motion. This results in a second-order differential equation governing the relative motion of the rotor and bearing liner. The rotor mass is expressed in terms of the initial mean pressure in the bearing and the gravitational acceleration.

The impact load is represented by a sinusoidal half-wave characterized by an overload factor k and an impact duration Δt. A dimensionless time variable is introduced to facilitate the numerical solution of the governing equation. The initial relative eccentricity is determined using relationships between the eccentricity ratio and the Sommerfeld number derived from classical hydrodynamic lubrication theory. Since sudden rotor stoppage produces a soft impact, the initial rate of change of relative eccentricity is taken to be zero.

The resulting nonlinear differential equation is solved numerically over a time interval covering both the impact stage and the subsequent post-impact response. The principal quantities evaluated are the time-dependent lubricant-film thickness and the maximum pressure in the lubricant film. The calculated results are then used to assess the transient behavior and impact resistance of the journal bearing.

Research results

The calculation scheme is shown in Fig. 1. Assume that the lubricant viscosity follows the Barus law.

$$\mu = \mu_0 \exp(\alpha_0 p), \tag{1}$$

where μ_0 – is the viscosity at atmospheric pressure; α_0 – is the piezoviscosity coefficient; p – is the pressure at an arbitrary point of the lubricant film.

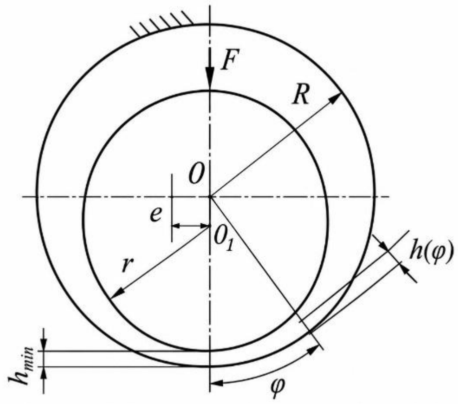

Fig. 1. Computational model of a journal bearing subjected to sudden rotor stoppage

The Reynolds equation for one-dimensional flow of a lubricant with variable viscosity has the form:

$$\frac{\partial}{\partial x} \cdot \left(\frac{h^3}{\mu} \cdot \frac{\partial \rho}{\partial x}\right) = 12 W_n,$$

where $h = h(\varphi)$ – is the lubricant-film thickness; $\frac{\partial \rho}{\partial x}$ – is the pressure gradient; $W_n = V \cos\varphi$ – is the journal velocity component directed normal to the surface at the given point; V – the velocity of approach of the journal to the bearing liner; x – is the linear coordinate.

Passing to the angular coordinate φ and substituting the expressions for the lubricant-film thickness and the approach velocity of the surfaces:

$$h = r\psi(1 - \chi\cos\varphi), \tag{2}$$
$$V = \frac{dh(0)}{dt} = -r\psi\frac{d\chi}{dt}, \tag{3}$$

where $\psi = (R - r)/r$ – is the dimensionless radial clearance; $\chi = e/(R - r)$ – is the dimensionless eccentricity; t – is time.

Integrating the resulting equation twice with respect to φ, taking into account the boundary conditions $\partial\rho/\partial\varphi = 0$ at $\varphi = 0$ and $p = 0$ at $\varphi = \pm\pi/2$. We obtain the pressure distribution function:

$$p(\varphi; t) = -\frac{1}{\alpha_0} ln\left\{1 - \frac{6\mu_0\alpha_0}{\psi^2\chi}\left[\frac{1}{(1-\chi\cos\varphi)^2} - 1\right]\frac{d\chi}{dt}\right\}.$$

Introduce a change of variable by defining the dimensionless time τ according to:

$$t = \frac{6\mu_0\alpha_0}{\psi^2}\tau, \tag{4}$$

then the pressure distribution function takes the following form:

$$p(\varphi, \tau) = -\frac{1}{\alpha_0} ln\left\{1 - \frac{\chi'}{\chi}\left[\frac{1}{(1-\chi\cos\varphi)^2} - 1\right]\right\}, \tag{5}$$

where $\chi' = d\chi/d\tau$.

The projections of the pressure forces onto the vertical axis produce the resultant force of the lubricant film, equal to

$$F_1(\tau) = 2rl\int_0^{\pi/2} p(\varphi, t)\cos\varphi\, d\varphi = -\frac{2rl}{\alpha_0}\int_0^{\chi/2} ln\left\{1 - \frac{\chi'}{\chi}\left[\frac{1}{(1-\chi\cos\varphi)^2} - 1\right]\right\}\cos\varphi\, d\varphi,$$

where l – is the bearing liner length.

The integral appearing on the right-hand side of the last expression can be found in analytical form. Thus, we obtain

$$F_1(\tau) = \frac{2rl}{\alpha_0}\mathcal{T}(\chi, \chi'), \tag{6}$$

where

$$\mathcal{T}(\chi, \chi') = \frac{2\sqrt{1-\chi^2}}{\chi}\left(\frac{\pi}{2} + arcsin\chi\right) - \frac{\sqrt{1-b_2^2}}{b^2}\left(\frac{\pi}{2} + arcsin\, b_2\right) - \frac{\sqrt{1-b_3^2}}{b_3}\left(\frac{\pi}{2} + arcsin\, b_3\right), \tag{7}$$
$$b_2 = \chi + \chi' - \sqrt{\chi'(\chi + \chi')}, \qquad b_3 = \chi + \chi' + \sqrt{\chi'(\chi + \chi')}.$$

If, as is customary in practical calculations, acceleration and, consequently, the inertial load of the rotor are neglected, the resultant force $F_1(\tau)$ of the lubricant film should be equated to the external dynamic load $F(\tau)$. As a result, a first-order differential equation is obtained that is not solved explicitly for the derivative χ'. In most practically important cases, it can be solved with respect to the independent variable τ and therefore admits a parametric representation of the solution:

$$\begin{cases} \tau = f_1(\chi); \\ \chi' = f_2(\chi). \end{cases}$$

It should be noted, however, that the numerical implementation of this solution method is complicated by the instability of the computational process, requiring, at a minimum, calculations with double precision. On the other hand, the equation accounting for the inertial force of the rotor, although it is of second order, can be solved on a computer without any difficulty. Taking the above into account, write the equation in the following form:

$$-m\frac{d^2h(0)}{dt^2} + \frac{2rl}{\alpha_0}\mathcal{T}(\chi, \chi') = F(t), \tag{8}$$

where m – is the rotor mass; $F(t)$ – is the prescribed external excitation.

Passing to dimensionless time according to relation (4) and taking equation (2) into account, we obtainτ

$$h(0) = r\psi(1 - \chi),$$
$$\frac{d^2h(0)}{dt^2} = -r\psi\frac{d^2x}{dt^2} = -\frac{r\psi^5}{36\mu_0^2\alpha_0^2}\chi", \tag{9}$$

where $\chi" = d^2\chi/d\tau^2$.

Let the rotor mass be represented as

$$m = G/g = p_0\,2r\,l/g, \tag{10}$$

where p_0 – is the initial, at $\tau = 0$, mean pressure on the bearing liner; g = 9.81 ms^{-2} – is the gravitational acceleration.

Substituting expressions (9) and (10) into equation (8), we obtain

$$\frac{\rho_0 r\psi^5}{36\mu_0^2\alpha_0 g}\cdot\frac{2rl}{\alpha_0}\chi'' + \frac{2rl}{\alpha_0}\mathcal{T}(\chi,\chi') = F(\tau),$$

or

$$\frac{\rho_0 r\psi^5}{36\mu_0^2\alpha_0 g}\chi'' + \mathcal{T}(\chi,\chi') = f(\tau), \tag{11}$$

where $f(\tau) = \alpha_0 F(\tau)/(2rl)$.

If, for example, the external impact $F(t)$ is specified in the form of a sinusoidal half-wave

$$F(t) = \begin{cases} G\left(1 + k\sin\frac{\pi}{\Delta t}t\right) & \text{при } 0 \le t \le \Delta t, \\ 0 & \text{при } t > \Delta t, \end{cases}$$

where k – is the overload factor, Δt – is the duration of the impact load; then the function $f(\tau)$ takes the corresponding form

$$f(\tau) = \begin{cases} p_0\alpha_0\left(1 + k\sin\frac{\tau}{T}\right) & \text{при } 0 \le \tau \le T, \\ \rho_0\alpha_0 & \text{при } \tau > T, \end{cases}$$

where

$$T = \frac{\psi^2\Delta t}{6\pi\mu_0\alpha_0}.$$

Then the equation of motion (11) can be written in the following form:

$$\chi'' + \frac{36\mu_0^2\alpha_0 g}{\rho_0 r\psi^5}\mathcal{T}(\chi,\chi') = \frac{36\mu_0^2\alpha_0^2 g}{r\psi^5}\left(1 + k\sin\frac{\tau}{T}\right), \tag{12}$$

where as at $\tau > T$ one should set $k = 0$.

It remains to determine the initial conditions for integration of equation (12). The initial value of the relative eccentricity can be obtained from the classical hydrodynamic theory of lubrication of a rotating rotor. In practice, the values χ_0 are determined from tables, which is inconvenient when solving problems on a computer.

For practical calculations, approximate relationships can be used, since, within the considered range of relative eccentricities $0.3 \le \chi_0 \le 0.7$, a simple relationship exists between the values of χ_0 and the Sommerfeld numbers

$$S_0 = \frac{\rho_0\psi^2}{\mu\omega},$$

where ω – is the angular velocity of the rotor before its sudden stoppage. For the specified range, the value χ_0 can be determined with sufficient accuracy from the formula

$$\chi_0 = a_0 + b_0\ln S_0,$$

where the constants a_0 and b_0 depend only on the ratio of the bearing liner length to its diameter.

Let us determine the initial value of the derivative χ_0'. The sudden stoppage of the rotor causes the load-carrying capacity of the lubricant film associated with circumferential velocity to instantly decrease from a certain steady-state value to zero. A corresponding finite discontinuity is also experienced by the acceleration of the rotor center of gravity. Thus, a "soft" impact occurs, in which the velocity does not change discontinuously. Therefore, the initial value χ'_0 should be taken as zero.

The results of the numerical solution of the equation for the following parameter values are given below: $r = 0.075\,m, l/2r = 1, p = 6MPa, \mu_0 = 0.03Pa\cdot s, \alpha_0 = 0.14\cdot10^{-7}Pa^{-1}, \psi = 1\cdot10^{-3}, \omega = 314s^{-1}, a_0 = 0.5329, b_0 = 0.25$.

The duration of the impact load was $\Delta t = 0.02$ s, the overload factor was $k = 5$, the initial value of the relative eccentricity $\chi_0 = 0.399$.

The calculation was performed for a time interval equal to $2\Delta t$ in order to investigate the behavior of the shaft–bearing dynamic system during the impact and after removal of the load. Simultaneously with determining the values of χ та χ' the maximum pressure in the lubricant film corresponding to these values was calculated $\varphi = 0$:

$$p_{max} = -\frac{1}{\alpha_0}\ln\left\{1 - \frac{\chi'}{\chi}\left[\frac{1}{(1-\chi)^2} - 1\right]\right\}.$$

The graphs $\chi(t), \chi'(t)$, i $p_{max}(t)$ are shown in Figs. 2 and 3. As can be seen from the figures, the lubricant-film thickness initially decreases rather rapidly, but then the rate of its change decreases sharply and, after the impact ceases, is $\chi' \approx 0.005$, which corresponds to a linear approach velocity of the shaft and bearing liner of less than 0.15 mm/s. At large values of t the lubricant-film thickness remains sufficient $(h_{min} > 10\ \mu\text{m})$ to maintain its integrity, significantly exceeding the height of the surface roughness of the friction surfaces. The maximum pressure in the lubricant film initially increases to 74 MPa, then decreases sharply and, after removal of the impact, oscillates with a small amplitude around the mean value of 14 MPa.

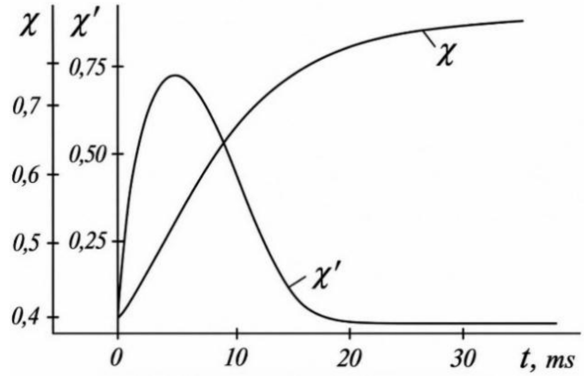

Fig. 2. Dependence of the lubricant film thickness on time under impact loading

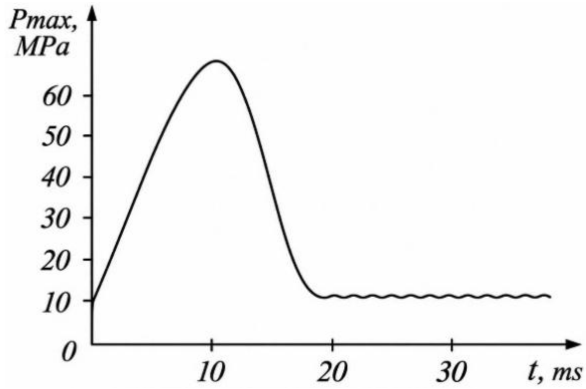

Fig. 3. Dependence of the maximum pressure in the lubricant film on time under impact loading

Comparison with calculations based on an approximate approach shows differences in the predicted displacements, velocities, and pressures, with the approximate approach providing higher values. Thus, the approximate approach can be used for assessing the serviceability of journal bearings under impact loading.

Finally, it should be noted that calculating the impact resistance of bearings at high overload factors requires taking the elasticity of the bearing liner into account. Such studies will be carried out in the future; however, it can already be noted that the compliance of the foundation leads to an increase in lubricant-film thickness and improves the impact resistance of bearings.

Conclusions

A mathematical model of the transient dynamics of a journal bearing during sudden rotor stoppage has been developed, accounting for rotor inertia and the pressure dependence of lubricant viscosity described by the Barus law.

The numerical results demonstrate a pronounced transient response of the rotor–bearing system after rotor stoppage. The lubricant-film thickness initially decreases rapidly, while the rate of its reduction subsequently decreases, allowing the lubricant film to remain continuous during the considered impact event.

Under the investigated impact conditions, the maximum lubricant-film pressure reaches approximately 74 MPa and subsequently decreases to low-amplitude oscillations around a mean value of about 14 MPa. These results indicate that the bearing retains its load-carrying capacity after the impact load is removed.

Comparison with the approximate approach shows that the approximate method overestimates the displacement, velocity, and pressure responses. Nevertheless, it can be used for preliminary engineering assessment of the serviceability and impact resistance of journal bearings. For higher overload factors, the model should additionally account for the elastic compliance of the bearing liner and its support.

References

1. Kumar, S., Kumar, V., & Singh, A. K. (2020). Influence of lubricants on the performance of journal bearings – A review. Tribology - Materials, Surfaces & Interfaces, 14(2), 67–78. https://doi.org/10.1080/17515831.2020.1712112
2. Wang, K., Yang, L., Wang, H., Ji, X., & Zhu, K. (2023). Transient analysis for offset-elliptical journal bearings under misalignment and dynamic loading. Proceedings of the Institution of Mechanical Engineers, Part J: Journal of Engineering Tribology, 237(7), 1511–1531. https://doi.org/10.1177/13506501231163920
3. Gu, C., Meng, X., Zhang, D., & Xie, Y. (2017). Transient analysis of the textured journal bearing operating with the piezoviscous and shear-thinning fluids. Journal of Tribology, 139(5), 051708. https://doi.org/10.1115/1.4035812
4. Alshaer, B. J., & Lankarani, H. M. (2023). An exact analytical solution for dynamic loads generated by lubricated long journal bearings. Mechanism and Machine Theory, 183, 105263. https://doi.org/10.1016/j.mechmachtheory.2023.105263
5. Xiong, G., Zhang, J., Mao, Z., Wang, Z., Wang, H., Lian, S., & Jiang, Z. (2024). Dynamic misalignment effects on performance of dynamically loaded journal bearings. International Journal of Mechanical Sciences, 264, 108839. https://doi.org/10.1016/j.ijmecsci.2023.108839
6. Xiong, G., Mao, Z., Zhang, J., Wang, Z., Wang, H., & Jiang, Z. (2023). Coupled effects of misalignment and viscoelastic deformation on dynamically loaded journal bearings. International Journal of Mechanical Sciences, 251, 108347. https://doi.org/10.1016/j.ijmecsci.2023.108347
7. Wang, K., Wang, C., Wang, X., Zhu, K., & Yang, L. (2024). Nonlinear tribo-dynamic performance and transient stability for marine dynamically loaded offset-halves journal bearings. Tribology International, 191, 109177. https://doi.org/10.1016/j.triboint.2023.109177
8. Shi, J., Zhao, B., Tu, L., Xin, Q., Xie, Z., Zhong, N., & Lu, X. (2024). Transient lubrication analysis of journal-thrust coupled bearing considering time-varying loads and thermal-pressure coupled effect. Tribology International, 194, 109502. https://doi.org/10.1016/j.triboint.2024.109502
9. Wang, G., Zhao, X., Zhang, Y., Li, C., & Du, J. (2025). Transient mixed lubrication analysis of the hydrodynamic bearing-rotor system during start-up considering misalignment and wear. Nonlinear Dynamics, 113, 17769–17789. https://doi.org/10.1007/s11071-025-11120-4
10. Singh, V., & Rajput, A. K. (2023). Piezoviscous-polar lubrication of capillary compensated hybrid conical undulated journal bearing. Tribology International, 186, 108588. https://doi.org/10.1016/j.triboint.2023.108588
11. Chen, Z., Wang, J., Li, R., & Liu, Y. (2025). Transient tribo-dynamic behavior of bi-directional misaligned water-lubricated bearings coupled with journal axial motion. Physics of Fluids, 37(3), 037113. https://doi.org/10.1063/5.0256919
12. Dykha, A. V., & Marchenko, D. D. (2018). Prediction the wear of sliding bearings. International Journal of Engineering and Technology, 7(2.23), 4–8. https://doi.org/10.14419/ijet.v7i2.23.11872
13. Marchenko, D. D., & Matvyeyeva, K. S. (2020). Investigation of tool wear resistance when smoothing parts. Problems of Tribology, 25(4/98), 40–44. https://doi.org/10.31891/2079-1372-2020-98-4-40-44
14. Wei, C., Liao, G., Wang, W., Xu, J., & Liu, K. (2023). Transient tribo-dynamic performance of journal bearings considering wear behavior during start-up. Proceedings of the Institution of Mechanical Engineers, Part J: Journal of Engineering Tribology, 237(9), 1809–1825. https://doi.org/10.1177/13506501231187316
15. Sangeetha, S., Saleh, A. A., Anandhababu, D., Marimuthu, K., Ali, N., Karabiyik, Ü., & Geethamalini, S. (2025). Viscosity variation with velocity slip effect using couple stress fluid between rough conical bearings. Boletim da Sociedade Paranaense de Matemática, 43, 1–12. https://doi.org/10.5269/bspm.78374

Марченко Д.Д., Матвєєва К.С. Динаміка підшипника ковзання при раптовій зупинці ротора з урахуванням інерційних властивостей та тискозалежної в'язкості мастила

Досліджено динамічну поведінку підшипника ковзання при раптовій зупинці ротора з урахуванням інерційних властивостей ротора та залежності в'язкості мастила від тиску. В'язкість мастила описано законом Баруса, а розподіл тиску в мастильному шарі визначено на основі рівняння Рейнольдса для одновимірного руху мастила зі змінною в'язкістю. Результуючу гідродинамічну силу враховано в рівнянні руху ротора–підшипника другого порядку. Зовнішню ударну дію задано у вигляді півхвилі синусоїди, а отримане нелінійне диференціальне рівняння розв'язано чисельно. Проаналізовано зміну товщини мастильного шару та максимального тиску в ньому під час ударної дії та після її припинення. За досліджуваних умов максимальний тиск у мастильному шарі досягає приблизно 74 МПа, після чого зменшується та здійснює коливання з малою амплітудою навколо середнього значення близько 14 МПа. Товщина мастильного шару протягом досліджуваного перехідного процесу залишається достатньою для збереження його цілісності. Порівняння з наближеним методом показало, що останній дає завищені значення переміщень, швидкостей і тисків. Запропонована модель може бути використана для оцінювання динамічної поведінки та ударостійкості підшипників ковзання при раптовій зупинці ротора та ударному навантаженні.

Ключові слова: підшипник ковзання, раптова зупинка ротора, ударне навантаження, інерція ротора, в'язкість мастила, залежність в'язкості від тиску, мастильний шар, динамічний аналіз; ударостійкість

ISSN 2079-1372 Problems of Tribology, V. 31, No 3/121-2026, 36-47

Problems of Tribology
Website: http://tribology.khnu.km.ua/index.php/ProbTrib
E-mail: tribosenator@gmail.com

DOI: https://doi.org/10.31891/2079-1372-2026-121-3-36-47

Characteristics of the lubricating action of oils under EHD conditions in the local friction contact zone

O. Milanenko* 0000-0002-8197-5277, **I. Bogdanov** 0000-0001-6346-4388, **D. Leusenko** 0000-0001-8024-6104, **O. Vansovskyi** 0009-0000-8451-6685, **D. Stetskyi** 0009-0005-2610-1947
National Transport University, Kyiv, Ukraine
**E-mail: milanmasla@gmail.com*

Received: 05 July 2026: Revised 30 July 2026: Accept: 15 August 2026

Abstract

Based on the newly developed interferometric test stand for evaluating lubricant film thickness — which enables the high-precision recording and analysis of transient processes under EHD lubrication conditions in the local friction contact zone of the non-conforming assemblies with varying actual contact geometries — across a wide range of operating (kinematic and load) parameters, an assessment was made of the influence of velocity, contact load, friction pair materials, the rheological properties of the lubricants and the geometry of the contact shape on the process of forming the minimum and central thicknesses of the lubricant film and the lubricating action of oils within the framework of determining the lubricant film parameter.

Key words: lubricating action of oils, elastohydrodynamic (EHD) lubrication, interferometric test stand, lubricant film thickness, local friction contact zone, non-conforming assemblies, contact geometries, actual contact shape, rheological properties, elliptical contact, point contact, ellipticity parameter.

An overview of unresolved issues based on the latest research and publications

Improving the lubricating performance of oils in bearing assemblies with localized contact is currently a promising and effective method for optimizing the design of rolling bearings by modifying the geometry of the contact patch and rationally selecting lubricants based on their viscosity and rheological properties. Ultimately, this leads to an increase in the service life of rolling bearing friction pairs (Fujita et al., 2019; Morales-Espejel & Félix-Quiñonez, 2021).

Theories of contact mechanics and lubrication, particularly the EHD theory, were originally based on the mechanics of continuous media, which assumes homogeneous and continuous (Newtonian) properties of lubricants regardless of scale in space and time. This approach is often valid when solving scientific and engineering problems related to surface interactions on a macroscopic scale. However, it has become clear that macroscale phenomena-such as load-carrying capacity, performance, efficiency and durability/reliability of various machines and their components-depend to a significant extent on the properties of interfaces at the macro- and microscales, where approaches that go beyond the mechanics of continuous liquid are required. Using existing EHD models, for example, it is possible to numerically simulate the entire transition from full-film (liquid) lubrication to mixed lubrication, or to boundary lubrication and surface contact, and the calculated thickness of the lubricant film can be as small as a few micrometers or even a few nanometers.

However, key questions remain unanswered, such as: Can we reliably predict interphase mechanisms using a model based on continuum mechanics if the thickness of the lubricating film is of the same order of magnitude as the oil molecules? What is the scope of application of the EHD theory? How can we model microfilms, which are commonly found under EHD and mixed lubrication conditions?

Comprehensive models and methods are currently being developed that combine continuum mechanics with the simulation of events at the micro- and even molecular levels. Recent studies include the work of Faraji et al. (2023) and Liu et al. (2020), among others. This appears to be a new and promising area of interfacial research. The mechanics of interphase regions allows for a better description of the complex nature of future studies and may be closely linked to research projects that delve into surface interactions. Today, there is a modern approach to lubrication regimes based on the consideration of two main physical aspects: elastic deformations of friction surfaces and the piezo viscosity coefficient of lubricant films (Kaneko, 2022, 2023, 2024a, 2024b, 2025). Thus,

Copyright © 2026 O. Milanenko, I. Bogdanov, D. Leusenko, O. Vansovskyi, D. Stetskyi. This is an open access article distributed under the Creative Commons Attribution License, which permits unrestricted use, distribution, and reproduction in any medium, provided the original work is properly cited.

the characteristics of the EHD lubrication regime lie in the formation of high pressure in the local friction contact zone, which leads to an increase in oil viscosity and elastic deformation of the interacting friction surfaces, thereby promoting the formation of a hydrodynamic lubricating film. This lubrication regime is predominantly observed in non-conformal friction assemblies (bearing assemblies) with a localized contact configuration. Under heavy loads, the pressure generated in the contact zone reaches 1 GPa. Since the lubrication regime is a complex phenomenon, there is a need to improve experimental methods for measuring lubricant film thickness and to conduct a comparative evaluation of calculated and experimental data on lubricant film thickness during the development of a mathematical model.

Problem Statement

The analysis of the characteristics of EHD lubrication discussed above showed that this operating regime is typical of non-conformal contact lubrication, which ensures minimal friction and a long service life for machine components. This occurs due to the formation of a continuous lubricating film, which prevents direct contact between the micro-irregularities of the contacting friction surfaces, as determined by the lubricating film parameter λ according to the following expression:

$$\lambda = \frac{h_{min}}{\sqrt{R_{a1}^2 + R_{a2}^2}}, \tag{1}$$

where h_{min} – minimum thickness of the lubricating film in the local contact zone for EHD friction conditions;

$\sqrt{R_{a1}^2 + R_{a2}^2}$ – the arithmetic mean deviation of the roughness profile from the centerline for each surface of a friction pair.

In this regime, the lubricating action of oils in the local contact zone will depend on the geometry of the actual contact shape and the rheological and viscosity properties of the lubricant film, since the pressure increases significantly under load, especially in the zone at the exit from the contact. Therefore, considering the geometry of the contact shape by evaluating the ellipticity coefficient and selecting the elastic-piezo viscous regime by evaluating the piezo viscosity coefficient will allow for a more accurate assessment of the lubricant film thickness under real operating conditions for bearing friction assemblies.

Thus, solving the multifactorial problem of estimating the lubricant film thickness under EHD lubrication conditions for non-conforming (bearing) friction assemblies requires the use of modern automated equipment capable of evaluating the transient processes occurring in the lubricant film within the actual local friction contact zone. Experimental methods for measuring the thickness of the lubricant film in the EHD lubrication systems in the local contact zone can be divided into the following groups: electrical, X-ray, acoustic, and optical methods.

Currently, optical measurement methods are the most accurate and visually representative methods for studying lubricant film thickness under EHD lubrication conditions for local friction contacts (Kazuyuki et al., 2021; Šperka et al., 2016). These methods allow for real-time measurement of film thickness with nanometer-level accuracy. Among them, the optical interference method is exceptionally effective, as it allows for measuring film thickness with an accuracy of 0.05 μm or less. The difference between theoretical and experimental film thickness values typically does not exceed 1%.

Four optical interference methods can be identified that are optimally suited for estimating the thickness of the lubricating film under EHD lubrication conditions: the traditional optical interference method, the spatial layer imaging method (SLIM), thin-film colorimetric interferometry and the method for determining the relative intensity of optical interference.

The traditional optical interference method reveals the complete relative topographical distribution of the contact area. Typically, this technique is used to measure film thicknesses of 0.05 μm and greater, with a 1% difference between theoretical and experimental values for the SAE 40 medium-viscosity oil.

The Spatial Layer Imaging Method (SLIM) measures lubricant film thickness at the nanoscale by incorporating a solid interlayer (Wolf et al., 2022) with a refractive index like that of the oil. The thickness of the intermediate layer is subtracted from the total thickness (oil and intermediate layer) to measure film thickness down to 10 nm. The difference between the theoretical and experimental values for the minimum and central film thicknesses at low shear rates is approximately 30% and 25%, respectively. In thin-film colorimetric interferometry, computer software is used for comprehensive image processing, which allows for the real-time determination of the film thickness distribution using colorimetric interferometry. The measurement range for this method is from 1 to 800 nm, with a resolution of 1 nm and a spatial resolution of 1 μm. The presence of the EHD film with a thickness on the order of several tens of molecular dimensions has been confirmed using this method.

The method for determining the relative intensity of optical interference uses monochromatic light, which produces Newton's interference rings. To measure the thickness of the lubricating film at a specific location, the relative intensity of light at the locations of the maximum and minimum Newton's rings is examined by analyzing a digitized image, where it was found that the thickness of the lubricating film is approximately 1 nm (Khan et al., 2021). This method was refined by Khan et al. (2021) for measuring film thickness, but it has certain limitations. For example, in the case of point (circular) contact, the film takes on a horseshoe shape, and the point of minimum film thickness is located on one of the sides distant from the centerline due to the use of a reflective sphere and a transparent disk with a high-precision coating.

The above considerations regarding experimental studies of the lubricating action of oils indicate that optical methods are widely used for measuring film thickness, as they allow for the measurement of lubricant layer thickness down to 1 nm or even less. However, according to the specified task, the complete test setup must have the following characteristics:

1) Visual observation of changes in the geometry of the actual contact shape, from point (circular) to elliptical contact with a wide range of ellipticity;

2) Color chromatic and filtered illumination of the entire local friction contact zone.

3) Computer software for comprehensive image processing and automated control of the operating characteristics of friction pairs, like the results obtained using thin-film colorimetric interferometry.

4) Stroboscopic illumination for photo and video recording of the interference pattern to evaluate transient processes occurring in the thin-film lubricant layer.

Thus, taking into account the specific nature of the research described above in accordance with the stated task, it is necessary to develop test equipment that implements the traditional method of optical interference using software for comprehensive image processing and automated control of the operating characteristics of friction pairs, as is characteristic of thin-film colorimetric interferometry.

Methodological tools for evaluating the lubricating performance of oils under EHD lubrication conditions in the local friction contact zone

The necessary information regarding the nature of many phenomena in local friction contact zones can be obtained only by applying a fundamentally new and modern approach to enhancing the lubricating performance of oils for specific operating conditions and lubrication regimes, as well as predicting the service life of friction assemblies for the range of lubricants under study. This is achieved by selecting an effective conceptual framework for conducting experimental research, utilizing the necessary modern and automated equipment, applying modern methods of mathematical analysis of research results, and implementing the findings of experimental studies at lubricant manufacturers or operators of friction assemblies.

To implement the above concept and taking into account the necessary requirements for testing equipment, an interference testing stand was developed based on the method of optical light interference, which allows for the assessment of the lubricant film thickness and lubrication regime in the local and elastic zones of the actual contact area, as well as beyond its boundaries at the entry and exit points of the contact, taking into account changes in the geometry of the contact shape due to the ellipticity coefficient and the viscous and rheological properties of the tested series of lubricants. The use of photo and video equipment makes it possible to record and analyze, with high precision, the transient processes under EHD lubrication conditions that occur in the micro zones of local friction contact in ball and barrel-shaped roller bearings, ball friction gears, ball bearings with an external self-aligning support and slewing ring over a wide range of operating (kinematic and load) parameters.

A general view of the test stand is shown in Fig. 1.

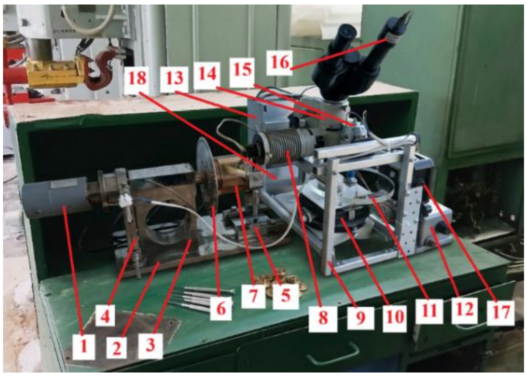

1 – D-38T electric motor; 2 – base plate; 3 – frame; 4 – centering device;
5 – carriage assembly with freely moving supports for the "glass outer ring (indenter 1) – steel ball (counterbody)" friction pair; 6 – perforated disc for determining rotational speed (linear velocity); 7 – glass outer ring (indenter 1);
8 – lighting unit; 9 – frame; 10 – specimen stage with a carriage featuring freely moving supports, assembled for the friction pair "glass disc (indenter 2) – steel ball (counterbody)"; 11 – glass outer disc (indenter 2);
12 – illumination lamp ignition unit; 13 – power supply unit; 14 – MMU-3 microscope; 15 – RS775 electric motor;
16 – camera; 17 – primary data processing unit (load, rotational speed, and temperature);
18 – power supply unit for the RS775 and D-38T electric motors

Fig. 1. Test setup for interference studies of lubricant film thickness, considering changes in the geometry of the actual local friction contact shape

The object of study (Fig. 2a, b) is the contact zone between an outer glass ring (see Fig. 2a) serving as indenter 1 or a glass disc (see Fig. 2b) serving as indenter 2, both made of the K7 optical glass with a surface finish of $Ra1 = 0.02$ μm (roughness class – 12b) and a standard steel ball serving as the counterbody, made of SHKH-15 steel with a surface finish of $Ra2 = 0.1$ μm (roughness class – 10b); the ball's diameter is 25.4 mm.

Thus, the arithmetic mean deviation of the roughness profile from the mean line of the friction pairs, $\sqrt{R_{a1}^2 + R_{a2}^2}$, will be 0.102 μm for determining the lubrication mode parameter λ using equation (1). The K7 optical glass, from which indenters 1 and 2 are made (see Fig. 2a, b), is a type of colorless crown optical glass (crown class) characterized by a refractive index of approximately n_d = 1.511. It belongs to the classic light crown glasses and is used for manufacturing lenses and other components of optical instruments.

The design of the carriage with freely moving supports (see Fig. 2a, b) allows the counterbody to be repositioned relative to the corresponding indenters 1 and 2 to change the geometry of the friction contact shape (the ellipticity coefficient k). Thus, this configuration enables rolling friction conditions for the "steel ball–glass ring" friction pair to simulate the operating conditions of ball and barrel-shaped roller bearings and ball friction gears, as well as for the "steel ball – glass disc" friction pair to simulate the operating conditions of ball bearings with an external self-aligning support and swivel ring (plate). Ball carriages with freely moving supports 2 (see Fig. 2a) for elliptical contacts and 3 (see Fig. 2b) for point contacts consist of a metal housing, two freely moving shafts onto which four small MR-series ball bearings (supports) measuring 4x8x3 mm are pressed to accommodate the ball as a counterbody, and the Type K thermocouple to determine the bulk temperature of oil.

To experimentally measure the optical thickness of the lubricating film, an MMU-3 microscope was used, as shown in the diagram (Fig. 3). This microscope is designed for examining opaque objects in reflected light and is used for both bright-field and dark-field observation under polarized light.

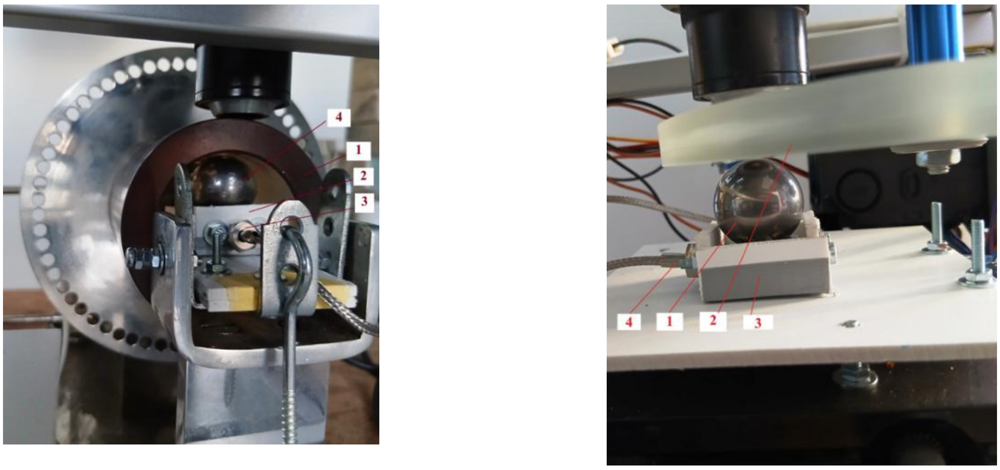

a **b**

a – "Glass outer ring (indenter 1) – steel ball (counterbody)" friction pair: 1 – glass outer ring (indenter 1); 2 – carriage with freely moving supports; 3 – thermocouple; 4 – steel ball (counterbody)

b – "Glass disk (indenter 2) – steel ball (counterbody)" friction pair: 1 – steel ball (counterbody); 2 – glass disk (indenter 2); 3 – carriage with freely moving supports; 4 – thermocouple

Fig. 2 a, b. Friction pairs of the test rig for interference studies of lubricant film thickness as the geometry of the actual local friction contact shape changes

To avoid having to reposition the microscope 14 (see Fig. 1), the following procedure was followed: the stand on which the microscope is mounted was raised an additional 200 mm from its baseline position using a special screw. This compensates for the difference in height between the disk and the ring. Additionally, the microscope can rotate 360° on the stand. If the upper power supply unit 13 (see Fig. 1) is in the way, it can be removed; the length of the wires allows for this. When performing point-contact experiments, the microscope is rotated 90° from its initial position (see Fig. 1). The high-speed camera 16 (see Fig. 1), mounted on the microscope, is used to transmit the image from the microscope's eyepieces to PC.

Power supplies 18 for motors (see Fig. 1) are connected to 230 V, 50 Hz power supply and feature switch buttons 15 for motor (RS775), a powerful brushed DC motor, and motor 1 (D-38T), an aviation DC motor. Power supply unit 13 (see Fig. 1), rated for 12 V, 5 V and 3.3 V, respectively, powers the rest of the system's electrical components: the lighting lamp ignition unit 12 and the primary data processing unit 17 (see Fig. 1).

The lighting lamp ignition unit 12 (see Fig. 1) features a dimmer for smoothly adjusting light brightness and saving electricity and provides an uninterrupted power supply to the lighting lamp unit 8 (see Figs. 1 and 3).

The primary data processing unit 17 (see Fig. 1) consists of:

– the type K thermocouple with a digital amplifier based on the MAX6675 integrated circuit (see Figs. 2a, b);

– the flat "Kvasolina"-type strain gauge for the low platform based on the HX711 (Fig. 4);

– the compact HW-201 infrared obstacle sensor based on reflected light, with adjustable range and a supply voltage from 3.3 to 5 V, which is also used in robotics for obstacle avoidance and in simple control systems (see Fig. 4);

– the compact and popular Arduino Nano V3.0 development board based on the ATmega328P microcontroller, which operates at 16 MHz at 5 V and can be easily mounted on a breadboard (see Fig. 4).

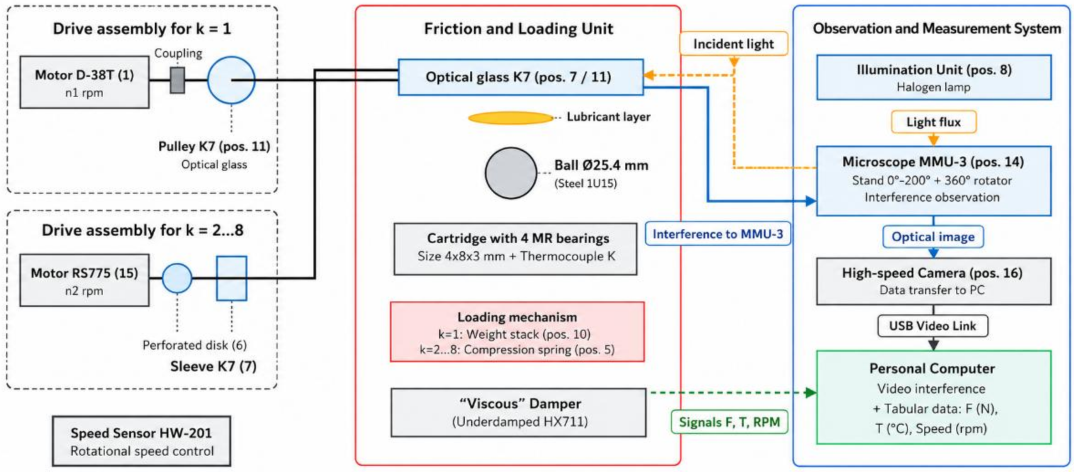

Fig. 3. Schematic kinematic and optical diagram of a test rig for interference studies of lubricant film thickness, considering changes in the geometry of the actual local friction contact shape

The initial results are transmitted to PC, where the input parameters are processed (see Figs. 3 and 4). The software used includes Windows 11 Pro 25H2 x64, the built-in "Camera" app, and Arduino IDE 2.3.5 to automate the measurement equipment.

To determine the rotational speed, a perforated disk for elliptical contacts 6 (see Fig. 1) with the ellipticity coefficient k > 1 (see Fig. 2a) and markings on a glass disk 11 (see Fig. 1) for point contacts for k = 1 (see Fig. 2b).

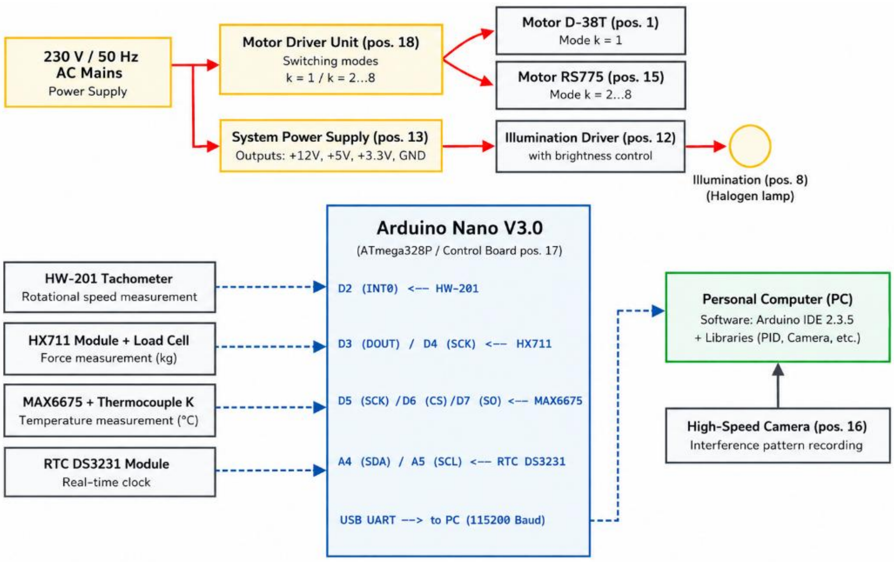

Fig. 4. Schematic electrical diagram of a test bench for interference studies of lubricant film thickness, considering changes in the geometry of the actual local friction contact

The HW-201 infrared obstacle sensor (see Figs. 3 and 4), which is part of the primary data processing unit 17 (see Fig. 1), is repositioned and mounted in a special hole in the base 3 or frame 9, depending on which contact shape is being tested: elliptical (base) or point (frame). The base 3 is mounted on a special plate 2 and has a centering device 4, which centers the entire "glass outer ring (indenter 1) – steel ball (counterbody)" friction pair system.

To study elliptical contacts, where k > 1, the "glass outer ring (indenter 1) – steel ball (counterbody)" friction pair is used (see Fig. 2a), in which the load is applied via a carriage and a lever system 5 (see Fig. 1). To study point contacts, where k = 1, a friction pair consisting of a "glass disk (indenter 2) – steel ball (counterbody)" is used, in which the load is applied via a specimen stage with a carriage assembly 10 (see Fig. 2b), which allows the stage to be moved within certain limits in the x and y directions, as well as rotated 360°. A membrane is mounted on the stage, on which the carriage is positioned and beneath which the “Kvasolina”-type load cell for the low platform on the HX711 is located (see Figs. 3 and 4).

The actual shapes (micro-interferograms) of elliptical and point contacts under dynamic friction conditions, shown in Fig. 5a, b, respectively, were obtained using the optical interference method on an interference testing bench.

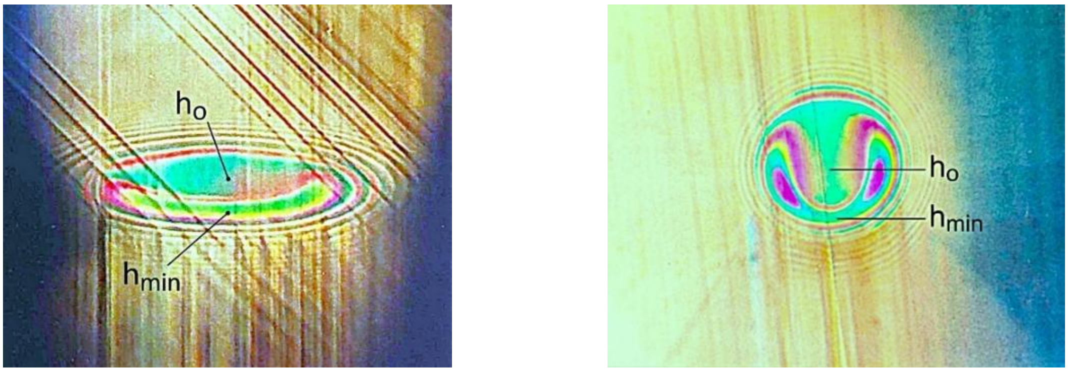

a b

h_{min} – minimum lubricant film thickness; h_o – central lubricant film thickness

Fig. 5 a, b. Actual shapes (micro-interferograms) of elliptical (a) and point (b) contacts under dynamic friction conditions

Fig. 5a, b shows all the characteristic features of lubrication under varying contact geometry, as observed on the developed interferometric test bench. The elliptical and point contact shapes (see Fig. 5a, b) have corresponding lubricant film thickness distributions with minimum thickness values at the contact exit (hmin) and in the central contact region (ho), which arise between the contact surfaces of friction bearing assemblies.

Results of the assessment of the influence of key parameters on lubricant film thickness

The most important practical aspect of lubrication analysis for local friction contact is determining the minimum (h_{min}) and central (h_o) lubricant film thicknesses in the local friction contact zone, since maintaining the required lubricant film thickness is crucial for the operational reliability of various friction bearing assemblies. The influence of the contact geometry—expressed in terms of ellipticity—and the dimensionless parameters of velocity, load, and materials on the corresponding lubricant film thicknesses and parameters is investigated for a local contact that is fully immersed in the lubricant (i.e., for a heavily lubricated contact).

Changes in the main input and dimensionless parameters used for the experimental studies are presented in Table 1.

The input and dimensionless parameters for the implementation of the EHD lubrication regime, as shown in Table 1 and considering changes in ellipticity in a point friction contact, do not cover all real-world lubrication conditions for local friction contacts. From a practical standpoint, it is important to estimate the thickness of the lubricant film, taking into account the influence of changes in the geometry of the contact shape—that is, its ellipticity—the rheology of lubricants, and the wear of the friction pair surfaces due to roughness, in order to achieve an optimal lubrication regime that enhances the lubricating effect of the oils.

1. Assessment of the effect of lubricant film thickness on rolling velocity

By varying one of the parameters, it is possible to determine the optimal lubricant film thickness that affects the lubricating performance of oils in the local contact zone of rolling bearings when using transmission oils for various technical applications.

The range of linear rolling velocity V varied from 0.05 to 1.0 m/s; the oil temperature T remained at 343 K throughout the experiment; the maximum contact pressure P_{max} = 474 MPa. The minimum thickness h_{min} and the thickness of the lubricant film in the central contact zone h_o were measured using the optical interference method on an interference testing stand for EHD point-contact (R_y/R_x = 1) based on a sample of micro-interferograms (Fig. 6).

A graphical interpretation of the experimental results showing the effect of rolling velocity V on the minimum lubricant film thickness h_{min} and the central lubricant film thickness h_o in the point contact zone (R_y/R_x = 1) for the entire range of oils studied is presented in Fig. 7a, b, respectively.

Fig. 7c shows the dependence of the lubricant film parameter λ on rolling velocity V, which demonstrates the need to ensure EHD friction conditions whilst maintaining linear rolling velocity V within the range of 0.1 to 0.5 m/s for ATF-III and SAE 75W-80 transmission oils, SAE 75W-90 and within the range of 0.05 to 0.2 m/s for SAE 80W-90 transmission oil.

Table 1

Key input and dimensionless parameters for the implementation of the EHD lubrication regime for local friction contact

№	Parameter	Symbol	Formula	Measurement range	Dimension
1) Geometric parameters of the local friction contact					
1	Ratio of Curvature Radii	R_y/R_x	-	1 - 25	-
2	Relative radius of curvature along the direction of rolling	R_x	-	0,01	m
3	Contact ellipticity	k	$k = \left[{R_y}/{R_x} \right]^n$	1 – 8	-
2) Friction pair parameters					
4	The modulus of elasticity	E'	$E' = \dfrac{2}{\left(\dfrac{1-\nu_1^2}{E_1} + \dfrac{1-\nu_2^2}{E_2} \right)}$	150 - 250	GPa
3) Specifications for lubricants (transmission oils)					
5	Dynamic viscosity at 20°C	η_o	-	0,15 – 0,5	Pa·s (cP)
6	Kinematic viscosity at 100°C	μ	-	6,4 – 24,0	mm²/s (cSt)
7	Piezo-viscosity coefficient	α	$\alpha \cdot P = A \cdot \left[\left(\frac{T-138}{T_0-138} \right)^{-S_0} \cdot B^Z - 1 \right]$	$(1,4 – 1,6) \cdot 10^{-8}$	Pa^{-1}
4) Operating parameters					
8	Linear rolling velocity	V	-	0,05 – 1,0	m/s
9	Contact load	F	-	5 – 50	H
10	Maximum pressure in the contact zone	P_{max}	-	600	MPa
11	Volume temperature in the oil bath	T	-	293 - 343	K
5) Measured lubricant film thicknesses and the calculated lubricant film parameter					
12	Minimum lubricant film thickness	h_{min}	-	0,08 (min)	µm
13	Central lubricant film thickness	h_o	-	1,77 (max)	µm
14	Lubricant film parameter within the range of contact ellipticity variation	λ	$\lambda = \dfrac{h_{min}}{\sqrt{R_{a1}^2 + R_{a2}^2}}$	2 - 4	-
6) Dimensionless parameters in the local EHD zone of friction contact					
15	Dimensionless velocity parameter	U	$U = \dfrac{\eta_o \cdot V}{E' \cdot R_x}$	$6{,}3 \cdot 10^{-12}$ – $4{,}2 \cdot 10^{-10}$	-
16	Dimensionless load parameter	W	$W = \dfrac{F}{E' \cdot R_x^2}$	$6{,}5 \cdot 10^{-7}$ – $4{,}0 \cdot 10^{-6}$	-
17	Dimensionless material parameter	G	$G = \alpha \cdot E'$	1500 - 4000	-
18	Dimensionless minimum lubricant film thickness	H_{min}	$H_{min} = \dfrac{h_{min}}{R_x}$	$0{,}8 \cdot 10^{-5}$ (min)	-
19	Dimensionless central lubricant film thickness	H_o	$H_0 = \dfrac{h_0}{R_x}$	$1{,}8 \cdot 10^{-4}$ (max)	-

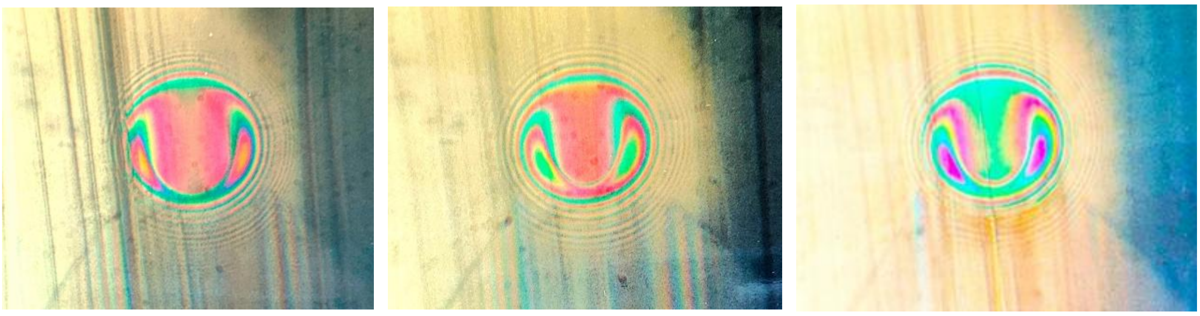

Fig. 6. Selection of micro-interferograms for point EHD contact (R_y/R_x = 1) over a range of linear rolling velocity V from 0.05 to 1.0 m/s (SAE 80W-90 transmission oil)

The presented selection of micro-interferograms (see Fig. 6) and the graphical interpretation of the dependence of the minimum and central thicknesses in the EHD contact zone on the rolling velocity (see Fig. 7a,

b) quite clearly indicate the dominant influence of the rolling speed under EHD lubrication conditions. Moreover, the SAE 80W-90 transmission oil, which has the highest viscosity grade, is characterized by greater sensitivity to high- velocity (high-RPM) operating conditions of rolling bearings.

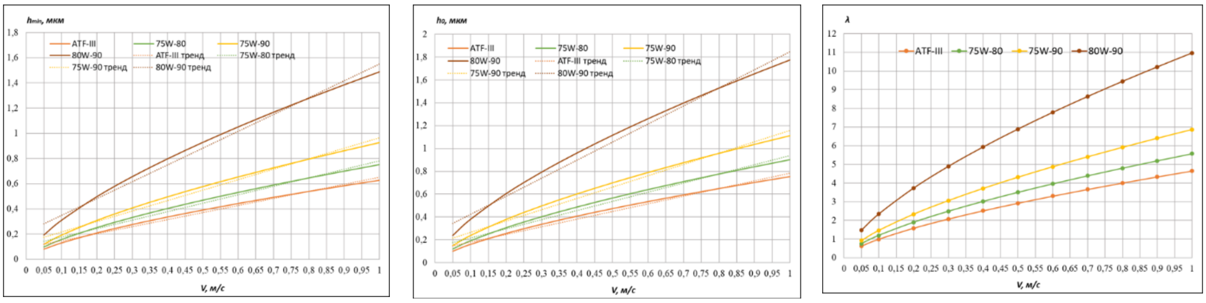

a b c

Fig. 7 a–c. Dependence of the minimum lubricant film thickness h_{min} (a), the central lubricant film thickness h_o (b) and the lubricant film parameter λ (c) in the point contact zone on the rolling velocity V

2. Assessment of the effect of contact load on the thickness of the lubricating film

By increasing the contact load from 7.78 to 46.68 N, corresponding to maximum contact pressures P_{max} ranging from 330 MPa to 600 MPa, at an oil temperature T of 343 K, the minimum and central thicknesses of the lubricant film in the point contact zone were determined on an interference measurement bench using a sample of micro-interferograms at $R_y/R_x = 1$ (Fig. 8).

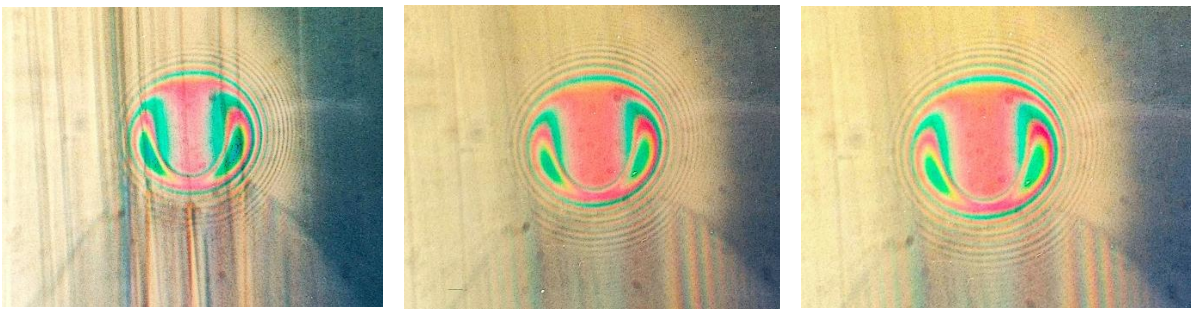

Fig. 8. Selection of micro-interferograms for a point EHD contact ($R_y/R_x = 1$) across a range of contact loads F from 7.78 to 46.68 N (the SAE 75W-90 transmission oil)

A graphical interpretation of the experimental results showing the effect of load F on the minimum lubricant film thickness h_{min} and the central lubricant film thickness h_o in the point contact zone ($R_y/R_x = 1$) for the entire range of oils studied is presented in Fig. 9a, b, respectively. Fig. 9c shows the dependence of the lubricant film parameter λ on the contact load F, which demonstrates the need to ensure the EHD friction conditions whilst maintaining the proposed contact load values F within the range of 7.78 to 46.68 N for all the transmission oils under investigation.

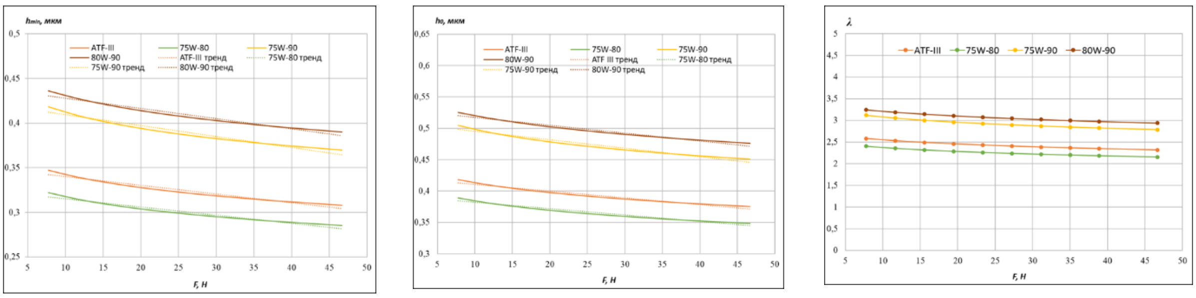

a b c

Fig. 9 a–c. Dependence of the minimum lubricant film thickness h_{min} (a), the central lubricant film thickness h_o (b) and the lubricant film parameter λ (c) in the point contact zone on the contact load F

The sample micro-interferograms presented (see Fig. 8) and the graphical interpretation of the relationship between the minimum and central thicknesses of the lubricant film in the EHD contact zone as a function of contact load (see Figs. 8 and 9a, b), clearly indicate that the load has a negligible effect on the respective thicknesses, which do not decrease significantly, as can also be seen from the color. Furthermore, as the contact load increases, the zone of central thickness expands in the transverse direction, whilst the minimum thickness at the exit from contact moves progressively further away from the central axis of the point of friction contact; this is, in our opinion, associated with the rheological effect of the oil's compressibility.

3. Assessment of the influence of materials on the lubricant film thickness

Unlike the determination of the influence of rolling velocity V and contact load F on the respective thicknesses under investigation, the influence of materials cannot be determined by simply changing just one parameter, since the dimensionless material parameter G comprises two variables (see Table 1), one of which characterizes the properties of the friction pair surfaces – the reduced modulus of elasticity E' – and the other – the rheological properties of the lubricant via the piezo-viscosity coefficient α. Therefore, four groups of materials, *G1–G4*, were formed, comprising three friction pairs made of different materials when using the range of lubricating oils under investigation, which have different viscosity classes and operational purposes and are used for the lubrication of modern rolling bearing assemblies. Three friction pairs, which are used in many rolling bearings for automotive and agricultural applications, were used as the friction pairs under investigation; their properties are given in Table 2.

Table 2

Input parameters for friction pair materials

№	Name of the friction pair	Modulus of elasticity E_1, GPa	Modulus of elasticity E_2, GPa	Poisson's ratio ν_1	Poisson's ratio ν_2	The reduced modulus of elasticity E', GPa
1	St40KH – SHKH15	210	220	0,25	0,3	235
2	BrO10F1 – SHKH15	120	220	0,33	0,3	170
3	BrOCS-4-4-17 – SHKH15	99	220	0,37	0,3	160

Experimental studies involving four groups of materials were conducted at an average rolling velocity of V = 0.4 m/s under EHD friction conditions, with an average contact load of F = 30 N; a temperature of T = 343 K, where the minimum thickness and the central thickness of the lubricant film in the point contact were determined on an interference measurement bench based on a sample of micro-interferograms at $R_y/R_x = 1$.

The experimental results showing the effect of material groups *G1–G4* on the minimum thickness h_{min} and the central thickness h_o of the lubricant film at $R_y/R_x = 1$ for the entire spectrum of oils studied are presented as a graphical interpretation of the data in Fig. 10a, b, respectively, for the four oils studied.

Based on the results of experimental studies of the effect of the material parameter G on the minimum thickness h_{min} and the central thickness h_o of the lubricating films in the point contact zone, a negligible effect—up to 3%—was found, specifically of the friction pair materials based on the reduced modulus of elasticity E', as indicated by the slight slope of the linear dependencies relative to the x-axis with respect to the dimensionless material parameter G. It is precisely the piezo-viscosity coefficient α that has a significant influence on the formation of film thicknesses under EHD conditions, as confirmed by the significant divergence of the dependencies for four transmission oils differing in viscosity class and intended use. If we take the material data for the groups (see Table 2) for the St40KH – SHKH15 friction pair, which experiences a maximum pressure P_{max} = 474 MPa in the point EHD contact zone, we obtain the following: for ATF II transmission oil, $\alpha \approx 0.014$ MPa^{-1}, and the dynamic viscosity η will increase by a factor of 762; for SAE 75W-80 transmission oil, $\alpha \approx 0.015$ MPa^{-1}, and the dynamic viscosity η will increase by a factor of 1 224; for SAE 80W-90 transmission oil — $\alpha \approx 0.016$ MPa^{-1}, and the dynamic viscosity η will increase by a factor of 1 970. In other words, the dynamic viscosity η of the high-viscosity SAE 80W-90 transmission oil increases by nearly three times compared to that of the low-viscosity ATF III transmission oil, which underscores the importance of the rheological properties of lubricants.

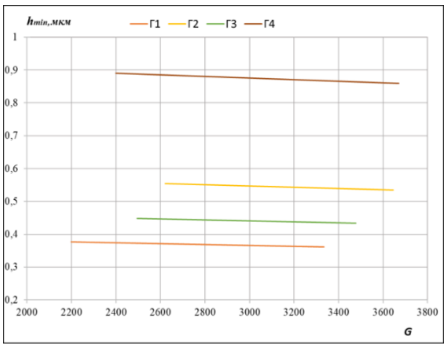

a

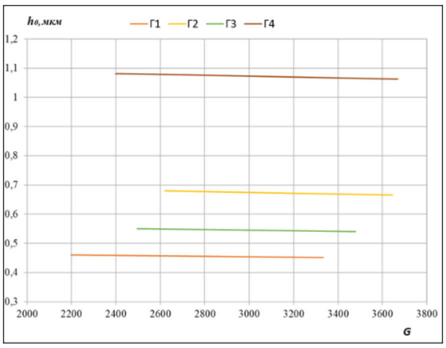

b

Fig. 10a, b. Effect of the dimensionless material parameter G on the minimum thickness h_{min} (a) and the central thickness h_o (b) lubricant films in the point contact zone for different of material groups G1–G4

From the perspective of the influence of materials G on the lubricant film parameter λ, this is not correct, since this parameter determines the lubrication regime, rather than the quality characteristics of the materials, which specifically affect the strength of the lubricant films and the durability of the friction pairs.

4. Assessment of the patterns of how contact ellipticity affects lubricant film thickness

One of the least studied aspects of the EHD theory of point contact lubrication is the effect of changes in contact geometry due to an increase in its ellipticity k. The ellipticity k depends on the dimensions of the contact ellipse in the Y and X directions (the rolling direction) and on the ratio of the relative radii of curvature R_y/R_x of the friction pair, ranging from unity for a disk–ball pair to approximately eight when the contact geometry is close to linear contact.

Thus, by varying the ratio of curvature radii R_y/R_x of the friction pair, while keeping the rolling velocity V, contact load F, and material groups *G1–G4* constant to ensure the friction conditions specified in Table 1, the minimum and central thicknesses of the lubricant film in the point-contact zone were determined on an interference measurement bench based on a sample of micro-interferograms at $R_y/R_x = 1$ (Fig. 11a) and at $R_y/R_x = 8$ (Fig. 11b) when maximum rolling velocities were reached.

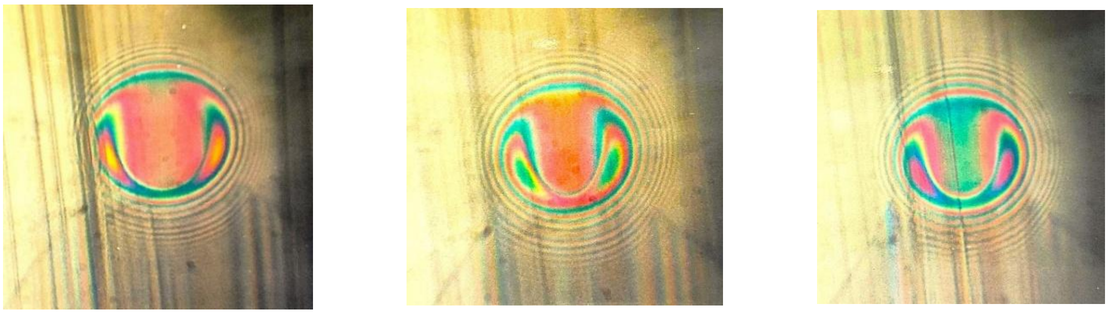

a

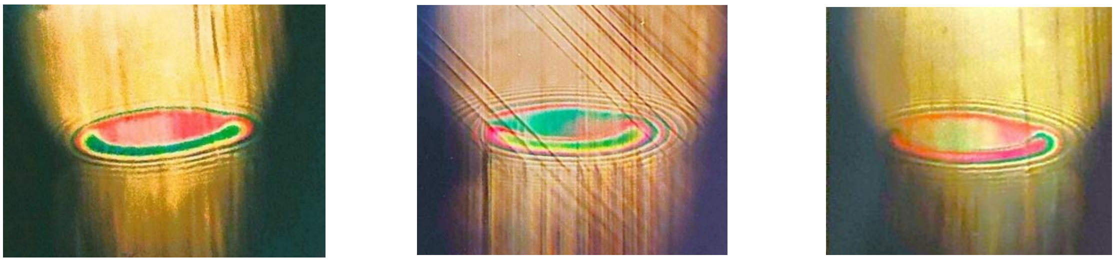

b

Fig. 11 a, b. Selection of micro-interferograms in the point EHD contact zone at $R_y/R_x = 1$ (a) and at $R_y/R_x = 8$ (b), while keeping the rolling velocity, contact load and material groups constant

At first glance, based on a sample of micro-interferograms (see Fig. 11a, b), it can be seen from the color that, while keeping the rolling velocity V, contact load F and material groups *G1–G4* remain constant, the minimum and central thicknesses of the lubricant film in the friction contact zone remain virtually unchanged as the contact ellipticity increases due to a change in the ratio of curvature radii from $R_y/R_x = 1$ *(a)* to $R_y/R_x = 8$ *(b)*. However, if we look closely at the micro-interferograms taken at the maximum rolling velocity (see Fig. 11a, b) and compare the minimum thicknesses at the exit from the contact zone, we see that when maximum rolling velocities are reached, the minimum thickness at the exit from the contact zone for the elliptical EHD contact ($R_y/R_x = 8$) will be slightly higher than that for the EHD point contact ($R_y/R_x = 1$). This effect is explained by the fact that as the ellipticity of the contact shape increases, the peak pressure decreases, which leads to a slight increase in the minimum thickness at the exit from the contact — this parameter that is more sensitive to changes in the contact geometry. The observed effect of reduced peak pressure can be a very important aspect of optimizing the design of friction bearing assemblies.

Experimental results showing the effect of contact ellipticity k on the minimum thickness h_{min} and the central thickness h_o of the lubricant film across the entire range of the curvature radius ratio R_y/R_x —from point-contact ($R_y/R_x = 1$) to practically linear ($R_y/R_x = 25$) contact, for the entire spectrum of oils studied, are presented in graphical form in Fig. 12a, b for the four oils under investigation.

Fig. 12c shows the dependence of the lubricant film parameter λ on the contact ellipticity k, with regard to ensuring the EHD friction conditions, where it is necessary to adhere to the proposed values of contact ellipticity ranging from 1 to 8 and the curvature radius ratio R_y/R_x ranging from point ($R_y/R_x = 1$) to practically linear ($R_y/R_x = 25$) contact for all the transmission oils under study.

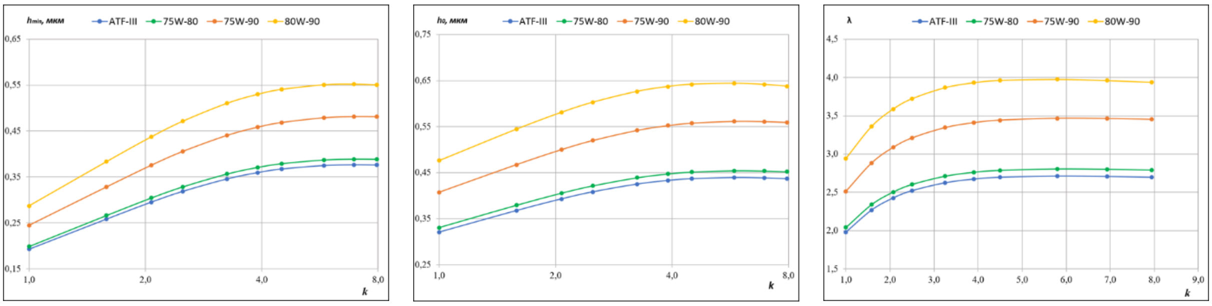

a b c

Fig. 12 a–c. Dependence of the minimum lubricant film thickness h_{min} (a), the central lubricant film thickness h_o (b) and the lubricant film parameter λ (c) on the contact ellipticity k across the entire range of the curvature radius ratio R_y/R_x

Conclusions

1. The dominant influence of rolling velocity under EHD lubrication conditions on the formation of the lubricant film thickness was established, with the dimensionless rolling velocity parameter varying by nearly two orders of magnitude when using four transmission oils differing in viscosity class and rheological properties. Furthermore, it was determined that transmission oils with a high viscosity class are characterized by greater sensitivity to high-speed (high-RPM) operating conditions of rolling bearings.

2. As the contact load increases by nearly one order of magnitude of the dimensionless load parameter when using four transmission oils differing in viscosity class and rheological properties, the manifestation of oil compressibility was observed, which is associated with the expansion of the central thickness zone in the transverse direction and the minimum thickness at the exit from contact becomes increasingly distant from the central axis of the point contact, which confirms the importance of taking into account the rheological properties of the studied series of transmission oils.

3. Using four groups of materials—comprising three pairs of friction materials and four transmission oils differing in viscosity class and rheological properties — we demonstrated a significant influence of the piezo-viscosity coefficient on the lubricant film thickness, as confirmed by the substantial divergence in the dependencies for the four transmission oils studied, in contrast to the negligible influence (up to 3%) of the friction pair materials.

4. It was established that transmission oils differing in viscosity class and rheological properties respond differently to the actual pressure exerted by the lubricating film formed within the point contact friction zone; for example, it was determined that the dynamic viscosity of a high- viscous SAE 80W-90 transmission oil compared to low-viscosity ATF III transmission oil under all other operating conditions being equal.

5. The effect of reduced peak pressure has been observed upon reaching maximum rolling velocities, when the minimum thickness at the exit from contact for an elliptical EHD contact exhibits a relative increase in thickness; that is, it is more sensitive to changes in contact geometry than for a point EHD contact.

References

1. Faraji, M., Seitz, A., Meier, C., & Wall, W. A. (2023). A mortar finite element formulation for large deformation lubricated contact problems with smooth transition between mixed, elasto-hydrodynamic and full hydrodynamic lubrication. *Tribology Letters*, *71*(1), Article 11. https://doi.org/10.1007/s11249-022-01682-4

2. Fujita, T., Hasegawa, N., Kamura, N., & Sasaki, T. (2019). Rolling contact fatigue of thrust ball bearing under low lambda condition. *Tribology Online*, *14*(4), 163–172. https://doi.org/10.2474/trol.14.163

3. Kaneko, M. (2022). High pressure rheology of lubricants (Part 5) - Derivation of van der Waals type viscosity equation. *Tribology Online*, *17*(4), 257–275. https://doi.org/10.2474/trol.17.257

4. Kaneko, M. (2023). High pressure rheology of lubricants (Part 1) - Deriving equation of relations of pressure, temperature, density and the viscosity. *Tribology Online*, *18*(4), 136–149. https://doi.org/10.2474/trol.18.136

5. Kaneko, M. (2024a). High pressure rheology of lubricants (Part 2) - Deriving equation of relations of pressure, temperature and the density. *Tribology Online*, *19*(1), 136–149. https://doi.org/10.2474/trol.19.33

6. Kaneko, M. (2024b). High pressure rheology of lubricants (Part 7) - Derivation of van der Waals type line density equation and estimation of high pressure density. *Tribology Online*, *19*(1), 87–94. https://doi.org/10.2474/trol.19.87

7. Kaneko, M. (2025). High pressure rheology of lubricants (Part 6) - Derivation of pressure temperature linear equation of dimensionless density and estimation of high pressure density. *Tribology Online*, *20*(1), 36–45. https://doi.org/10.2474/trol.20.36

8. Kazuyuki, Y., Kazuyuki, N., & Joichi, S. (2021). Influence of the heat transfer field on anomalous lubricant film formation in elastohydrodynamic lubrication conditions. *Tribology Letters*, *114*, Article 114. https://doi.org/10.1177/1350650121997240

9. Khan, T., Tamura, Y., Yamamoto, H., Morina, A., & Neville, A. (2021). Investigation of the tribological and tribochemical interactions of different ferrous layers applied to nitride surfaces. *Journal of Tribology*, *143*(1), Article 011705. https://doi.org/10.1115/1.4047588

10. Liu, H. C., Zhang, B. B., Bader, N., Venner, C. H., & Poll, G. (2020). Simplified traction prediction for highly loaded rolling/sliding EHL contacts. *Tribology International*, *148*, Article 106335. https://doi.org/10.1016/j.triboint.2020.106335

11. Morales-Espejel, G. E., & Félix-Quiñonez, A. (2021). Application of a rolling bearing life model with surface and subsurface survival to hybrid bearings in high-load and high-speed applications. *Tribology Online*, *16*(4), 216–222. https://doi.org/10.2474/trol.16.216

12. Šperka, P., Krupka, I., & Hartl, M. (2016). Lubricant flow in thin-film elastohydrodynamic contact under extreme conditions. *Friction*, *4*(4), 380–390. https://doi.org/10.1007/s40544-016-0134-6

13. Wolf, M., Šperka, P., & Fatemi, A. (2022). Film thickness in elastohydrodynamically lubricated slender elliptic contacts: Part II – Experimental validation and minimum film thickness. *Proceedings of the Institution of Mechanical Engineers, Part J: Journal of Engineering Tribology*, *236*(12), 2361–2372. https://doi.org/10.1177/13506501221080289

Міланенко О., Богданов І., Леусенко Д., Вансовський О. Особливості мастильної дії олив в умовах ЕГД змащування в локальній зоні контакту тертя

На базі створеного стенду інтерференційних досліджень щодо оцінки товщини мастильного шару, що дозволяє реєструвати та аналізувати з високою точністю швидкоплинні процеси в умовах ЕГД змащування в зоні локального контакту тертя неконформних вузлів зі зміненою геометрією фактичної форми контакту, в широкому діапазоні робочих (кінематичних та навантажувальних) параметрів, було зроблено оцінку впливу швидкості, контактного навантаження, матеріалів пар тертя, реологічних властивостей мастильного матеріалу, геометрії форми контакту на процесс формування мінімальної і центральної товщини мастильного шару та режим мастильної дії олив в рамках визначення параметру мастильного шару.

Ключові слова: мастильна дія олив, еластогідродинамічне (ЕГД) змащування, інтерференційний випробувальний стенд, товщина мастильного шару, локальна зона контакту тертя, неконформні вузли, геометрія контакту, фактична форма контакту, реологічні властивості, еліптичний контакт, точковий контакт, параметр еліптичності.

ISSN 2079-1372 Problems of Tribology, V. 31, No 3/121-2026, 48-60

Problems of Tribology
Website: *http://tribology.khnu.km.ua/index.php/ProbTrib*
E-mail: *tribosenator@gmail.com*

DOI: https://doi.org/10.31891/2079-1372-2026-121-3-48-60

Prediction and analysis of the Tribological Behaviors of hybrid Polymer Composites under reciprocating tribometer

L.B. Abhang[1] 0000-0002-6960-4035, **A.A. Sambare**[2] 0000-0002-0476-7562, **P.M. Karandikar**[1] 0009-0004-3564-3484, **Y. Dalwe**[3]*

[1] *Pravara Rural Engineering College (PREC), Loni, Savitribai Phule Pune University (SPPU), Pune, India*
[2]*Dr. Babasaheb Ambedkar Marathwada University, Chhatrapati Sambhajinagar, India*
[3] *Vishwabharati Academy's College of Engineering (VACOE), Ahmednagar, India*
**E-mail: asambare.ddukk@bamu.ac.in*

Received: 25 August 2025: Revised 30 June 2026: Accept: 10 August 2026

Abstract

This study investigates the tribological behavior of polyether ether ketone (PEEK) composites with polytetrafluoroethylene (PTFE) as a solid lubricant filler under dry reciprocating sliding conditions. Polymer specimens (80% PEEK/20% PTFE and 30% PEEK/70% PTFE) were tested against a steel counterpart using a linear reciprocating tribometer. The Taguchi L4 (2^3) orthogonal array was employed to evaluate the effects of load (100 N, 150 N), frequency (1.20 Hz, 2.30 Hz), and temperature (40°C, 80°C) on frictional force, coefficient of friction, and wear rate. Results showed that adding PTFE significantly reduced wear, with the 30% PEEK/70% PTFE composite achieving a minimum coefficient of friction (0.037) and wear rate (0.001 g) at 150 N, 30 Hz, and 40°C. ANOVA revealed load as the dominant factor for friction (61.28% contribution) and temperature for wear rate. Regression models predicted tribological outcomes with 99% accuracy. These findings highlight the potential of PEEK/PTFE composites for high-performance applications like bearings and seals.

Keywords: Hybrid composites, friction, wear, frictional force, orthogonal array

Introduction

Composite materials have emerged as a superior alternative to traditional monolithic materials due to their enhanced functional properties and diverse applications, ranging from sports equipment to aerospace systems. Ongoing global research continues to focus on developing advanced composites with improved performance. Among these, glass fiber-reinforced polymer (GFRP) composites have gained prominence, particularly in tribological applications such as bearings, gears, bushes, piston rings, and riders, where the use of liquid lubricants is often limited. Natural fiber-reinforced composites, such as abaca fiber-based fiber metal laminates (FMLs), have shown promising mechanical performance, as reported by Iqbal et al. [1], where a 5.18% fiber content achieved a flexural strength 19.5% higher than conventional glass fiber FMLs. Similarly, in high-performance polymer composites like PEEK/PTFE, tailoring the composition—such as increasing PTFE content—has demonstrated significant improvements in tribological behavior, emphasizing the importance of optimizing material constituents to enhance specific functional properties. Wakchaure and Abhang [2] conducted an experimental investigation on the tribological performance of PEEK/PTFE composites reinforced with fillers such as glass fibers, MoS_2, and bronze, highlighting that filler composition significantly influences wear resistance. Their findings support the trend observed in the present study, where an increased PTFE content in PEEK composites led to a reduction in wear rate, demonstrating that strategic modification of composite formulations can enhance performance in tribological applications such as oil-less compressor piston rings. Polyetheretherketone (PEEK) is a high-performance, semi-crystalline thermoplastic known for its exceptional combination of thermal and mechanical properties. It exhibits high strength, toughness, and excellent resistance to wear, creep, and fatigue. PEEK maintains stability under high temperatures, with a typical glass transition temperature around 143°C, melting point near 338°C, and continuous service temperature up to 250°C. Its inherent processability, including suitability for injection molding, allows for ease of manufacturing. Additionally, the incorporation of short fibers such as glass or carbon can further enhance its mechanical and tribological

Copyright © 2026 L.B. Abhang, A.A. Sambare, P.M. Karandikar, Y. Dalwe. This is an open access article distributed under the Creative Commons Attribution License, which permits unrestricted use, distribution, and reproduction in any medium, provided the original work is properly cited.

performance, making PEEK a versatile material for demanding engineering applications.

Research has shown that increasing the PTFE content in PEEK composites significantly improves their tribological behavior. For example, Burris et al. [3] and Escobar Nunez & Polycarpou [4] observed that PEEK/PTFE composites with higher PTFE content exhibit lower friction coefficients and improved wear resistance. Similarly, other studies have highlighted the effectiveness of fillers such as MoS_2, bronze, and glass fibers in enhancing the tribological performance of PEEK composites. Additionally, the tribological behavior of PEEK composites under varying operational conditions, such as temperature and load, has been widely investigated, but the influence of these parameters on wear rate and friction coefficient remains inadequately characterized.

Leyu Lin and Alois K. Schlarb [5] developed and optimized high-performance PEEK/CF/nanosilica hybrid composites, evaluating their mechanical properties through tensile testing and their tribological behavior using block-on-ring (BoR) tests under dry sliding conditions. Worn surfaces and transfer films were analyzed using scanning electron microscopy (SEM) with energy-dispersive X-ray (EDX) spectroscopy. Their results showed that PEEK composites reinforced with carbon fibers (CF) and nanosilica exhibited significantly improved friction and wear performance compared to unfilled PEEK (PEEK-Tr), with the best performance observed at 2 wt.% nanosilica across the full range of pressure-velocity (pv) conditions. The morphology and composition of the transfer film remained consistent regardless of nanosilica content or pv values, and the dominant wear mechanisms were identified as abrasive and adhesive wear.

Mr. Mankar N.A. et al. [6] aimed to develop self-lubricating PEEK-based composites suitable for applications such as piston rings, bearings, and impellers under both room and elevated temperatures. Using disc-on-pin wear tests, they found that pure PEEK exhibited a high wear rate, while the addition of MoS_2 and bronze significantly improved its tribological performance. The PEEK/PTFE/MoS_2 composite demonstrated the lowest specific wear rate (5.38×10^{-7} mm³/Nm) under ambient and low-load conditions, while the PEEK/PTFE/bronze composite showed favorable wear resistance (4.28×10^{-6} mm³/Nm) under harsher conditions. They concluded that solid lubricants like MoS_2 and bronze enhance transfer film stability and reduce wear by filling surface asperities, thereby increasing the wear life of PEEK composites.

Prashant Vishwas Parab et al. [7] conducted a comprehensive review on the friction and wear performance of PTFE and its composites, considering parameters such as sliding velocity, applied load, temperature, counter surface roughness, and contact area. They concluded that wear behavior was more sensitive to applied load than sliding velocity within the tested range. The coefficient of friction for pure PTFE and its composites was observed to decrease with increasing load. However, the addition of fillers such as bronze, carbon, glass fibers, graphite, or MoS_2 enhanced hardness and wear resistance, though it slightly reduced the self-lubricating property and marginally increased the coefficient of friction.

R. R. Neela Rajan et al. [8] investigated the tribological behavior of piston rings and cylinder liners lubricated with Jatropha Curcas oil and SAE 15W40 heavy-duty oil using response surface methodology (RSM) under varying test conditions. Reciprocating wear tests were performed on cast iron piston rings (chrome-coated) against cast iron cylinder liners, with test load, sliding velocity, and oil quantity as input parameters, and piston ring weight loss as the output response. Predictive models for weight loss were developed using polynomial regression equations for both lubricants, revealing that the lowest wear occurred at low load, low sliding velocity, and high oil quantity. The study concluded that Jatropha oil resulted in less piston ring wear compared to SAE 15W40, and that sliding velocity was the most significant factor influencing wear behavior.

S. Gokulakannan [9] reviewed the wear behavior of clutch plates made from PEEK composite materials, using pin-on-disc tests on samples with a 96 mm outer diameter and 56 mm inner diameter. He found that PEEK composites exhibited superior mechanical and tribological properties compared to pure PEEK, with wear rate influenced by the stacking structure and counter surface roughness. The addition of solid lubricants like MoS_2 and bronze helped reduce wear by filling surface asperities and stabilizing the transfer film, thereby extending the component's wear life. Saša Milojević et al. [10] studied the effect of tribological plugs as reinforcements on the tribological behavior of patented aluminum cylinders used in air brake compressors. They compared aluminum alloy base materials with ferrous and graphite-based reinforcements, concluding that friction and wear could be reduced by applying tribological coatings, surface texturing, and using low-viscosity oils with additives. This approach, by transferring piston ring contact to reinforced areas, significantly extends the service life of both cylinders and piston rings. T.J. Hoskins et al. [11] investigated the rolling–sliding wear behavior of poly-ether-ether-ketone (PEEK) discs running against each other to better understand the dynamic response of high-performance polymeric gear teeth. They found that PEEK showed promising wear resistance under low slip ratio conditions across a range of loads, even at high temperatures, despite some increase in wear. Wear, friction, and temperature all increased with higher slip ratios and loads, with failure mechanisms such as surface melting and contact fatigue occurring mainly under severe conditions. Their study suggests that optimizing gear tooth geometry to reduce slip ratios near the pitch point could enhance service life and minimize wear in polymeric gear systems. Zainab M. Shukur et al. [12] studied the tribological behavior of poly-ether-ether-ketone (PEEK) and its composite with 30% carbon fiber (PEEK CA30%) sliding against AISI 52100 steel under dry and marginal lubrication conditions using various lubricants including deionized water, ethylene glycol, silicone, and SN100 oil. They found that the highest coefficient of friction (CoF) occurred during dry sliding for both materials, while lubricated tests generally showed lower CoF values. Silicone lubricant resulted in the lowest CoF, about 50%

better than SN100 oil for PEEK, whereas water lubricant showed the highest CoF among lubricated tests. The volume of wear track was greatest under dry sliding and lowest with silicone lubrication, with PEEK CA30% showing better friction performance than pure PEEK when lubricated with water and ethylene glycol. David L. Burris et al. [13] studied functionally graded polymer composites based on PEEK and PTFE, primarily molded from Victrex 450 PF PEEK with a sliding interface containing 50 wt% cryoground PEEK filled with DuPont 7C PTFE. Samples were compression molded in layers with increasing PEEK content, milled, CNC machined, and finished to an average surface roughness (Ra) of about 50 nm. Tribological tests were performed using a linear reciprocating tribometer, a rotating pin-on-disk tribometer, and a custom thrust washer tribometer with 304 stainless steel counterfaces, showing friction coefficients of $\mu = 0.11$, 0.09, and 0.07 respectively. The functionally graded PEEK composites exhibited friction coefficients equal to or lower than bulk components, with the thrust washer configuration having the lowest friction due to its flat continuous sliding profile minimizing deformation. Kharat Amol et al. [14] investigated the friction and wear properties of PEEK and its composites filled with PTFE, Bronze, and MoS_2 under heavy loading conditions at ambient temperature to improve tribological behavior without compromising mechanical properties. They developed hybrid polymer composites combining Polyether-ether-ketone (PEEK) and Polytetrafluoroethylene (PTFE) and studied the effects of contact temperature and pressure on friction and wear under dry and wet conditions. PEEK, a semi-crystalline engineering plastic, has excellent mechanical, chemical, and thermal stability but suffers from high friction and wear rates, limiting its wider application. The addition of PTFE improved the tribological performance of PEEK composites, making them suitable for heavy-duty applications like compressor piston rings, bearings, and impellers operating under harsh conditions. Penin et al. [15] explored the enhancement of mechanical and tribological properties of PEEK composites by incorporating 0.3 wt.% of various nanoparticles: carbon nanofibers (CNF), copper (Cu), copper ferrite ($CuFe_2O_4$), and silicon dioxide (SiO_2). The addition of nanoparticles resulted in a 10–15% increase in elastic modulus, with Shore D hardness slightly increased for SiO_2 and marginally decreased for Cu. Tensile strength remained comparable to neat PEEK for SiO_2 and $CuFe_2O_4$ composites, while elongation at break decreased by 5–10% across all samples. Tribological tests under dry sliding conditions showed a reduction in friction coefficients from 0.34 (neat PEEK) to 0.23–0.28 for metal counterparts, with the CNF composite exhibiting the lowest friction (~0.20) on ceramic surfaces. Wear resistance improved by 1.5–2.3 times in metal–polymer contacts, attributed to polymer transfer film formation that protected contacting surfaces from micro-abrasive wear and oxidation. These results demonstrate that low concentrations of nanofillers can significantly enhance the stiffness and tribological performance of PEEK composites, making them suitable for demanding engineering applications. B. Suresh et al. [16] studied the mechanical and tribological properties of polyamide66/polypropylene (PA66/PP) blends filled with graphite, nanoclay (NC), and NC plus short carbon fiber (SCF). Samples were prepared by drying, mixing, and injection molding, then tested for tensile, flexural, impact, and wear properties. Results showed that NC + SCF composites had improved flexural strength and modulus, while NC and graphite fillers caused a decrease. Impact strength was highest in unfilled and graphite-filled composites. Overall, 5 wt.% graphite addition provided the best mechanical performance. Jayashree Bijwe et al. [17] investigated the effect of PTFE content on the mechanical and tribological properties of PEEK-PTFE blends. Samples were prepared by melt blending PEEK with varying PTFE amounts, followed by injection molding. Low Amplitude Oscillating Wear tests showed that blends exhibited no measurable wear under low loads and significantly improved wear resistance and friction performance at higher loads compared to neat PEEK. The PEEK-PTFE blends demonstrated up to 30 times reduction in wear rate and five timeslower friction coefficient, with no scuffing observed, indicating enhanced durability due to PTFE addition. J.R. Vail et al. [18] studied the tribological behavior of PEEK and ePTFE/PEEK composites using a linear reciprocating tribometer under controlled lab conditions. The addition of PTFE significantly reduced the friction coefficient from an average of 0.37 for unfilled PEEK and lowered the wear rate by forming thin, stable transfer films containing carbon, oxygen, and fluorine. The interfacial shear strength between ePTFE fibers and the PEEK matrix was found to be approximately 7.7 MPa based on filament pull-out tests. The ePTFE/PEEK composites showed consistent low friction and wear over extended cycling (over 2 million cycles), demonstrating that PTFE inclusion effectively improves the durability and tribological performance of PEEK by acting as a lubricant reservoir. E.Z. Li et al. [19] investigated the mechanical and tribological properties of neat PEEK and 30% short glass fiber-reinforced PEEK (GF/PEEK) composites. Injection-molded samples were tested for tensile and flexural properties at room temperature, showing that GF/PEEK composites exhibited higher tensile strength, tensile modulus, flexural strength, and flexural modulus compared to pure PEEK. Tribological tests using a ball-on-disc setup under dry conditions revealed that friction coefficient and wear loss increased with sliding time and load for all samples; however, GF/PEEK composites demonstrated superior wear resistance relative to neat PEEK. Surface morphology was examined via SEM, and thermal stability was analyzed using TGA, confirming improved mechanical and tribological performance due to glass fiber reinforcement. Mankar N.A et al. [20] investigated the tribological behavior of PEEK and PTFE-based composites reinforced with MoS_2 and Bronze. The composites were prepared by melt blending and processed via compression and injection molding. Tribological tests conducted under ambient conditions on a pin-on-disc setup following ASTM G99 revealed that pure PEEK exhibited a higher wear rate, while the addition of MoS_2 and Bronze significantly improved wear resistance. The PEEK/PTFE/MoS_2 composite showed a low coefficient of friction and a specific wear rate of 4.70×10^{-6} mm³/Nm under low load (20 N), whereas the PEEK/PTFE/Bronze composite demonstrated a low friction coefficient and superior wear resistance with a specific wear rate of 4.28

× 10^{-6} mm³/Nm under higher loading conditions.

Felipe Darabas et al. [21] studied the tribological behavior of a PEEK composite filled with 10% PTFE, 10% graphite, and 10% carbon fiber under varying temperatures (30°C and 80°C) and atmospheres (air and tetrafluoroethene). Using a cylinder-on-plate configuration against AISI 304 stainless steel, tests were performed under a constant 175 N load with linear reciprocating motion. Surface roughness was carefully controlled and characterized by white-light interferometry. Results showed that wear rates of the PEEK composite increased significantly with temperature, while the atmosphere had little effect. The stainless steel counterface experienced surface roughening but no volumetric wear. Elevated temperatures promoted tribo-layer formation, and humid air caused graphite structures to become more disordered, lowering the friction coefficient. Abhang et al. [22] critically reviewed the mechanical and tribological characteristics of hybrid polymer composites and emphasized that the inclusion of fillers such as PTFE, glass fibers, MoS_2, and bronze significantly improves wear resistance and reduces friction in polymers like PEEK and polyamide 66. Their review aligns with the current investigation, which also demonstrates that tailored filler content in PEEK/PTFE composites plays a vital role in optimizing tribological performance for demanding applications. The tribological performance of PEEK/PTFE polymer composites under variable operational parameters—such as load, temperature, sliding frequency, and humidity—remains inadequately characterized, limiting their optimization for high-demand engineering applications like bearings, oil seals, and actuators. Current literature lacks comprehensive studies on the wear mechanisms and frictional behavior of these composites at elevated temperatures and varying loads. Furthermore, there is a deficiency in systematically optimized processing and testing protocols to correlate composite composition with wear resistance and friction coefficient. This study aims to fill these gaps by quantitatively evaluating the wear and frictional behavior of PEEK/PTFE composites using a linear reciprocating tribometer. The study will apply the Taguchi orthogonal array design to optimize key parameters and enhance the performance of these composites under different operating conditions. Through this approach, we aim to provide valuable insights into the potential of PEEK/PTFE composites for high-performance tribological applications, contributing to their optimization for use in critical engineering systems.

Methodology

The wear behavior of PEEK/PTFE composites was systematically evaluated using a state-of-the-art linear reciprocating tribometer under controlled dry sliding conditions, adhering to ASTM G99 standards for wear testing. Specimens were precisely machined to specified dimensions and thoroughly cleaned before initial weighing using a high-precision digital electronic balance to ensure accurate mass loss measurements. The tribometer setup as shwn in figure 1, equipped with a pivoted lever mechanism, applied controlled normal loads of 100 N and 150 N against a hardened EN8 steel plate with a surface roughness of 0.4 µm, providing a consistent and reproducible contact interface. Test parameters such as stroke length (5 mm), frequency (1.20 Hz and 2.30 Hz), temperature (ambient 40°C and elevated 80°C), and humidity (maintained at 30% RH) were precisely regulated through integrated software control. Post-test wear loss was determined gravimetrically, complemented by frictional force and coefficient of friction data acquired in real time. Additionally, the experimental design was optimized using the Taguchi L4 orthogonal array method to systematically assess the influence of multiple variables on tribological performance, thereby enhancing experimental efficiency and reliability. This rigorous approach ensures comprehensive characterization of the tribological properties and provides critical insights for optimizing composite formulations for advanced engineering applications. The wear behavior of the composites was evaluated using a linear reciprocating tribometer under dry sliding conditions. Figure 2 illustrates the schematic of the tribometer setup. The materials were tested in mating pairs under nominally non-abrasive conditions. Wear was quantified by measuring the weight loss of the specimens before and after testing, using a high-precision electronic balance. Tests were conducted over a fixed reciprocating distance and under selected load values to ensure consistency and repeatability of results.

Fig 1: Schematic Linear Reciprocating Tribometer fixture plate

Fig 2: Schematic Linear Reciprocating Tribometer

In the test apparatus, the normal load was applied via a pivoted lever arm loaded with calibrated dead weights, as shown in Figure 3. A pin specimen was pressed against a stationary EN8 steel plate, with the contact surface of the pin machined flat to ensure uniform contact. This method of load application offers key advantages, including minimal frictional losses within the loading mechanism and improved mechanical efficiency, which contributes to more accurate and reliable test conditions.

Prior to testing, the specimens were thoroughly cleaned and their initial weights were recorded using a high-precision digital electronic balance. Each specimen was then securely mounted on the holder or mounting block, ensuring that the flat face of the composite was in direct contact with the stationary hardened EN8 steel plate, as illustrated in Figure 3. The tribometer setup was software-controlled, allowing precise adjustment of testing parameters such as temperature, stroke frequency, duration, and ambient humidity, based on specific experimental requirements.

The reciprocating track on the counter plate was carefully selected to avoid overlapping wear paths. Stroke distance, frequency, and temperature were defined accordingly. After completion of each test, the specimens were cleaned and their final weights were measured. The wear loss was calculated as the difference in weight before and after testing, expressed in grams.

The counterface material used was EN8 steel with a surface roughness of 0.4 µm. A series of wear tests was conducted using a fixed reciprocating stroke length of 5 mm, under two different normal loads of 100 N and 150 N.

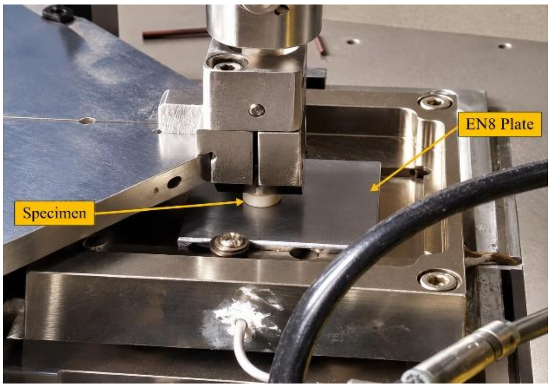

Fig 3. Linear Reciprocating Tribometer: Specimen & EN8 Plate

Raw material and rubbing plate /bottom plate have purchased directly from supplier as per requirement. Raw Material: PEEK & PTFE; Sizes: Diameter 8 x15mm length; Disc-EN8 – 40x40x5 mm.

Commercially available Polyetheretherketone (PEEK) and polytetrafluoroethylene (PTFE/Teflon) was supplied by M/s. Ayush Enterprises. Here PTEF plays a role of filler. According to the requirement, required sizes are manufactured (Diameter- ϕ8mm & Length- 15mm). Corresponding EN8 plate (40x40x5 mm) was supplied AM Technology and Engineering as a counterpart.

Table 1

Designation of Specimens

Specimens	Compositions	Quantity
1	PEEK (80%) + PTFE (20%)	04
2	PEEK (30%) + PTFE (70%)	04

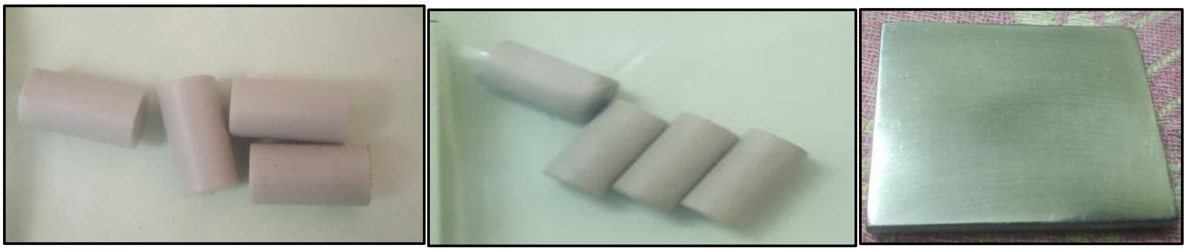

a b c

Fig 4. Specimens 1(a) and 2(b) & EN-8 Plate (c)

Test are performed on Linear Reciprocating Tribometer at different temperatures and frequencies with ambient humidity (30 %Rh) but varying load. Operating parameters were set as per test requirements and they are mentioned as below.

Table 2

Operating Parameters of Linear Reciprocating Tribometer

Stroke Length	5mm
Frequency	1.20 Hz, 2.30 Hz
Humidity	30 %Rh
Load	100N. 150N
Temperature	40ºC, 80ºC
Duration of Experiment/Specimen	20min

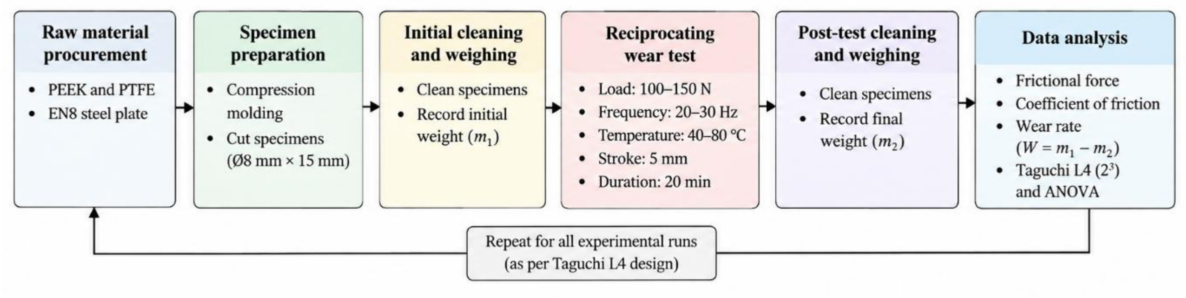

Fig.5. Flowchart of Experimental Methodology for Wear Test of PEEK/PTFE Composites

The time-dependent behavior of the PEEK and PEEK/PTFE composites under different operating conditions is discussed in the following section.

Results and discussions

The tribological behavior of PEEK and PEEK/PTFE composites was investigated under various operating conditions, including two different temperatures (40 °C and 80 °C), frequencies (20 Hz and 30 Hz), and normal loads (100 N and 150 N). Tests were conducted using a linear reciprocating tribometer to evaluate the wear rate of various pin specimens. The variation in coefficient of friction, wear rate, and frictional force was analyzed with respect to time.

The results clearly demonstrated that the wear resistance of PEEK was significantly enhanced by the addition of PTFE as a filler. In the absence of fillers, the base PEEK material exhibited substantial material removal due to the abrasive action of the hard asperities on the EN8 steel counterface, resulting in high wear loss. In contrast, when PEEK was blended with PTFE, a transfer film formed on the surface of the EN8 disc. This polymeric film reduced direct metal-to-polymer contact, thereby lowering both friction and wear loss.

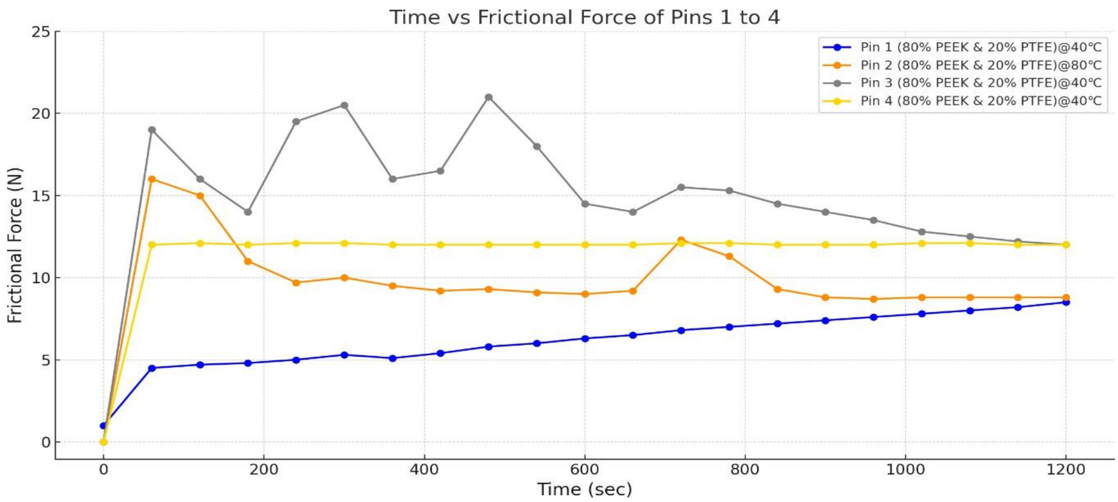

Fig.6. Effect of Time on Frictional Force of Pins 1 to 4

The frictional behavior of four pins, each composed of 80% PEEK and 20% PTFE, was analyzed by plotting frictional force (N) against time (s) over a 1200-second duration, as depicted in the figure 5 graph titled "Time vs Frictional Force of Pins 1 to 4." Each pin was tested under distinct operating conditions: Pin 1 (100 N load, 20 Hz speed, 40°C temperature, blue line), Pin 2 (100 N load, 30 Hz speed, 80°C temperature, orange line), Pin 3 (150 N load, 20 Hz speed, 80°C temperature, gray line), and Pin 4 (150 N load, 30 Hz speed, 40°C temperature, yellow line). Initially, all pins exhibited a sharp increase in frictional force within the first 60 seconds, with values rising from near 0 N to 4.5 N for Pin 1, 15.9 N for Pin 2, 12 N for Pin 3, and 10 N for Pin 4. In the steady-state phase (60 to 1200 s), Pin 1 showed a gradual increase to 8.3 N, Pin 2 fluctuated significantly before stabilizing at ~9 N, Pin 3 remained stable at ~11.9-12.0 N, and Pin 4 stabilized around 9-10 N with a slight peak at 600 s. The analysis revealed that higher loads increased friction (e.g., Pin 3 vs. Pin 1), higher speeds reduced it (e.g., Pin 4 vs. Pin 3), and temperature effects varied—higher temperatures increased friction at lower speeds (Pin 3 vs. Pin 1) but had less impact at higher speeds (Pin 2 vs. Pin 4). These findings highlight the interplay of operating parameters on the tribological performance of PEEK/PTFE composites, offering valuable insights for optimizing material applications in frictional environments.

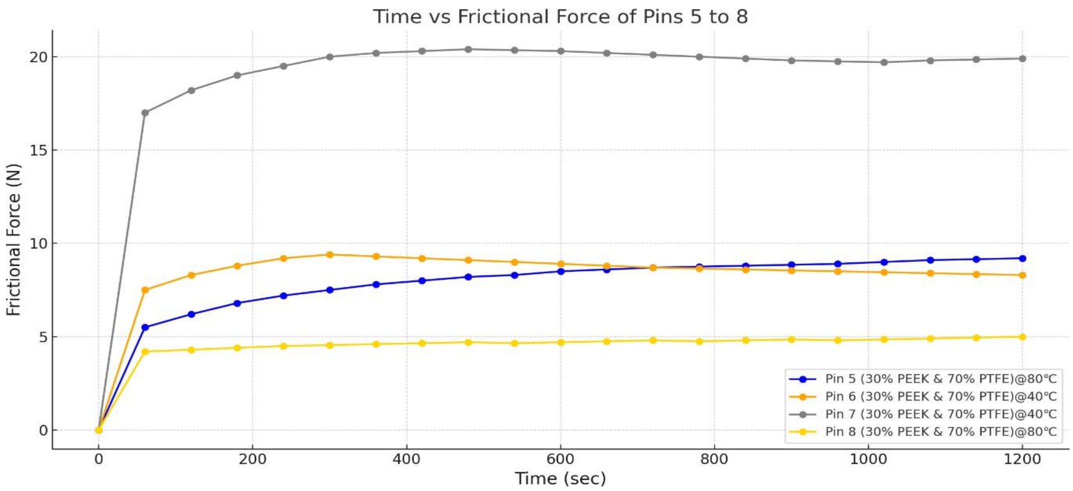

Fig. 7. Effect of Time on Frictional Force of Pins 5 to 8

The frictional behavior of four pins, each composed of 30% PEEK and 70% PTFE, was evaluated by plotting frictional force (N) against time (s) over a 1200-second duration, as illustrated in the figure 6 graph titled "Time vs Frictional Force of Pins 5 to 8. Each pin was subjected to distinct operating conditions: Pin 5 (100 N load, 20 Hz speed, 40°C temperature, blue line), Pin 6 (100 N load, 30 Hz speed, 80°C temperature, orange line), Pin 7 (150 N load, 20 Hz speed, 80°C temperature, gray line), and Pin 8 (150 N load, 30 Hz speed, 40°C temperature, yellow line). All pins exhibited a sharp increase in frictional force within the first 60 seconds, starting near 0 N and peaking at approximately 19.0 N for Pin 5, 7.6 N for Pin 6, 16.8 N for Pin 7, and 4.0 N for Pin 8. In the steady-state phase (60 to 1200 s), Pin 5 decreased steadily to ~12.2 N, Pin 6 stabilized around 7.5-8.5 N with minor fluctuations, Pin 7 showed a gradual increase to ~19.5 N, and Pin 8 remained stable at ~4.0-4.9 N. The analysis revealed that higher loads significantly increased friction (e.g., Pin 7 vs. Pin 5), higher speeds reduced it (e.g., Pin 6 vs. Pin 5, Pin 8 vs. Pin 7), and temperature effects were pronounced—lower temperatures combined with higher speeds minimized friction (Pin 8 vs. Pin 6). These findings underscore the sensitivity of 30% PEEK and 70% PTFE composites to operating conditions, providing critical insights for optimizing their tribological performance in high-friction applications. The graphs depicting time versus frictional force for Pins 1 to 4 (80% PEEK & 20% PTFE) and Pins 5 to 8 (30% PEEK & 70% PTFE) provide significant insights into the tribological performance of these polymer composites under varying operating conditions. For Pins 1 to 4, the frictional force ranged from 8 to 12 N in the steady-state phase, with Pin 1 showing a gradual increase, Pin 2 stabilizing after initial fluctuations, and Pins 3 and 4 maintaining relatively stable values, highlighting the material's moderate and predictable frictional behavior. In contrast, Pins 5 to 8 exhibited a broader range of frictional forces (4 to 19.5 N), with Pin 5 decreasing over time, Pin 6 stabilizing, Pin 7 increasing steadily, and Pin 8 maintaining the lowest friction, underscoring the material's higher sensitivity to operating parameters. Across both sets, higher loads consistently increased friction, while higher speeds generally reduced it, particularly for the PTFE-rich composite. Temperature effects were complex, with lower temperatures often minimizing friction at higher speeds, especially for Pins 5 to 8. These findings emphasize the critical role of material composition and operating conditions in dictating frictional behavior, offering valuable guidance for optimizing PEEK/PTFE composites in applications requiring tailored tribological properties, such as in high-performance bearings or seals. Further studies could explore additional parameters, such as surface roughness or environmental humidity, to enhance the understanding of these composites' performance.

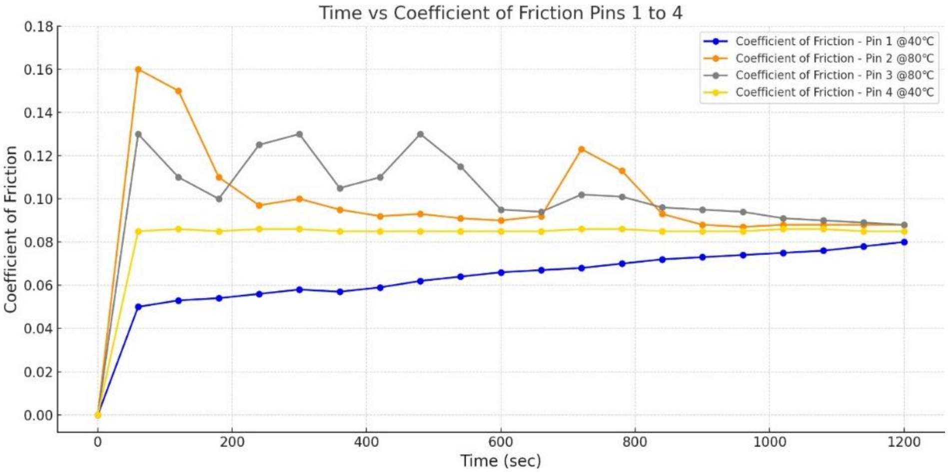

Fig. 8. Effect of Time on Coefficient of Friction of Pins 1 to 4

The frictional behavior of four pins, each composed of 80% PEEK and 20% PTFE, was evaluated by plotting the coefficient of friction against time (s) over a 1200-second duration, as shown in the figure 7 graph titled "Time vs Coefficient of Friction Pins 1 to 4." The x-axis represents time (0 to 1200 s), while the y-axis spans the coefficient of friction from 0 to 0.18. Each pin was tested under distinct operating conditions: Pin 1 (100 N load, 20 Hz speed, 40°C temperature, blue line), Pin 2 (100 N load, 30 Hz speed, 80°C temperature, orange line), Pin 3 (150 N load, 20 Hz speed, 80°C temperature, gray line), and Pin 4 (150 N load, 30 Hz speed, 40°C temperature, yellow line). All pins exhibited a sharp increase in the coefficient of friction within the first 60 seconds, starting near 0 and peaking at approximately 0.045 for Pin 1, 0.159 for Pin 2, 0.08 for Pin 3, and 0.067 for Pin 4. In the steady-state phase (60 to 1200 s), Pin 1 gradually increased to ~0.083, Pin 2 fluctuated significantly before stabilizing at ~0.09, Pin 3 remained stable at ~0.079, and Pin 4 stabilized around 0.061 with minor fluctuations. The analysis revealed that higher loads increased the coefficient of friction (e.g., Pin 3 vs. Pin 1), higher speeds reduced it (e.g., Pin 4 vs. Pin 3), and temperature effects varied—higher temperatures increased the coefficient at lower speeds (Pin 3 vs. Pin 1) but had less impact at higher speeds (Pin 2 vs. Pin 4). These findings highlight the influence of operating parameters on the frictional performance of 80% PEEK and 20% PTFE composites, providing critical insights for their application in tribological systems.

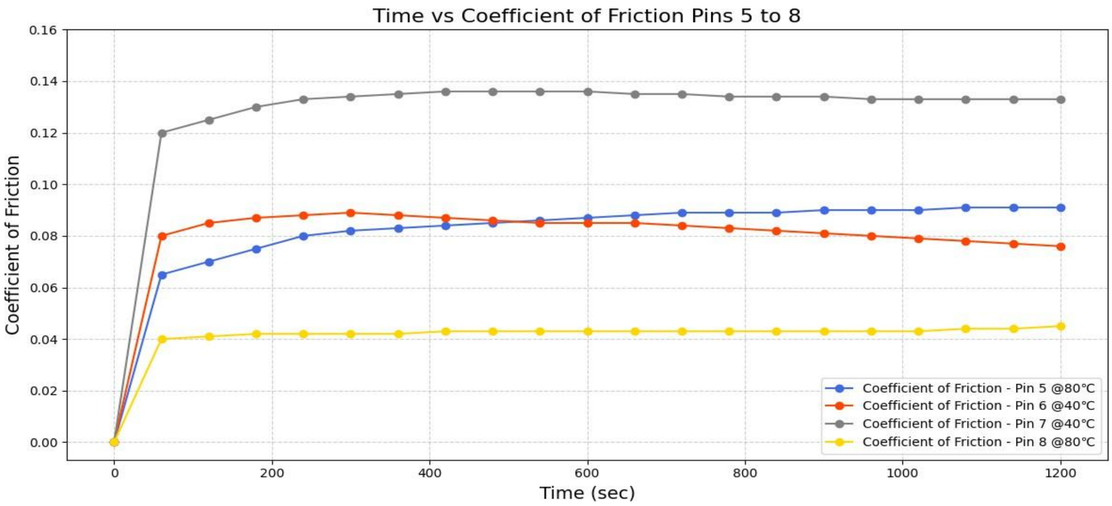

Fig. 9. Effect of Time on Coefficient of Friction of Pins 5 to 8

The frictional behavior of four pins, each composed of 30% PEEK and 70% PTFE, was assessed by plotting the coefficient of friction against time (s) over a 1200-second duration, as depicted in the figure 8 graph titled "Time vs Coefficient of Friction Pins 5 to 8." The x-axis represents time (0 to 1200 s), while the y-axis spans the coefficient of friction from 0 to 0.16. Each pin was tested under distinct operating conditions: Pin 5 (100 N load, 20 Hz speed, 40°C temperature, blue line), Pin 6 (100 N load, 30 Hz speed, 80°C temperature, orange line), Pin 7 (150 N load, 20 Hz speed, 80°C temperature, gray line), and Pin 8 (150 N load, 30 Hz speed, 40°C temperature, yellow line). All pins exhibited a sharp increase in the coefficient of friction within the first 60 seconds, starting near 0 and peaking at approximately 0.19 for Pin 5, 0.076 for Pin 6, 0.112 for Pin 7, and 0.027 for Pin 8. In the steady-state phase (60 to 1200 s), Pin 5 decreased steadily to ~0.122, Pin 6 stabilized around 0.075-0.085 with minor fluctuations, Pin 7 showed a gradual increase to ~0.129, and Pin 8 remained stable at ~0.027-0.033. The analysis revealed that higher loads significantly increased the coefficient of friction (e.g., Pin 7 vs. Pin 5), higher speeds reduced it (e.g., Pin 6 vs. Pin 5, Pin 8 vs. Pin 7), and temperature effects were pronounced—lower temperatures combined with higher speeds minimized friction (Pin 8 vs. Pin 6). These findings underscore the sensitivity of 30% PEEK and 70% PTFE composites to operating conditions, offering critical insights for optimizing their tribological performance in high-friction applications.

The graphs illustrating time versus coefficient of friction for Pins 1 to 4 (80% PEEK & 20% PTFE) and Pins 5 to 8 (30% PEEK & 70% PTFE) offer critical insights into the frictional performance of these polymer composites under varied operating conditions. For Pins 1 to 4, the coefficient of friction stabilized between 0.061 and 0.09 in the steady-state phase, with Pin 1 showing a gradual increase, Pin 2 stabilizing after initial fluctuations, Pin 3 maintaining consistent values, and Pin 4 exhibiting the lowest friction, reflecting the material's moderate and relatively stable frictional behavior. Conversely, Pins 5 to 8 displayed a wider range of coefficients (0.027 to 0.129), with Pin 5 decreasing over time, Pin 6 stabilizing, Pin 7 increasing steadily, and Pin 8 maintaining the lowest friction, highlighting the material's greater sensitivity to operating parameters. Across both sets, higher loads consistently increased the coefficient of friction, while higher speeds generally reduced it, particularly for the PTFE-rich composite. Temperature effects varied, with lower temperatures at higher speeds significantly minimizing friction, especially for Pins 5 to 8. These findings underscore the pivotal influence of material composition and operating conditions on frictional behavior, providing essential guidance for optimizing PEEK/PTFE composites in tribological applications such as bearings or seals. Future research could explore additional variables, such as surface treatments or environmental factors, to further enhance the performance of these materials in diverse engineering contexts.

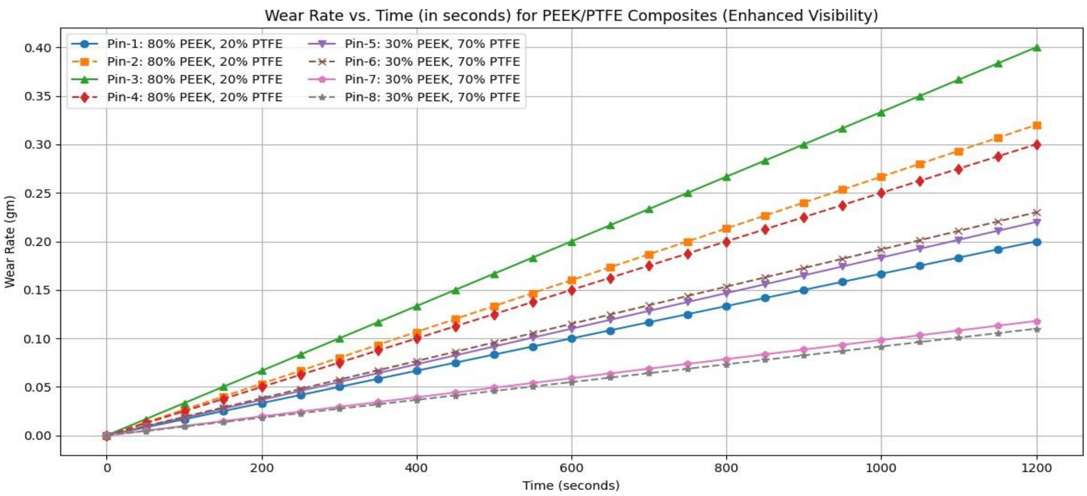

Fig 10. Wear rate for various composition of PEEK &PTFE composite

The wear behavior of eight pins, composed of either 80% PEEK and 20% PTFE (Pins 1-4) or 30% PEEK and 70% PTFE (Pins 5-8), was analyzed by plotting wear rate (in grams) against time (in seconds) over a 1200-second duration, as shown in the figure 9 graph titled "Wear Rate vs. Time (in seconds) for PEEK/PTFE Composites (Enhanced Visibility)." The x-axis represents time (0 to 1200 s), while the y-axis spans wear rate from 0 to 0.40 g. Each pin was tested under distinct operating conditions: Pin 1 (100 N load, 20 Hz speed, 40°C, blue circles), Pin 2 (100 N load, 30 Hz speed, 80°C, orange triangles), Pin 3 (150 N load, 20 Hz speed, 80°C, red diamonds), Pin 4 (150 N load, 30 Hz speed, 40°C, green triangles), Pin 5 (100 N load, 20 Hz speed, 40°C, purple circles), Pin 6 (100 N load, 30 Hz speed, 80°C, brown crosses), Pin 7 (150 N load, 20 Hz speed, 80°C, gray stars), and Pin 8 (150 N load, 30 Hz speed, 40°C, pink stars). All pins exhibited a linear increase in wear rate over time, starting near 0 g at t≈0. By 1200 seconds, the wear rates reached approximately 0.18 g for Pin 1, 0.22 g for Pin 2, 0.28 g for Pin 3, 0.31 g for Pin 4, 0.14 g for Pin 5, 0.19 g for Pin 6, 0.37 g for Pin 7, and 0.09 g for Pin 8. The analysis revealed that higher loads significantly increased wear rates (e.g., Pin 3 vs. Pin 1, Pin 7 vs. Pin 5), higher speeds also increased wear (e.g., Pin 2 vs. Pin 1, Pin 4 vs. Pin 3), and higher temperatures exacerbated wear, particularly at lower speeds (e.g., Pin 3 vs. Pin 1, Pin 7 vs. Pin 5). Notably, the 30% PEEK and 70% PTFE composite showed greater variability, with Pin 8 exhibiting the lowest wear rate due to high speed and low temperature, while Pin 7 had the highest due to high load and temperature.

SEM Analysis

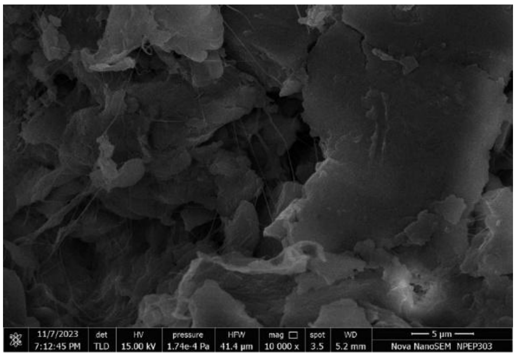

Fig.11. SEM image of PIN 8 material

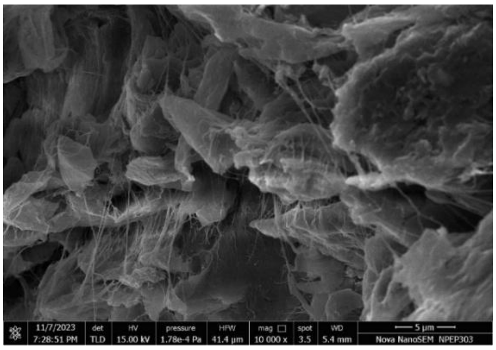

Fig.12. SEM image of PIN 3

The scanning electron microscopy (SEM) analysis provides clear evidence of the differing wear behaviors between specimens Pin 8 and Pin 4. Specimen Pin 8, which exhibited a lower coefficient of friction and reduced wear rate during tribological testing, shows a relatively smooth and uniform surface morphology. The worn surface of Pin 8 lacks deep grooves or cracks and displays minimal debris formation, indicating excellent wear resistance and effective load distribution during sliding. In contrast, specimen Pin 3, associated with higher wear and friction, reveals pronounced surface damage characterized by deep wear tracks, micro-cracks, and fragmented debris. Higher magnification image of clearly illustrate material pull-out and severe surface degradation. These observations confirm the superior tribological performance of the Pin 8 composite, which may be attributed to its optimized microstructure and material composition that contribute to enhanced surface integrity under operational stress.

Taguchi Analysis and Optimization

The effects of load, sliding frequency, and temperature on the tribological behavior of PEEK/PTFE composites were evaluated using a Taguchi L4 (2^3) orthogonal array. Three control factors were considered at two levels: load (100 and 150 N), frequency (20 and 30 Hz), and temperature (40 and 80 °C). The evaluated responses were frictional force, coefficient of friction, and wear rate. The experimental results obtained for both composite compositions are summarized in Table 3.

Table 3

Experimental results according to the Taguchi L4 design

Composite	Specimen	Load, N	Frequency, Hz	Temperature, °C	Frictional force, N	Coefficient of friction	Wear rate, g
80% PEEK / 20% PTFE	Pin 1	100	20	40	8.33	0.088	0.002
	Pin 2	100	30	80	9.09	0.100	0.003
	Pin 3	150	20	80	12.62	0.110	0.004
	Pin 4	150	30	40	12.36	0.080	0.003
30% PEEK / 70% PTFE	Pin 5	100	30	80	8.29	0.089	0.002
	Pin 6	100	20	40	7.78	0.088	0.002
	Pin 7	150	30	40	18.46	0.136	0.001
	Pin 8	150	20	80	4.87	0.037	0.001

The 80% PEEK/20% PTFE composite exhibited frictional forces of 8.33–12.62 N, coefficients of friction of 0.080–0.110, and wear rates of 0.002–0.004 g. For the 30% PEEK/70% PTFE composite, the corresponding ranges were 4.87–18.46 N, 0.037–0.136, and 0.001–0.002 g, respectively. The lowest coefficient of friction (0.037) and wear rate (0.001 g) were recorded for Pin 8, indicating the favorable tribological behavior of the PTFE-rich composite under this combination of operating conditions. The relative effects of the investigated operating parameters were evaluated using the Taguchi response analysis and ANOVA. The percentage contributions obtained from the original analysis are summarized in Table 4.

Table 4

Summary of ANOVA results for the investigated tribological responses

Composite / response	Load, %	Frequency, %	Temperature, %	Dominant factor
80% PEEK / 20% PTFE – frictional force	51.28	45.73	2.99	Load
30% PEEK / 70% PTFE – frictional force	97.01	2.17	0.82	Load
30% PEEK / 70% PTFE – wear rate	64.56	21.58	13.86	Load
30% PEEK / 70% PTFE – coefficient of friction	21.84	52.32	25.84	Frequency

For the 80% PEEK/20% PTFE composite, applied load showed the largest contribution to the variation in frictional force (51.28%), followed by frequency (45.73%) and temperature (2.99%). For the 30% PEEK/70% PTFE composite, the contribution of load to frictional force was 97.01%, indicating a substantially stronger dependence of this response on the applied load.

For the PTFE-rich composite, load was also the dominant factor affecting wear rate, with a contribution of 64.56%, followed by frequency (21.58%) and temperature (13.86%). In contrast, the coefficient of friction was primarily affected by frequency (52.32%), followed by temperature (25.84%) and load (21.84%).

Linear regression models were additionally used to describe the relationships between the operating parameters and the tribological responses. For the 80% PEEK/20% PTFE composite, the frictional force was described by:

$$F = -0.2400 + 0.07560L + 0.02500f + 0.011275T$$

where F is the frictional force (N), L is the applied load (N), f is the frequency (Hz), and T is the temperature (°C). The confirmation experiment reported a difference of approximately 0.70% between the predicted and experimental frictional-force values.

For the 30% PEEK/70% PTFE composite, the corresponding regression relationships reported in the experimental analysis were:

$$F = 11.09 + 0.06277L + 0.02888f + 0.01174T$$

$$W = 0.004000 - 0.000020L$$

$$\mu = 0.1440 - 0.000040L - 0.005000f + 0.001225T$$

where W is the wear rate (g) and μ is the coefficient of friction. The reported differences between predicted and experimental values were approximately 0.59% for frictional force, 4% for wear rate, and 0.45% for the coefficient of friction.

Overall, the Taguchi analysis demonstrates that the tribological behavior of PEEK/PTFE composites depends on both composition and operating conditions. Increasing the PTFE content from 20% to 70% provided lower minimum values of wear and coefficient of friction. Among the investigated conditions, Pin 8 exhibited the lowest coefficient of friction (0.037) together with a wear rate of 0.001 g. The factor analysis further showed that load predominantly affected frictional force and wear rate, whereas frequency had the greatest contribution to the coefficient of friction for the 30% PEEK/70% PTFE composite.

Conclusion

The study systematically explored the tribological behavior of PEEK/PTFE composites under various operational conditions, focusing on both low and high temperatures. The results demonstrated a significant enhancement in wear resistance with the incorporation of PTFE, particularly in the 30% PEEK and 70% PTFE composite, which outperformed the 80% PEEK and 20% PTFE composite in terms of frictional force, coefficient of friction, and wear rate. Pin 8, in particular, exhibited the most favorable performance, with the lowest frictional force, coefficient of friction (0.03), and wear rate, which can be attributed to its high PTFE content, high speed (2.30 Hz), and low temperature (40°C). SEM analysis further confirmed that Pin 8 had minimal wear and maintained a smooth surface morphology, whereas Pin 3 showed significant surface degradation, highlighting its lower wear resistance and higher frictional effects.

This study reinforced the positive impact of increasing PTFE content on the tribological properties of PEEK composites, particularly in enhancing wear resistance. The use of the Taguchi L4 (2^3) orthogonal array successfully identified load as the primary factor influencing the coefficient of friction, with temperature being the main driver of wear rate. As load and temperature increased, both the wear rate and coefficient of friction also increased, further supporting the higher efficiency of hybrid polymer composites over conventional alloys. ANOVA analysis confirmed the statistical significance of the findings, with p-values below 0.05, and the confirmation tests validated the predictive power of the Taguchi L4 model.

This study also highlights the effectiveness of the Taguchi method as a robust and efficient approach for analyzing and optimizing tribological properties, including frictional force, coefficient of friction, and sliding wear rate. The findings provide essential insights for the design and application of PEEK/PTFE composites in high-performance tribological systems, particularly in industrial applications that demand superior wear resistance and reduced frictional performance.

Funding

The authors received the following financial funding for the research, authorship, and/or the publication of this paper and wish to acknowledge their heartfelt gratitude and appreciation towards All India Council for Technical Education (AICTE), New Delhi, for the financial assistance under the scheme of research promotion project no. File No. 8-35/FDc/RPs (Policy-1)/2019-20.

References

1.Iqbal, M., Satrianda, M. S., Firsa, T., Azan, S. A., & Abhang, L. B. (2021). Bending strength of fiber metal laminate based on abaca fiber reinforced polyester and aluminum alloy metal sheet. *Key Engineering*

Materials, 892, 134–141. DOI: 10.4028/www.scientific.net/KEM.892.134

2.Wakchaure, K. B., & Abhang, L. B. (2020). Experimental investigation of tribological properties of compressor piston ring with PEEK. *International Journal of Engineering Development and Research, 8*(2), 207–216.

3.Burris, D. L., & Sawyer, W. G. (2006). A low friction and ultra-low wear rate PEEK/PTFE composite. *Wear, 261*(3–4), 410–418. DOI: 10.1016/j.wear.2005.12.016

4.Escobar Nunez, E., & Polycarpou, A. A. (2015). The effect of surface roughness on the transfer of polymer films under unlubricated testing conditions. *Wear, 326–327*, 74–83. DOI: 10.1016/j.wear.2014.12.049

5.Lin, L., & Schlarb, A. K. (2021). Development and optimization of high-performance PEEK/CF/nanosilica hybrid composites. *Polymers for Advanced Technologies, 32*(8), 3150–3159. DOI: 10.1002/pat.5327

6.Mankar, N. A., & Rijumon, K. (2015). Investigation and development of tribological behavior of PEEK and PEEK composites under harsh operating condition. *International Engineering Research Journal, Special Issue 2*, 2647–2652.

7.Parab, P. V., & Firke, V. L. (2016). Friction and wear performance of PTFE and its composites: A review. *International Journal of Engineering Research & Technology, 5*(9), 327–329. DOI: 10.17577/IJERTV5IS090318

8.Neela Rajan, R. R., & Rajesh, R. (2017). Experimental wear study between piston ring and cylinder liner pair using Jatropha oil as lubricating oil. *International Journal of Mechanical and Production Engineering Research and Development, 7*(3), 301–312. DOI: 10.24247/ijmperdjun201730

9.Gokulakannan, S. (2017). A review on wear behaviour of clutch plate made of PEEK composite material. *Journal of Science and Technology, 2*(3), 19–26.

10. Milojević, S., Džunić, D., Taranović, D., Pešić, R., & Mitrović, S. (2018). Experimental determination of tribological characteristics of composite materials in use for parts in aluminum air compressor (piston and cylinder). In *Proceedings of the VII International Congress Motor Vehicles & Motors 2018* (pp. 383–392). University of Kragujevac.

11. Hoskins, T. J., Dearn, K. D., Chen, Y. K., & Kukureka, S. N. (2014). The wear of PEEK in rolling–sliding contact: Simulation of polymer gear applications. *Wear, 309*(1–2), 35–42. DOI: 10.1016/j.wear.2013.09.014

12. Shukur, Z. M., & Dearn, K. D. (2020). The tribological behaviours of PEEK and PEEK based composites PEEK under sliding contact. *Journal of Mechanical Engineering Research and Developments, 43*(7), 389–405.

13. Burris, D. L., & Sawyer, W. G. (2007). Tribological behavior of PEEK components with compositionally graded PEEK/PTFE surfaces. *Wear, 262*(1–2), 220–224. DOI: 10.1016/j.wear.2006.03.045

14. Kharat, A., Talekar, S., Jadhav, S., More, S., & Shelke, R. (2019). Investigation of tribological behavior of PEEK composite with glass fiber. *Journal of Emerging Technologies and Innovative Research, 6*(2), 214–216.

15. Panin, S. V., Nguyen, D. A., Buslovich, D. G., Alexenko, V. O., Pervikov, A. V., Kornienko, L. A., & Berto, F. (2021). Effect of various type of nanoparticles on mechanical and tribological properties of wear-resistant PEEK + PTFE-based composites. *Materials, 14*(5), 1113. DOI: 10.3390/ma14051113

16. Suresha, B., Ravi Kumar, B. N., Venkataramareddy, M., & Jayaraju, T. (2010). Role of micro/nano fillers on mechanical and tribological properties of polyamide66/polypropylene composites. *Materials & Design, 31*(4), 1993–2000. DOI: 10.1016/j.matdes.2009.10.031

17. Bijwe, J., Sen, S., & Ghosh, A. (2005). Influence of PTFE content in PEEK–PTFE blends on mechanical properties and tribo-performance in various wear modes. *Wear, 258*(10), 1536–1542. DOI: 10.1016/j.wear.2004.10.008

18. Vail, J. R., Krick, B. A., Marchman, K. R., & Sawyer, W. G. (2011). Polytetrafluoroethylene (PTFE) fiber reinforced polyetheretherketone (PEEK) composites. *Wear, 270*(11–12), 737–741. DOI: 10.1016/j.wear.2010.12.003

19. Li, E. Z., Guo, W. L., Wang, H. D., Xu, B. S., & Liu, X. T. (2013). Research on tribological behavior of PEEK and glass fiber reinforced PEEK composite. *Physics Procedia, 50*, 453–460. DOI: 10.1016/j.phpro.2013.11.071

20. Mankar, N. A., Rijumon, K., Karandikar, P. M., & Kadu, R. L. (2015). Investigation and development of tribological behavior of PEEK and PEEK composites. *International Journal on Recent Technologies in Mechanical and Electrical Engineering, 2*(6), 107–111.

21. Rzatki, F. D., Barboza, D. V. D., Schroeder, R. M., Barra, G. M. O., Binder, C., Klein, A. N., & De Mello, J. D. B. (2015). Effect of temperature and atmosphere on the tribological behavior of a polyether ether ketone composite. *Friction, 3*(4), 259–265. DOI: 10.1007/s40544-015-0091-5

22. Abhang, L. B., Dalwe, Y. D., Pawar, D. S., & Karandikar, P. M. (2023). A critical review on tribological and mechanical characteristics of hybrid polymer composite materials. *Macromolecular Symposia, 412*(1), 2200194. DOI: 10.1002/masy.202200194

Абханг Л. Б., Самбаре А. А., Карандікар П. М., Далве Я. Прогнозування та аналіз трибологічної поведінки гібридних полімерних композитів при випробуваннях на трибометрі зворотно-поступального руху

У роботі досліджено трибологічну поведінку композитів на основі поліефірефіркетону (PEEK) з політетрафторетиленом (PTFE) як твердим мастильним наповнювачем в умовах сухого тертя при зворотно-поступальному русі. Зразки двох складів — 80 % PEEK/20 % PTFE та 30 % PEEK/70 % PTFE — випробовували в контакті зі сталевим контртілом на лінійному трибометрі зворотно-поступального руху. Для оцінювання впливу навантаження (100 і 150 Н), частоти (1,20 і 2,30 Гц) та температури (40 і 80 °C) на силу тертя, коефіцієнт тертя та інтенсивність зношування застосовано ортогональний план Тагучі L4 (2^3). Встановлено, що збільшення вмісту PTFE суттєво покращує трибологічні характеристики композиту. Для складу 30 % PEEK/70 % PTFE отримано мінімальний коефіцієнт тертя 0,037 та втрату маси внаслідок зношування 0,001 г. Метод ANOVA використано для оцінювання внеску досліджуваних факторів у зміну трибологічних характеристик, а регресійні моделі — для прогнозування результатів випробувань. Отримані результати підтверджують перспективність композитів PEEK/PTFE для застосування у високонавантажених вузлах тертя, зокрема підшипниках і ущільненнях, де необхідні низьке тертя та підвищена зносостійкість.

Ключові слова: гібридні полімерні композити, PEEK, PTFE, тертя, зношування, сила тертя, коефіцієнт тертя, трибометр зворотно-поступального руху, ортогональний план Тагучі, ANOVA.

ISSN 2079-1372 Problems of Tribology, V. 31, No 3/121-2026, 61-66

Problems of Tribology
Website: http://tribology.khnu.km.ua/index.php/ProbTrib
E-mail: tribosenator@gmail.com

DOI: https://doi.org/10.31891/2079-1372-2026-121-3-61-66

The impact of deposition method on wear mechanisms of NiAl-15 wt.% CrB2 coatings

M.S. Ukrainets[1*] 0000-0001-9009-0940, **O.P. Umanskyi**[1] 0000-0003-3629-7224, **O.M. Poliarus**[1, 2] 0000-0003-3181-419X, **V.P. Konoval**[1] 0000-0003-2780-9064, **T.O. Levchuk**[1] 0009-0008-5818-6684

[1]Frantsevich Institute for Problems of Materials Science National Academy of Sciences of Ukraine
[2]Institute of Metallurgy and Materials Science Polish Academy of Sciences, Poland
**E-mail: maximukrainets22@gmail.com*

Received: 15 July 2026: Revised 05 August 2026: Accept: 01 September 2026

Abstract

In this work, the effect of the deposition method on the wear mechanisms of NiAl–15% CrB_2 composite coatings was investigated. The wear rates of coatings produced by Plasma spraying, Detonation spraying and Electric-Spark Alloying (ESA) were evaluated using room-temperature “pin-on-disc” tribological tests. The worn surfaces and corresponding wear mechanisms were analyzed via SEM. The results demonstrate that incorporating CrB_2 into the NiAl matrix significantly enhances the wear resistance of the composite coatings, shifting the dominant wear mechanism from abrasive-adhesive to oxidative wear, regardless of the deposition technique.

Keywords: Plasma coatings, APS, Detonation coatings, D-gun, Electric-Spark Alloying coatings, ESA, intermetallic, NiAl, chromium diboride, CrB_2, friction, wear resistance

Statement of the problem (Introduction)

Due to its low density, high melting point, and excellent resistance to oxidation and corrosion, nickel aluminide (NiAl) is widely used in the aerospace industry as a protective coating for gas turbine engine components [1], [2], [3]. However, the application of NiAl as a high-temperature wear-resistant material is limited due to its thermal softening at temperatures above 500 °C [4], [5]. Under thermal and mechanical stress, high plastic deformation of the intermetallic compound leads to the destruction of protective Ni- and Al-based oxide films formed on its surface. The destroyed oxide films fail to prevent direct metal-to-metal contact of the friction pair components, triggering severe adhesive wear.

Analysis of recent research and publications (Literature review)

To improve wear resistance, intermetallic matrices are dispersion-reinforced with refractory compounds, which increase the strength and stiffness of the composite at elevated temperatures while acting as wear-resistant phases [6], [7], [8], [9], [10], [11], [12], [13], [14]. Based on previous studies of physicochemical interactions in NiAl–MeB_2 systems (where Me is Cr, Ti, or Zr), chromium diboride (CrB_2) was identified as a promising reinforcing phase [15]. Prior research has investigated the high-temperature friction behavior of NiAl–CrB_2 composite coatings deposited via Plasma, Detonation, and Electric-Spark methods. The introduction of chromium diboride was shown to enhance the strength and stiffness of the composite coating, preventing the degradation of surface oxide films on the intermetallic matrix and facilitating a transition to an oxidative wear mechanism [16], [17], [18], [19].

Highlighting previously unresolved parts of the general problem

Despite existing studies on the behavior of NiAl–CrB_2 coatings under high-temperature friction conditions, the specific wear mechanisms occurring under room-temperature testing, especially for Electric-Spark Alloyed coatings, remain insufficiently understood. During sliding contact, intense frictional heating leads to a significant localized temperature rise within the friction zone [20], [21], [22]. The dissipation of this heat is dictated by a range of factors, including coating morphology.

Copyright © 2026 M.S. Ukrainets, O.P. Umanskyi, O.M. Poliarus, V.P. Konoval, T.O. Levchuk. This is an open access article distributed under the Creative Commons Attribution License, which permits unrestricted use, distribution, and reproduction in any medium, provided the original work is properly cited.

Coatings deposited by Plasma spraying, Detonation spraying, and Electric-Spark Alloying (ESA) exhibit fundamentally different microstructural characteristics (porosity, phase distribution, defect density, and interface boundary features) [16], [17], [19]. Consequently, these structural variations can result in substantial differences in their wear mechanisms.

Formulation of the purpose of the article (Purpose)

The purpose of this work is to investigate the effect of the coating deposition method on the wear mechanisms of NiAl-15% CrB_2 (wt. %) composite coatings under friction conditions at room temperature.

Methods

Commercial NiAl powders with a particle size of -40 μm and CrB_2 powders with a particle size of – 12 μm were used to deposit the coatings. NiAl coatings were obtained from the as-received powder, whereas composite powder materials for deposition of NiAl–15% CrB_2 coatings were manufactured by mixing intermetallic and boride powders in the required proportions, followed by hot pressing at 1300 °C. The sintered CPM briquettes were either crushed and classified to the required size for Plasma and Detonation spraying or cut to the required size for Electric-Spark Alloying. Further details on the deposition parameters of Ni and NiAl–15% CrB_2 coatings can be found in previous works [16], [17], [19].

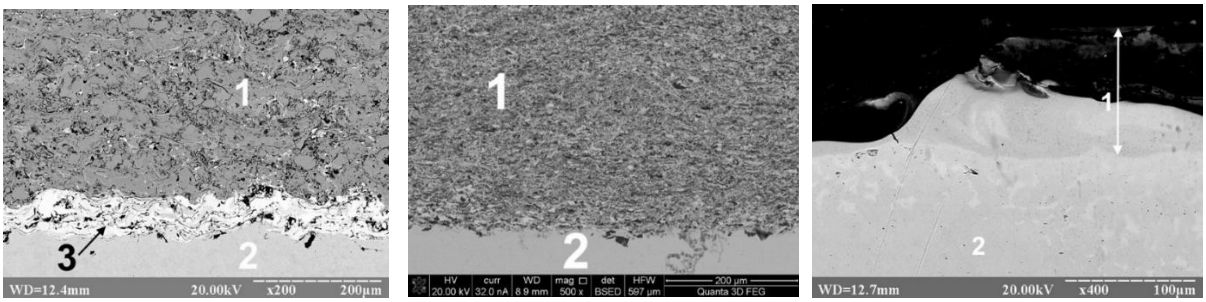

a b c

Fig. 1. Microstructure of Plasma (a), Detonation (b) and ESA (c) coatings: 1 – coating; 2 – substrate; 3 – bond layer

To investigate wear resistance, the coatings were deposited onto steel pins (Ø 5 × 15 mm) made of Steel 20. In case of the Plasma spraying bond coating of Ni_3Al was used. The sprayed coatings were polished to a surface roughness of R_a = 2.5…0.63 μm.

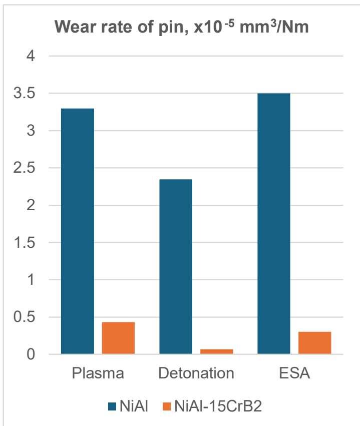

Fig. 2. Wear rate of NiAl–15% CrB_2 coatings (NiAl data provided for comparison)

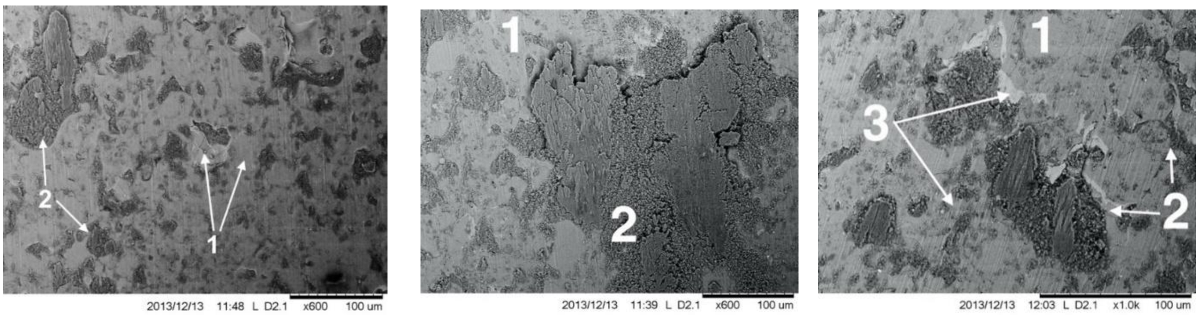

a b c

Fig. 3. Worn surfaces of NiAl-15%CrB_2 Plasma coatings: 1 – coating, 2 – wear debris, 3 – wear tracks

The wear resistance of the coatings was determined by "pin-on-disc" scheme using a CETR UMT-2 micro-tribotester (Fig. 4). The pins were positioned at a distance *R*, pressed against the coating surface 4 with a specified force, and the disc holder 6 began to rotate at a programmed speed. The pins and counterbodies were mounted on the tribotester using custom-designed holders. Tribological testing was carried out at room temperature under the following conditions: S = 1.0 km, V = 0.157 m/s, P = 1 MPa.

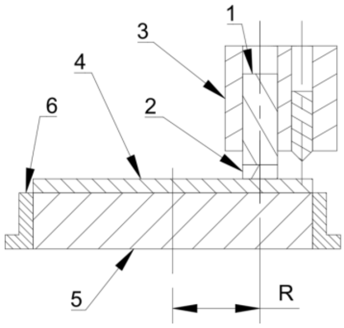

Fig. 4. Schematic of tribological testing: 1 – pin, 2 – NiAl-15% CrB_2 coating, 3 – pin holder, 4 – NiAl coating, 5 – disc, 6 – disc holder

To determine weight loss, the samples were cleaned before and after tribotesting in an ultrasonic bath filled with isopropyl alcohol (99.9%) and weighed on electronic scales with an accuracy of 0.0001 g. The determined weight loss of the coatings and the linear wear of the tribopair were converted to wear rate W_s using the following formula:

$$W_s = \frac{\Delta V}{P \cdot S} \quad (1)$$

where ΔV is the volume of worn material, mm^3; P is the normal load on the rod, N; S is the friction path, m.

Steel discs ∅ 40 × 10 mm (Fig. 4, 5) with a NiAl Plasma coating [17] (Fig. 4, 3) and a roughness of R_a = 2.5…0.63 μm were used as a counterbodies. Two tests were conducted on each disc. Initially, the pin was positioned at a distance R = 10 mm for the first test. After cleaning and taking all necessary measurements, disc 5 (Fig. 4) was reinserted into holder 6, and the holder with the new pin was positioned at a distance of R = 5 mm for the next test.

The composite coatings and worn surfaces were examined by scanning electron microscopy using REM-106I, Thermo Fisher Scientific Quanta 3D FEG, and Hitachi TM-1000 microscopes.

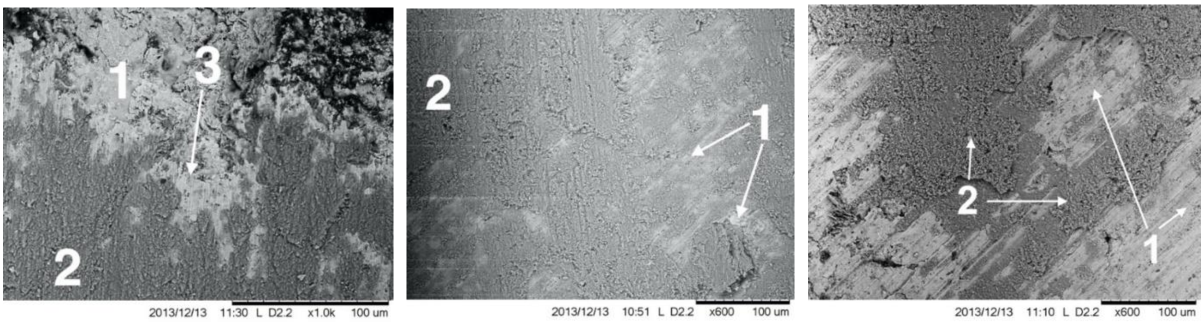

a b c

Fig. 5. Worn surfaces of NiAl-15%CrB_2 Detonation coatings: 1 – coating, 2 – wear debris, 3 – wear tracks

Results

The microstructures of deposited coatings are shown in Fig. 1. Plasma and Detonation coatings exhibit a microstructure typical of thermally sprayed coatings: particles of CrB_2 evenly distributed in NiAl matrix. Detonation coating (Fig. 2, b) typically has noticeably smaller size of NiAl particles compared with Plasma coating (Fig. 1, a).

The different nature of the ESA method compared to thermal spraying results in a distinct microstructure. ESA coating is formed by an array of crystalized welding pools of different shapes and sizes (Fig. 1, c) without clear segregation of NiAl and CrB_2 particles. Additionally, it contains Steel 20 components, mainly Fe (around 10%). The coating is more than two times thinner than those produced by Plasma or Detonation spraying.

As expected, different microstructure of coatings resulted in difference of their wear behavior (Fig. 2). NiAl–15% CrB_2 Detonation coatings have the lowest wear rate. NiAl–15% CrB_2 Plasma and ESA coatings demonstrated similar wear rates, with the ESA coating performing slightly better. As expected, composite coatings showed a wear rate ~7 times lower than NiAl ones which goes in line with the previous studies [16], [17], [18], [19]. It is worth noting that intense tribo-oxidation was observed during testing of the NiAl–15% CrB_2 Detonation coating. The surfaces of both the pin and disc were covered with pale-green films.

In order to investigate the nature of the processes that took place during the friction of NiAl–15% CrB_2 composite coatings, the worn surfaces were examined by SEM-EDX (Figs. 3–6). The worn surface of the plasma-sprayed coating is covered with conglomerates of wear debris (Fig. 3, point 2). The wear debris predominantly consists of Ni and Al oxides formed on the NiAl counterbody. Evidently, small volumes of the NiAl counterbody material in the contact zones were plasticized, leading to the shearing of oxide films and metallic NiAl fragments by the pin, which were then transformed into wear debris. During further sliding, this debris accumulated in surface defects of the composite coating (Fig. 3c, point 2). In some cases, either large individual defects or clusters of closely spaced defects trapped significant quantities of debris (Fig. 3b, point 2). These conglomerates of wear debris acted as a solid lubricant, thereby reducing the wear of the plasma-sprayed NiAl–15% CrB_2 coating. Evidently, a fraction of the wear debris not trapped by surface defects acted as an abrasive, leaving characteristic wear tracks on the NiAl matrix of the composite coating (Fig. 3c, 3).

The wear mechanism of the detonation coating is similar to that of the plasma-sprayed coating; however, in this case, the wear debris was predominantly trapped within surface grooves remaining from the polishing process (Fig. 5c, 2). On the leading edge (Fig. 5a), besides the wear debris (point 2) covering nearly the entire area, characteristic wear tracks (point 3) are also present. Intensive tribo-oxidation of the counterbody, followed by material transfer, resulted in almost the entire surface of the NiAl–15% CrB_2 detonation coating being covered with wear debris (Fig. 1b, 2). This debris acted as a solid lubricant, significantly reducing composite wear. Consequently, the NiAl–15% CrB_2 detonation coating exhibited the lowest wear rate.

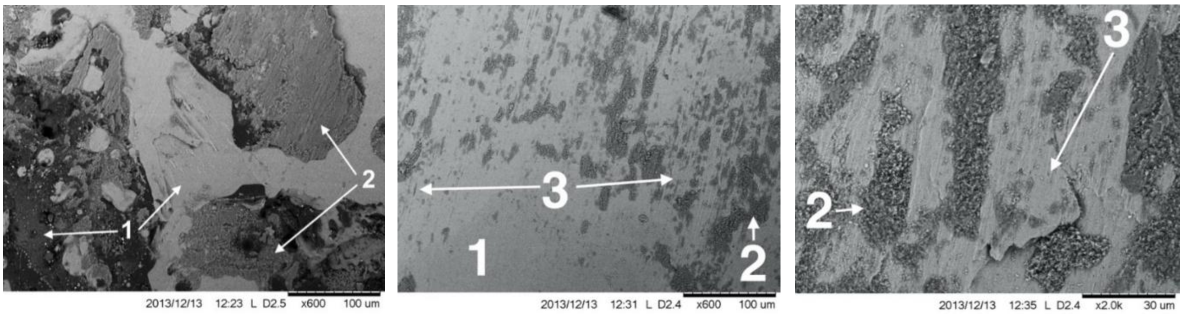

a b c

Fig. 6. Worn surfaces of NiAl-15%CrB_2 ESA coatings: 1 – coating, 2 – wear debris, 3 – wear tracks

NiAl–15% CrB_2 Electric-Spark Alloyed (ESA) coatings exhibit a distinctly discrete surface topography, where variations in weld pool heights result in large depressions that accumulate wear debris (Fig. 6a, point 2). Additionally, regions with minor surface defects also trap wear debris (Fig. 6b and 6c, point 2). Furthermore, noticeable wear tracks and localized plastic deformation zones are observed within the ESA coating (Fig. 6a, point 1 and Fig. 6c, point 3). Evidently, owing to this discrete morphology, the normal load—and consequently the frictional heat—in certain contact zones is sufficiently high to induce plastic deformation of the NiAl matrix. However, this remains a localized phenomenon, as the majority of the coating surface is covered with wear debris acting as a solid lubricant.

Conclusions

In conclusion, the addition of CrB_2 into the NiAl matrix enhances its strength and suppresses noticeable plastic deformation, effectively shifting the primary wear mechanism from abrasive-adhesive (typical of the plain NiAl counterbody) to oxidative wear in the NiAl–15% CrB_2 Plasma, Detonation or ESA coatings. As a result, the wear rate of the composite coatings is ~7 times lower than that of the initial intermetallic ones.

NiAl–15% CrB_2 Detonation coating exhibited the highest wear resistance primarily due to the formation of a protective wear debris film covering nearly its entire surface. Despite differences in surface topologies and content both Plasma and Detonation composite coatings exhibited a similar level of wear resistance.

Reference

1. Miracle, D. B., & Darolia, R. (2000). NiAl and its alloys. In J. H. Westbrook & R. L. Fleischer (Eds.), *Structural applications of intermetallic compounds* (p. 20). John Wiley & Sons. http://www.ewp.rpi.edu/hartford/users/papers/engr/ernesto/morens/EP/References/NiAl.pdf
2. Rajendran, R. (2012). Gas turbine coatings: An overview. *Engineering Failure Analysis, 26*, 355–369. https://doi.org/10.1016/j.engfailanal.2012.07.007
3. Xue, W., Gao, S., Duan, D., Zhang, J., Liu, Y., & Li, S. (2017). Ti6Al4V blade wear behavior during high-speed rubbing with NiAl-hBN abradable seal coating. *Journal of Thermal Spray Technology, 26*(3), 539–553. https://doi.org/10.1007/s11666-016-0511-8

4. Hawk, J. A., & Alman, D. E. (1999). Abrasive wear behavior of NiAl and NiAl–TiB_2 composites. *Wear, 225–229*, 544–556. https://doi.org/10.1016/S0043-1648(99)00006-X
5. Umanskyi, O. P., Brodnikovskyi, M. P., Ukrainets, M. S., Poliarus, O. M., Stelmakh, O. U., & Brodnikovskyi, D. M. (2018). Effect of chromium diboride additives on strength properties of NiAl–CrB_2 composites in a wide temperature range. *Powder Metallurgy and Metal Ceramics, 56*(11–12), 681–687. https://doi.org/10.1007/s11106-018-9943-7
6. Shi, X., et al. (2013). Friction and wear behavior of NiAl–10 wt% Ti_3SiC_2 composites. *Wear, 303*, 9–20. https://doi.org/10.1016/j.wear.2013.02.013
7. Liu, E., Gao, Y., Jia, J., Bai, Y., & Wang, W. (2014). Microstructure and mechanical properties of in situ NiAl–Mo_2C nanocomposites prepared by hot-pressing sintering. *Materials Science and Engineering: A, 592*, 201–206. https://doi.org/10.1016/j.msea.2013.06.078
8. Sheng, L. Y., Guo, J. T., Xi, T. F., Zhang, B. C., & Ye, H. Q. (2012). ZrO_2-strengthened NiAl/Cr(Mo,Hf) composite fabricated by powder metallurgy. *Progress in Natural Science: Materials International, 22*(3), 231–236. https://doi.org/10.1016/j.pnsc.2012.04.003
9. Movahedi, B. (2013). Fracture toughness and wear behavior of NiAl-based nanocomposite HVOF coatings. *Surface and Coatings Technology, 235*, 212–219. https://doi.org/10.1016/j.surfcoat.2013.07.035
10. Ramazani, M., Ashrafizadeh, F., & Mozaffarinia, R. (2013). The influence of temperature on frictional behavior of plasma-sprayed NiAl–Cr_2O_3-based self-adaptive nanocomposite coatings. *Journal of Thermal Spray Technology, 22*, 1120–1132. https://doi.org/10.1007/s11666-013-9962-3
11. Hou, S., Liu, Z., Liu, D., & Ma, Y. (2012). Oxidation behavior of NiAl–TiB_2 coatings prepared by electrothermal explosion ultrahigh-speed spraying. *Physics Procedia, 32*, 71–77. https://doi.org/10.1016/j.phpro.2012.03.520
12. Sheng, L. Y., Yang, F., Guo, J. T., Xi, T. F., & Ye, H. Q. (2013). Investigation on NiAl–TiC–Al_2O_3 composite prepared by self-propagation high-temperature synthesis with hot extrusion. *Composites Part B: Engineering, 45*, 785–791. https://doi.org/10.1016/j.compositesb.2012.05.038
13. Zhu, S., Bi, Q., Niu, M., Yang, J., & Liu, W. (2012). Tribological behavior of NiAl matrix composites with addition of oxides at high temperatures. *Wear, 274–275*, 423–434. https://doi.org/10.1016/j.wear.2011.11.006
14. Shi, X., et al. (2014). Synergetic lubricating effect of MoS_2 and Ti_3SiC_2 on tribological properties of NiAl matrix self-lubricating composites over a wide temperature range. *Materials & Design, 55*, 93–103. https://doi.org/10.1016/j.matdes.2013.09.072
15. Umanskyi, O., Poliarus, O., Ukrainets, M., & Antonov, M. (2015). Physical-chemical interaction in NiAl–MeB_2 systems intended for tribological applications. *Welding Journal, 94*, 225–230.
16. Ukrainets, M. S. (2016). Regularities of deposition and wear of electrospark coatings of the NiAl–CrB_2 system. *Problems of Tribology, 2*, 21–27. https://tribology.khmnu.edu.ua/index.php/ProbTrib/article/view/530
17. Poliarus, O., et al. (2019). Effect of powder preparation on the microstructure and wear of plasma-sprayed NiAl/CrB_2 composite coatings. *Journal of Thermal Spray Technology, 28*(5), 1039–1048. https://doi.org/10.1007/s11666-019-00861-5
18. Umanskyi, O., Poliarus, O., Ukrainets, M., Antonov, M., & Hussainova, I. (2016). High-temperature sliding wear of NiAl-based coatings reinforced by borides. *Materials Science (Medžiagotyra), 22*(1), 49–53. https://doi.org/10.5755/j01.ms.22.1.8093
19. Poliarus, O., et al. (2019). Microstructure and wear of thermal-sprayed composite NiAl-based coatings. *Archives of Civil and Mechanical Engineering, 19*(4), 1095–1103. https://doi.org/10.1016/j.acme.2019.06.002
20. Kennedy, F. E., Lu, Y., & Baker, I. (2015). Contact temperatures and their influence on wear during pin-on-disk tribotesting. *Tribology International, 82*, 534–542. https://doi.org/10.1016/j.triboint.2013.10.022
21. Abrasive, erosive, and cavitation wear. (2014). In *Engineering tribology* (pp. 525–576). Elsevier. https://doi.org/10.1016/B978-0-12-397047-3.00011-4
22. Fundamentals of contact between solids. (2014). In *Engineering tribology* (pp. 475–524). Elsevier. https://doi.org/10.1016/B978-0-12-397047-3.00010-2

Українець М.С., Уманський О.П., Полярус О.М., Коновал В.П., Левчук Т.О. Вплив методу осадження на механізми зношування покриттів NiAl-15 мас.% CrB2

У цій роботі досліджено вплив методу нанесення на механізми зношування композиційних покриттів NiAl–15% CrB_2. Інтенсивність зношування покриттів, отриманих шляхом плазмового напилення, детонаційного напилення та електроіскрового легування (ЕІЛ), оцінювали за допомогою трибологічних випробувань за схемою «стрижень–диск» за кімнатної температури. Поверхні тертя та відповідні механізми зношування аналізували за допомогою растрової електронної мікроскопії (РЕМ). Результати демонструють, що введення CrB_2 у матрицю NiAl значно підвищує зносостійкість композиційних покриттів, змінюючи домінуючий механізм зношування з абразивно-адгезійного на окиснювальний, незалежно від технології нанесення.

Ключові слова: плазмові покриття, детонаційні покриття, електроіскрове легування, ЕІЛ, інтерметалід, NiAl, диборид хрому, CrB_2, тертя, зносостійкість

ISSN 2079-1372 Problems of Tribology, V. 31, No 3/121-2026, 67-76

Problems of Tribology
Website: http://tribology.khnu.km.ua/index.php/ProbTrib
E-mail: tribosenator@gmail.com

DOI: https://doi.org/10.31891/2079-1372-2026-121-3-67-76

Dependence of the quality indicators of transient processes in the hydraulic drive for rotation of the garbage truck manipulator arm on the wear of friction pairs

O.V. Bereziuk [1] 0000-0002-2747-2978, **V.O. Kharzhevskyi** [2] 0000-0003-4816-2781, **S. Cv. Ivanov** [3] 0000-0002-7719-6086, **V.Ye. Yavorskyi**[1] 0009-0002-8724-3963

[1] *Vinnytsia National Technical University, Ukraine*
[2] *Khmelnytskyi National University, Ukraine*
[3] *Technical University Sofia, Branch Plovdiv, Bulgaria*
E-mail: berezyukoleg@i.ua

Received: 19 July 2026: Revised 15 August 2026: Accept: 04 September 2026

Abstract

This article is dedicated to determining the analytical relationships between the quality indicators of transient processes in the hydraulic drive of the manipulator arm rotation mechanism of a garbage truck, taking into account the wear of friction pairs, which can be used to develop an improved method for the design calculation of the parameters of the manipulator arm rotation mechanism during the loading of municipal solid waste. The drive for the working components of the garbage truck manipulator arm rotation mechanism is hydraulic, powered by the garbage truck's pump station. During the operation of this drive, transient processes inevitably occur, associated with the operation of the control unit, the activation of the positive-displacement hydraulic pump, changes in the load on the actuator, and so on. Graphical dependencies of the quality indicators of transient processes in the hydraulic cylinder of the garbage truck manipulator arm rotation mechanism on the wear of friction pairs were plotted based on initial data corresponding to the parameters of a real production model of the KO 436 garbage truck manufactured by Turbivskyi Machine-Building Plant LLC (Ukraine). These results showed that accounting for friction pair wear significantly affects the quality indicators of transient processes in the hydraulic drive of the garbage truck manipulator arm rotation mechanism. It was established that an increase in the wear of the friction pairs in the garbage truck manipulator arm rotation mechanism leads to a decrease in the quality indicators of the transient processes of its hydraulic drive.

Keywords: transient processes, quality indicators, consideration of wear, hydraulic drive, wear, friction components, arm rotation mechanism, manipulator, garbage truck, municipal solid waste.

Introduction

One of the key directions in the development of modern municipal machinery in Ukraine is the improvement of mobile manipulator-type machines, which include garbage trucks [1]. Within this field, particular attention is paid to improving the wear resistance, reliability, and durability of the design elements of these machines, as these operational characteristics significantly influence their performance. Improving these indicators makes it possible to reduce costs associated with repairs and maintenance, increase the serviceability of the machines, and ensure a longer service life under conditions of long-term and intensive operation [2, 3]. In Ukraine, the majority of work involved in collecting and transporting municipal solid waste (MSW) to sites for further processing, recycling, or disposal is carried out using body-type garbage trucks [4, 5]. An integral part of the design of these specialized vehicles is the loading mechanisms [6–8], which enable the mechanized performance of operational tasks such as gripping, lifting, and tilting waste containers to empty them into the garbage truck's body. The vast majority of such devices are implemented as manipulator mechanisms of various designs [9–13], which are operated by a hydraulic drive [14–16]; during operation, transient processes inevitably occur at startup [17] associated with the activation of a positive-displacement hydraulic pump, the operation of the control mechanism, changes in the load on the actuator, and so on. Currently, there are approximately 3,700 garbage trucks in operation

Copyright © 2026 O.V. Bereziuk, V.O. Kharzhevskyi, S. Cv. Ivanov, V.Ye. Yavorskyi. This is an open access article distributed under the Creative Commons Attribution License, which permits unrestricted use, distribution, and reproduction in any medium, provided the original work is properly cited.

in Ukraine, which, in addition to transporting municipal solid waste, mechanically compact it directly in the truck body. Implementing this process makes it possible to significantly increase the mass of waste transported per trip, reduce the number of transport cycles, and, consequently, lower transportation costs. In addition, compacting MSW contributes to a more efficient use of landfill capacity by reducing the area required for disposal, which provides a significant economic benefit while also positively impacting the environment through a more rational use of land resources. During the process of loading municipal solid waste into the body of a garbage truck, the friction components of the manipulator mechanism—primarily its hinged joints and hydraulic cylinders—are subjected to the highest mechanical loads. The rate of wear on these components is determined by the combined effect of operational factors. The main factors include the significant weight of waste containers, which in some cases can reach 500 kg; the operation of the mechanism under conditions of frequent reversing loads with repetitive reverse-rotational movements of the links; and the performance of a large number of work cycles during a single transport trip. The combined effect of these factors leads to accelerated wear, deterioration of the technical condition of the manipulator's components, increased clearances in the couplings, and, as a result, reduced reliability and operational efficiency of the garbage truck's loading equipment. Operating conditions for the manipulator mechanism are further complicated by the influence of unfavorable environmental factors, including significant fluctuations in temperature and relative humidity, as well as high dust levels in the work area. The combined effect of these factors accelerates the wear of friction assemblies and the mechanism's working parts, leading to a deterioration in their technical condition, a decrease in operational reliability, and a reduction in the service life of garbage trucks. In addition, the deterioration of the tribological properties of the materials used in the parts, as well as insufficient lubrication, cause an increase in friction forces in the hinged joints of the manipulator mechanism. The rapid progression of wear processes in the friction assemblies of the manipulator mechanism not only leads to a deterioration in its technical and operational characteristics but also significantly affects the overall operational safety of the garbage truck. Increased clearances in mating surfaces, increased internal leakage in the hydraulic drive, and higher levels of vibration and dynamic loads can disrupt normal equipment operation, cause individual components to fail, or lead to emergency situations. In accordance with the provisions of Resolution No. 265 of the Cabinet of Ministers of Ukraine [18], one of the priority tasks for the development of the housing and utilities sector is the introduction of modern, high-performance garbage trucks, which serve as the basic technical equipment for the mechanized collection, transportation, and initial compaction of municipal solid waste. Equipping municipal utilities with modern specialized equipment ensures greater efficiency in carrying out technological processes, optimization of transportation and logistics operations, a reduction in operating costs, and a more rational use of material and energy resources. Planning the modernization, maintenance, and repair of garbage trucks is facilitated by identifying analytical dependencies of the quality indicators of the transient processes in the hydraulic drive of the garbage truck's manipulator-arm rotation mechanism, taking into account the wear of friction pairs, which can be used to develop an improved methodology for the design calculation of the parameters of the manipulator arm rotation mechanism during the loading of municipal solid waste.

Analysis of recent research and publications

The scientific article [19] presents an algorithm for determining the key quality indicators of transient processes to optimize the components of a system and improve control quality. The key quality indicators of transient processes that were considered include: relative overshoot, the number of overshoots, and the settle duration. For high-quality transient processes, relative overshoot should not exceed 30%, and the number of overshoots during the settling time period should not exceed 2–3 [20].

The results of the structural analysis of garbage truck components subject to intense wear are presented in the scientific paper [21]. In the study [22], a design for a robotic manipulator was proposed, along with its three-dimensional geometric model in SOLIDWORKS, and a motion analysis was also performed. During the structural optimization of the design, a detailed analysis of the manipulator's key parameters was carried out; in particular, the stresses and strains of its components were evaluated, and the objective functions and system of constraints necessary for improving the design were formed. This approach helps reduce the probability of failures in the manipulator mechanism under conditions of prolonged operation under high loads and ensures more efficient interaction of its components with other systems of the garbage truck, which ultimately increases the productivity of MSW collection and transportation processes.

In the paper [23], the effect of an increase in radial clearance due to wear on the quality characteristics of a servo valve's transient processes was investigated using MATLAB/Simulink. The following changes were analyzed: overshoot, settling time, damping, and dynamic accuracy. It was found that an increase in the servo valve's flow rate as the clearance increases due to wear leads to a reduction in overshoot and a shorter settling time. An analysis of the correlation between wear progression and performance degradation will enable the formulation of maintenance strategies and proposals for design improvements, thereby ensuring the durability and operational efficiency of servo valves.

The authors of [24] proposed a mathematical model for determining the optimal geometric parameters of the manipulator's structural elements, taking into account the maximum boom reach, load capacity, and other kinematic characteristics of the machine. Particular attention is paid to hinged joints operating in a cyclic mode, which is characteristic of manipulator-type machines. It has been established that under such conditions, the hydrodynamic friction mode is practically nonexistent, and the friction process occurs predominantly in the semi-dry or boundary friction modes. In this regard, the properties of the materials, the quality of surface finishing, and the effectiveness of the lubrication system are of decisive importance for ensuring the wear resistance and durability of the hinge assemblies. The operation of sliding bearings under these conditions is accompanied by accelerated wear of the contact surfaces, a decrease in kinematic accuracy, and the occurrence of additional dynamic loads and vibrations. To reduce friction forces, it is recommended to apply special coatings to the contact surfaces (lead, phosphate, or indium-based), use grease, as well as phosphate and anodic coatings, which improve lubricant retention and increase the service life of hinge assemblies.

In the paper [25], the effect of wear on the throttle edges after a certain period of operation on the transient processes of a servo system based on a hydraulic servo-spool valve was experimentally investigated. It was found that the diameter of the hydraulic servo valve opening increases due to erosive wear caused by contamination with solid particles in the oil, which leads to a decrease in the valve's static and dynamic characteristics and a deterioration in performance. A control method with a variable amplification coefficient is proposed to address the problem of erosive wear of the valve opening. After applying variable amplification control, the static and dynamic characteristics of the servo valve closely resemble those of an ideal servo valve, with a maximum deviation between the flow characteristics and the ideal valve orifice of approximately 1%.

In the article [26], a method for optimizing the operation of a robotic cell is proposed, which involves selecting an optimal position for the robotic manipulator within the work area for programs with a specified end-effector motion trajectory. The aim of the study was to reduce the total wear of the manipulator's joints and to balance their loads by preventing excessive mechanical stress on individual joints. Wear was assessed based on an approximation of the integral of the mechanical work of each joint along the motion trajectory, using values of angular velocities and torques. The proposed approach is based on dynamic modeling, which enables the determination of rotational velocities and torques at various positions of the manipulator. The research results show that optimizing the robot's base configuration reduces the total wear of its joints by 22–53%, depending on the motion trajectory configuration.

In the scientific article [27], which investigates the deterioration in the performance of hydraulic servo-spool valves caused by erosive wear of the valve opening, the micromorphological characteristics of the spool's working edge were investigated, the transient process of solid-particle erosion was visualized, and the factors influencing the erosion rate of the working edge were modeled.

The study [28] analyzes the main mechanisms of wear in the hinged joints of forestry manipulators and identifies promising approaches for improving their wear resistance depending on operating conditions. It has been established that the operation of manipulators under significant temperature fluctuations significantly affects the properties of structural materials and lubricants. At low temperatures, the brittleness and stiffness of materials increase, friction conditions deteriorate, and lubricants lose their fluidity or become significantly more viscous, which accelerates wear. At high temperatures, the lubricant thins, is less effectively retained in the friction zone, and fails to provide adequate cooling of the contact surfaces, resulting in increased wear rates. To increase the service life of hinge assemblies, it is recommended to use combined contact-labyrinth seals, which effectively protect them from the ingress of dust, moisture, and other contaminants and ensure that the lubricant is retained in the friction zone.

In the paper [29], the effect of erosive wear of the spool pair on the dynamic characteristics of an electrohydraulic servo valve was investigated. It was found that as wear increases, the following parameters deteriorate: pressure amplification factor, internal leakage, characteristic linearity, and dynamic performance of the control system.

A study [30] justified the feasibility of applying a comprehensive approach to the selection of scientific and technical solutions when designing new hinged joint structures. It is shown that their performance is determined by the combined effect of design features, the properties of the friction pair materials, loading conditions, lubrication modes, and the operating environment. Taking these factors into account makes it possible to create designs with improved reliability, durability, and wear resistance. This comprehensive approach improves both the mechanical and tribological characteristics of hinged joints, optimizes their thermal behavior, and contributes to increased operational efficiency of forestry machines, reduced maintenance costs, and extended service life of manipulator systems.

The paper [31] proposes a method for synthesizing the motion trajectory of a manipulator robot, taking into account its kinematic characteristics and the degrees of freedom of its links. The effect of rod bending on the formation of support reactions and contact loads in the interaction zone between the hydraulic cylinder, the rod, and the ground bushing is examined to assess the distribution of forces and predict the wear rate of friction surfaces. It has been established that, in the absence of a risk of rod failure, contact stresses accounting for about one-third of the material's tensile strength can significantly accelerate wear due to cyclic loading. It has also been shown that the contact pressure and the wear rate depend on the angle of the rod's extension, its velocity, and the manipulator's operating mode.

The paper [32] investigates the design features of the grippers on garbage truck manipulators and evaluates their reliability. Based on the results obtained, a computational model of the garbage truck as an oscillatory system was developed, which made it possible to analyze the vibrations of the frame and the regularities of load distribution in the “gripper–bin–gripper” system. It was found that the highest loads are received by the pull rod and the hydraulic cylinder rod, and their magnitude increases with the increase in the container’s mass, whereas the mass of the garbage truck affects only the frequency characteristics of the oscillations. Operational studies have shown that the main causes of garbage truck failures are wear and corrosion of working equipment components, and approximately 32% of hydraulic drive malfunctions are attributable to hydraulic cylinders. Their failures are caused by wear on mating surfaces, deformation of the piston rod and cylinder, uneven loading, and abrasive wear. The spools and housings of hydraulic distributors, as well as the hydraulic cylinder rods, are subject to the most intense wear. The deterioration of technical condition is promoted by hydro-abrasive damage caused by contamination of the working fluid and wear of seals. To restore the performance of the parts, it is recommended to use chrome plating in a cold, self-regulating electrolyte, which ensures the formation of wear-resistant coatings and helps extend the service life of the hydraulic drive components.

In the article [33], an improved nonlinear mathematical model of the hydraulic drive for the mechanism that loads municipal solid waste into a garbage truck during container tipping was developed. Unlike other models, it accounts for the wear of the friction pairs in the main components of the hydraulic drive, which ensures a more accurate representation of real operating conditions. Based on the results of numerical simulations, the dynamic characteristics of the system during the startup phase were investigated, and the effect of wear on its key parameters was evaluated. It was found that increased wear significantly worsens the speed and force characteristics of the hydraulic drive and prolongs the duration of the operational cycle. It was shown that the duration of container tipping increases in a power-law relationship with the degree of wear on the hydraulic cylinder, confirming the nonlinear nature of the effect of wear on the mechanism’s performance. The results obtained can be used to predict the operational performance of the hydraulic drive, determine optimal maintenance schedules, and improve the reliability of MSW loading systems.

In the paper [34], an analytical study was conducted of an improved mathematical model of the hydraulic drive for a garbage truck container-tipping mechanism, taking into account wear of the friction pairs. Based on the linearized model, approximate analytical dependencies of the pressure in the hydraulic cylinder’s pressure line, the angular velocity, and the container’s rotation angle as a function of time were obtained for the first phase of tipping—its rotation to the equilibrium position. A regression equation was also derived, which allows for an approximate determination of the duration of this phase, taking into account the wear of friction pairs. The proposed relationships can be used in the design of new garbage truck configurations and the optimization of hydraulic drive parameters without the need to analyze a full nonlinear mathematical model.

In the paper [35], using a first-order experimental design methodology that accounts for the effects of factor interactions according to the Box-Wilson method, an adequate mathematical dependence was obtained that describes the influence of the properties of anti-friction materials on the wear rate of the friction components in the garbage truck’s loading mechanism. In the study [36], using a similar approach, an adequate dependence was established for the variation of maximum dynamic impact stresses in the most heavily loaded section of the garbage truck manipulator’s boom, depending on the degree of wear of the hinged joint and the manipulator’s load level.

However, during their analysis of the available literature, the authors did not identify any specific analytical dependencies between the quality indicators of the transient processes in the hydraulic drive of the garbage truck’s manipulator arm rotation mechanism, taking into account the wear of the friction pairs.

Aims of the article

Determination of analytical dependencies of the quality indicators of transient processes in the hydraulic drive of the manipulator arm rotation mechanism of a garbage truck, taking into account the wear of friction pairs, which can be used to develop an improved method for the design calculation of the parameters of the manipulator arm rotation mechanism during the loading of municipal solid waste.

Methods

The following methods were used in this study: analysis of scientific literature; mathematical modeling of processes in hydraulic drives using the fundamental laws of solid-body mechanics, the theory of hydraulic drives and hydropneumatic automation, and the theory of modeling; synthesis of mathematical interdependencies of the main geometric, force, and velocity parameters of the equipment; a systematic approach to account for the interaction of all the machine’s subsystems.

Analytical dependencies of the quality indicators of transient processes in the hydraulic drive of the manipulator-arm rotation mechanism of a garbage truck, without accounting for wear of friction pairs, are determined in [37]:

$$\sigma = \left[\sin\left(\frac{\pi Q_P}{4 l_p^2 S_{C1}^2} \sqrt{\frac{K W_{12} J}{2 \sin \lambda_{av}}} + \frac{\pi}{4} \right) + \frac{Q_P}{2 G R \cos \delta} \sqrt{\frac{J \sin \lambda_{av}}{K W_{12}}} e^{-\frac{\pi \sigma_l}{4 l_p S_{C1}} \sqrt{\frac{J}{2 K W_{12} \sin \lambda_{av}}}} - 1 \right] 100\%; \quad (1)$$

$$N = \frac{l_p S_{C1}}{\pi \sigma_l} \sqrt{\frac{2KW_{12} \sin \lambda_{av}}{J}} \ln \left\langle \left\{ 1.05 - \sin \left[\frac{\pi Q_P}{4 l_p^2 S_{C1}^2} \times \right.\right.\right.$$
$$\left.\left.\left. \times \sqrt{\frac{KW_{12} J}{2 \sin \lambda_{av}}} + \frac{\pi}{4} \right] \right\} \frac{2GR \cos \delta}{Q_P} \sqrt{\frac{KW_{12}}{J \sin \lambda_{av}}} \right\rangle^{-1} + 0.75; \quad (2)$$

$$t_{set} = \frac{2KW_{12}}{\sigma_l} \ln \left\langle \left\{ 1.05 - \sin \left[\frac{\pi Q_P}{4 l_p^2 S_{C1}^2} \sqrt{\frac{KW_{12} J}{2 \sin \lambda_{av}}} + \frac{\pi}{4} \right] \right\} \frac{2GR \cos \delta}{Q_P} \sqrt{\frac{KW_{12}}{J \sin \lambda_{av}}} \right\rangle^{-1}, \quad (3)$$

де σ – relative pressure overshoot of the working fluid in the rod-side chamber of the hydraulic cylinder of the arm-rotation mechanism of the waste collection vehicle, %; J – moment of inertia of moving parts, kg·m^2; Q_P – actual flow rate of the hydraulic pump, m^3/s; R – radius of rotation of moving parts, m; G – weight of moving parts, N; S_{C1} – rod-side chamber area of the hydraulic cylinder, m^2; l_p – distance between the centers of rotation of the manipulator arm and the hydraulic cylinder rod, m; λ_{av} – the average angle of inclination of the hydraulic cylinder axis relative to the horizontal,°; δ – angle between the arm axis and the horizontal, °; σ_l – the coefficient of working fluid loss due to flow from a high-pressure region to a low-pressure region m^5/(N·s); K – compressibility coefficient of the working fluid, Pa^{-1}; W_{12} – the volume of the piping between the hydraulic pump and the rod chamber of the hydraulic cylinder, m^3; N – the number of pressure overshoots of the working fluid in the rod-side chamber of the hydraulic cylinder of the arm-rotation mechanism of the waste collection vehicle manipulator during the settling time, times; t_{set} – the settling time of the working fluid pressure in the rod-side chamber of the hydraulic cylinder of the arm-rotation mechanism of the waste collection vehicle, s (Fig. 1).

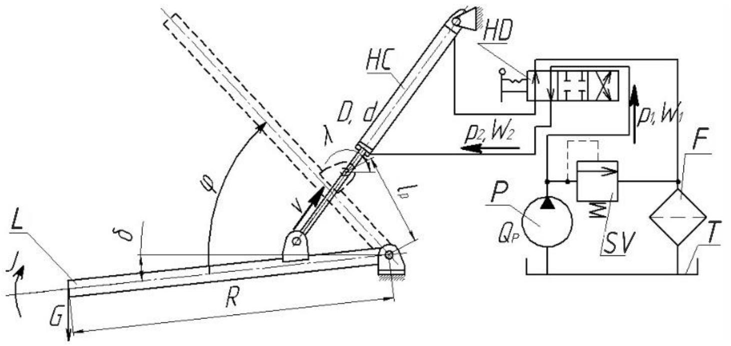

Fig. 1. Schematic diagram of the linearized mathematical model of the hydraulic drive for the manipulator arm rotation mechanism of a garbage truck

Fig. 1 also includes the following designations: HC – hydraulic cylinder, L – lever, HD – hydraulic distributor, SV – safety valve, P – hydraulic pump, T – tank with working fluid, F – filter. The coefficient of working fluid loss due to flow from the high-pressure region to the low-pressure region, taking into account wear caused by friction pairs, can be determined using the formula [34]:

$$\sigma_l = \frac{\pi D \left(\delta_0 + u \cdot 10^{-6} \right)^3}{12 \nu \rho l} \text{ [m}^5\text{/(N·s)]}, \quad (4)$$

where D – hydraulic cylinder piston diameter, m; δ_0 – nominal clearance, m; u – wear on the manipulator hinge, µm; ν – kinematic viscosity of the working fluid, m^2/s; ρ – density of the working fluid, kg/m^3; l – length of the annular gap, m.

Results

Substituting formula (4) into expressions (1)–(3), we obtain the relationships for the quality indicators of the transient processes in the hydraulic drive of the garbage truck manipulator's arm rotation, taking into account the wear of the friction pairs:

$$\sigma = \left[\sin\left(\frac{\pi Q_P}{4 l_p^2 S_{C1}^2} \sqrt{\frac{K W_{12} J}{2 \sin \lambda_{av}}} + \frac{\pi}{4} \right) + \frac{Q_p}{2 G R \cos \delta} \sqrt{\frac{J \sin \lambda_{av}}{K W_{12}}} e^{-\frac{\pi^2 D \left(\delta_0 + u \cdot 10^{-6} \right)^3}{48 l_p S_{C1} \nu \rho l} \sqrt{\frac{J}{2 K W_{12} \sin \lambda_{av}}}} - 1 \right] 100\%; \quad (5)$$

$$N = \frac{12 l_p S_{C1} \nu \rho l}{\pi^2 D \left(\delta_0 + u \cdot 10^{-6} \right)^3} \sqrt{\frac{2 K W_{12} \sin \lambda_{av}}{J}} \ln \left\langle \left\{ 1.05 - \sin \left[\frac{\pi Q_P}{4 l_p^2 S_{C1}^2} \times \right.\right.\right.$$
$$\left.\left.\left. \times \sqrt{\frac{K W_{12} J}{2 \sin \lambda_{av}}} + \frac{\pi}{4} \right] \right\} \frac{2 G R \cos \delta}{Q_P} \sqrt{\frac{K W_{12}}{J \sin \lambda_{av}}} \right\rangle^{-1} + 0.75; \quad (6)$$

$$t_{set} = \frac{24 K W_{12} \nu \rho l}{\pi D \left(\delta_0 + u \cdot 10^{-6} \right)^3} \ln \left\langle \left\{ 1.05 - \sin \left[\frac{\pi Q_P}{4 l_p^2 S_{C1}^2} \sqrt{\frac{K W_{12} J}{2 \sin \lambda_{av}}} + \frac{\pi}{4} \right] \right\} \frac{2 G R \cos \delta}{Q_P} \sqrt{\frac{K W_{12}}{J \sin \lambda_{av}}} \right\rangle^{-1}. \quad (7)$$

The proposed analytical dependencies (5)–(7) for the quality indicators of transient processes in the hydraulic drive of the manipulator arm rotation mechanism of a garbage truck, taking into account the wear of friction pairs, can be used to develop an improved method for the design calculation of the parameters of the manipulator arm rotation mechanism during the loading of municipal solid waste, which will significantly reduce design time and avoid unnecessary costs associated with labor-intensive experimental and theoretical studies.

Using expressions (5)–(7), graphical dependencies of the quality indicators of transient processes in the hydraulic cylinder of the garbage truck manipulator's arm rotation mechanism as a function of friction pair wear were obtained, as shown in Figs. 2–4, based on the following initial data, which correspond to the parameters of a real production model of the KO 436 garbage truck manufactured by Turbivskyi Machine-Building Plant LLC (Ukraine): $K = 10^{-9}$ Pa^{-1}; $W_{12} = 1.98 \cdot 10^{-3}$ m^3; $S_{C1} = 4.222 \cdot 10^{-3}$ m^2; $D = 80$ mm; $Q_P = 55$ l/min; $GR = 4627$ Nm; $\delta = 6°$; $l_p = 450$ mm; $\lambda_{av} = 54°$; $J = 1151$ kg·m^2; $\delta_0 = 0{,}136$ mm; $\nu = 1.83 \cdot 10^{-5}$ m^2/s; $\rho = 890$ kg/m^3; $l = 35$ mm.

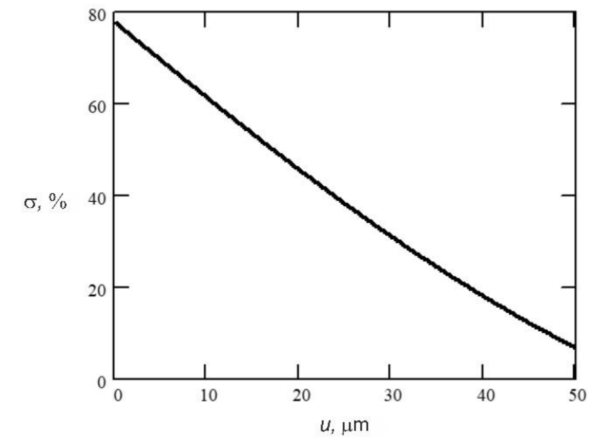

Fig. 2. Dependence of the relative overshoot of the working fluid pressure in the rod chamber of the hydraulic cylinder of the garbage truck manipulator's arm rotation mechanism on the wear of the friction pairs

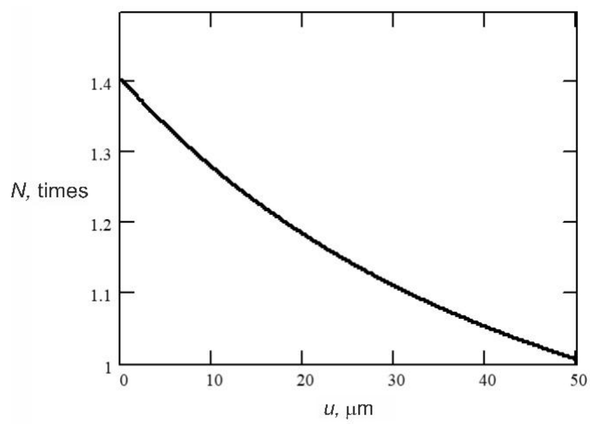

Fig. 3. Change in the number of overshoots of the working fluid pressure in the rod chamber of the hydraulic cylinder of the garbage truck's manipulator arm mechanism during the during the settling time due to wear of the friction pairs

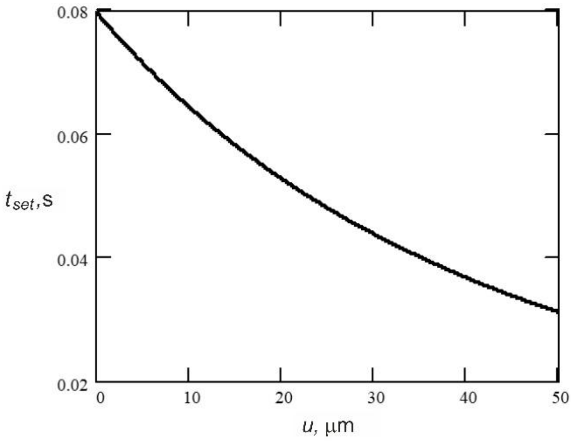

Fig. 4. Dependence of the settling time of the working fluid pressure in the rod chamber of the hydraulic cylinder of the garbage truck manipulator's arm rotation mechanism on the wear of the friction pairs

Figs. 2–4 show that accounting for wear on friction pairs significantly affects the quality indicators of the transient processes in the hydraulic drive of the garbage truck manipulator's arm rotation mechanism. It has been established that an increase in the wear of the friction pairs in the garbage truck manipulator arm rotation mechanism leads to a decrease in the quality indicators of the transient processes of its hydraulic drive.

The development of an improved method for the design calculation of the parameters of the manipulator arm rotation mechanism during the loading of municipal solid waste into a garbage truck, taking into account friction pair wear, requires further research.

Conclusions

Analytical dependencies of the quality indicators for the transient processes of the hydraulic drive of the manipulator arm rotation mechanism on a garbage truck, taking into account the wear of friction pairs, have been proposed. They can be used to develop an improved method for the design calculation of the parameters of the manipulator arm rotation mechanism during the loading of municipal solid waste, which will significantly reduce design time and avoid unnecessary costs associated with labor-intensive experimental and theoretical studies. For a garbage truck with the actual parameters of the KO 436 production model manufactured by Turbivskyi Machine-Building Plant LLC (Ukraine), graphical dependencies of the quality indicators of transient processes in the hydraulic drive of the manipulator arm rotation mechanism were established. The obtained dependencies revealed a significant influence of wear on the quality of transient processes in the hydraulic drive of the garbage truck's manipulator arm rotation mechanism. It was found that the development of an improved method for the design calculation of the parameters of the manipulator arm rotation mechanism for loading municipal solid waste into a garbage truck, taking into account the wear of friction pairs, requires further research.

References

1. Holenko K., Dykha O., Koda E., Kernytskyy I., Horbay O., Royko Y., Fornalchyk Y., Berezovetska O., Rys V., Humenuyk R., Berezovetskyi S., Żółtowski M., Baryłka A., Markiewicz A., Wierzbicki T., Bayat H. (2024) Structure and strength optimization of the Bogdan ERCV27 electric garbage truck spatial frame under static loading. Applied Sciences, 14(23), 11012, https://doi.org/10.3390/app142311012

2. Kindrachuk M.V., Kharchenko V.V., Marchuk V.Y., Humeniuk I.A., Leusenko D.V. (2024) Methodology for Selecting Compatible Metal Materials for Friction Pairs During Fretting-Corrosion Wear. Metallophysics & Advanced Technologies, 46(7), 637-648, https://doi.org/10.15407/mfint.46.07.0637

3. Dykha A., Sorokatyi R., Pasichnyk O., Yaroshenko P., Skrypnyk T. (2020, December) Machine wear calculation module in computer-aided design systems. In IOP Conference Series: Materials Science and Engineering, 1001(1), 012040, https://doi.org/10.1088/1757-899X/1001/1/012040

4. Hao Y., Zhang Y., Ma N., Li P., Liu Y. (2024) Developing driving cycles for garbage trucks to estimate fuel consumption. Transportation Research Part D: Transport and Environment, 136, 104469, https://doi.org/10.1016/j.trd.2024.104469

5. Giel R., Dąbrowska A. (2021) Estimating time spent at the waste collection point by a garbage truck with a multiple regression model. Sustainability, 13(8), 4272, https://doi.org/10.3390/su13084272

6. Guo J., Wang D., Li T., Gao S., Chen W., Fan R. (2018) Triaxial loading device for reliability tests of three-axis machine tools. Robotics and computer-integrated manufacturing, 49, 398-407, https://doi.org/10.1016/j.rcim.2017.05.009

7. Chulkov A.S., Chaplygin M.E., Shaykhov M.M. (2024) Justifying the Operation Parameters of a Robotic Cassette Loading Device of the Carousel Type for a Selection Seeder. Engineering Technologies and Systems,

34(4), 549-562, https://doi.org/10.15507/2658-4123.034.202404.549-562

8. Zhu B., Wang L., Wu J. (2022) Optimal design of loading device based on a redundantly actuated parallel manipulator. Mechanism and Machine Theory, 178, 105084, https://doi.org/10.1016/j.mechmachtheory.2022.105084

9. Kuang X., Zhou S. (2024) Robotic Manipulator in Dynamic Environment with SAC Combing Attention Mechanism and LSTM. Electronics, 13(10), 1969, https://doi.org/10.3390/electronics13101969

10. Tinoco V., Silva M.F., Santos F.N., Morais R., Magalhães S.A., Oliveira P.M. (2025) A review of advanced controller methodologies for robotic manipulators. International Journal of Dynamics and Control, 13(1), 36, https://doi.org/10.1007/s40435-024-01533-1

11. Bronnikov A., Bendeberia M. (2024) Development of a manipulator kinematic model using ABB RobotStudio. Innovative Technologies and Scientific Solutions for Industries, 4(30), 5-18, https://doi.org/10.30837/2522-9818.2024.4.005

12. Han R., Sang H., Liu F., Huang F. (2024) State of the Art and Development Trend of Laparoscopic Surgical Robot and Master Manipulator. International Journal of Medical Robotics and Computer Assisted Surgery, 20(6), e70020, https://doi.org/10.1002/rcs.70020

13. Calzada-Garcia A., Victores J.G., Naranjo-Campos F.J., Balaguer C. (2025) A Review on Inverse Kinematics, Control and Planning for Robotic Manipulators With and Without Obstacles via Deep Neural Networks. Algorithms, 18, 23, https://doi.org/10.3390/a18010023

14. Polishchuk L.K., Piontkevych O.V., Burdeinyi M.S., Trehubov V.O. (2024) Justification for choosing the type of belt conveyor drive. Journal of Mechanical Engineering and Transport, 19(1), 115-122, https://doi.org/10.31649/2413-4503-2024-19-1-115-122

15. Petrov O.V., Slabkyi A.V., Kozlov L.H., Rybko N. (2021) Energy Saving Load-Sensing Hydraulic Drive Based on Multimode Directional Control Valve. Lecture Notes in Mechanical Engineering, 4, 371-380, https://doi.org/10.1007/978-3-030-77823-1_37

16. Polishchuk L.K., Piontkevych O.V., Svietlov A.V., Adler O.O., Lozinskyi D. (2025) Development and optimization of the control devicefor the hydraulic drive of the belt conveyor. Informatyka, Automatyka, Pomiary w Gospodarce i Ochronie Środowiska, 15, 124-129, http://doi.org/10.35784/iapgos.7051

17. Lobov N.V., Maltsev D.V., Genson E.M. (2019) Improving the process of transport of solid municipal waste by automobile transport. IOP Conference Series: Materials Science and Engineering, 632, 012033, https://doi.org/10.1088/1757-899X/632/1/012033

18. The Cabinet of Ministers of Ukraine (2004) Resolution No. 265 "Pro zatverdzhennia Prohramy povodzhennia z tverdymy pobutovymyvidkhodamy" ["On Approval of the Program for Solid Waste Management"]. URL: http://zakon1.rada.gov.ua/laws/show/265-2004-%D0%BF.

19. Godorozha S., Protopopov A., Ryabinin M. (2020) Development of an algorithm for determining the main quality indicators of the transition process on the example of a LUDV hydraulic system. IOP Conference Series: Materials Science and Engineering, 963(1), 012034, https://doi.org/10.1088/1757-899X/963/1/012034

20. Markov V.A., Barchenko F.B., Neverov V.A., Savastenko A.A., Lotfullin Sh.R. (2022) Computational Analysis of the Dynamic Qualities of a Diesel Engine and a Tracked Vehicle. BMSTU Journal of Mechanical Engineering, 744(3), 31-52, https://doi.org/10.18698/0536-1044-2022-3-31-52

21. Lazea M., Constantin G.A., Stoica D., Voicu G. (2020) Analiza structurala cu elemente finite a pieselor de uzura de pe placa de contrapresiune a unei autogunoiere. Revista Romana de Materiale, 50(2), 283-293.

22. Li H., Li Y. (2025) Finite element analysis and structural optimization design of multifunctional robotic arm for garbage truck. Frontiers in Mechanical Engineering, 11, 1543967, https://doi.org/10.3389/fmech.2025.1543967

23. Popovici A.-I. (2025) Wear Analysis on the Dynamic Performance of Electrohydraulic Servovalves. Romanian Journal of Acoustics and Vibration, 22(2), 229-234.

24. Chernik D.V., Chernik K.N. (2020) Mathematical model of a combined manipulator of a forest machine. In IOP Conference Series: Materials Science and Engineering, 5(919), 052037, https://doi.org/10.1088/1757-899X/919/5/052037

25. Liu X., Qi M., Ji H., Liu F., Lin G., Xiao Y. (2024) Orifice erosion effect and variable gain control method for hydraulic servo spool valve. Flow Measurement and Instrumentation, 100, 102714, https://doi.org/10.1016/j.flowmeasinst.2024.102714

26. Kot T., Bobovský Z., Vysocký A., Krys V., Šafařík J., Ružarovský R. (2021) Method for robot manipulator joint wear reduction by finding the optimal robot placement in a robotic cell. Applied Sciences, 11(12), 5398, https://doi.org/10.3390/app11125398

27. Liu X., Liu F., Ji H., Li N., Wang C., Lin G. (2023) Particle erosion transient process visualization and influencing factors of the hydraulic servo spool valve orifice. Flow Measurement and Instrumentation, 89, 102273, https://doi.org/10.1016/j.flowmeasinst.2022.102273

28. Serebryanskii A. (2014) Except the negative reverse effect and automatically compensate for wear in the hinge manipulators. DOAJ – Lund University: Concept: Scientific and Methodological e-magazine, 4 (Collected works, Best Article).

29. Zhang K., Yao J., Jiang T. (2014) Degradation assessment and life prediction of electro-hydraulic servo valve under erosion wear. Engineering Failure Analysis, 36, 284-300.

https://doi.org/10.1016/j.engfailanal.2013.10.017.

30. Zadorozhnaya E., Levanov I., Kandeva M. (2018, May) Tribological research of biodegradable lubricants for friction units of machines and mechanisms: Current state of research. In International Conference on Industrial Engineering, 939-947, https://doi.org/10.1007/978-3-319-95630-5_98

31. Beisembayev A., Yerbossynova A., Pavlenko P., Baibatshayev M. (2023) Planning trajectories of a manipulation robot with a spherical coordinate system for removing oxide film in the production of commercial lead, zinc. Eastern-European Journal of Enterprise Technologies, 124(2), 80, https://doi.org/10.15587/1729-4061.2023.286463

32. Kargin R.V., Yakovlev I.A., Shemshura E.A. (2017) Modeling of workflow in the grip-container-grip system of body garbage trucks. Procedia Engineering, 206, 1535-1539, https://doi.org/10.1016/j.proeng.2017.10.727

33. Bereziuk O.V., Yavorskyi V.Ye. (2025) Udoskonalena matematychna model roboty hidropryvodu mekhanizmu zavantazhennia tverdykh pobutovykh vidkhodiv u smittievoz iz urakhuvanniam znosu par tertia [Improved mathematical model of the hydraulic drive of the mechanism for loading solid household waste into a garbage truck, taking into account friction pair wear]. Scientific Works of Vinnytsia National Technical University, 1, 154-164, https://doi.org/10.31649/2307-5376-2025-1-154-164

34. Bereziuk O.V., Savulyak V.I., Kharzhevskyi V.O., Ivanov S.Cv., Yavorskyi V.Ye. (2025) Analytical study of a hydraulic drive model for a municipal waste container overturning mechanism in a garbage truck considering the wear of friction pairs. Problems of Tribology, 30(3/117), 30-49, https://doi.org/10.31891/2079-1372-2025-117-3-30-40

35. Bereziuk O.V., Savulyak V.I., Kharzhevskyi V.O., Serdiuk O.V., Yavorskyi V.Ye. (2024) Dependence of wear of friction pairs of the mechanism for loading solid household waste into a garbage truck on the characteristics of antifriction materials. Problems of Tribology, 29(3/113), 24-30, https://doi.org/10.31891/2079-1372-2024-113-3-15-23

36. Bereziuk O.V., Savulyak V.I., Kharzhevskyi V.O., Yavorskyi V.Ye. (2023) The influence of hingeswear on the dynamic load of the articulated boom of a garbage truck’s manipulator. Problems of Tribology, 28(3/109), 18-24, https://doi.org/10.31891/2079-1372-2023-109-3-18-24

37. Bereziuk O., Petrov O., Lemeshev M., Slabkyi A., Sukhorukov S. (2023) Transient Processes Quality Indicators of the Rotation Lever Hydraulic Drive for the Dust-Cart Manipulator. Lecture Notes in Mechanical Engineering, 2, 3-12, https://doi.org/10.1007/978-3-031-32774-2_1

Березюк О.В., Харжевський В.О., Ivanov S.Cv., Яворський В.С. Залежність показників якості перехідних процесів гідроприводу повороту важеля маніпулятора сміттєвоза від зносу пар тертя

Стаття присвячена визначенню аналітичних залежностей показників якості перехідних процесів гідроприводу механізму повороту важеля маніпулятора сміттєвоза із урахування зносу пар тертя, які можуть бути використані для розробки удосконаленої методики проєктного розрахунку параметрів механізму повороту важеля маніпулятора під час завантаження твердих побутових відходів. Привод робочих органів механізму повороту важеля маніпулятора сміттєвоза – гідравлічний з живленням від насосної станції сміттєвоза. Під час роботи даного приводу неминуче виникають перехідні процеси, пов'язані з роботою органу управління, включенням гідронасоса об'ємного типу, зміною навантаження виконавчого органу тощо. Побудовано графічні залежності показників якості перехідних процесів в гідроциліндрі механізму повороту важеля маніпулятора сміттєвоза від зносу пар тертя, на основі вихідних даних, що відповідають параметрам реальної серійної моделі сміттєвоза КО-436 виробництва ТОВ "Турбівський машинобудівний завод" (Україна), які показали, що врахування зносу пар тертя суттєво вливає на значення показників якості перехідних процесів гідроприводу механізму повороту важеля маніпулятора сміттєвоза. Встановлено, що збільшення величини зносу пар тертя механізму повороту важеля маніпулятора сміттєвоза призводить до зниження значень показників якості перехідних процесів його гідроприводу. Виявлено, що розробка удосконаленої методики проєктного розрахунку параметрів механізму повороту важеля маніпулятора під час завантаження твердих побутових відходів у сміттєвоз із урахуванням зносу пар тертя вимагає проведення подальших досліджень.

Ключові слова: перехідні процеси, показники якості, урахування зносу, гідропривод, знос, вузли тертя, механізм повороту важеля, маніпулятор, сміттєвоз, тверді побутові відходи

ISSN 2079-1372 Problems of Tribology, V. 31, No 3/121-2026, 77-88

Problems of Tribology
Website: http://tribology.khnu.km.ua/index.php/ProbTrib
E-mail: tribosenator@gmail.com

DOI: https://doi.org/10.31891/2079-1372-2026-121-3-77-88

Evaluation of the Stress-Strain State of Aircraft Spherical Plain Bearings Based on Titanium Alloys and Antifriction Composite Materials and the Feasibility of Their Use

A. Khimko[1]009-0009-8059-880X, M. Khimko[2]0009-0005-4364-5444, O. Mikosyanchyk[1]0000-0002-2438-1333

[1] *National University "Kyiv Aviation Institute", Ukraine*
[2] *Air Company LLC "H3Operations", Ukraine*
E-mail: andreykhimko@ukr.net

Received: 20 July 2026: Revised 25 August 2026: Accept: 09 September 2026

Abstract

The paper presents an analysis of the use of titanium alloys for spherical bearings with antifriction composite materials. An analytical assessment of the use of titanium in spherical bearings is given. A model of the stress-strain state of spherical bearings with composite antifriction materials is presented. It was determined that Zedex ZX324VMT and Iglidur TX1 composite materials, when modeling the stress-strain state, reduce the maximum specific stress by 50 % in the material at loads of 3, 100 and 200 kN, compared to the base bearing on steel. Modeling the stress-strain state of spherical plain bearings with composite antifriction materials proved a reduction in specific stresses in the surface layers of bearing materials when using titanium alloys Ti5Al5V5Mo1Cr1Fe instead of bearing steel X105CrMo17 up to 20 %, depending on the material and load conditions. Economic calculations of the use of spherical plain bearings made of titanium alloys for aircraft were carried out. It was determined that under the conditions of operation of spherical plain bearings for 3000 hours of operation, the economic benefit is about 150 thousand dollars per aircraft. It was also determined that modified maintenance-free bearings with composite materials allow the operation of equipment to be closer to its technical condition by reducing maintenance costs when using aircraft.

Keywords: titanium alloys, spherical bearings, wear resistance, stress-strain state, composite coatings, economic calculations

Introduction

The use of titanium alloys in the aviation industry has been an urgent task for decades. However, the use of titanium alloys for spherical bearings is a revolutionary task that will allow reducing the weight of the aircraft, as well as, for example, the use of titanium alloy bolts in aircraft. Of course, given that titanium alloys do not work well on friction, they will be used together with protective coatings and modern composite materials.

One of the main tasks of the aviation industry is also to reduce the cost of aircraft maintenance. This is achieved either by optimizing maintenance costs or by transferring some components and assemblies of equipment to maintenance according to the actual condition. In turn, this is implemented in several ways:

1. By introducing a large number of sensors and an on-board computer to monitor the technical condition of the equipment.
2. By using special diagnostic devices for non-destructive testing and automatic drones for quick and effective detection of defects.
3. By developing modular structures and components for quick replacement.
4. Using special virtual models (digital twins, information storage and processing systems, etc.) and maintenance strategies.
5. Replacing components and creating maintenance-free structures.

The creation of new components that do not require maintenance during the operation of equipment is one of the main tasks of transferring equipment to maintenance according to the actual condition. The use of titanium alloys with anti-friction composite materials allows for immediate reduction of aircraft weight and the creation of components that last their entire service life without the need for maintenance.

Copyright © 2026 A. Khimko, M. Khimko, O. Mikosyanchyk. This is an open access article distributed under the Creative Commons Attribution License, which permits unrestricted use, distribution, and reproduction in any medium, provided the original work is properly cited.

Literature review

Titanium alloys are widely used in aircraft as a material with low weight, high strength and excellent corrosion resistance [1-3]. The growing demand for titanium alloys in the aviation industry is also due to their effective compatibility with carbon plastics in terms of their corrosion resistance and thermal expansion coefficient [4]. The use of titanium alloy-composite material combinations is widely used in the latest generation of aircraft, although this contact has certain problems [5-10] in the conditions of aircraft operation. According to works [6, 8, 11], it is the titanium alloy that is 2-10 times more damaged than composite materials. The authors of works [9-12] note the formation of fatigue cracks on the surfaces of titanium alloys during contact, and therefore it is necessary to use antifriction composite materials or appropriate technological treatment of the metal in such joints [13-15].

The amount of titanium alloys used in Airbus A320, A350, A380, etc. series aircraft with low fuel consumption has increased more than twice that of conventional aircraft [16, 17]. In addition, at the general meeting of ITA (International Titanium Association), it was reported that the demand for titanium alloys for the aviation industry will remain stable in the future [18, 19]. The global size of the aerospace titanium processing market is expected to reach 7.9 billion US dollars by 2033, accounting for 4.89 % during the forecast period from 2023 to 2033 (Fig. 1).

The maintenance costs of aircraft airframes can be effectively reduced by using titanium alloys, which have excellent characteristics of fatigue strength, crack propagation resistance, fracture toughness and corrosion resistance. The advantages of using titanium alloys for aircraft are: weight saving, heat resistance, low brittleness at low temperatures, high corrosion resistance, low thermal expansion. The external temperature during flight can be minus 60 ˚C or lower; however, titanium is resistant to brittleness at low temperatures. In addition, there is no concern about corrosion even when dew condenses after the temperature drops. Moreover, since its low thermal expansion is close to that of carbon fiber, titanium alloys are ideal materials for aircraft [20].

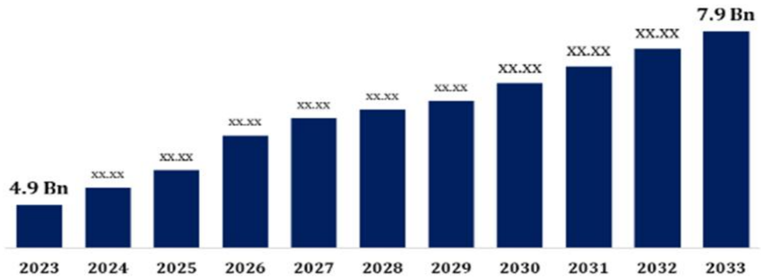

Fig. 1. Global market demand trend (billion USD) for aerospace titanium alloy products in the United States through 2033 [11].

Currently, the percentage of titanium alloy in the weight of the aircraft structure has become one of the important indicators. Titanium alloys occupy 39 % of the F-22 aircraft structure, 42 % for the F-35A/B and F-35C, and close to 40 % for the J-20 and Su-57. The use of titanium alloys increases with the improvement of the aircraft structure and its characteristics. It is used for about 50 % of the structure for fighter aircraft TF-X KAAN, J-31, X-2 (ATD-X) [21]. High resistance to damage is an important indicator of the characteristics of the material for durability, high mobility, low cost and resistance to damage of the structure of new generation fighters [22-24].

Spherical bearings in the aviation industry are used extensively. In aircraft such as: An-124, An-225, B-777, B-787, A330, A340, etc. more than a thousand such bearings are used. Spherical bearings are used in the bearings of rocket and gas turbine engines in civil aircraft. They are used in landing gear bearings and aircraft control systems. The design of spherical bearings with composite materials has not changed for decades.

With the development of modern technologies, many highly engineered composite materials have appeared on the market. Standardized bearings and sliding bushings with composite materials are produced by a number of companies: INA, SKF, FLURO, Koyo, FAG, etc. There are also companies (IGUS, ZEDEX, ELGES) that offer antifriction materials for use in friction units. The range includes almost 250 types of antifriction materials for one company.

Thus, conducting research aimed at evaluating the use of titanium alloys in spherical bearings with composite materials is a relevant task for the aviation industry.

Purpose

The aim of the work is to develop a model of a spherical bearing with titanium alloys and modern composite materials and to study its stress-strain state depending on the combination of materials.

Development of a model of the stress-strain state of spherical plain bearings with composite materials

The process of friction and wear of tribosystems with composite materials can be considered as a process of sequential change in the structure and properties of materials in the contact zone under external energy influence. External influences consist of forces and energy (mechanical, electrical, thermal). For some tribosystems, the spectrum of external influences can be described with quite high accuracy. But for most tribosystems, this is practically impossible, because the forces change at each point of the system and in time [25, 26]. A tribopair (tribological system) must have a certain structure and a set of interconnected elements that determine its composition. These elements are in a certain mutual relationship that determines their belonging to the tribosystem and structure. Friction includes a complex of physicochemical processes and is determined by a large number of parameters, therefore, to simplify and streamline their description, it is advisable to use system analysis [27-30].

The structural diagram of a tribological system, which corresponds to the system approach in tribology, is presented in Fig. 2. This structural diagram includes elements that are in relative motion and mutual connections between the elements of the system. The input characteristic of the tribological system is the work, which is determined by the parameters of the mechanical effect on the material in the contact zone. The output characteristic of the system is the useful work, which is realized in the transmission of force by the spherical bearing and its rotation by a certain angle. The output characteristics of the tribosystem are also the results of the friction and wear processes, which ultimately lead to the destruction of the tribosystem (separation of wear particles, irreversible change in the shape of the contacting elements, heat generation, noise, accumulation of defects in the material structure, etc.). Additional factors act on the tribosystem, for example: increased temperature, vibration, pollution, corrosion, disturbances in the kinematics of motion (for example, radial runout of rotating machine parts), etc. The properties of tribosystems are determined by their composition and structure and are characterized by wear resistance, friction coefficient, heat resistance, and compatibility of materials of the tribological system.

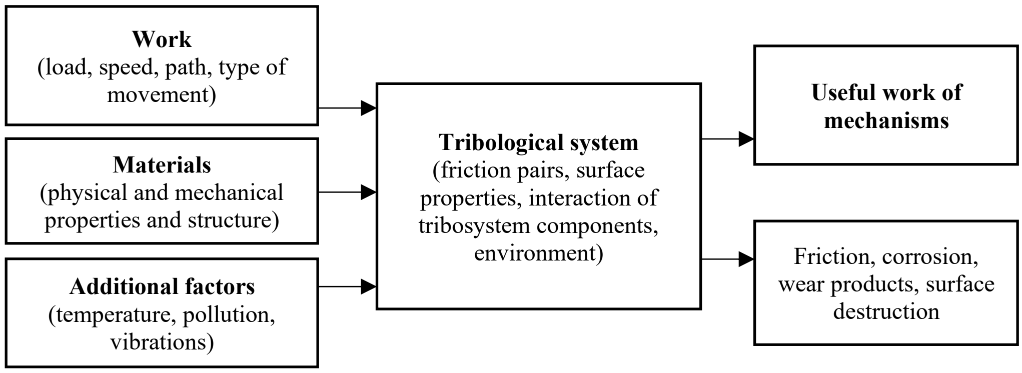

Fig. 2. Structural diagram of a tribological system that corresponds to the systems approach in tribology.

Analysis of a tribological system allows us to determine the internal connections, input and output parameters in the implementation of the purpose of its functioning, which can be the transformation of motion, energy, information and mass. In this case, the system is characterized as an open, dynamic, limit-controlled system [26]. Tribosystems, as a rule, are multiphase (material properties differ) and heterogeneous (properties are not uniform). Tribological systems can be open or closed. Open systems can exchange energy, matter and information with the environment, closed systems - only energy. There are also isolated thermodynamic systems that do not exchange energy or matter with the environment. In tribological systems, various friction and wear processes are implemented, the nature and intensity of which are determined by the functional characteristics of materials. In the general case, functional characteristics describe the transformation of input parameters X into output Y during the interaction of elements of the tribological system (Fig. 3).

The input to the tribological system is equivalent to the influence of the environment on the system, including a combination of mechanical and electrical forces, chemical reactions and thermal effects. External influences have the main influence on tribological processes and are of an energetic nature. Mechanical influences directly affect the parts of the friction pair and through them the lubricants (if any). Thermal influences can cause changes in the properties of the materials of the parts and thermochemical changes in the lubricants (if any).

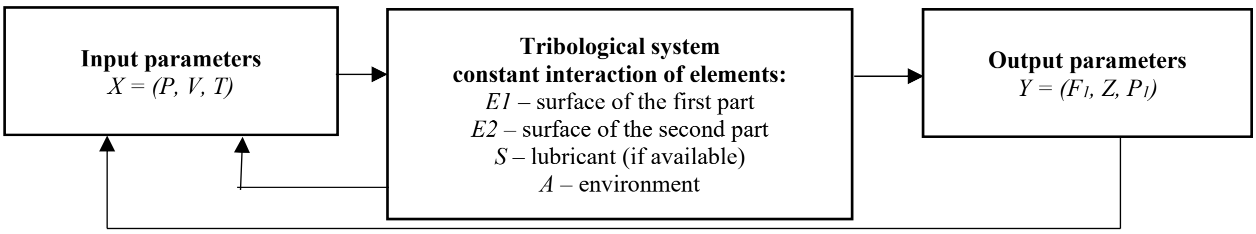

Fig. 3. Scheme of the functioning of the tribological system.

The output of the tribological system can be considered as the system's reaction to an external influence and as a result of tribological processes: friction resistance F_1, wear Z, accompanying processes P_1, for example, an increase in the temperature of the friction surface, triboelectric, tribochemical, thermomechanical, etc. processes. When energy is applied to the friction zone, friction work occurs in the system and the actual contact surface is formed. As a result of the interaction, energy dissipation (dispersion) occurs, which includes the processes [29-31]:

1. Energy accumulation: formation of local defects and dislocations, energy accumulation in the deformed volume of the material.
2. Emission of acoustic waves, light, electrons (Cramer effect).
3. Conversion of accumulated energy into heat, increase in entropy production and dissipation.

When a tribological system transitions from a static state to a dynamic state, processes arise and develop that affect the structure of the system. As a result of the action of the dynamic state, changes occur in the properties of the materials of the parts and the lubricant (if any) and their interaction: $Y = (F_1, Z, P_1)$. There is feedback between the output and the input, the effect of which is manifested in a change in the speed of mechanical-physical-chemical processes when the force changes.

A tribological system can change its functional characteristics in the process of operation, and its state also changes. The period of running-in of the parts of the tribological system (the first state of the system) is a non-stationary state. During this period, the system automatically adapts to the optimal conditions of interaction of the parts (E_1 and E_2) and it can be called the period of self-regulation (running-in). The properties of the parts and the interaction between them change in such a way that, with a constant external energy impact, the intensity of wear decreases. During this period, the formation of the optimal microgeometry of the mating surfaces and favorable changes in the structure and material properties of the parts, which are called tribological adaptations, occur.

After the period of running-in and adaptation, a period of steady state with constant wear intensity (the second state of the system) begins. This period is the main one for the tribological system and has the longest duration compared to other periods of system operation. The longer the steady state lasts, the longer the period of normal operation of the tribosystem.

With the accumulation of defects and degradation of the elements of the tribological system, it enters a state characterized by high and increasing wear intensity (the third state of the system), which can acquire an avalanche character. High-intensity wear occurs due to changes in the properties of materials and parts in frictional interaction, changes in lubricants (aging), the development of adverse side (dynamic) processes, etc. The reliability and durability of tribosystems largely depend on the properties of materials and the correctness of their selection for the given operating conditions of the friction unit. When choosing materials for the tribosystem, it is necessary to take into account their compatibility.

To simulate the stress-strain state of metal-polymer and polymer composite materials in spherical bearings, the Simulation module, which is part of the SOLIDWORKS software package, was used. SOLIDWORKS Simulation Premium allows for effective analysis of nonlinear and dynamic responses, dynamic loads in friction nodes, and also includes three additional types of studies: nonlinear static, nonlinear dynamic, and linear dynamic.

To simulate the stress-strain processes of composite materials in spherical bearings, a bearing model (Fig. 4) was developed with two layers of materials between the metal bearing cages.

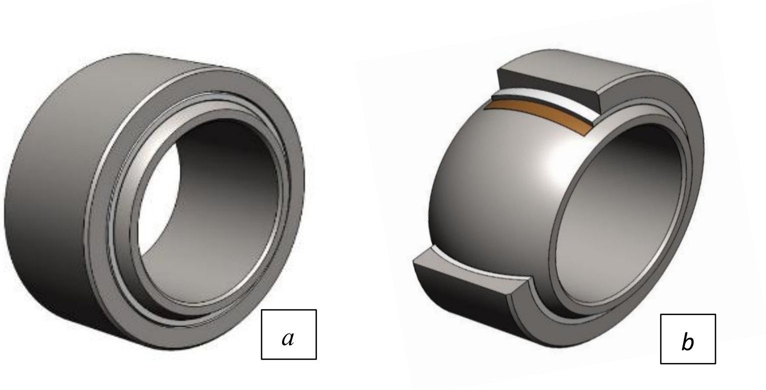

Fig. 4. Calculation model of a spherical plain bearing with antifriction composite materials: a – assembled bearing, b – bearing with an intersection of the outer ring and composite materials

To simplify the calculations and modeling processes, it was determined that the total thickness of the antifriction composite material is 1 mm, which corresponds to a real GE30EW-2RS bearing, and consists of two main layers of material. The first layer of material, which is located closer to the inner ring, has a thickness of 100 microns, is made of PTFE material and remains the same in all study variants. This is the so-called running-in layer, which helps in the running-in processes of the composite materials and in the future helps to reduce the friction coefficient and the displacement moment of the bearing. The second layer of the composite material has a thickness of 0.9 mm and is the main material that works on friction during the operation of the spherical bearing.

Choice of materials

For the production of plane bearings with metal-polymer filling, metal-fluoroplastic tape is usually used. It consists of: a surface made of PTFE+MoS_2 with a thickness of 0.01-0.05 mm, a layer of babbitt (for example, B-

83) with a thickness of 0.20-0.5 mm, a steel base with a low carbon content with a thickness of 0.25-2.70 mm. Provides reliable adhesion between layers, improves heat dissipation during operation.

Thus, the first and basic material for our study is PTFE+15%C+5% MoS_2 or F-4K15M5 material applied to the B-83 babbitt base.

Analyzing the materials of the Zedex series, it should be noted that the company offers mainly two materials for the use of plain bearings, under our bearing operating conditions: ZX-100K and ZX-324.

The base material ZX-100 K is proposed to be used up to temperatures of +110 °C. This material is created on the basis of PET with modifying fillings, which are the secret of the company. If we compare it with PTFE, then the material has the following differences: greater dimensional stability under load (not cold); higher wear resistance due to strength (5 times stronger than fluoroplastic); the maximum operating temperature is also lower (for PTFE +250 °C versus +110 °C for ZX-100K); lower chemical resistance than PTFE.

The ZX-324 material is also offered by the company for the use of plain bearings. ZX-324 thermoplastic polycrystalline polymer is designed as a modification of PEEK and has all the advantages of this polymer. The ZX-324VMT material is a modification of this material for difficult working conditions. The material can be used for a long time at temperatures from -50 to +250 °C, while maintaining high mechanical properties. This polymer is characterized by a high tensile strength and a bending endurance limit for the alternating cycle.

Thus, we can say that the ZX-100K material is an analogue of the F-4K15M5 material, and the ZX-324VMT material is an analogue of a metal-polymer tape. In our case, the second material for research was chosen ZX-324VMT, as an analogue of the intermediate material between the races of the plane bearing.

IGLIDUR materials are divided into the following base materials: G, A350, M250, P210, J, TX1, X, P, J260, J350, J3, L250, R, D, Z. All these materials can work as full-fledged plain bearings, but depending on the operating conditions and load, it is necessary to determine the most optimal material for research. The IGLIDUR line of materials includes both pure polymer materials PTFE, PEEK, PEK, PA, and their combinations with various fillers.

After analyzing the material characteristics and operating conditions of the plane bearing, it was determined that the most suitable materials for such operating conditions are IGLIDUR G (for heavy duty, static load up to 200 MPa, dynamic load 140 MPa, high wear resistance and geometry stability, good resistance to liquid media) and IGLIDUR TX1 (exceptionally long service life in extreme conditions, wear resistance and impact resistance even under high loads and temperatures, high wear resistance, especially under high loads, high heat resistance, the material is recommended for extreme loads).

For use in plane plain bearings, taking into account the operating conditions and loads that the bearing perceives, the optimal of those considered will be the IGLIDUR TX1 material, which is chosen as the third material for research.

FLURO specializes in the production of plain bearings and hinge heads. Bearings of this manufacturer work in modern machines around the world: the operating temperature range is from -50 to +150 °C. FLUROGLIDE materials are divided into two types: WEAR SOLID (for maximum static and dynamic loads) and MEDIA SOLID (for heavy dynamic loads). For example, the GE30EW-2RS bearing is a complete analogue of the CH30UT aircraft bearing. A distinctive feature of all bearings is that the special FLUROGLIDE material works in the contact of a polished chrome coating, which is applied to the inner race of the bearing.

Thus, the fourth material for the study was chosen FLUROGLIDE WEAR SOLID, which best meets the conditions of bearing operation in the aviation industry.

Therefore, the following materials were selected for the study:

1. Metal-polymer tape with PTFE+15%C+5%MoS_2 material, with babbit (B-83) on a steel tape.
2. ZX-324VMT material, which is a polymer composite material with a PEEK matrix reinforced with nanocarbon fiber with the addition of PTFE, MoS_2 and other functional additives.
3. IGLIDUR TH1 is a polymer composite material (engineering plastic) reinforced with long fibers with the addition of functional additives. In its composition, it is similar to the design of the ZX-324VMT material.
4. FLUROGLIDE material is a composite material: a reinforced fabric that includes PTFE material and other fillers that are the company's secret.

Analysis of the results of modeling the stress-strain state of spherical plain bearing elements with composite antifriction materials

For the completeness of the simulations of the plane bearing, it is necessary to determine, in addition to combinations of polymeric materials, also options with a change in the materials of the bearing races. Therefore, two sets of planes bearing with materials of the races of steel X105CrMo17 and titanium alloy Ti5Al5V5Mo1Cr1Fe were determined for modeling. Also, all materials and combinations of the plane bearing must be matched to the original bearings. Figure 5 shows the material layers for modeling processes in plane bearings, and Table 1 shows the material options that we used to simulate stress-strain state processes of antifriction composite materials. Sample No. 1 corresponds to real bearings, which use metal-polymer tape as an anti-friction material and are mass-produced for aircraft. Samples No. 2, 3, 4 are combinations of high-performance anti-friction materials for plane bearings, which are located between the steel cages of X105CrMo17 bearing steel. Samples No. 5, 6, 7 are the same materials, but the outer and inner clips are titanium alloy

Ti5Al5V5Mo1Cr1Fe. In reality, titanium alloy performs very poorly on friction due to its tendency to set. Therefore, the friction surface of the bearing cage must be covered with a layer of molybdenum, about 100 microns thick, to increase wear resistance. For studies of the stress-strain state of bearings, molybdenum coating was not taken into account because the main attention will be paid to the distribution of the load during the operation of the bearing with titanium alloys and anti-friction composite materials.

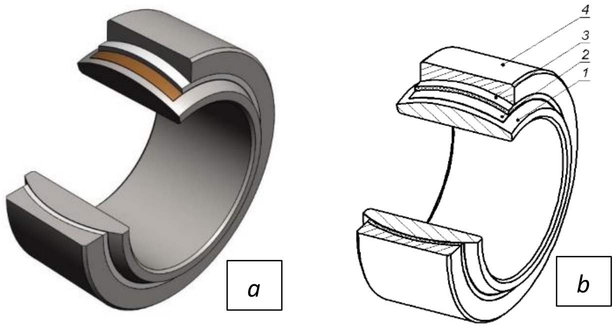

Fig. 5. Layers of materials for modeling the stress-strain state in a spherical bearing, general view (a) and cross-section (b): 1 - inner bearing cage, 2 - inner layer of composite anti-friction material (PTFE), 3 - main layer of composite anti-friction material, 4 - outer bearing cage.

Table 1

Variants of combinations of plane bearing elements with composite antifriction materials for research

Sample	Bearing layer material			
№	**Element 1**	**Element 2**	**Element 3**	**Element 4**
1	X105CrMo17	PTFE	Bronze leads.	X105CrMo17
2	X105CrMo17	PTFE	ZX-324VMT	X105CrMo17
3	X105CrMo17	PTFE	TX1	X105CrMo17
4	X105CrMo17	PTFE	Carbon fibers	X105CrMo17
5	Ti5Al5V5Mo1Cr1Fe	PTFE	ZX-324VMT	Ti5Al5V5Mo1Cr1Fe
6	Ti5Al5V5Mo1Cr1Fe	PTFE	TX1	Ti5Al5V5Mo1Cr1Fe
7	Ti5Al5V5Mo1Cr1Fe	PTFE	Carbon fibers	Ti5Al5V5Mo1Cr1Fe

As a basis for calculating the stress-strain state of bearing options, a GE30EW-2RS bearing was chosen, which was calculated at loads of 3, 100 and 200 kN and dimensions of 30x47x22 mm. The load on the bearing occurred over a distributed area from the outer cage to the inner one. The location of the bearing on the shaft with the external distributed load from the lever of the aircraft structure is simulated. Simulation of the stress-strain state of composite coatings was carried out with the reverse movement of the inner cage relative to the outer one at a frequency of 3 Hz and an oscillation amplitude of ±15 °. The physical and mechanical properties of materials for modeling the stress-strain state are given in Table 2.

Having analyzed the results of the stress-strain state of plane bearing models with different variants of anti-friction composite materials and cages, it is possible to neglect element 2 (PTFE) when analyzing the stress distribution and safety margin of the model elements, since at loads of 100 and 200 kN, PTFE material with a thickness of 100 μm completely loses its bearing capacity relative to load distribution (Fig. 6) and acts in a real bearing, as a layer for running in the main composite material (element 3).

Table 2

Physical and Mechanical Properties of Materials of Plane Bearing Elements

Characteristics of materials	**X105CrMo17**	**Bronze**	**PTFE**	**Carbon fiber**	**ZX324VMT**	**TX1**	**Ti5Al5V5Mo1Cr1Fe**
Modulus of elasticity, 10^{10}, Pa	20.4	11	0.5	14	0.78	1.2	11.5
Poisson's ratio	0.27	0.33	0.4	0.25	0.3	0.3	0.3
Shear modulus, 10^9, Pa	-	37	0.75	6.0	-	-	43
Material density, kg/m^3	7750	8300	2320	1750	1480	2100	4620
Tensile strength, MPa	770	262	27	490	142	203	470
Compressive strength, MPa	-	-	12	2000	120	220	-
Yield strength, MPa	420	110	4.24	-	-	184	380

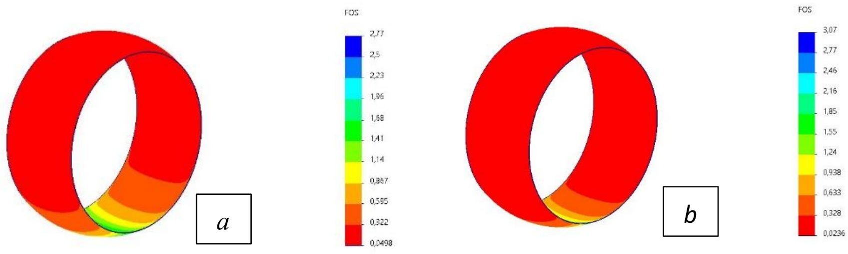

Fig. 6. Safety margin of element 2 of the composite antifriction material of the bearing model (sample No. 3) under loads: a - 100 kN, b - 200 kN.

Also, when analyzing the results of the introduction of titanium cages in models of samples No. 5, 6, 7, we see a decrease in specific stresses in the surfaces of plane bearings, compared to the material X105CrMo17 for samples No. 2, 3, 4. This effect is observed at all stages of modeling the stress-strain state of bearings when comparing samples No. 2-5 (Fig. 7), 3-6 (Fig. 8), 4-7 (Fig. 9) at loads of 3, 100 and 200 kN.

With an increase in the load, stress distribution is more efficiently implemented over all elements of a plane bearing with titanium races than with steel ones. Stress reduction in models reaches up to 20% at loads of 200 kN for individual sections of elements of plane bearing models. This effect can be explained by the fact that the titanium alloy is more ductile than the X105CrMo17 material (see Table 2) and damps and redistributes the load among the elements of the plane bearings.

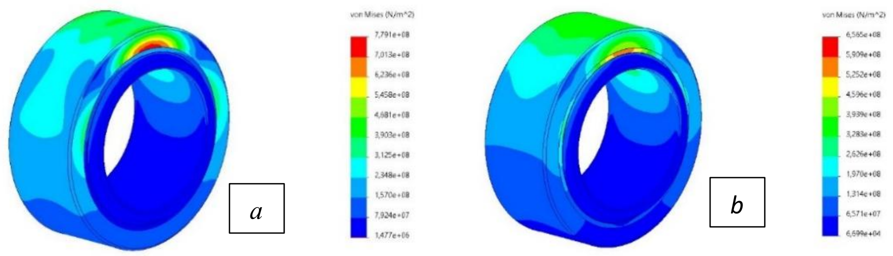

Fig. 7. The nature of the stress distribution in the bearing model at a load of 200 kN: a - sample No. 2, b - sample No. 5.

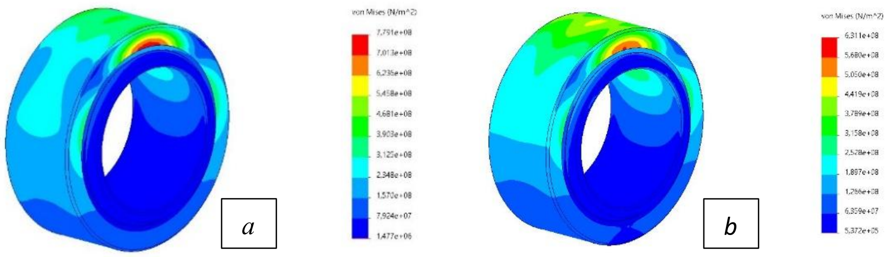

Fig. 8. The nature of the stress distribution in the bearing model at a load of 200 kN: a - sample No. 3, b - sample No. 6.

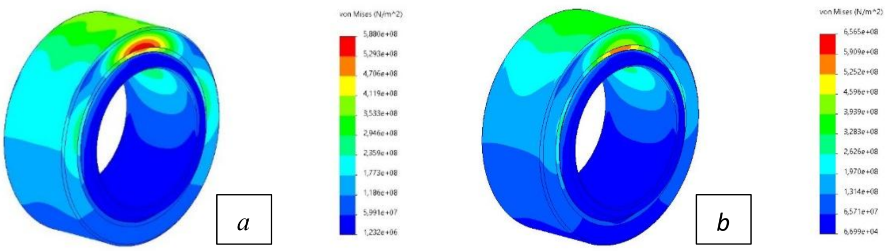

Fig. 9. The nature of the stress distribution in the bearing model at a load of 200 kN: a - sample No. 4, b - sample No. 7.

In works [32-35] the advantages of titanium materials in terms of load distribution during wear resistance tests are shown. Thus, in work [32] the authors investigated the wear resistance of gas-thermal coatings on titanium alloy and steel. The work indicates that the titanium alloy Ti5Al5V5Mo1Cr1Fe, on which the wear-resistant VKNA coating was applied, can increase the wear resistance of the plasma coating at loads up to 30 MPa in fretting corrosion studies due to a more ductile base. On harder steels, wear-resistant high-strength coatings had lower wear resistance at moderate loads.

This is confirmed by the analysis of stresses and the margin of safety of composite materials (element 3) when modeling the stress-strain state of plane bearings, if we compare races made of titanium alloy and steel.

When analyzing the stresses and safety margin of composite materials of materials (element No. 3, samples No. 2-4) in comparison with the model of the original bearing (element No. 3, sample No. 1), it can be stated that at stresses of 3 kN, materials ZX-324VMT and TX1 have stresses 50 % less, compared to the original bearing and material of the model based on carbon fibers, without a conjunction. The carbon fiber model has even 10-15 % higher stresses compared to the metal-polymer tape. This is due to the high physical and mechanical characteristics of carbon fibers (see Table 2), namely the compressive strength of 2 GPa, which is the highest among the materials under study. At the same time, this model lacks a conjunction, the function of which is to redistribute stresses over the entire surface of the material combination. A similar picture can be traced at loads of 100 and 200 kN. There is a decrease in specific stresses in the surfaces of ZX-324VMT and TX1 composite materials by 30-50 % compared to carbon fiber and bronze [7].

Having analyzed the safety margin of composite materials (element No. 3, samples 1-4) at a load of 3 kN, it can be argued that composite materials with carbon fibers have the highest safety margin among the tested materials of 98.4 at the point of maximum load. ZX-324VMT and TX1 materials have a safety margin of 31.7 and 46.2, respectively. These values are higher than those of the material with bronze (15.1) and may indirectly indicate the wear resistance of composite materials.

At loads of 100 and 200 kN, a similar dependence is maintained when calculating the safety margin of composite materials. At loads of 200 kN, the calculations show the safety margins of materials of samples No. 1-4 in 0.2: 0.47: 0.69 and 1.48 units, respectively, at the point of maximum load. That is, theoretically, all materials, except for carbon fibers, have a value of less than one, which means plastic deformation of composite materials in the contact zone.

For a more visual analysis of the stress-strain state of plane bearings using races made of materials X105CrMo17 and Ti5Al5V5Mo1Cr1Fe, we present histograms for a bearing with a metal-polymer tape (sample No. 1) and carbon fiber (sample No. 4 and 7). Figure 10 shows the maximum values of the distribution of normal stresses in composite materials (element No. 3) at loads of 100 and 200 kN. A similar relationship occurs at a load of 3 kN.

The generalized results of modeling the stress-strain state are presented in Table 3 [7]. Based on the results of the assessment, it was found that the use of carbon fibers in their pure form increases the normal equivalent stresses according to Miser by 1.27 times and 1.2 times when modeling the location of fibers of this type on a cage made of X105CrMo17 steel and alloy Ti5Al5V5Mo1Cr1Fe, respectively, compared to a metal-polymer tape. The increase in stresses is due to the stiffness of carbon fibers, their low relaxation capacity, the absence of a connector that provides high damping properties in polymer composite materials. These factors are not taken into account in modeling, the safety factor increases by 5-6 times.

The use of polymer composite materials Zedex ZX-324VMT and Iglidur TX1 on X105CrMo17 steel provides a reduction in normal stresses along the Miser by 1.45 and 1.27 times, respectively, compared to metal-polymer tape. In the case of using a titanium alloy bearing Ti5Al5V5Mo1Cr1Fe as a material of the inner and outer race, the normal stresses in Miser in models made of polymeric materials Zedex and Iglidur are reduced by 2.08 and 1.55 times, compared to metal-polymer tape on steel. It should be noted that when using the alloy Ti5Al5V5Mo1Cr1Fe, the reduction of normal stresses during modeling was set by 11 and 7 % for Zedex and Iglidur polymeric materials, compared to the stresses in these polymer materials on steel cages. The safety factor for the model with these polymer composite materials increases by 2.1 and 3 times for Zedex ZX-324VMT and Iglidur TX1 on the Ti5Al5V5Mo1Cr1Fe alloy, compared to the metal-polymer tape on steel [7].

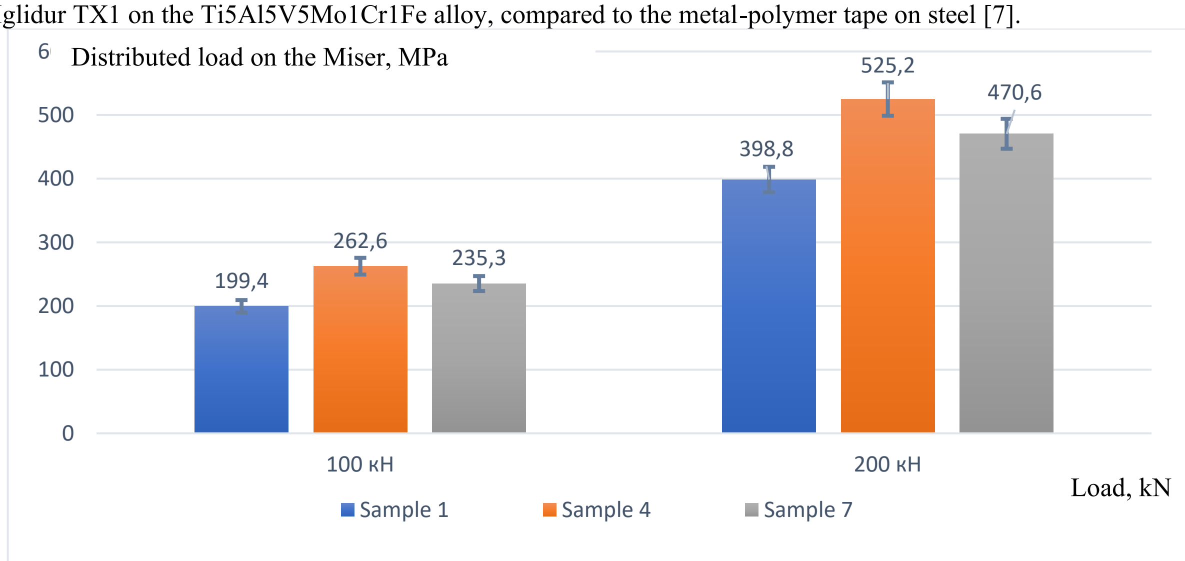

Fig. 10 – Histogram of stress distribution in composite materials (element No. 3) when modeling the stress-strain state of plane bearings under loads of 100 and 200 kN: Sample No. 1 – bronze tin, bearing cage material X105CrMo17; Sample No. 4 – carbon fiber, bearing cage material X105CrMo17; Sample No. 7 - carbon fiber, bearing cage material Ti5Al5V5Mo1Cr1Fe.

Table 3

Results of Simulation of the Stress-Strain State in a Plane Bearing Model

Sample	Materials of the elements of the plane bearing model		Distributed load on the Miser, MPa			Safety factor (by maximum stresses)		
№	3	1, 4	3 kN min/max	100 kN min/max	200 kN min/max	3 kN	100 kN	200 kN
1	Bronze	X105CrMo17	5.458/6.365	199.4/232.5	398.8/465.0	15.1	0.463	0.232
2	ZX-324VMT	X105CrMo17	2.902/3.869	96.75/129.0	193.5/258.0	30.9	0.816	0.463
3	TX1	X105CrMo17	3.792/4.738	126.4/157.9	252.8/315.8	44.4	1.33	0.66
4	Carbon fibers	X105CrMo17	7.879/8.863	262.6/295.4	525.2/590.9	76.1	2.28	1.14
5	ZX-324VMT	Ti5Al5V5Mo1Cr1Fe	2.481/3.708	82.72/123.6	165.5/247.2	31.7	0.951	0.475
6	TX1	Ti5Al5V5Mo1Cr1Fe	3.521/4.688	117.4/156.3	234.8/312.5	46.2	1.39	0.693
7	Carbon fibers	Ti5Al5V5Mo1Cr1Fe	7.059/7.939	235.3/264.6	470.6/529.3	98.4	2.95	1.48

Thus, the results of simulation of the stress-strain state indicate the effectiveness of using polymer composite materials Zedex ZX-324VMT and Iglidur TX1, reinforced with carbon fibers, as wear-resistant anti-friction composite materials for the outer cage of the plane bearing. Replacing the steel cage with a cage made of surface-reinforced titanium alloy provides more effective stress relaxation and an increase in the safety factor during modeling.

Calculation of the economic feasibility of replacing steel races of plane bearings with titanium alloys

The calculation of the economic feasibility of introducing titanium alloys into the plane bearing cages will be calculated using the example of a medium-haul aircraft of the Boeing-737 type, which is the most massive and in demand for 2025 for the countries of the European Union.

Plane bearings are used in aircraft everywhere to connect the arms of units to the hull. The purpose of using bearings is to compensate for distortions that may occur during the operation of aircraft under the influence of external forces - they are also used in movable joints, which during operation make oscillatory movements with an amplitude of up to 60 degrees.

Any version of the aircraft uses plane bearings that require maintenance and those that do not require maintenance during the overhaul period. In the presented calculations, it is assumed that all plane bearings that are on the aircraft will be maintenance-free. Since more and more parts and assemblies have recently transferred maintenance to their actual condition, the idea of replacing bearings with maintenance-free ones is relevant.

A feature of the Boeing-737 aircraft families and their modifications is the use of a large range of plane bearings from 6 mm to 35 mm. small diameter plane bearings (up to 12 mm) are used mainly for static objects in aircraft control systems. Medium-diameter plane bearings (up to 20 mm) are used in hydraulic reinforcement systems for control systems and tail units of aircraft. Bearings with diameters up to 35 mm are used in fasteners for landing gear assemblies and power elements of the aircraft. The total number of all bearings is very dependent on the dimensions and modifications of the aircraft and has about 1000 pcs. all options.

For the selected calculation option, we take the average diameter of the bearings equal to 20 mm. Because, for example, a bearing with a diameter of 20 mm weighs 0.1 kg, a bearing with a diameter of 10 mm weighs 0.01 kg, and a bearing with a diameter of 35 mm weighs 0.25 kg. We calculate the weight of bearings from steel cages:

$W_{steel} = 1000*0.1 = 100$ kg.

We determine the weight of the bearing, which is made of titanium alloy. The density for steel is 7.9 g/cm^3, and for titanium alloy - 4.5 g/cm^3. Assuming that the volume of the plane bearing is the same, we have that titanium alloy is 57 % lighter than steel. Then the weight of the bearing with a diameter of 20 mm will be 0.57 kg. We calculate the weight of bearings made of titanium alloys:

$W_{titanium} = 1000*0.57 = 57$ kg.

That is, the weight advantage for an aircraft, provided that a titanium alloy is used, will be 43 kg.

The price of X105CrMo17 stainless steel in the form of a pipe costs from 150 UAH/kg.

The price of titanium alloy Ti5Al5V5Mo1Cr1Fe in the form of a pipe costs from 1200 UAH/kg.

We determine that the price of steel bearings will cost 15 thousand UAH, and the price of titanium bearings will cost 68.4 thousand UAH. The difference in cost is 53.4 thousand UAH or 1335 $ USA.

A Warsaw-Amsterdam ticket for April 2026 will cost about $200 with a flight length of 2 hours for a Boeing-737 aircraft. That is, an hour of flight for a person will cost $100. When calculating aircraft, a person's weight is considered to be 70 kg plus the weight of luggage. If simplified, it can be said that a gain of 43 kg is approximately 50 $ per hour of commercial aircraft flight. That is, the cost of using titanium bearings for the aircraft will be compensated for in the first 27-30 hours of flight.

We believe that the service life of the plane bearing will be about 3000 hours of operation, then we calculate the net profit from the use of races made of titanium alloys will be equal to:

Profit = 2970*50 = 148.5 thousand dollars of profit for the aircraft.

Conclusions

1. A model of the stress-strain state of plane bearings with composite antifriction materials has been developed. It was determined that the composite materials Zedex ZX324VMT and Iglidur TX1 when modeling the stress-strain state reduce the maximum specific stress by 50 % in the material at loads of 3, 100 and 200 kN, compared to metal-polymer tape.

2. Simulation of the stress-strain state of plane bearings with composite antifriction materials has proven a decrease in specific stresses in the surface layers of bearing materials when using titanium alloys Ti5Al5V5Mo1Cr1F instead of X105CrMo17 bearing steel up to 20 %, depending on the material and load conditions.

3. The calculation of the economic feasibility of using titanium alloys for bearings with composite materials established that the benefit is about 150 thousand dollars per aircraft, provided that the plane bearings operate for 3000 hours.

References

1. Additive manufacturing of titanium and its alloys. (2024). In *Titanium alloys* (pp. 263–288). World Scientific. https://doi.org/10.1142/9789811291487_0010 [English]

2. Peters, M. (2005). Titanium alloys for aerospace applications. In M. Peters & C. Leyens (Eds.), *Titanium and titanium alloys* (pp. 333–350). Wiley-VCH. https://doi.org/10.1002/3527602119.ch13 [English]

3. Khimko, A. M. (2025). Analysis of the use and damage of titanium alloy parts in aircraft. In *Eighteenth International Scientific and Practical Conference "Integrated Intelligent Robotic Complexes" (IIRTK-2025), May 20-21, 2025* (pp. 65–68). KAI. [Ukrainian]

4. Mamat, R., Rashid, M. I. M., Syahir, A. Z., Erdiwansyah, Yusop, A. F., & Tamimi, A. (2025). Carbon fibre for applications in aerospace: A review. *Journal of Alloys and Metallurgical Systems*, *12*, Article 100227. [1] https://doi.org/10.1016/j.jalmes.2025.100227 [English]

5. Kralya, V. O. at al. (2010). Defects of steel units of the high-lift devices of aircraft wings caused by fretting corrosion. *Materials Science*, *46*(1), 108–114. https://doi.org/10.1007/s11003-010-9270-8 [English]

6. Khimko M. at al. (2024). Wear resistance of polymer composite materials for spherical bearings. *Problems of Friction and Wear*, *(2)*, 29–42. https://doi.org/10.18372/0370-2197.2(103).18670 [Ukrainian]

7. Khimko, A. M., Khimko, M. S., Popov, O. V., & Klipachenko, V. V. (2025). Estimation of the stress-strain state of composite materials for hinged bearings. *Problems of Friction and Wear*, (1), 4–16. https://doi.org/10.18372/0370-2197.1(106).19819 [Ukrainian]

8. Khimko, A., Mikosianchik, O., Khimko, M., & Filonenko, O. (2025). Wear resistance of contact of titanium alloys with composite materials depending on the technology of their manufacturing under conditions of nominally fixed contact. *Problems of Friction and Wear*, (3), 28–37. https://doi.org/10.18372/0370-2197.3(108).20445 [English]

9. Khimko, A. (2025). The influence of corrosive and aggressive environments on the contact of aluminum and titanium alloys with CFRP under vibration loading conditions. *Problems of Friction and Wear*, (4), 95–104. https://doi.org/10.18372/0370-2197.4(109).20757 [English]

10. Kralya, V. A. at al (2007). Wear resistance of plasma coatings for a constant work of friction. *Strength of Materials*, *39*(5), 523–528. https://doi.org/10.1007/s11223-007-0058-5 [English]

11 Mikosyanchyk, O. O., Pedan, Y., Mnatsakanov, R., Khimko, A., Bohdan, S., & Chava, K. (2023). Analysis of models and methods for assessing the strength characteristics of polymer composite materials. *Problems of Friction and Wear*, *(3)*, 15–29. https://doi.org/10.18372/0370-2197.3(100).17891 [Ukrainian]

12. Khimko, A., Popov, O., & Khimko, M. (2026). Effect of temperature on the wear resistance Ti6Al4V-CFRP/GFRP contact under vibration conditions. *Problems of Friction and Wear*, *(1)*, 4–12. https://doi.org/10.18372/0370-2197.1(110).20915 [English]

13. Khimko, M. at al. (2024). Influence of thermophysical properties of metal-polymer composite materials on wear resistance. *Problems of Friction and Wear, (3),* 91–100. https://doi.org/10.18372/0370-2197.3(104).18984 [Ukrainian]

14. Khimko, A., Mikosyanchyk, O., Khimko, M., & Klipachenko, V. (2026). Increasing the durability of the Ti-GFRP/CFRP contact with a layer of wear-resistant polymer composite coatings under vibration load conditions. *Problems of Tribology*, *31*(2), 16–22. https://doi.org/10.31891/2079-1372-2026-120-2-16-22 [English]

15. Khimko, M., Khimko, A., Mnatsakanov, R., & Mikosyanchyk, O. (2024). Resource testing of modified plain bearings for the aviation industry. *Problems of Tribology*, *29*(2), 16–22. https://doi.org/10.31891/2079-1372-2024-112-2-16-22 [English]

16. Gruppe, B. (2010). *Airbus: Airbus A400M, Airbus A380, Airbus-A320-Familie, Airbus A330, Airbus A340, Airbus A300, Airbus A350, Airbus A310, Christian Streiff*. Books LLC. [English]

17. Kufer, A., Guinaudeau, I., & Premat, C. (2015). AIRBUS / Airbus Group. In *Handwörterbuch der deutsch-französischen Beziehungen* (S. 22–24). Nomos. https://doi.org/10.5771/9783845254012-22 [German]

18. Titanium Development Association. (1995). *Titanium 1995: A statistical review 1983–1995*. [English]

19. Cao, P., & Zhang, L. (2024). *Titanium alloys: Basics and applications*. World Scientific Publishing. https://doi.org/10.1142/9789811291487 [English]

20. Davies, P., John, S., Davies, H., Bache, M., Fox, K., Collins, C., Martin, N., & Sandala, R. (2025). The low-cycle fatigue performance of emerging titanium alloys for aeroengine applications. *Metals*, *15*(11), Article 1274. https://doi.org/10.3390/met15111274 [English]

21. Baker, D. (2022). *Fifth generation fighters: The world's most dangerous combat aircraft*. Morton's Media Group. [English]

22. Schóber, T., Nečas, P., & Puliš, P. (2013). New light fighters from Asia on the global markets. *INCAS Bulletin*, *5*(1), 151–156. https://doi.org/10.13111/2066-8201.2013.5.1.14 [English]

23. Peters, M., Kumpfert, J., Ward, C. H., & Leyens, C. (2003). Titanium alloys for aerospace applications. *Advanced Engineering Materials*, *5*(6), 419-427. https://doi.org/10.1002/adem.200310095 [English]

24. Alieieksieiev, V. (2018, April 12). Flaws and weaknesses of the highly touted Russian Su-35S and Su-30SM. *Narodna armiia*, 19. [Ukrainian]

25. Mate, C. M., & Carpick, R. W. (2019). *Tribology on the small scale: A modern textbook on friction, lubrication, and wear* (2nd ed.). Oxford University Press. [English]

26. Saunders, J. J., Plummer, A. R., & Keogh, P. S. (2020). Friction and wear characteristics of self-lubricating spherical plain bearings. *Tribology International*, *143*, Article 106065. https://doi.org/10.1016/j.triboint.2019.106065 [English]

27. Oppenheim, A. V., Willsky, A. S., & Nawab, S. H. (2022). *Signals and systems* (2nd ed.). Pearson. [English]

28. Ivanov D., & Dolgui A. A (2021) Digital supply chain twin for managing the disruption risks and resilience under conditions of unprecedented demand volatility. *International Journal of Production Research, 59(24),* 7671-7688. https://doi.org/10.1080/00207543.2020.1803531 [English]

29. Luo, L., Zhao, N., Zhu, Y., & Sun, Y. (2023). A* guiding DQN algorithm for automated guided vehicle pathfinding problem of robotic mobile fulfillment systems. *Computers & Industrial Engineering*, *178*, 109112. https://doi.org/10.1016/j.cie.2023.109112 [English]

30. Oevermann, D., Bhagat, R., Fernandes, R., & Wilson, D. (2018b). Quantitative modelling of the erosive removal of a thin soil deposit by impinging liquid jets. *Wear, 422–423,* 27–34. https://doi.org/10.1016/j.wear.2018.12.056 [English]

31. Kamps T. J., Harvey P. S., & Blackwell J. W. (2022) Dynamic evolution and nano-structural adaptation of polymer transfer films on steel counterfaces. *Tribology International, 167*. Art. 107391. https://doi.org/10.1016/j.triboint.2021.107391 [English]

32. Khimko A., Kralya V., Yakobchuk A., Kostuchik V., & Sidorenko A. (2011) Units wearability of aircraft wing lift devices. *Problems of Friction and Wear, 55.* https://doi.org/10.18372/0370-2197.55.3249 [English]

33. Khimko, A., Hrechukha, A., & Khimko, M. (2024). Research of the impact of ambient temperature on the wear resistance of metal-polymer composite materials used in aviation plain bearings. In *Aviation in the XXI-st century: Safety in aviation and space technologies* (pp. 1.3.60–1.3.63). NAU. [English]

34. Tareq M.A. Al-Quraan at al. (2026) Increasing the Wear Resistance of Titanium Alloys in Plain Bearings with Galvanic and Vacuum-Arc Coatings. *Tribology in Industry*, *48(1),* 72-82. https://doi.org/10.24874/ti.2043.10.25.11 [English]

35. Khimko A., Khimko M., Makarenko R., & Tokaruk V. (2026) Effectiveness evaluation of the conversion coatings application on titanium alloys in contact with GFRP under nominally stationary contact conditions. *Problems of friction and wear*. *№ 2 (111).* 31-39. https://doi.org/10.18372/0370-2197.2(111).21334 [English]

Хімко А.М., Хімко М.С., Мікосянчик О.О. Оцінка напружено-деформованого стану авіаційних шарнірних підшипників ковзання на основі титанових сплавів та антифрикційних композитних матеріалів та доцільність їх використання.

У статті представлено аналіз використання титанових сплавів в авіаційній промисловості на літаках нового покоління та оцінена можливість застосування титану для шарнірних підшипників з антифрикційними композитними матеріалами. Представлено аналіз антифрикційних композиційних матеріалів для авіаційної промисловості із підвищеними фізико-механічними характеристиками. Метою роботи було розробка моделі шарнірних підшипників із полімерними композиційними матеріалами та аналіз економічної доцільності використання титанових сплавів в таких підшипниках ковзання в повітряних суднах. Наведено аналітичну оцінку використання титану в сферичних підшипниках. Розроблено модель напружено-деформованого стану сферичних підшипників з композиційними антифрикційними матеріалами. Визначено, що композиційні матеріали Zedex ZX324VMT та Iglidur TX1 при моделюванні напружено-деформованого стану знижують максимальні питомі напруження в матеріалі на 50 % при навантаженнях 3, 100 та 200 кН, порівняно з базовим підшипником на сталі. Моделювання напружено-деформованого стану шарнірних підшипників ковзання з композиційними антифрикційними матеріалами довело зниження питомих напружень у поверхневих шарах матеріалів при використанні титанових сплавів Ti5Al5V5Mo1Cr1Fe замість підшипникової сталі X105CrMo17 до 20 %, залежно від матеріалу та умов навантаження. Було проведено економічні розрахунки використання шарнірних підшипників ковзання з титанових сплавів для літаків. Визначено, що застосування шарнірних підшипників протягом 3000 годин під час експлуатації повітряного судна економічна вигода становить близько 150 тисяч доларів на один літак. Також представлено, що модифіковані необслуговувані підшипники з композитними матеріалами дозволяють наблизити експлуатацію деяких вузлів повітряних суден до обслуговування за фактичним станом за рахунок зниження витрат на технічне обслуговування.

Ключові слова: титанові сплави, шарнірні підшипники, зносостійкість, напружено-деформований стан, композиційні покриття, економічні розрахунки.

ISSN 2079-1372 Problems of Tribology, V. 31, No 3/121-2026, 89-96

Problems of Tribology
Website: http://tribology.khnu.km.ua/index.php/ProbTrib
E-mail: tribosenator@gmail.com

DOI: https://doi.org/10.31891/2079-1372-2026-121-3-89-96

Analysis of modern methods for reducing welding residual stresses

D.V. Bakalets 0000-0003-1528-2066, **V.V. Polishchuk** 0009-0000-0293-8711

[1] *Vinnytsia National Technical University, Ukraine*
E-mail: BacaletsDima@gmail.com

Received: 20 July 2026: Revised 28 August 2026: Accept: 10 September 2026

Abstract

This paper presents a systematic comparative analysis of the physical mechanisms governing internal stress generation in structural weldments, evaluates the efficiency of existing stress relaxation techniques, and provides scientific substantiation for promising dynamic approaches aimed at extending the operational life of welded structures. The research methodology is based on the synthesis of thermomechanical models of the welding thermo-deformation cycle, dislocation concepts of micro-plastic metal flow, and an analytical comparison of thermal, mechanical deformation, and vibratory technologies according to stress relief depth, energy demand, and structural degradation risks. It was established that conventional post-weld tempering of creep-resistant alloy steels under prolonged holding leads to the dissolution of strengthening nano-carbides and their boundary coagulation, resulting in a 4 – 5-fold reduction in long-term creep resistance. Surface plastic deformation methods, such as weld rolling and ultrasonic impact treatment, induce beneficial compressive stresses but remain restricted to a shallow depth of 1.5–2.0 mm or require extreme contact loads, whereas standard electromechanical vibration treatment with monochromatic excitation proves ineffective for thick-walled, high-rigidity structures with natural frequencies exceeding 200 Hz. Consequently, the transition toward dynamic pulse excitation is substantiated, as it generates shock deformation waves with steep-fronted rise times, excites higher-order spatial poly-harmonics, refines primary solidification dendrites by 25–32%, and relieves peak macro-stresses by 60 – 80%. The scientific novelty lies in determining the physical regularities of multi-mode dynamic stress relaxation within welded concentration zones through non-linear wave processes and intensified dislocation mobility without prolonged resonant structural overloading. The practical significance of the obtained results enables the justified selection of resource-saving stress relief technologies for heavy-duty and thick-walled fabrications, eliminating expensive furnace annealing while minimizing dimensional distortion.

Keywords: welding residual stresses, thermo-deformation cycle, vibratory stabilization, dislocation mobility, shock-wave effect.

Introduction

The presence of high tensile residual macrostresses (Type I), whose magnitude in welded joints frequently approaches or exceeds the standard yield strength of the parent metal [1, 3, 5, 18, 21], significantly impairs structural performance. In combination with operational cyclic loads and geometric seam stress concentrators, they act as the driving force for the initiation and accelerated growth of fatigue cracks [7, 9, 21], induce loss of dimensional precision and distortion during machining or initial service loading [1, 10, 22], and trigger stress-corrosion cracking in aggressive working environments [16, 21]. This problem is particularly critical in thick-walled welded structures and tubular components [10, 15], where inherent welding stresses are superimposed onto technological stresses from prior forming, creating a complex bi-axial or tri-axial stress state and an elevated risk of premature failure [1, 18, 19].

Analysis of recent research and publications

Ensuring the operational reliability, cyclic fatigue life, and geometric stability of welded metal structures necessitates the mandatory implementation of technological measures aimed at reducing or redistributing residual welding stresses [1, 10, 11, 21, 22]. Depending on the execution stage and the underlying physical mechanisms, all methods for mitigating the internal stress-strain state (SSS) are classified into thermal, mechanical

Copyright © 2026 D.V. Bakalets, V.V. Polishchuk. This is an open access article distributed under the Creative Commons Attribution License, which permits unrestricted use, distribution, and reproduction in any medium, provided the original work is properly cited.

(deformation), vibrational, and combined multi-physical technologies [11, 22, 27]. The most conventional and standardized method for residual stress relief remains post-weld heat treatment (PWHT), primarily global or localized high tempering and annealing [11, 13, 18, 21, 22]. In this process, the structural assembly is heated to temperatures of 600 – 700 °C (governed by the steel alloy composition, such as 670 – 690 °C for 12% Cr creep-resistant steel), soaked for a specified design duration (1–3 hours or longer), and subsequently cooled at a controlled slow rate [11, 13]. As the temperature increases, the yield strength of the material (σ_T) decreases drastically, and the peak residual stresses, upon exceeding this thermally reduced threshold, relax via localized macro- and micro-plastic deformation mechanisms [1, 18]. Experimental and theoretical studies demonstrate that over 70 – 80% of stress relaxation occurs during the heating stage and within the initial 1 – 2 hours of isothermal soaking; further extension of holding time yields virtually no additional reduction in the final level of macroscopic residual stresses [21].

When applying thermal methods, an engineering compromise between material toughness and creep rupture strength must be attained, as thermal activation stabilizes the microstructure via the precipitation of *MX(V, Nb)(C, N)*, carbonitrides that pin mobile dislocations through the Orowan strengthening mechanism [17, 24]. However, excessive thermal holding periods (exceeding 32 hours) trigger carbide coarsening via Ostwald ripening, characterized by the agglomeration of $M_{23}C_6$ boundary particles up to 100 – 500 nm and the simultaneous dissolution of fine intragranular strengthening nanocarbides (see Fig. 1) [24]. This degradation induces significant matrix softening and deteriorates long-term creep rupture strength despite maintaining impact toughness [24]. Within an optimal soaking range of 8–16 hours, finely dispersed MX precipitates establish formidable barriers against dislocation creep; conversely, extending heat treatment past 32 hours results in the near-total depletion of fine intragranular precipitates and the breakdown of subgrain dislocation networks [24]. Consequently, Orowan threshold stresses decrease, precipitating a 4 – 5-fold reduction in time-to-rupture under elevated-temperature service conditions [24].

Multi-pass weldments also exhibit thermal stability inversions: in the as-welded condition, interpass HAZ regions remain softer due to secondary austenitization [17, 24], whereas prolonged thermal exposure (exceeding 12 hours) reverses this relationship, rendering the HAZ more creep-resistant than the weld center owing to its refined prior austenite grain size and stabilized carbide distribution [24]. Significant industrial drawbacks of thermal treatment include: severe energy consumption and protracted production schedules reaching 8 – 12 hours [11, 13, 18, 21, 22]; surface oxidation scale demanding abrasive grit-blasting that reintroduces harmful superficial tensile stresses [11]; thermal distortion and geometric buckling of asymmetric or thin-walled assemblies caused by unconstrained thermal expansion [3, 11]; furnace dimensional constraints preventing the processing of large vessels, pipelines, and skeletal frames [2, 4, 8]; and detrimental carbon diffusion causing decarburization layers across dissimilar steel weld interfaces [11].

Mechanical post-weld mitigation techniques rely on the artificial generation of tensile plastic strains across the weld metal and the heat-affected zone to counteract the longitudinal shrinkage force F_{yc} [13, 22, 25]:

– static loading (stretching, bending): Executed by applying global external tensile forces to the welded assembly before or immediately after joint completion [1, 13, 22], which reduces residual peak tensile stresses in the active zone while generating favorable compressive fields near geometric notches [1, 10]; however, this approach requires massive, high-tonnage pressing fixtures, fundamentally limiting its applicability for complex 3D structures [22];

– weld rolling: Involves localized plastic compressive deformation of the weld crown or adjacent HAZ utilizing cylindrical or contoured rollers [9, 11]. Introducing through-thickness compressive deformations of fractions of a percent flattens the longitudinal residual stress profile, neutralizing peak tensile zones or shifting them into compression [9, 11]. Key limitations include the requirement for excessive contact loads up to 150 – 200 kN for plate thicknesses exceeding 10 – 12 mm, risks of localized over-rolling accompanied by reverse distortion, an associated 15 – 20% reduction in bend ductility, and physical tool-access constraints along curved weld paths [10, 12, 13, 24]. Direct weld-crest rolling with a profiled roller induces compressive stresses within the weld core and eliminates plate angular distortion at lower loads of 25 – 50 kN, whereas side-rolling the HAZ with flat dual rollers exhibits inferior efficiency due to high transverse alignment sensitivity (see Fig. 2) [25];

– peening and high-velocity impact deformation: Interpass or post-weld percussive hammering of the cooling weld deposit using pneumatic strikers at impact velocities of 6 – 7 m/s to 25 – 30 m/s induces planar flattening strains that convert residual tension into compression [2, 3]; nonetheless, it provokes superficial strain-hardening, exhausts local dislocation plasticity, and demands rigorous calibration of the specific impact energy (a/δ) to prevent cold embrittlement and a 15 – 20% drop in bend angles [26];

– explosive and magnetic pulse treatment: utilizing contact strip explosive charges or pulsed electromagnetic drivers propagates an elastoplastic shock wave through the joint, attenuating peak stresses and elevating cyclic endurance [2, 4]. Wider industrial adoption is hampered by strict explosion safety regulations, detonation chamber requirements, and inferior technological flexibility [2, 4];

– ultrasonic impact treatment: transmitting high-frequency acoustic oscillations coupled with mechanical needle impact (frequencies above 20 kHz) eliminates up to 80 – 100% of residual tensile stresses in the superficial layer (depths up to 1.5 – 2.0 mm) while enhancing fatigue durability [11, 21, 22]; its main drawbacks are the shallow treatment depth, restricted acoustic source power, and prohibitive labor intensity for heavy, multi-pass structures [2, 4, 22].

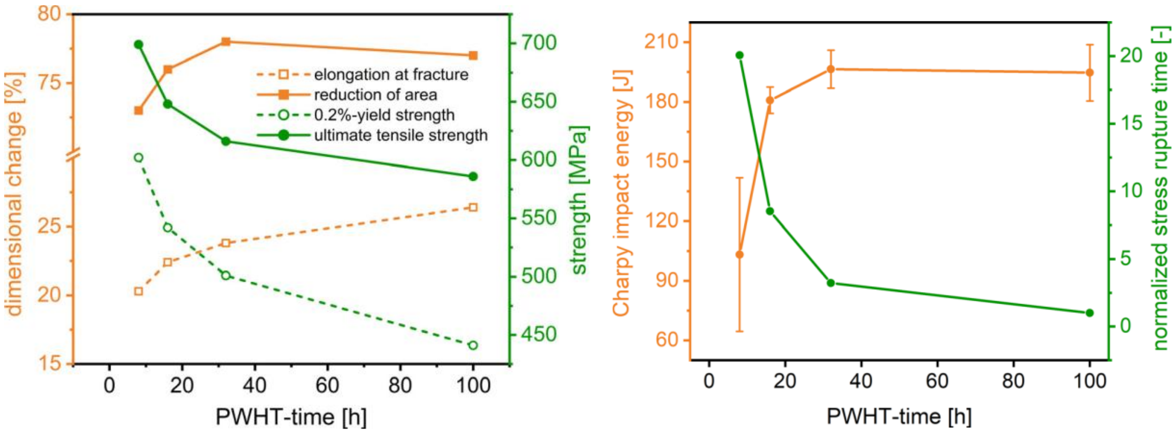

a) *b)*

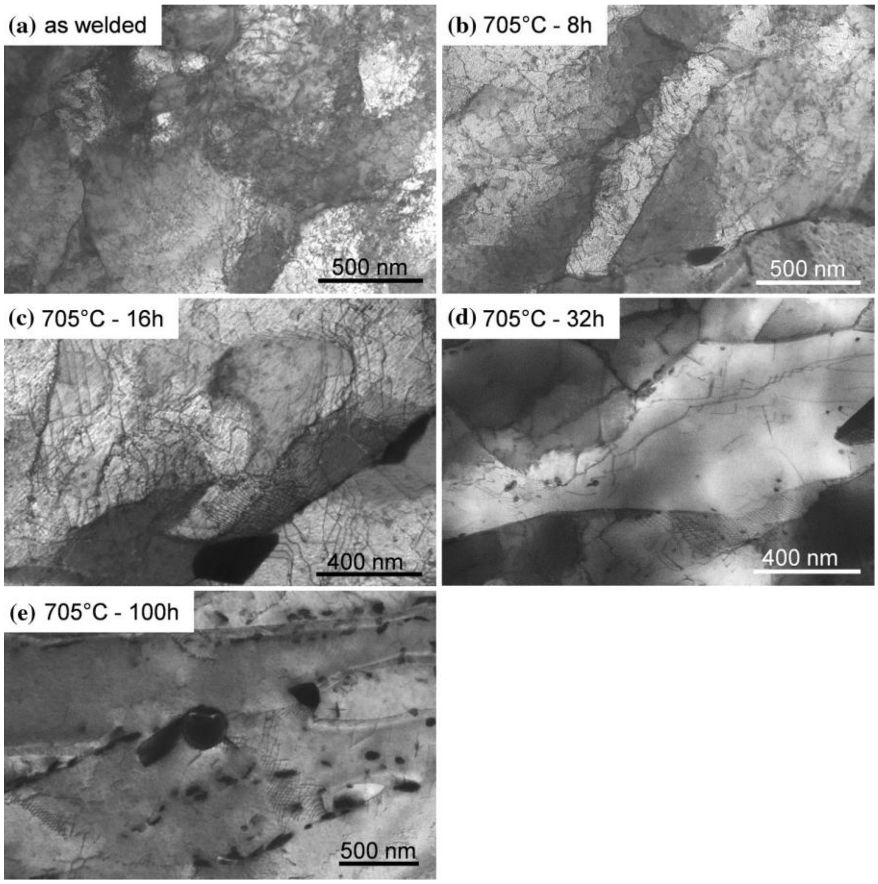

c)

Fig. 1. The effect of the duration of post-weld heat treatment (at 705 °C) on the microstructure and complex of mechanical properties of the weld metal of 2.25Cr-1Mo-0.25V steel: a) change in strength and plastic characteristics depending on the holding time; b) comparative dynamics of impact toughness and long-term creep; c) STEM micrographs of the evolution of the dislocation structure and size of MX carbidonitriles

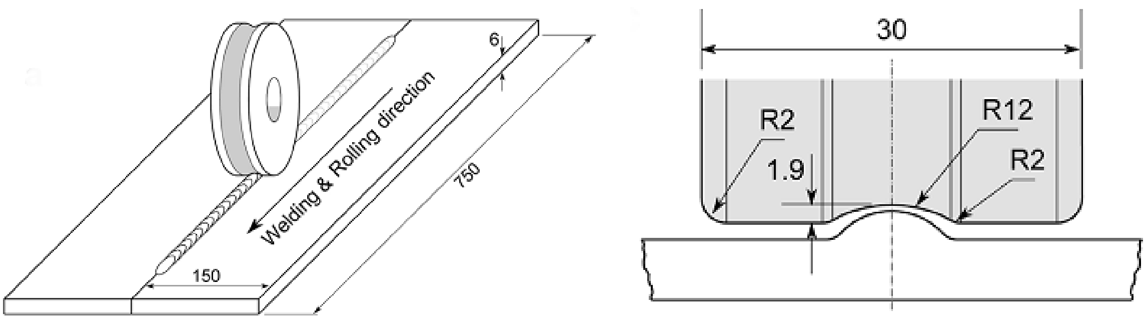

a)

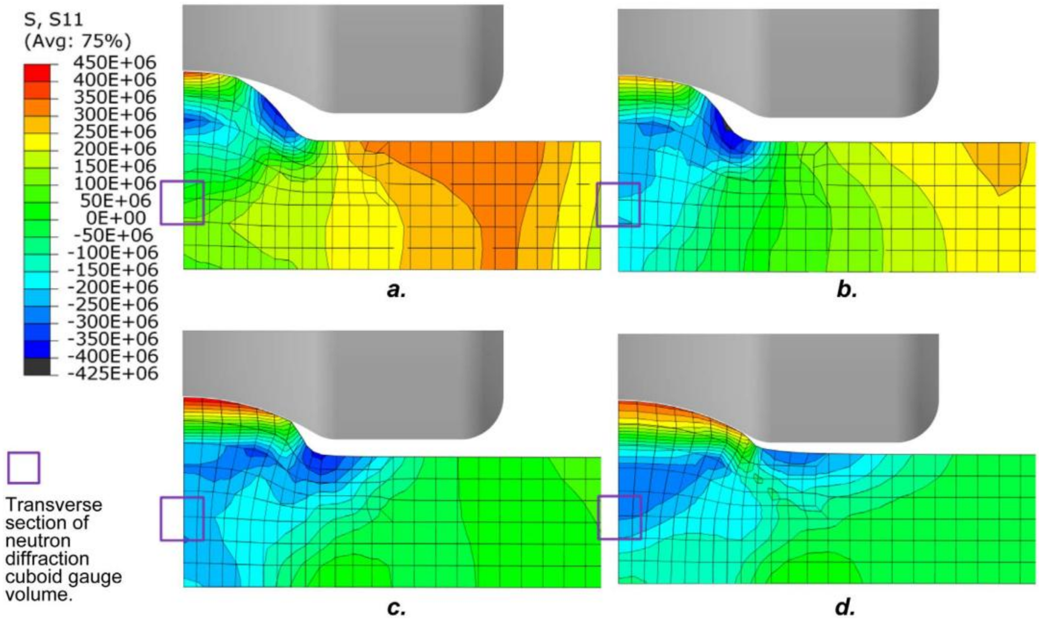

b)

Fig. 2. Rolling of a welded seam with a profile roller [25]: *a*) – three-dimensional diagram of the position of the roller on the seam and geometric parameters of the profile roller; b) – 2D maps of the distribution of longitudinal stresses σ_x in the seam zone at different loads (25, 50, 100, 150 kN)

Vibratory Stress Relief (VSR) serves as an economically viable, energy-efficient alternative to conventional furnace annealing [10, 11, 20, 22] and branches into two fundamental operational strategies:

1. Post-weld vibratory stress relief: the finished component is mounted on elastomeric isolators, and an eccentric unbalance exciter drives it at structural resonant frequencies [11]. Cyclic dynamic stresses σvib superimpose onto existing internal residual stresses σres [11, 14]. In peak tension zones, the microyielding threshold is surpassed:

$$\sigma_{res} + \sigma_{vib} \geq \sigma_T^{cyc}, \quad (1)$$

which triggers dislocation glide, microplastic relaxation, and elastic strain energy dissipation [11, 22]. Macroscopic residual stresses of Type I decrease by 50–60%, and intergranular stresses of Type II decrease by 40 –45%, establishing dimensional stabilization while cutting energy consumption by a factor of 40 – 50 and process time by a factor of 15 – 20 relative to furnace heating [11, 22];

2. Vibration during welding: introducing low-frequency dynamic oscillations (f = 50...150 Hz, A = 0.5–2.0 mm) directly during arc execution and pool solidification mechanically breaks developing columnar dendrites, refining the microstructure by 25 – 32%, accelerating hydrogen degassing, reducing pore formation, and mitigating cold and hot cracking susceptibility [11, 16, 18]. As-welded residual stresses are lowered by 16 – 25% (and up to 2 – 2.5 times in localized zones), eliminating the requirement for energy-intensive preheating in hardenable structural steels [11, 16].

Advanced combined multi-physical technologies also encompass: thermo-vibrational treatment (combining mild heating to 140 – 210 °C with resonant vibrations, lowering peak stresses by 46 – 50% within 1–2 hours) [22, 23]; magneto-vibrational processing (superimposing a 0.5 – 2.0 T magnetic field to induce the magnetoplastic effect, achieving a 40 – 60% stress drop) [22]; and pulsed electro-treatment (short current impulses of 103...104 A/mm2 exerting an "electron wind" force that relaxes microscopic lattice strains within fractions of a second) [22].

Accurate monitoring and characterization of residual welding stress distributions rely on measuring elastic or released strains, followed by stress recalculation using Hooke's constitutive law [6, 26]. These evaluation techniques are structured into destructive, semi-destructive, and non-destructive categories [6, 22, 26]:

– Hole-drilling method (ASTM E837): employs a 3- or 6-element strain gauge rosette coupled with high-speed precision drilling of a hole (Ø1.5–2.0 mm, depth 1.0 – 2.0 mm) [6, 26]. This technique is accurate for stresses within 50–60% of σ_T; higher magnitudes induce localized plastic yield around the hole boundary, distorting measurement linearity [6, 26];

– Deep hole drilling (DHD): designed for heavy cross-sections up to 100 mm, involving the precision drilling of a reference hole through the component thickness, followed by coaxial core trepanning and diameter change mapping to resolve full-depth stress profiles [26];

– Contour method (CM): involves sectioning the welded part via wire electrical discharge machining (WEDM) along the plane of interest, scanning surface de-planing contours on a coordinate measuring machine, and feeding these displacement deviations as boundary conditions into a finite element model to construct full 2D cross-sectional normal stress maps [26];

Diffraction non-destructive methods: utilize atomic lattice plane spacings (d_{hkl}) as internal strain sensors governed by Bragg's law [18, 22, 26]:

$$n\lambda = 2d_{hkl} \sin\theta \ , \tag{2}$$

where represents λ the radiation wavelength, and θ is the Bragg diffraction angle [26].

X-ray diffraction (XRD) guarantees precision when resolving biaxial stress components ($\sin^2\varphi$) in superficial layers restricted to 10 – 30 µm [15, 26]. Neutron diffraction (ND), capitalizing on the neutral charge of thermal neutrons and their superior nuclear penetration, evaluates the full triaxial stress tensor (σ_x, σ_y, σ_z) non-destructively at depths reaching 50 mm in structural steels and 100 mm in aluminum alloys [13, 24, 26].

Aims of the article

Systematic comparative analysis of the physical mechanisms governing internal stress generation in structural weldments, evaluation of existing relaxation techniques, and scientific justification of advanced dynamic approaches based on non-linear hydraulic pulse excitation to enhance the operational durability of welded assemblies.

Methods

The study synthesizes thermomechanical and dislocation models of the welding thermo-deformation cycle, micro-plastic metal flow mechanics, multi-criteria analytical benchmarking of thermal, mechanical, and vibratory stress relief methods based on relaxation depth, energy consumption, and structural degradation risks, as well as the principles of fluid transient wave dynamics and non-linear pressure pulse generation.

Results

Among existing approaches for the dynamic regulation of weldment stress-strain states, introducing mechanical oscillations directly during arc burning and weld pool solidification represents the most technologically expedient method [10, 11, 28]. Low-frequency vibrations excite shear waves in the liquid melt and mushy zone [11, 28], inducing intense hydrodynamic mixing, dendrite fragmentation, and heterogeneous nucleation [11, 28]. This transforms coarse columnar grains into a refined equiaxed microstructure (decreasing average grain area by 25 – 32%), promotes hydrogen desorption, and reduces residual stresses by 16 – 25% relative to rigidly clamped welding [11, 16, 28]. Operational parameters center on a frequency bandwidth of 50 – 150 Hz (corresponding to the secondary structural resonance mode with peak shear at the joint) [26] and vibration amplitudes of 0.5 – 1.0 mm [11, 28]. Exceeding an amplitude of 1.2 – 1.5 mm is unacceptable due to molten pool spatter, shielding gas disruption, and solidification cracking [11, 16].

In industrial practice, vibration treatment is conventionally performed using electromechanical unbalance exciters [11, 20, 22], which possess severe physical drawbacks:

– Monochromatic harmonic waveform: sinusoidal oscillations transfer energy exclusively at a single resonant mode, requiring prolonged run times (15 – 45 min) and risking localized cyclic fatigue damage at vibration nodes [11, 22];

– Stiffness limitations: for heavy, thick-walled, or box-type weldments, fundamental natural frequencies exceed 200 – 400 Hz, where mechanical unbalance motors cannot generate the requisite dynamic excitation forces [20, 22];

– Operational reliability issues: unbalance shaft bearing assemblies experience premature mechanical failure under sustained, severe centrifugal loading [11, 12].

For massive 3D welded components, sinusoidal forces prove insufficient to overcome the Peierls-Nabarro barrier and unlock pinned dislocation tangles without inducing fatigue [11, 22]. They generate monochromatic sinusoidal oscillations, transmitting energy exclusively at a single resonant mode; this requires long operating durations (15 – 45 min) and risks inducing localized fatigue degradation at vibration nodes [11, 22]. Furthermore, in massive, tubular, or high-rigidity box-shaped weldments, fundamental natural frequencies exceed 200 – 400 Hz, where mechanical unbalance motors cannot produce the required dynamic force amplitudes due to bearing load failures caused by excessive centrifugal forces [20, 22]. Consequently, despite considerable research efforts, the issues of effective force action on rigid, large-scale structures utilizing poly-frequency non-linear impulses remain insufficiently explored, substantiating the necessity for developing novel dynamic methods and drives.

A promising scientific direction is the implementation of hydraulic pulse drives [27–33], which convert high-pressure fluid flow into periodic, steep-fronted shock pressure pulses, fundamentally transforming dynamic process capabilities [27 – 33]:

1. Generation of steep vibro-impact fronts: unlike smooth sinusoidal inputs, pressure pulses exhibit near-instantaneous rise times ($\Delta t \rightarrow 0$) transmitting high-amplitude shock deformation waves directly into the workpiece [27–33];

2. Poly-frequency excitation spectrum: the non-linear impulse profile simultaneously excites higher spatial harmonics, relieving low-frequency structural bending modes as well as high-frequency plate and stiffener vibrations [27 – 33];

3. Energy localization at stress peaks: high impact acceleration gradients cause localized stresses to exceed the dynamic yield point specifically within stress concentrations (HAZ, fusion boundaries), initiating dislocation mobility and annihilation without global fatigue overloading [27 – 33];

4. Superior force density: hydraulic pulse systems generate dynamic working forces spanning tens to hundreds of kilonewtons while maintaining compact modular exciter dimensions [27 – 33].

Conclusions

Based on the analysis of the current state of the art regarding the nature of residual welding stress formation, measurement methods, and stress-strain state (SSS) mitigation technologies, the following conclusions can be drawn:

1. Residual welding macrostresses (Type I) reach the yield strength of the parent metal and serve as the primary factor reducing cyclic fatigue life, promoting stress-corrosion cracking, and inducing geometric distortion in welded assemblies [1, 3, 7, 21].

2. Conventional post-weld heat treatment (PWHT) provides deep stress relaxation, but it is characterized by high energy consumption, prolonged cycle durations, surface scaling, thermal warping, and limited applicability to large-scale or field-assembled structures [11, 21, 22, 28]. Furthermore, prolonged holding times during PWHT in creep-resistant alloy steels induce the coarsening of strengthening nano-carbides and $M_{23}C_6$ precipitates, resulting in a severe degradation of long-term creep rupture strength [24].

3. In-process mechanical and vibration treatment methods applied directly during welding enable the refinement of the primary as-cast dendritic structure, lower final residual stresses, and partially eliminate energy-intensive preheating [11, 16, 28]. However, conventional electromechanical unbalance exciters generate purely harmonic oscillations, possess restricted force capacity, and prove ineffective for high-rigidity, thick-walled structures featuring high natural frequencies [11, 20, 22].

4. A promising scientific and engineering direction is the transition toward hydraulic pulse drives capable of generating high-power, non-linear vibro-impact pressure waves with steep-fronted rise times. This ensures the excitation of a broad poly-frequency oscillation spectrum, local dislocation un-pinning within stress concentration zones, and effective peak stress relaxation with minimal energy expenditure [22, 27–33].

References

1. Lobanov, L. M., Yermolaiev, H. V., & Kvasnytskyi, V. V. (2016). *Stresses and deformations in welding and brazing*. NUK.
2. State Standard of Ukraine. (1994). *DSTU 2825-94. Strength calculations and tests: Terms and definitions of basic concepts*.
3. Hosford, W. F. (2005). Residual stresses. In *Mechanical behavior of materials* (pp. 308–321). Cambridge University Press. https://doi.org/10.1017/CBO9780511810947.019
4. Totten, G. E. (Ed.). (2002). *Handbook of residual stress and deformation of steel*. ASM International.
5. Cary, H. B., & Helzer, S. C. (2005). *Modern welding technology*. Pearson Education.
6. Schajer, G. S. (Ed.). (2013). *Practical residual stress measurement methods*. Wiley. https://doi.org/10.1002/9781118402832
7. Watanabe, O., Matsumoto, S., Nakano, Y., & Saito, Y. (1995). Fatigue strength of welded joint of high strength steel and its controlling factor: Effects of stress concentration factor and welding residual stress. *Quarterly Journal of the Japan Welding Society, 13*(3), 438–443. https://doi.org/10.2207/qjjws.13.438
8. Ota, A., Shiga, C., Maeda, Y., Suzuki, N., Watanabe, O., Kubo, T., et al. (2000). Fatigue strength improvement of box-welded joints using low transformation temperature welding material. *Welding International, 14*(10), 801–805. https://doi.org/10.1080/09507110009549271
9. Fricke, W. (2005). Effects of residual stresses on the fatigue behaviour of welded steel structures. *Materials Science and Engineering Technology, 36*(11), 642–649. https://doi.org/10.1002/mawe.200500933
10. Savkin, S. V. (2021). *Development of calculation methods and improvement of resource-saving technology for the production of welded pipes using vibration* [Doctoral dissertation, National Metallurgical Academy of Ukraine].
11. Lashchenko, G. I. (2016). Technological capabilities of vibration treatment of welded structures (Review). *The Paton Welding Journal*, (7), 26–31. https://doi.org/10.15407/tpwj2016.07.05
12. Bi, T., Deng, D., Liu, X., & Tong, Y. (2015). Investigation of influence of solid state phase transformation on welding residual stress in P91 steel joint. *Transactions of the China Welding Institution, 36*(9), 55–59.

13. Luo, Y., Deng, D., & Jiang, X. (2006). Prediction of welding residual stress in 2.25Cr-1Mo steel pipe. *Journal of Shanghai Jiaotong University (Science), 11*(1), 77–83. https://doi.org/10.1007/BF02831742
14. Liu, X., Jiang, X., Deng, D., Tong, Y., & Bi, T. (2013). Investigation of influence of phase transformation on welding residual stress in P91 steel. In *Proceedings of WSE2013* (2 pp.).
15. Hempel, N., Nitschke-Pagel, T., & Dilger, K. (2014). Residual stresses in multi-pass butt-welded tubular joints. *Advanced Materials Research, 996*, 488–493. https://doi.org/10.4028/www.scientific.net/AMR.996.488
16. Martyniuk, R. T. (2025). Main defects of welded joints. *Oil and Gas Energetics, 1*(43), 109–116. https://doi.org/10.31471/1993-9868-2025-1(43)-109-116
17. Olson, D. L., Siewert, T. A., Liu, S., & Edwards, G. R. (Eds.). (1993). *ASM handbook: Vol. 6. Welding, brazing, and soldering*. ASM International.
18. Prokhorenko, V. V., & Prokhorenko, O. V. (2009). *Stresses and deformations in welded joints and structures*. NTUU "KPI".
19. Kvasnytskyi, V. V., Yehorov, H. V., Yermolaiev, H. V., & Matviienko, M. V. (2019). *Strength of welded and brazed joints* (L. M. Lobanov, Ed.). NUK.
20. Kelso, T. (1968). Stress relief by vibration. *Tool and Manufacturing Engineer, 61*(3), 48–51.
21. Falodun, O., Oke, S., & Bodunrin, M. (2025). A comprehensive review of residual stresses in carbon steel welding: Formation mechanisms, mitigation strategies, and advanced post-weld heat treatment techniques. *The International Journal of Advanced Manufacturing Technology, 136*, 4107–4140. https://doi.org/10.1007/s00170-025-15088-8
22. Hu, S., & Huang, G. (2026). Residual stress relief in metallic materials: Traditional methods, emerging techniques, and multi-field synergies. *Materials, 19*(12), 2431. https://doi.org/10.3390/ma19122431
23. Chen, S.-G., Zhang, Y.-D., Wu, Q., Gao, H.-J., & Yan, D.-Y. (2019). Residual stress relief for 2219 aluminum alloy weldments: A comparative study on three stress relief methods. *Metals, 9*(4), 419. https://doi.org/10.3390/met9040419
24. Schönmaier, H., Fleißner-Rieger, C., Krein, R., Schmitz-Niederau, M., & Schnitzer, R. (2021). On the impact of post weld heat treatment on the microstructure and mechanical properties of creep resistant 2.25Cr-1Mo-0.25V weld metal. *Journal of Materials Science, 56*, 20208–20223. https://doi.org/10.1007/s10853-021-06618-2
25. Cozzolino, L. D., Coules, H. E., Colegrove, P. A., & Wen, S. (2017). Investigation of post-weld rolling methods to reduce residual stress and distortion. *Journal of Materials Processing Technology, 247*, 243–256. https://doi.org/10.1016/j.jmatprotec.2017.04.018
26. Paradowska, A. M., Price, J. W. H., & Finlayson, T. R. (2008). Efficient use of available techniques to measure residual stresses in welded components. In *International Workshop on Thermal Forming and Welding Distortion (IWOTE08)* (pp. 1–12). Bremen, Germany.
27. Iskovych-Lototskyi, R. D. (2006). *Fundamentals of the theory of calculation and development of processes and equipment for vibro-impact pressing*. Universum-Vinnytsia.
28. Iskovych-Lototskyi, R. D., Obertiukh, R. R., & Arkhypchuk, M. R. (2008). *Pressure pulse generators for controlling hydraulic pulse drives of vibration and vibro-impact technological machines*. Universum-Vinnytsia.
29. Obertiukh, R. R., & Slabkyi, A. V. (2015). *Devices for vibration turning based on a hydraulic pulse drive*. VNTU.
30. Iskovych-Lototskyi, R. D., Obertiukh, R. R., & Sevostianov, I. V. (2006). *Processes and machines of vibration and vibro-impact technologies*. Universum-Vinnytsia.
31. Iskovych-Lototskyi, R. D., Obertiukh, R. R., & Polishchuk, O. V. (2013). *The use of hydraulic pulse drive in processing equipment*. VNTU.
32. Virnyk, M. M., Iskovych-Lototskyi, R. D., & Veselovska, N. R. (2007). *Vibration and vibro-impact processes and machines in foundry production*. Universum-Vinnytsia.
33. Sevostianov, I. V. (2020). *Technology and equipment for vibro-impact dewatering of wet dispersed materials*. VNAU.

Бакалець Д.В., Поліщук В.В. Аналіз сучасних методів зниження залишкових зварювальних напружень.

У роботі проведено системний порівняльний аналіз фізичних закономірностей зародження внутрішніх напружень у металоконструкціях, оцінено ефективність існуючих способів їх релаксації та науково обґрунтовано перспективні динамічні підходи для підвищення експлуатаційного ресурсу зварних виробів. Методологія дослідження ґрунтується на узагальненні термомеханічних моделей зварювального термодеформаційного циклу, дислокаційних концепціях пластичної течії металів, а також на аналітичному зіставленні термічних, деформаційних та вібраційних технологій за критеріями глибини зняття напружень, енерговитрат і ризику структурної деградації матеріалу. Встановлено, що традиційний післязварювальний відпуск теплостійких легованих сталей за тривалої витримки спричиняє розчинення нанорозмірних зміцнюючих карбідів та їх коагуляцію на межах зерен, знижуючи опір тривалій повзучості у 4 – 5 разів. Механічні методи поверхневого пластичного деформування (прокатка, ультразвуковий наклеп), попри ефективне створення стискальних напружень, обмежені глибиною дії 1,5 – 2,0 мм або вимагають надмірних контактних зусиль, тоді як стандартна електромеханічна віброобробка монохроматичної дії виявляється малоефективною для товстостінних і жорстких оболонок із частотами понад 200 Гц. З огляду на це обґрунтовано доцільність переходу до динамічного імпульсного збудження, яке формує ударні хвилі деформації з крутим фронтом наростання навантаження, збуджує спектр просторових полігармонік, подрібнює первинні дендрити кристалізації на 25 – 32% і забезпечує релаксацію пікових макронапружень на 60 – 80%. Наукова новизна полягає у встановленні фізичних закономірностей багатомодового динамічного розвантаження зон концентрації зварювальних напружень шляхом активації нелінійних хвильових процесів та інтенсифікації дислокаційного руху без тривалого резонансного перевантаження металу. Отримані результати комплексного аналізу мають практичну значимість, оскільки дозволяють обґрунтовано обирати ресурсозберігаючі технології зняття напружень для великогабаритних та товстостінних конструкцій, виключаючи дорогий пічний відпал і мінімізуючи залишкове короблення.

Ключові слова: залишкові зварювальні напруження, термодеформаційний цикл, вібраційна стабілізація, рухливість дислокацій, ударно-хвильова дія.

ISSN 2079-1372 Problems of Tribology, V. 31, No 3/121-2026, 97-108

Problems of Tribology
Website: http://tribology.khnu.km.ua/index.php/ProbTrib
E-mail: tribosenator@gmail.com

DOI: https://doi.org/10.31891/2079-1372-2026-121-3-97-108

Optimization of the composition of the composite material of contact inserts for electric vehicles based on the criterion of wear resistance

O.V. Dykha* 0000-0003-3020-9625, **O.S. Kovtun** 0009-0000-6036-6723, **V.O. Dytyniuk** 0000-0001-6377-524X, **S.F. Posonskiy** 0000-0002-4697-7699

[1]*Khmelnytskyi national University, Ukraine*
**E-mail: tribosenator@gmail.com*

Received: 05 August 2026: Revised 05 September 2026: Accept: 14 September 2026

Abstract

The paper considers the problem of reusing spent graphite contact inserts of electric transport and improving their functional properties by modifying the composition of the composite material. Modern approaches to the formation of graphite and copper-graphite electrical contact composites, the influence of the granulometric composition, conductive and solid lubricating additives on the electrical and tribological characteristics are analyzed. The prospects for using secondary graphite as the main raw material are shown, provided that the structural integrity and electrically conductive contacts between particles are restored. The feasibility of using carbon black to form an additional conductive network, copper powder to reduce contact resistance, and molybdenum disulfide to stabilize friction and reduce wear is substantiated. It has been established that the properties of such composites are multifactorial and nonlinear in nature, therefore the choice of composition requires comprehensive optimization with simultaneous consideration of the electrical resistance, wear resistance of the insert, and the effect on the contact wire.
Keywords: secondary graphite, contact insert, copper powder, carbon black, molybdenum disulfide, electrical conductivity, wear resistance.

Introduction

The use of secondary graphite material for the manufacture of contact inserts is accompanied by a decrease in electrical conductivity and wear resistance, which is due to the violation of the material structure and increased porosity. In this regard, the task of optimizing the composition of the restorative composition arises by introducing functional additives and adjusting the structural parameters of the material. A feature of this task is the multi-criteria nature of assessing the effectiveness of the material, since it is necessary to simultaneously ensure high electrical conductivity and wear resistance of the contact insert and minimal wear of the contact wire. The purpose of this section is to establish the optimal composition of the composite material based on secondary graphite using methods of mathematical experimental design and construction of a quadratic regression model.

Literature review

One of the closest to the topic of reuse of current-collecting materials is the study [1], which shows the principle possibility of returning spent carbon raw materials to the production cycle. For the manufacture of traction brushes, secondary carbon and copper components with a polymer binder were used and the material was formed by hot pressing. For individual compositions, performance characteristics comparable or better than commercial analogues were obtained. This confirms the prospects of using spent graphite current-collecting elements as raw materials for new products. In [2], the electrical sliding contact between copper and copper-graphite materials was investigated. It was found that the presence of graphite contributes to a decrease in the friction coefficient and wear intensity, while the copper component improves the electrical characteristics of the contact. The important role of the tribofilm formed during friction and determining the stability of the electrical contact interaction was also shown. The results obtained are important for substantiating the simultaneous use of carbon and metal phases in composite contact materials. In the study [3], various graphite materials were compared in pairs with copper under varying sliding speeds, normal loads and electric current. It was found that the contact

Copyright © 2026 O.V. Dykha, O.S. Kovtun, V.O. Dytyniuk, S.F. Posonskiy. This is an open access article distributed under the Creative Commons Attribution License, which permits unrestricted use, distribution, and reproduction in any medium, provided the original work is properly cited.

characteristics depend not only on the properties of the base material, but also on the nature and stability of the surface films. Polymer-bound graphite materials provided more uniform contact and more stable electrical characteristics. This confirms the importance of structural uniformity and the binder phase in the formation of composites based on secondary graphite. In [4], the influence of polarity and various combinations of electrographite, polymer-bound graphite and copper on the characteristics of a sliding electrical contact was investigated. It was shown that the direction of the current can significantly change the intensity of wear and the condition of the contact surfaces. This result indicates the need to evaluate a promising material not only by its own wear resistance, but also by its effect on the contact wire, which is fundamentally important for the selection of the composition of the current-collecting insert. In the study [5], a carbon-carbon composite material modified with copper mesh and lamellar graphite was considered for operation under conditions of electric current flow. It was shown that the combined introduction of carbon and metal phases allows to simultaneously improve mechanical, electrical and tribological properties. The graphite component performs an antifriction function, and the copper component increases electrical conductivity, which confirms the feasibility of multiphase modification of contact materials. In [6], modification of graphite by applying a copper coating with subsequent compaction was proposed. It was shown that the formation of a conductive copper shell on graphite particles improves the interfacial contact, reduces the electrical resistance and increases the wear resistance of the composite. These results indicate that for materials based on secondary graphite, not only the content of the metal phase is of significant importance, but also the nature of its distribution and contact with the carbon base.In the study [7], the non-monotonic nature of the influence of graphite content on the tribological properties of copper compositions was established. When the concentration of the graphite phase increased to a certain level, the friction coefficient and wear intensity decreased, but a further increase in its content led to a deterioration in the characteristics. This confirms the need to optimize the composition of the composite, since an increase in the amount of functional additive does not guarantee a proportional improvement in properties. In [8], conductive composites with simultaneous introduction of graphite and molybdenum disulfide were investigated. A synergistic lubricating effect of these components was established, which was manifested in a decrease in the intensity of wear and stabilization of contact resistance. SEM and XPS studies showed that MoS_2 contributes to the formation and preservation of a continuous friction film, while graphite participates in the formation of its carbon component. This is an important justification for the use of MoS_2 in graphite compositions of contact inserts. In the study [9] it was shown that the size of graphite particles significantly affects the density, hardness, thermal conductivity and wear resistance of graphite-copper composites. The obtained results confirm that the particle size distribution should be considered as an independent structural factor that determines the nature of compaction and the formation of interparticle contacts. For materials based on secondary raw materials, this is especially important, since the use of different fractions allows you to control the porosity and structural uniformity of the composite. In [10], gradient copper-graphite composites under electric current conditions were investigated. It was found that the wear intensity depends on the normal load and has a non-monotonic nature. It was also shown that the operational properties are determined by the joint action of the material composition, contact load and the formation of a surface tribolayer. This confirms the need for a comprehensive assessment of electrical and tribological characteristics when choosing a contact insert material. The generalization of the considered studies shows that for composite contact materials the structure of the carbon phase, the nature of the interfacial contact with copper, the particle size composition, the presence of solid lubricating components and the conditions of electrofriction loading are of decisive importance. In this case, the improvement of one indicator may be accompanied by the deterioration of another, which necessitates the need for multi-criteria optimization of the composition.

However, the known studies have not sufficiently considered the complex restoration of the properties of crushed spent contact inserts by simultaneously adjusting the fractional composition of secondary graphite and introducing technical carbon, copper powder and MoS_2. There are practically no works in which the composition of such a material would be optimized simultaneously for specific electrical resistance, contact resistance, insert wear and contact wire wear. This determines the feasibility of further research into a multicomponent composition based on secondary graphite material.

Choosing the composition of the composite

The choice of the composition of the modified composite material for trolleybus contact inserts is based on the analysis of the physical processes occurring in the zone of electrical contact interaction “contact insert – contact wire”, as well as on the need to simultaneously ensure high electrical conductivity, low contact resistance, and increased wear resistance. The basis of the composite material was selected secondary graphite, obtained by grinding used contact inserts. This approach allows to implement resource-saving technology and reduce the cost of the material. At the same time, it was found that the reuse of graphite elements is accompanied by a violation of their structural integrity, an increase in porosity and a rupture of conductive channels, which leads to an increase in electrical resistivity and intensification of wear.

In order to compensate for these shortcomings, functional additives of various physical nature were introduced into the composition, each of which plays a specific role in shaping the properties of the material.

The introduction of nanocarbon black (CB) is due to its ability to form an additional conductive network in the composition due to the percolation effect. Nanocarbon black particles have a high specific surface area and are able to fill the intergranular spaces between graphite particles, which helps restore broken electrical contacts. In addition, nanocarbon black improves the uniformity of the material structure, but with excessive content it can lead to increased porosity and reduced mechanical strength. Copper powder is introduced as a component that ensures the formation of metal conductive bridges between graphite particles. Due to the high electrical conductivity of copper, a significant reduction in the contact resistance of the composition is achieved, which is critically important for the stability of current collection. However, excessive copper powder content can cause increased wear of the contact wire due to the abrasive action of solid metal inclusions, which necessitates the optimization of its concentration. Molybdenum disulfide (MoS_2) is introduced as a solid lubricant component, which provides a reduction in the coefficient of friction and wear intensity. In the contact zone, MoS_2 forms a thin tribological film, which reduces contact stresses and stabilizes the sliding process. At the same time, this component has a relatively low electrical conductivity, which can lead to an increase in electrical resistance if its excess content is present. An important structural parameter of the composition is the fractional composition of secondary graphite. The use of a two-fraction system (coarse and fine fractions) allows for a denser packing of particles and a reduction in the porosity of the material. The fine fraction fills the intergranular space between coarse particles, which contributes to the formation of a stable electrically conductive structure and an increase in the mechanical integrity of the composition. Thus, each component of the composite material performs a specific function: nanosoot ensures the formation of an electrically conductive network, copper powder reduces contact resistance, molybdenum disulfide increases wear resistance, and optimization of the fractional composition of secondary graphite contributes to the formation of a dense structure of the material. The combined effect of these factors determines the need for their comprehensive optimization. Given the contradictory nature of the influence of individual components on the operational properties of the material, the task of choosing the optimal composition is multi-criteria and requires the application of methods of mathematical experimental planning and the construction of a generalized quality criterion. The influence of the percentage content of the components of a composite material on its operational characteristics is nonlinear and interdependent, which is due to the different physical nature of the components and the mechanisms of their interaction in the composite structure.

In this work, the content of functional additives was varied within the following limits: nanocarbon black (CB) – 0.5–2.5%, copper powder (Cu) – 0–6%, molybdenum disulfide (MoS_2) – 0–3%, with a fixed proportion of the fine fraction of secondary graphite at 35%.

Initial parameters of the optimization model and their characteristics

The selection of initial criteria for optimizing the composition of the composite material of trolleybus contact inserts is based on the analysis of their operating conditions and physical processes occurring in the zone of electrical contact interaction "contact insert - contact wire". During operation, the insert simultaneously performs the functions of a current-collecting element and an element of a tribological pair that operates under conditions of sliding, variable loads, the influence of temperature factors and the external environment. Under such conditions, the effectiveness of the material is determined not by a separate parameter, but by a set of electrical and mechanical characteristics, which necessitates a comprehensive approach to the selection of optimization criteria. The initial criteria selected were the material's electrical resistivity (ρv), contact electrical resistance (Rc), the wear rate of the contact insert (W), and the wear rate of the contact wire (Wwire). Electrical resistivity (ρv) characterizes the material's ability to conduct electric current and determines the level of energy losses within the current collection system. For materials based on secondary graphite, this parameter tends to increase due to the disruption of the conductive structure—a result of the breakdown of the original graphite texture and increased porosity. Therefore, reducing ρv is a key objective when modifying the composition.

Contact electrical resistance determines the quality of electrical contact between the insert and the contact wire and depends not only on the electrical conductivity of the material, but also on the actual contact area, surface microgeometry and the presence of intermediate films in the contact zone. Increased resistance leads to local overheating, sparking and accelerated destruction of the contact pair, which makes it one of the determining optimization criteria.

The wear rate of a contact insert characterizes its durability and directly affects operating costs. This indicator is determined by the tribological properties of the material, its structure and the ability to form protective films in the contact area. Reduction is a necessary condition for increasing the service W is the life of the insert, but this indicator is often in conflict with the electrical characteristics of the material.

No less important is the wear of the contact wire, since this element of the system is much more expensive and more difficult to replace. The introduction of solid or metallic components into the composition, which improve electrical conductivity, can simultaneously increase the abrasive effect on the wire surface. Therefore, control is a prerequisite for optimizing the material composition.

An analysis of the selected criteria reveals their mutually contradictory nature. Specifically, reducing electrical resistivity (ρv) and contact resistance (Rc) by incorporating conductive or metallic components can lead to increased wear rates (W and Wcond), whereas the use of solid lubricant additives helps reduce W but may impair the material's electrical conductivity. This conflict of properties precludes optimization based on a single parameter and necessitates a multi-criteria approach.

To comprehensively evaluate material quality, an integral criterion J is employed, combining all key indicators into a single generalized function. To achieve this, each criterion is normalized against a baseline value (ρv0, Rc0, W0, Wwire0) - thereby converting disparate parameters into dimensionless forms-followed by weighted summation. In general form, the integral criterion can be expressed as

$$J = w_1 \frac{\rho_v}{\rho_{v0}} + w_2 \frac{R_c}{R_{c0}} + w_3 \frac{W}{W_0} + w_4 \frac{W_{\text{wire}}}{W_{\text{wire0}}},$$

where are the weighting factors reflecting the relative importance of each criterion.

In this work, we have adopted $w_1 = w_2 = w_3 = w_4 = 0{,}25$, which corresponds to the equivalent consideration of all operational characteristics.

Minimization of the integral exponent$J$ corresponds to the simultaneous decrease of ρ_v, R_c, Wта W_{wire} which ensures the achievement of the optimal balance of electrical and tribological properties of the composite material.

Thus, the choice of initial optimization criteria is due to the need to take into account the complex of electrical and tribological properties of the material, and their mutually contradictory nature determines the feasibility of using an integral approach to optimizing the composition.

Designing an experiment to build a quadratic model

To establish the regularities of the influence of the composition of the modified composite on the operational characteristics of trolleybus contact inserts, the methodology of experimental design based on the response surface was used. This approach allows not only to assess the individual influence of each component, but also to take into account the nonlinearity of processes and the interaction of factors with each other. This is fundamentally important for composite materials, since changing the content of one additive can simultaneously affect the electrical conductivity, contact resistance, wear of the insert and wear of the contact wire.

In this work, the proportion of the fine fraction of secondary graphite material at the level of was taken as the main structural parameter, since such a content provides rational compaction of the structure and filling of the intergranular space. Further optimization was performed for three functional additives: the content of nanocarbon black, copper powder$A = 35\%BC$ and molybdenum disulfide. These components were chosen as controlled factors because nanosoot affects the formation of a conductive percolation network, copper powder ensures the formation of metal conductive bridges, and molybdenum disulfide acts as a solid lubricating component.

To construct a quadratic regression model, a Box–Behnken design was used for three factors *B,C,D* This design includes combinations of factors at three levels and central points, which allows us to estimate not only linear effects, but also quadratic terms and pairwise interactions of factors. Based on the obtained data, a model of the form was constructed:

$$J = b_0 + b_1 B + b_2 C + b_3 D + b_{11} B^2 + b_{22} C^2 + b_{33} D^2 + b_{12} BC + b_{13} BD + b_{23} CD,$$

where J is the integral material quality criterion; B is the carbon black content (%); C is the copper powder content (%); D is the molybdenum disulfide content (%); b_i, b_{ii}, b_{ij} are the regression model coefficients.

The initial experimental design for constructing a quadratic model is given in Table 1.

Table 1

Initial experimental design for constructing a quadratic RSM model

Exp, No.	Point type	A, % fine fraction	B: CB, %	C: Cu, %	D: MoS_2, %
1	RSM	35	0.5	0	1.5
2	RSM	35	0.5	6	1.5
3	RSM	35	2.5	0	1.5
4	RSM	35	2.5	6	1.5
5	RSM	35	0.5	3	0
6	RSM	35	0.5	3	3
7	RSM	35	2.5	3	0
8	RSM	35	2.5	3	3
9	RSM	35	1.5	0	0
10	RSM	35	1.5	0	3
11	RSM	35	1.5	6	0
12	RSM	35	1.5	6	3
13	Center of the plan	35	1.5	3	1.5
14	Center of the plan	35	1.5	3	1.5
15	Center of the plan	35	1.5	3	1.5

The central point repetition was used to assess the reproducibility of the results and the residual variance of the model. The resulting plan makes it possible to build a quadratic model, perform an analysis of variance, assess the significance of linear, quadratic and interaction terms, and also determine the region of the optimal composition of the composite by the integral quality criterion. This approach corresponds to the logic of the materials collected in your section file, where the main emphasis is placed on the quadratic RSM model, Pareto analysis, p-value and analytical determination of the optimum.

Conducting an experiment

In accordance with the established experimental design, test samples of composite material for contact inserts—based on recycled graphite with the addition of functional additives—were fabricated for each combination of factors. The composites were prepared by mixing the components in specified mass fractions, followed by pressing and heat treatment; this process ensured the formation of a material structure approximating industrial insert manufacturing conditions.

A comprehensive experimental study was conducted for each composition, involving the determination of electrical resistivity (ρv), contact electrical resistance (Rc), the wear rate of the contact insert (W), and the wear rate of the contact wire (Wwire). Measurements were performed in replicates, and the results were subsequently averaged to minimize the influence of random errors.

The electrical resistivity was determined by the standard method of measuring the electrical resistance of the samples, taking into account their geometric parameters. The contact resistance was measured under conditions of modeling the electrical contact "insert – wire". The wear resistance was assessed by the results of tribological tests with the determination of mass losses of the insert and contact wire material.

Table 2

Experiment results

No.	B (CB), %	C (Cu), %	D (MoS_2), %	ρv, μΩ·m	Rc, mOhm	W, mg/km	Wconduct, mg/km	J
1	0.5	0	1.5	32.1	17.6	138	50.2	0.94
2	0.5	6	1.5	25.3	13.8	129	56.4	0.88
3	2.5	0	1.5	26.7	15.2	134	52.0	0.90
4	2.5	6	1.5	22.4	12.9	126	57.8	0.86
5	0.5	3	0	29.8	15.9	142	54.1	0.93
6	0.5	3	3	31.2	16.8	108	49.6	0.89
7	2.5	3	0	27.1	14.8	136	55.3	0.91
8	2.5	3	3	28.5	15.6	102	50.7	0.87
9	1.5	0	0	30.6	16.5	139	53.0	0.92
10	1.5	0	3	32.4	17.4	104	48.9	0.90
11	1.5	6	0	24.8	13.5	133	58.2	0.88
12	1.5	6	3	26.2	14.3	100	52.6	0.85
13	1.5	3	1.5	26.0	14.1	118	51.0	0.86
14	1.5	3	1.5	26.3	14.3	120	51.5	0.87
15	1.5	3	1.5	25.9	14.0	119	50.8	0.86

Building a quadratic regression model

Based on the experimental data obtained, a mathematical model was constructed to describe the dependence of the integral quality index J on the composition of the composite material. The response surface method was employed for this purpose, enabling the consideration of both the individual effects of factors and their interactions, as well as the non-linear nature of the processes under investigation.

The contents of carbon black (B), copper powder (C), and molybdenum disulfide (D) were selected as independent variables and varied within the factor space in accordance with the experimental design. The proportion of the fine fraction of recycled graphite was fixed at A = 35%, a value corresponding to an optimal composition structure in terms of densification and inter-particle contact formation.

The estimation of the model coefficients was carried out by the least squares method based on the experimental values of the integral quality indicator . The resulting regression equation has the form:

$$J = 1{,}1482 - 0{,}1099B - 0{,}0312C - 0{,}0860D + 0{,}0230B^2 + 0{,}0036C^2 + 0{,}0148D^2 - 0{,}0014BC - 0{,}0027BD - 0{,}0006CD.$$

Analysis of the coefficients of the regression model shows that all the studied factors have a significant impact on the integral quality indicator J. Negative values of the coefficients for the linear terms B, C, D indicate that an increase in the content of nanosoot, copper powder and molybdenum disulfide in the studied range generally contributes to a decrease in the integral indicator , i.e., an improvement in the overall operational characteristics of the material.

The presence of positive quadratic coefficients B^2, C^2, D^2 indicates a nonlinear nature of the dependence and the existence of optimal values of factors, beyond which a further increase in their content leads to a deterioration in the properties of the material. This corresponds to the physical nature of the processes: an excess of nanosoot can cause porosity, an excessive content of copper powder - increased wear, and an excess of the concentration of molybdenum disulfide - an increase in electrical resistance.

The interaction coefficients BC, BD, CD characterize the joint effect of the composition components. In particular, BC the interaction reflects the combined effect of percolation and metallic conductivity, BD is a compromise between electrical conductivity and wear resistance, CD is the effect of the metallic phase on the efficiency of the tribological film. Thus, the constructed quadratic regression model adequately describes the process of forming the performance characteristics of a composite material and can be used for further analysis of the influence of factors and determination of the optimal composition.

Model adequacy check and variance analysis

In order to assess the adequacy of the constructed quadratic regression model and determine the statistical significance of the factors, an analysis of variance (ANOVA) was conducted. This method allows dividing the total response variation into components due to the influence of factors and a random component associated with experimental error.

The results of the analysis of variance of the quadratic model for the integral quality indicator are given in the table.

Table 3

Results of analysis of variance

Source of variation	Sum of squares SS	Degrees of freedom df	Mean square MS	F-criterion	p-value
Regression	0.0826	9	0.00918	48.7	<0.001
Error	0.00094	5	0.00019	-	-
General	0.0835	14	-	-	-

The analysis of the obtained results shows that the main part of the variation of the integral quality indicator is explained by the influence of the studied factors, since the sum of the squares of the regression accounts for the majority of the total variance. This is confirmed by the high value of the coefficient of determination:

$$R^2 = 0{,}989,$$

which indicates a high level of agreement between the model and the experimental data.

The calculated value of the F-criterion (48.7) significantly exceeds the tabulated value for the given significance level, which indicates the statistical significance of the constructed regression model as a whole. The low p-value (<0.001) further confirms that the influence of the factors on the response is significant and cannot be explained by random causes.

The small value of the residual variance indicates a small influence of random errors and a high accuracy of approximation of experimental data. This means that the constructed model adequately describes the dependence of the integral quality indicator on the composition of the composite material within the studied factor space.

Additionally, the adequacy of the model is confirmed by the results of the analysis of residuals, which have a random distribution and do not reveal systematic deviations from the zero level, and also satisfy the condition of normality of the distribution. This allows us to conclude that the use of regression analysis to describe the studied process is correct. Thus, the results of the analysis of variance confirm the statistical significance and adequacy of the quadratic regression model, which gives grounds to use it for further analysis of the influence of factors, construction of response surfaces, and determination of the optimal composition of the composite material of contact inserts. Given that the model is built on the basis of experimental data obtained within the given plan, its application is correct only within the studied factor space, which should be taken into account when further interpreting the results.

Factor significance analysis (Pareto and p-value)

In order to determine the relative contribution of factors and their interactions in the formation of the integral quality indicator, an analysis of the statistical significance of the coefficients of the quadratic regression model was performed. The assessment j was carried out on the basis of the t-test and the corresponding p-value, which allows us to quantitatively determine the influence of each member of the model.

To visually present the results, a Pareto diagram of standardized effects was constructed (Fig. 1), which shows the absolute values of the t-statistics for each factor and their interactions. The critical line corresponds to the threshold value of the t-test at a significance level of 0.05 and degrees of freedom of the residual variance. Factors whose values exceed this threshold are considered statistically significant.

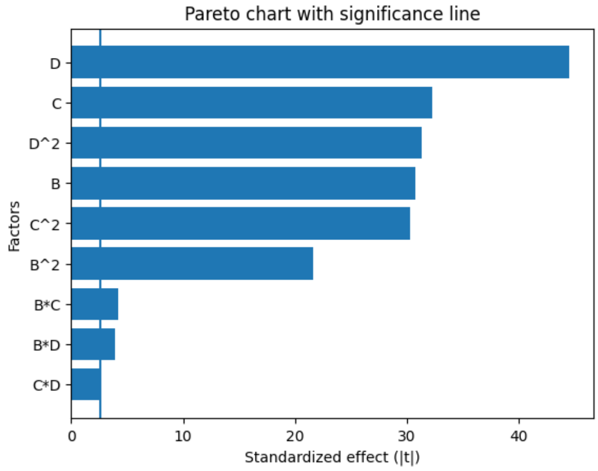

Fig. 1. Pareto diagram of standardized effects of factors and their interactions for the integral indicator J with a critical significance line

An analysis of Fig. 1 reveals that the linear factors B (nanocarbon black content) and D (molybdenum disulfide content), as well as the quadratic term B^2, exert the greatest influence on the integral quality indicator; this indicates a significant non-linear effect of nanocarbon black on the material's properties. Factor C (copper powder content), which determines the level of contact resistance, is also significant.

The interaction terms *BC, BD* and *CD* also exceed the critical threshold, indicating a mutual influence among the composition's components. Specifically, the BC interaction reflects the combined effect of percolation and metallic conductivity; BD characterizes the trade-off between electrical conductivity and wear resistance; and CD represents the influence of the metallic phase on the effectiveness of the tribological film.

To quantitatively confirm the significance of the factors, the p-values for each regression model coefficient were analyzed. The results showed that all linear terms (B, C, D) have p-values significantly lower than 0.05, indicating a high level of statistical significance. Similarly, the quadratic terms (B^2, C^2, D^2) are also statistically significant, confirming the non-linear nature of the relationship.

Although the interaction terms BC, BD, and CD have slightly higher p-values, they remain within the range of statistical significance, confirming the necessity of including them in the model. This demonstrates that the influence of the composition's components is not additive and must be considered as the result of their combined action.

Summarizing the results of Pareto analysis and p-value analysis, the following order of influence of factors on the integral quality indicator was established:

$$B > D > C > B^2 > BD > BC > C^2 > D^2 > CD.$$

The obtained results confirm that the determining role in shaping the properties of the composite material is played by the content of nanosoot, which ensures the formation of an electrically conductive structure, as well as molybdenum disulfide, which is responsible for wear resistance. Copper powder performs an auxiliary but important function of improving contact characteristics. Thus, the analysis of the significance of factors allowed us to establish the dominant parameters of the composition and confirmed the feasibility of using a quadratic regression model to describe the processes of forming its operational properties.

Response surface analysis

For a more detailed study of the influence of the composition of the composite material on the integral quality indicator, response surfaces were constructed based on the quadratic regression model. Analysis of the surfaces allows us to assess the nature of the response change in the entire factor space, identify areas of minimum, and establish the interaction between factors.

Figures 2–4 show the response surfaces for the main combinations of factors at fixed valuesof the third parameter.

The effect of nanocarbon black and copper powder (Fig. 2). Figure 2 shows the response surface at a fixed value of $J = f(B, C)D = 1{,}5\%$.

Surface analysis shows that an increase in the content of nanosoot and copper powder within the studied range is accompanied by a decrease in the integral index, which indicates an improvement in the operational characteristics of the material. The most intense decrease is observed with a simultaneous increase in both factors, which confirms the presence of a synergistic effect of their interaction.

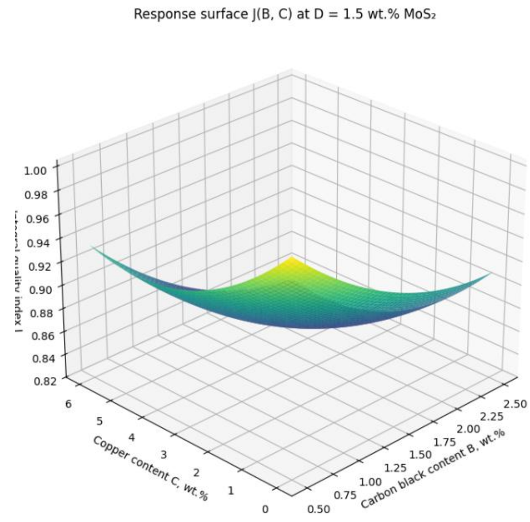

Fig. 2. Effect of nanocarbon black and copper powder

Physically, this is explained by the fact that nanosoot forms a percolation conductive network, while copper powder ensures the formation of metal conductive bridges. Their combined action contributes to the restoration of the damaged structure of secondary graphite and the reduction of electrical losses. However, in the upper region of the factor values, a decrease in the surface steepness is observed, which indicates the achievement of the saturation region and the presence of a quadratic effect that limits further improvement of the properties.

Effect of carbon black nanoparticles and copper powder (Fig. 2). Figure 2 shows the response surface J=f(B,C) at a fixed value of D=1.5%.

Analysis of the surface reveals that increasing the content of carbon black nanoparticles and copper powder within the studied range leads to a decrease in the integral parameter J, indicating an improvement in the material's performance characteristics. The most pronounced decrease in J is observed when both factors are increased simultaneously, confirming a synergistic effect resulting from their interaction.

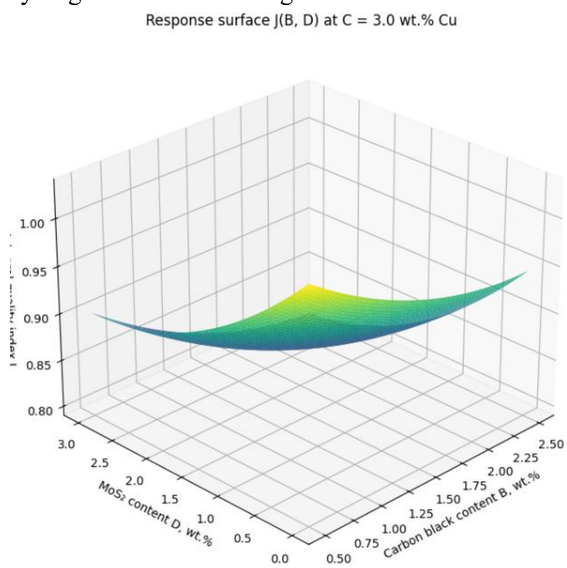

Fig. 3. Effect of nanocarbon black and molybdenum disulfide

However, at a simultaneous high content of both components, a slowdown in the response change is observed, which is associated with the opposite effect of MoS_2 on electrical conductivity. Thus, the surface has a pronounced nonlinear character and demonstrates the existence of a region of optimal factor values.

Effect of copper powder and molybdenum disulfide (Fig. 4). Figure 14 shows the dependence of J=f(C,D) at a fixed value of B=1.5%. Surface analysis shows that increasing the copper powder content leads to a decrease in the integral index due to improved contact characteristics, while the introduction of molybdenum disulfide helps reduce insert wear.

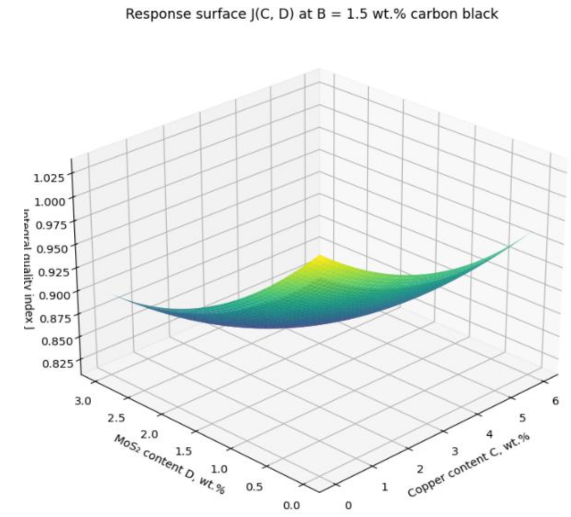

Fig. 4. Effect of copper powder and molybdenum disulfide

At the same time, in the upper ranges of factor values, there is a decrease in the effectiveness of their influence, which indicates the presence of quadratic effects and confirms the limitations of the expedient increase in the concentration of components. A feature of this surface is a weakly expressed, but present effect of the interaction of factors, which manifests itself in a change in the curvature of the surface and indicates the mutual influence of the metal phase and the solid lubricating component. Analysis of response surfaces confirms that the dependence of the integral quality indicator on the composition has a pronounced nonlinear character and is determined by both the individual influence of factors and their interaction.

The most effective combination is: nanocarbon black for forming an electrically conductive structure; copper powder for reducing contact resistance; molybdenum disulfide for increasing wear resistance. The results obtained are consistent with the data of Pareto analysis and confirm the feasibility of using a quadratic model to describe the processes of forming the properties of a composite material.

Optimization of the composition of the composite material by derivatives

Optimization of the composition of the composite material was performed on the basis of the constructed quadratic regression model of the integral quality indicator, which allows taking into account the simultaneous influence of the content of nanosoot, copper powder and molybdenum disulfide on the set of electrical and tribological characteristics of the material. The optimization of the composite material's composition was performed based on a constructed quadratic regression model of the integral quality index J, which accounts for the simultaneous influence of the content of carbon black (B), copper powder (C), and molybdenum disulfide (D) on the material's combined electrical and tribological characteristics. The optimization problem is formulated as finding valuesfor factors B, C, and D that minimize the integral index J within the investigated factor space:

$$J(B, C, D) \to \min.$$

To determine the extremum of the function, an analytical approach was used, based on equating the partial derivatives of the response function to zero:

$$\frac{\partial J}{\partial B} = 0, \frac{\partial J}{\partial C} = 0, \frac{\partial J}{\partial D} = 0.$$

The solution of the system of equations obtained on the basis of the quadratic model allowed us to determine the theoretical coordinates of the stationary point, which correspond to the minimum value of the integral quality indicator. It was established that the theoretical optimum is achieved at the values of the factors:

$$B = 2{,}74\%, C = 5{,}18\%, D = 3{,}26\%.$$

However, the obtained values partially go beyond the studied factor space, which is limited by the experimental conditions:

$$0{,}5 \leq B \leq 2{,}5{,}0 \leq C \leq 6{,}0 \leq D \leq 3.$$

In this regard, the practical optimum is determined taking into account the boundary conditions of variation of factors. The most appropriate is the choice of composition that corresponds to the upper limits of the effective influence of the components:

$$B = 2{,}5\%, C \approx 5{,}1\%, D = 3{,}0\%.$$

For this composition, the regression model obtained the minimum value of the integral indicator:

$$J_{\min} \approx 0{,}78,$$

which corresponds to the optimal combination of electrical conductivity, contact characteristics and wear resistance of the material.

Physically, the obtained result is explained by the fact that at a nanosoot content of about 2.5%, a developed percolation structure is formed, copper powder in an amount of about 5% provides effective electrical contact, and molybdenum disulfide at a concentration of 3% forms a stable tribological film, which reduces the intensity of wear. Further increase in the content of any of the components does not lead to an improvement in properties and may have a negative effect. Predicted properties for this composition:

Indicator	Predicted value
Specific electrical resistance ρv	≈ 23.0 μΩ m
Contact resistance Rc	≈ 13.4 mOhm
Insert wear W	≈ 88.6 mg/km
Contact wire wear Wwire	≈ 54.2 mg/km
Integral exponent J	≈ 0.779

Thus, the optimization made it possible to determine the rational composition of the composite material, which provides the minimum value of the integral quality indicator and meets the requirements for the operational characteristics of trolleybus contact inserts.

In order to verify the obtained optimal composition, the substitution of the found values of the factors into a quadratic regression model was performed, which made it possible to determine the predicted values of the integral quality indicator and individual operational parameters. The calculation results showed that for the optimal composition of B=2.5%, C≈5.1%, D=3.0%, the integral index is J≈0.78, which is the minimum within the investigated factor space. The obtained values testify to the consistency of the analytical optimization results with the nature of the response surfaces and confirm the correctness of the constructed regression model. Thus, the determined composition can be accepted as rational for further practical use and experimental verification.

The optimization of the quadratic regression model showed that the stationary point of the response function for factor D (molybdenum disulfide content) partially exceeds the limits of the investigated factor space. This is explained by the fact that the mathematical model describes a continuous response surface and is not limited by the conditions of the experimental design. The obtained result indicates the preservation of the tendency to decrease the integral quality index with increasing D content within the investigated range. At the same time, since the experimental data were obtained only in the interval 0≤D≤3%, further extrapolation of the model beyond this area may be incorrect. In this regard, the practical optimum is adopted at the upper limit of variation of the factor D=3%.

You can also check it through the Hessian matrix. For our quadratic model:

$$J = 1{,}1482 - 0{,}1099B - 0{,}0312C - 0{,}0860D + 0{,}0230B^2 + 0{,}0036C^2 + 0{,}0148D^2 - 0{,}0014BC - 0{,}0027BD - 0{,}0006CD$$

The Hessian matrix has the form:

$$H = \begin{pmatrix} 2b_{11} & b_{12} & b_{13} \\ b_{12} & 2b_{22} & b_{23} \\ b_{13} & b_{23} & 2b_{33} \end{pmatrix}$$

that is:

$$H = \begin{pmatrix} 0{,}0460 & -0{,}0014 & -0{,}0027 \\ -0{,}0014 & 0{,}0072 & -0{,}0006 \\ -0{,}0027 & -0{,}0006 & 0{,}0296 \end{pmatrix}$$

To check the minimum, you need to determine the signs of the major minors:

$$\Delta_1 = 0{,}0460 > 0$$

$$\Delta_2 = \begin{vmatrix} 0{,}0460 & -0{,}0014 \\ -0{,}0014 & 0{,}0072 \end{vmatrix} = 0{,}000329 > 0$$

$$\Delta_3 = \det(H) \approx 0{,}0000097 > 0$$

Since all principal minors of the Hessian matrix are positive, the matrix is positive definite. This implies that the stationary point found for the quadratic model corresponds to a local minimum of the function J. To verify the nature of the stationary point, the Hessian matrix of the quadratic regression model was analyzed. Since the principal minors of the Hessian matrix are positive, the matrix is positive definite. This indicates that the stationary point of the response function corresponds to a local minimum of the integral quality index J. However, some coordinates of the theoretical minimum lie outside the investigated factor space; therefore, the practical optimum is determined at the boundary of the experimental design.

Conclusion

To determine the optimal composition of the composite material, an analytical optimization of the quadratic regression model was carried out by equating the partial derivatives of the integral index J with respect to the factors B, C, and D to zero. The theoretical minimum of the function corresponds to the values B = 2.74%, C = 5.18%, D = 3.26%. Since some of the obtained values go beyond the studied factor space, the practical optimum is taken at the boundary of the plan: B = 2.5%, C ≈ 5.1%, D = 3.0%. For this composition, the predicted value of the integral index is J ≈ 0.779, which corresponds to the best combination of electrical conductivity and wear resistance.

References

1. Jakubas, A., Chwastek, K., Cywiński, A., Gnatowski, A., & Suchecki, Ł. (2020). An analysis of the performance of trolleybus brushes developed from recycled materials. Applied Sciences, 10(21), 7929. https://doi.org/10.3390/app10217929

2. Grandin, M., & Wiklund, U. (2018). Wear phenomena and tribofilm formation of copper/copper-graphite sliding electrical contact materials. Wear, 398–399, 227–235. https://doi.org/10.1016/j.wear.2017.12.012

3. Kalin, M., & Poljanec, D. (2018). Influence of the contact parameters and several graphite materials on the tribological behavior of graphite/copper two-disc electrical contacts. Tribology International, 126, 192–205. https://doi.org/10.1016/j.triboint.2018.05.024

4. Poljanec, D., & Kalin, M. (2019). Effect of polarity and various contact pairing combinations of electrographite, polymer-bonded graphite and copper on the performance of sliding electrical contacts. Wear, 426–427, 1163–1175. https://doi.org/10.1016/j.wear.2019.01.002

5. Wang, P., Zhang, H., Yin, J., Xiong, X., Tan, C., Deng, C., & Yan, Z. (2017). Wear and friction behaviors of copper mesh and flaky graphite-modified carbon/carbon composite for sliding contact material under electric current. Wear, 380–381, 59–65. https://doi.org/10.1016/j.wear.2017.02.045

6. Bai, L., Ge, Y., Zhu, L., Chen, Y., & Yi, M. (2021). Preparation and properties of copper-plated expanded graphite/copper composites. Tribology International, 161, 107094. https://doi.org/10.1016/j.triboint.2021.107094

7. Li, H., Liu, Y., Zheng, B., Wang, S., Yi, Y., Zhang, Y., & Li, W. (2023). On the tribological behaviors of Cu matrix composites with different Cu-coated graphite content. Journal of Materials Research and Technology, 25, 83–94. https://doi.org/10.1016/j.jmrt.2023.05.221

8. Zhou, T., Wang, X., Qin, L.-X., Qiu, W.-T., Li, S.-F., Jiang, Y.-B., Jia, Y.-L., & Li, Z. (2024). Electrical sliding friction wear behaviors and mechanisms of Cu–Sn matrix composites containing MoS_2/graphite. Wear, 548–549, 205388.https://doi.org/10.1016/j.wear.2024.205388

9. Sun, Y., Xu, L., Tang, Z., Zuo, C., Zheng, G., & Xia, H. (2024). Fabrication of high thermal conductivity and wear resistance graphite/copper composites by microwave hot press sintering. Tribology International, 194, 109522. https://doi.org/10.1016/j.triboint.2024.109522

10. Lu, J., Ma, C., Zhang, L., He, Z., Guo, B., Wei, J., Zeng, D., Li, W., & Liu, Y. (2025). Effect of normal load on damage mechanism of gradient copper-graphite composites under electric current. Wear, 562–563, 205653.https://doi.org/10.1016/j.wear.2024.205653

Диха О.В., Ковтун О.С., Дитинюк В.О., Посонський С.Ф. Оптимізація складу композиційного матеріалу контактних вставок електротранспорту за критерієм зносостійкості

У роботі розглянуто проблему повторного використання відпрацьованих графітових контактних вставок електротранспорту та підвищення їх функціональних властивостей шляхом модифікування складу композиційного матеріалу. Проаналізовано сучасні підходи до формування графітових і мідно-графітових електроконтактних композитів, вплив гранулометричного складу, провідних та твердих мастильних добавок на електричні й трибологічні характеристики. Показано перспективність застосування вторинного графіту як основної сировини за умови відновлення структурної цілісності та електропровідних контактів між частинками. Обґрунтовано доцільність використання технічного вуглецю для формування додаткової провідної мережі, мідного порошку для зниження контактного опору та дисульфіду молібдену для стабілізації тертя і зменшення зношування. Встановлено, що властивості таких композитів мають багатофакторний і нелінійний характер, тому вибір складу потребує комплексної оптимізації з одночасним урахуванням електроопору, зносостійкості вставки та впливу на контактний провід.

Ключові слова: вторинний графіт, контактна вставка, мідний порошок, технічний вуглець, дисульфід молібдену, електропровідність, зносостійкість.

ISSN 2079-1372 Problems of Tribology, V. 31, No 3/121-2026, 109-114

Problems of Tribology
Website: http://tribology.khnu.km.ua/index.php/ProbTrib
E-mail: tribosenator@gmail.com

DOI: https://doi.org/10.31891/2079-1372-2026-121-3-109-114

Kinetics of boundary layers in non-conformal contact under non-stationary conditions

Y. Turytsia* 0000-0002-2205-0426, **V. Akhmatov** 0009-0003-6325-5262

[1] *Ntional Transport University, Ukraine*
**E-mail: Yuliya_tur@ukr.net*

Received: 15 August 2026: Revised 05 September 2026: Accept: 15 September 2026

Abstract

In this work, the conditions for the formation of adsorbed boundary layers on friction surfaces under rolling with sliding were studied. The tests were carried out according to the roller-on-roller scheme on an SMC-2 rig, the specimens being cylindrical rollers of steel 45 with hardness HRC 32. The studies were performed in the mode of frequent starts and stops: acceleration 4 s, stop 3.5 s, the cycles following one another without pauses. The total rolling speed was 1.91 m/s, the slip 20 %, the contact stress 550 MPa, the total number of operating cycles N = 2350. The lubricant layer thickness was determined by the voltage drop method in the normal glow discharge mode. For the base oil, over the first $N \leq 250$ operating cycles a breakdown of the lubricant layer was recorded in 75 % of the cycles. At $250 \leq N \leq 1000$ an adsorbed boundary layer 0.036 – 1.056 µm thick is formed, and at $N \geq 1280$ the film thickness is 0.150 – 1.524 µm and the frequency of breakdowns decreases on average to 10 % of the cycles. The suspension forms boundary layers more intensively, however their stability is lower: repeated adaptation occurs only at $N \geq 2100$ cycles, the layer thickness in this case being h = 0.130 – 1.620 µm. On 55 % of the contact area chemisorbed films 0.051 – 0.186 µm thick were recorded. A mechanism of the formation and adaptation of boundary adsorption layers on friction surfaces under conditions of frequent starts and stops has been revealed, which consists in the fact that activation of the metal surfaces under multi-cycle action and polarization of hydrocarbon molecules by the electric field of the solid phase initiate the formation of the layer, while its subsequent failure exposes the nascent metal surface, and the escape of electrons from it (exoelectron emission) creates conditions for the formation of anions and radicals and the growth of chemisorbed films. The obtained dependences of the boundary layer thickness on the number of operating cycles make it possible to predict the lubrication regime of non-conformal friction units under conditions of frequent starts and stops and to choose the concentration of the fullerene additive in a justified way.

Key words: friction, lubrication, boundary adsorption layer, chemisorbed film, fullerene C_{60}, lubrication regime, non-stationary conditions, durability.

Introduction

The durability of contacting surfaces in a non-conformal friction unit is to a considerable extent determined by the lubricating film [1].

Its thickness must be greater than the root-mean-square sum of the highest asperities of the friction surfaces. The most favorable conditions occur when a hydrodynamic or elastohydrodynamic film is realized in the contact, at the same time between these two states there lies a transition region with intermediate properties.

It is important to note that the service life of non-conformal friction units in real operating conditions never covers the whole active friction surface of the mating parts, since manufacturing errors, shaft misalignment and initial roughness leave only a third or a half of the nominal area in work. Because of this the actual contact stress can exceed the calculated one, which is able to cause failure of the tribosystem. Therefore the service life of such a friction unit is determined not by a calculation from nominal parameters, but by the ability to maintain the required lubricant layer thickness in the contact.

Literature Review

Copyright © 2026 Y. Turytsia, V. Akhmatov. This is an open access article distributed under the Creative Commons Attribution License, which permits unrestricted use, distribution, and reproduction in any medium, provided the original work is properly cited.

In unsteady operating regimes boundary friction prevails. The boundary, mixed and hydrodynamic regimes are distinguished by the mechanism of friction in the contact [2]. Under boundary lubrication the elastic and plastic deformation of the substrate is decisive, under mixed lubrication the adsorbed layer of liquid dominates, and under the hydrodynamic regime shear of the lubricant layer takes place between the surface and the asperity.

Under such conditions the interaction of metal surfaces in a lubricating medium is determined by a complex of mechano-physicochemical processes which depend on the composition and properties of the medium [3]. The wear resistance of a polymolecular boundary layer is determined by molecular-kinetic factors, whereas for a monomolecular adsorption layer the strength of the adsorption bond and the kinetics of its restoration on the nascent surface become decisive.

An additive operating under boundary friction conditions must consist of a mixture of different substances. Their molecules must exhibit effective adsorption capacity, which ensures the formation of an adaptive boundary film, at the same time such a film protects the friction pairs from direct contact. Chemisorption provides a stronger interaction with the surface than physical adsorption, and therefore better protects the film from abrasion [4].

In the crystal, fullerene C_{60} molecules are bound by weak van der Waals forces. A calculation by the molecular orbital method shows that the face-centered cubic lattice of fullerite is described by a series of bands which do not overlap. The band width is 1.5 – 1.8 eV, which makes fullerite a semiconductor. The valence band is able to accept no more than six doped electrons.

At $0 < x < 3$, where x is the number of doped electrons, the conductivity of the sample increases with increasing x, while at $x = 6$ the conduction band is filled completely, and the properties of the sample are determined by the structure of the next free band.

The regularities of the formation of boundary layers under lubrication with a fullerene C_{60} suspension in conditions of frequent starts and stops remain unclarified. Among the mechanisms of action of nanoscale additives, the formation of a tribofilm, the rolling effect of spherical particles, the healing of microdefects, surface polishing and a synergistic effect are named [5]. It has not been established how the additive concentration affects the thickness of the adsorption layers and the lubrication regime in a non-conformal contact of point form.

Purpose

To investigate the mechanism of the formation and adaptation of boundary adsorption layers on contacting surfaces under lubrication with I-20 mineral oil and an 18 % fullerene C_{60} suspension in unsteady operating regimes.

To evaluate the role of the activated metal surface and the temperature factor in the formation of boundary films.

Methods

The lubricant layer thickness was determined by the voltage drop method in the normal glow discharge mode. A voltage close to zero corresponds to direct metal-to-metal contact, and its rise corresponds to the presence of an insulating film [6]; electrical methods for assessing the state of the lubricant layer are systematized in the review [7].

In order to establish the lubrication regime in the contact, the dimensionless criterion λ was used, which is determined by the ratio of the lubricant layer thickness to the height of the asperities of the contacting surfaces. The proportion of cycles with breakdown of the layer at standstill was recorded separately.

The tests were performed according to the roller-on-roller scheme on the SMC-2 laboratory rig, the specimens being cylindrical rollers of steel 45 with hardness HRC 32.

The studies were carried out in the mode of frequent starts and stops. The total rolling speed of the test specimens reached 1.91 m/s with a subsequent instantaneous stop.

The recording of the lubricant layer thickness was performed during the start-up period, at the maximum friction torque, under conditions of rolling with 20 % sliding. The duration of one cycle was 7.5 s: 4 s of acceleration and 3.5 s of stop. The cycles were repeated continuously. The total number of operating cycles in the experiment amounted to N = 2350 at a contact stress of 550 MPa.

Within the operating cycles up to N = 1000 the bulk temperature of the oil was 20 °C, subsequently it gradually increased and at $N \leq 2350$ reached 66 °C.

Results

Formation of boundary layers under lubrication with the base oil I-20

Over the first 250 operating cycles a loss of layer continuity at stop was recorded in 75 % of the cases, which caused the appearance of direct contact without lubricant.

It was established that an increase in the rotational speed of the test specimens leads to an increment of the oil film thickness within 0.360 – 0.420 μm, which is practically independent of the bulk temperature in the contact.

Within the experiment it was recorded that the formation of the boundary layer is ensured by the acquisition of polarity by hydrocarbon molecules in the field of the solid phase and by the activation of the contacting surfaces under cyclic loading. In work [8] it was established that the thickness of the boundary layer, like the distance of interaction of the molecules with the surface, is determined by the field strength of the surface and the energy of thermal vibrations.

In the range of operating cycles $250 \leq N \leq 1000$ the lubricant layer thickness is 0.036 – 1.056 μm. The layer adapts to the variable load, which makes it possible to reduce the proportion of direct contact of the surfaces to 25 % of the starts and stops.

In work [9] it was established that the accumulation and ordering of adsorbed molecules occurs under the action of repeated rolling.

Heating of the oil shifts the balance between the energy of thermal vibrations and the energy of retention of the molecules on the surface. With the predominance of the former, the ordering of the layer is lost, and the proportion of cycles in which the layer was not recorded at standstill increases.

At $N \geq 1280$ operating cycles a repeated restoration of the layer to 0.150 – 1.524 μm is observed, and ruptures of the lubricant film are recorded within 10 % of the starts and stops.

Heating is accompanied by an intensification of the oxidation processes in the friction pair. The joint action of the activated metal surface and the oxidized hydrocarbons causes polymerization reactions, the products of which are fixed on the metal chemisorptively; the thickness of the formed films is 0.059 – 0.148 μm.

The serviceability of the I-20 oil under non-stationary conditions is determined not by viscosity but by the ability to retain the boundary layer (Fig. 1). Up to $N \leq 250$ the boundary regime is realized in the contact; with the growth of the layer it changes to mixed, which is maintained up to $N \leq 1000$.

As a result of heating of the lubricant, the boundary lubrication regime is established. The subsequent restoration of the adsorption films at t = 50 – 66 °C ensures the mixed regime until the end of the experiment.

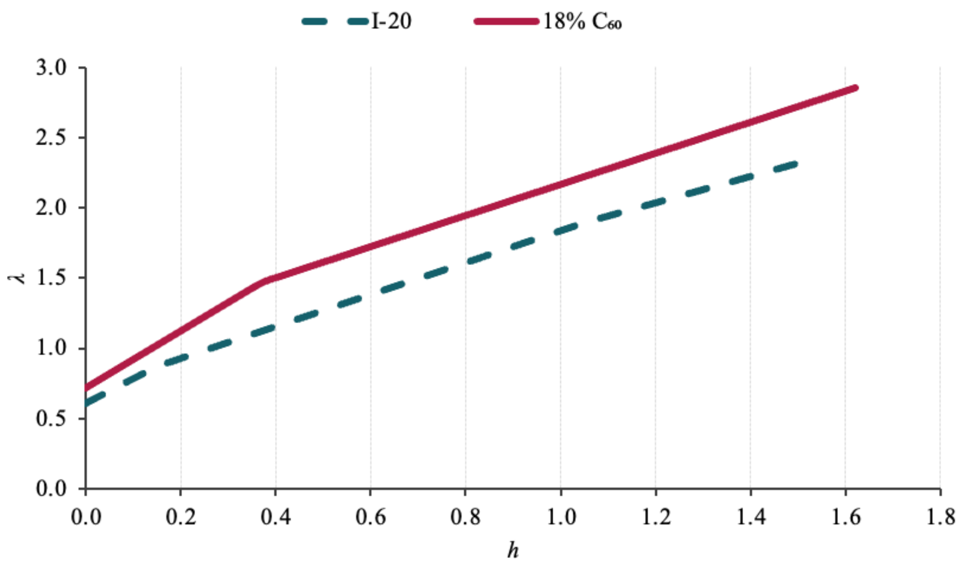

Fig. 1 Dependence of the lubrication regime criterion λ on the thickness of the adsorbed boundary layer h, μm: dashed line – I-20 oil, solid line – 18 % fullerene C_{60} suspension

Effect of the 18 % fullerene C_{60} suspension on the kinetics of the adsorption layers

It was found that the 18 % suspension based on fullerene C_{60} forms boundary adsorption layers more effectively than the base mineral oil I-20 at t = 20 °C. It was experimentally established that at $N \leq 190$ the thickness of the boundary films is 0.063 – 0.371 μm. During the stop, a breakdown of the lubricant layer was found in only 10 % of the cycles.

With an increase in the number of operating cycles of the tribosystem it was established that in 35 % of the cycles the thickness of the layers reaches 0.700 – 1.400 μm, however the formed boundary layers are unstable, which leads to their gradual failure.

The thermal effect in combination with frequent starts and stops causes a disturbance of the stability of the boundary lubricating film and its gradual removal from the contacting areas of the surfaces. Repeated adaptation of the layer occurs at $N \geq 2100$, its thickness in this case being h = 0.130 – 1.620 μm. The low stability of the formed layers is associated with the weak adhesive interaction with the metal surface, as a result of which they are easily removed. A breakdown of the lubricant layer was recorded in 40 % of the cycles.

Fig. 2 shows the state of the contact zone after the formation of the lubricant layer. According to the experimental results, the formation of a chemisorbed film with a thickness of h = 0.051 – 0.186 μm was established, extending over 55 % of the area of interaction of the surfaces.

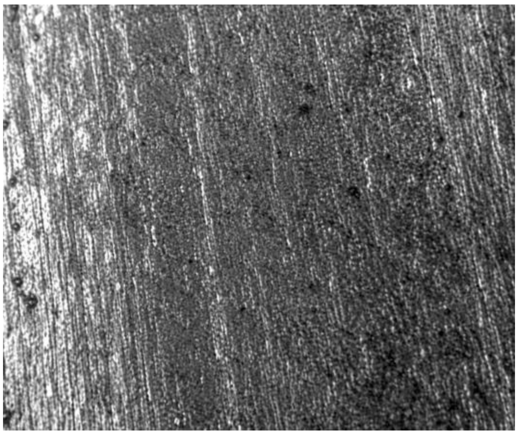

Fig. 2 Friction surface after lubrication with the 18 % fullerene C60 suspension

Lubrication regime and the mechanism of formation of chemisorbed films

With an increase in the number of operating cycles the mixed lubrication regime is realized in 25 % of the cycles ($\lambda \geq 2.860$), whereas at the initial stage of operation of the contact the boundary regime prevails ($\lambda = 0.845 – 1.471$). The established regularities were obtained for multi-cycle dynamic loading in the presence of the fullerene C_{60} additive, Fig. 1.

Chemisorbed films are formed on the friction surfaces, which include resinous products, friction polymers and oxidation products. Their formation is caused by the attachment of activated anions and radicals to positively charged microsurfaces.

The source of these particles is the hydrocarbon components of the oil, which are converted into anions, radical anions and radicals. Under variable loading the adsorption layers are destroyed, and the exposure of nascent areas is accompanied by exoelectron emission. The exoelectrons react with the molecules desorbed from the boundary film, whose reactivity, in view of their activated state, should be the highest.

It can be assumed that two interrelated processes develop in the contact zone. Electrons pass from the metal surface into the conduction band of the semiconductor, whereas polarized hydrocarbon molecules accept them from the valence band. Because of the frequent renewal of the physically adsorbed layers the second of them prevails, and the hydrocarbon molecules play the role of p-type dopants.

The absence of the lubricant layer observed in the stationary state is probably associated with the presence of a fullerene layer as a semiconductor phase, which is retained on the contact surface. Under optical magnification this layer becomes noticeable. The experimentally confirmed ability of the I-20 oil to form chemisorbed films is consistent with known data. The polarization of aromatic hydrocarbons by the electric field of the solid phase with the subsequent formation of friction polymers was described earlier [1]. The layer of spherical fullerene C_{60} molecules polymerized on the surface reduces the shear resistance of the crystallites in the tangential direction. Together with the intensity with which the hydrocarbon components of the oil form the film, this determines the stability of the boundary layers upon the introduction of an additive with a layered structure of the crystal lattice.

With a significant cohesive component of the interaction of the polarized molecules, failure of the adsorption layer becomes less probable.

Conclusions

It has been established that the start-stop mode leads to activation of the friction surfaces, which initiates the formation of boundary adsorption layers and their subsequent adaptation to the variable load. The mechanism of this process is the polymerization of the hydrocarbon components, characteristic both of I-20 and of the 18 % fullerene suspension.

A comparison of the lubricating media showed that at the initial stage of the operating cycles the suspension provides a substantially more stable boundary layer: a breakdown was recorded in 10 % of the cycles against 75 % for the base oil. With further operating cycles the ratio changes to the opposite, and a breakdown of the suspension layer is observed in 40 % of the cycles against 10 % for the oil, which indicates the predominantly physical nature of the layers formed by it.

It follows from this that the concentration of the fullerene additive is a means of controlling the composition of the boundary layer, and the maintenance of a stable lubrication regime under unsteady operating conditions ensures the durability and reliability of non-conformal friction units.

References

1. Dmytrychenko, M. F. (1980). Doslidzhennia vplyvu hazovykh seredovyshch na zmashchuvalnu zdatnist mineralnykh olyv, yikh protyznosnoi ta dempfuvalnoi dii v zacheplenni zubtsiv zubchastykh peredach [Study of

the effect of gaseous media on the lubricating capacity of mineral oils and their antiwear and damping action in gear tooth meshing] [Candidate's dissertation, KIIGA]. Kyiv.

2. Stephan, S., Schmitt, S., Hasse, H., & Urbassek, H. M. (2023). Molecular dynamics simulation of the Stribeck curve: Boundary lubrication, mixed lubrication, and hydrodynamic lubrication on the atomistic level. Friction, 11(12), 2342–2366. https://doi.org/10.1007/s40544-023-0745-y

3. Chen, Y., Renner, P., & Liang, H. (2023). A review of current understanding in tribochemical reactions involving lubricant additives. Friction, 11(4), 489–512. https://doi.org/10.1007/s40544-022-0637-2

4. Minami, I. (2017). Molecular science of lubricant additives. Applied Sciences, 7(5), Article 445. https://doi.org/10.3390/app7050445

5. Jiang, Z., Sun, Y., Liu, B., Yu, L., Tong, Y., Yan, M., Yang, Z., Hao, Y., Shangguan, L., Zhang, S., & Li, W. (2024). Research progresses of nanomaterials as lubricant additives. Friction, 12(7), 1347–1391. https://doi.org/10.1007/s40544-023-0808-9

6. Tsai, A. E., & Komvopoulos, K. (2024). Dynamics of tribofilm formation in boundary lubrication investigated using in situ measurements of the friction force and contact voltage. Materials, 17(6), Article 1335. https://doi.org/10.3390/ma17061335

7. Becker-Dombrowsky, F. M., & Kirchner, E. (2024). Electrical impedance based condition monitoring of machine elements – a systematic review. Frontiers in Mechanical Engineering, 10, Article 1412137. https://doi.org/10.3389/fmech.2024.1412137

8. Kosolapov, V. B. (2021). Formuvannia adsorbtsiinoho sharu PAR na mikronerivnostiakh poverkhon tertia [Formation of an adsorption layer of surface-active substances on microasperities of friction surfaces]. Visnyk Kharkivskoho natsionalnoho avtomobilno-dorozhnoho universytetu, 95, 38–42. https://doi.org/10.30977/BUL.2219-5548.2021.95.0.38 (in Ukrainian)

9. Watanabe, S., Tadokoro, C., Miyake, K., Sasaki, S., & Nakano, K. (2022). Processes of molecular adsorption and ordering enhanced by mechanical stimuli under high contact pressure. Scientific Reports, 12(1), Article 3870. https://doi.org/10.1038/s41598-022-07854-5

Турица Ю., Ахматов В. Кінетика граничних шарів у неконформному контакті в умовах нестаціонарного режиму

У роботі досліджено умови утворення адсорбційних граничних шарів на поверхнях тертя в умовах кочення з проковзуванням. Випробування проводили за схемою ролик-ролик на установці СМЦ-2, зразками слугували циліндричні ролики зі сталі 45 твердістю HRC 32. Дослідження виконували в режимі частих пусків-зупинок: розгін 4 с, зупинка 3.5 с, цикли слідували один за одним без пауз. Сумарна швидкість кочення становила 1.91 м/с, проковзування 20 %, контактна напруга 550 МПа, загальне напрацювання N = 2350 циклів. Товщину змащувального шару визначали методом падіння напруги в режимі нормального тліючого розряду. Для базової оливи на перших $N \leq 250$ циклах напрацювання зафіксовано зрив змащувального шару в 75 % циклів. При $250 \leq N \leq 1000$ формується адсорбційний граничний шар завтовшки 0.036 – 1.056 мкм, а при $N \geq 1280$ товщина плівки складає 0.150 – 1.524 мкм і частота зривів знижується в середньому до 10 % циклів. Суспензія формує граничні шари інтенсивніше, проте їх стійкість нижча: повторна адаптація настає лише при $N \geq 2100$ циклів, товщина шару при цьому складає h = 0.130 – 1.620 мкм. На 55 % площі контакту зафіксовано хемосорбційні плівки завтовшки 0.051 – 0.186 мкм. Виявлено механізм утворення й адаптації граничних адсорбційних шарів на поверхнях тертя за умов частих пусків-зупинок, який полягає в тому, що активація поверхонь металу при багатоциклових діях і поляризація вуглеводневих молекул електричним полем твердої фази запускають формування шару, а подальше його руйнування оголює ювенільну поверхню металу, і вихід електронів з неї (екзоелектронна емісія) створює умови для утворення аніонів і радикалів та наростання хемосорбційних плівок. Одержані залежності товщини граничного шару від напрацювання дозволяють прогнозувати режим мащення неконформних вузлів тертя в умовах частих пусків-зупинок та обґрунтовано обирати концентрацію фулеренової присадки.

Ключові слова: тертя, мащення, граничний адсорбційний шар, хемосорбційна плівка, фулерен C_{60}, режим мащення, нестаціонарні умови, довговічність.

.

ISSN 2079-1372 Problems of Tribology, V. 31, No 3/121-2026, 115-122

Problems of Tribology
Website: http://tribology.khnu.km.ua/index.php/ProbTrib
E-mail: tribosenator@gmail.com

DOI: https://doi.org/10.31891/2079-1372-2026-121-3-115-122

Microscopic studies of the degradation processes of dental composite materials

V.I. Savulyak *[1] 0000-0002-4278-5155, **M. O.Vitavskyi** [1] 0009-0003-1024-9758, **A. V. Perlova** [2] 0000-0003-2501-9069, **A. P. Korol** [2] 0009-0009-2406-5283

[1] *Vinnytsia National Technical University, Ukraine*
[2] *Vinnytsia National Medical University, Ukraine*
E-mail: korsav84@gmail.com

Received: 15 August 2026: Revised 05 September 2026: Accept: 15 September 2026

Abstract

The article addresses the strength of dental composite materials, with particular emphasis on their resistance to compression. This type of loading is predominant in the anterior and posterior chewing teeth of humans. Understanding the mechanisms of initiation and development of internal stresses in materials used for restorative procedures is essential for the informed selection of materials and the further improvement of their properties.

The dental composite materials Estelite Asteria and Estelite Posterior, manufactured by Tokuyama Dental, were used in the experiments. A specimen preparation technique for compression loading was considered, and experimental studies were conducted with the recording of ultimate forces and stresses. The fractured specimens were examined to determine the type of failure. It was established that the plastic component during the deformation process is practically absent, while the load–deformation relationship is quasi-linear.

For further investigation, fragments of the materials were embedded in epoxy resin, after which cubic specimens were prepared. Based on these specimens, metallographic sections were produced for a detailed examination of the mechanisms of damage accumulation and the formation and propagation of microcracks within the material structure.

It was found that the fracture mechanisms and microcrack configuration depend on the size of the inorganic fillers in the composites. It was demonstrated that the avalanche-like loss of structural integrity of a composite material occurs when a certain microcrack density is reached, defined as the total crack length per unit area. At the same time, the sizes of the fragments bounded by cracks vary within a relatively narrow range. It was also found that the process of filling cracks with fracture products and substances from the service environment requires further investigation.

Keywords: composite materials, Estelite Asteria, Estelite Posterior, compression loading, strength, structure, microcracks, microscopic examination.

Introduction

Modern restorative dentistry is characterized by the widespread use of composite materials for the restoration of defects in the hard tissues of teeth. The use of such materials makes it possible to accurately restore the anatomical shape of a tooth while ensuring the required aesthetic and functional characteristics of the restoration [1–6].

One of the most important properties of dental composite materials is their ability to withstand mechanical loading [1, 2]. During the functioning of the dentoalveolar system, the dentition and the restorative materials used in it are subjected to compression, tension, bending, and shear forces [1, 9]. Among these, compressive loading is one of the major mechanical factors affecting restorations, particularly in the posterior regions of the dentition [1–3].

The mechanical behavior of a composite material is determined by its structure, the composition of the polymer matrix, and the characteristics of the inorganic filler [4, 7–9, 23]. The filler content, particle size and

Copyright © 2026 V.I. Savulyak, Vitavskyi M. O, Perlova A. V., Korol A. P. This is an open access article distributed under the Creative Commons Attribution License, which permits unrestricted use, distribution, and reproduction in any medium, provided the original work is properly cited.

shape, their distribution within the polymer matrix, and the strength of interfacial bonding are of particular importance [7–9, 23].

One of the modern composite materials is Estelite Asteria, manufactured by Tokuyama Dental. According to the manufacturer's information, the material contains 82% filler by weight and 72% by volume; its filler includes, among other components, silicon dioxide and zirconium dioxide, while the average size of the spherical particles is approximately 200 nm. Estelite Posterior is recommended for restorations in the posterior regions of the dentition, including occlusal surfaces. The manufacturer declares high mechanical properties of the material, which are important for its functional application. According to the manufacturer, the material contains 84% filler by weight and 70% by volume; the average particle size of the silicon–zirconium filler is approximately 2 µm [20–22, 24].

For composite materials, the composition and morphology of fillers play a critical role in the mechanical load-bearing and stress-transfer mechanisms, as well as in the distribution of internal mechanical stresses within the material structure, thereby influencing the kinetics of microcrack initiation and propagation under loading. [14–17]. One of the important indicators among the set of physicomechanical properties specified by the international standard ISO 4049:2019 is resistance to compressive failure. Ultimate compressive forces and stresses should be complemented by an investigation of the mechanisms of microcrack initiation and propagation, particularly in the region preceding failure [9–13]. Microscopic analysis of microcracks makes it possible to identify structural defects and assess their geometric characteristics [1, 9, 16, 25].

Therefore, the combination of mechanical testing and microscopic examination is appropriate for a comprehensive characterization of modern dental composite materials [20].

The aim of this study is to compare the mechanical strength of light-cured dental composite materials under compressive loading, based on their ultimate load-bearing capacity and microstructural changes, for Estelite Asteria and Estelite Posterior.

Materials and Methods. Two dental composite materials manufactured by Tokuyama Dental were investigated in this study: Estelite Asteria and Estelite Posterior. The materials were examined separately, without mixing them with each other. Five cylindrical specimens were prepared for each material (Fig. 1).

a b

Fig. 1. Specimens of composite materials for mechanical compression testing: a **– geometric dimensions;** b **– examples of actual specimens**

After the specimens had been formed and polymerized, their mass and geometric parameters were determined. Profield electronic scales with a weighing range of 0.1–500 g (YT02820), with an accuracy of at least 0.01 g, were used for mass measurements, while MK25 micrometers were used to measure the specimen dimensions.

The width of the microcracks was measured using a Euromex iScope IS.1152-EPL microscope. The area of the structural components on the surface of the metallographic sections and the lengths of the microcracks bounding them were measured using SOLIDWORKS software based on images of the metallographic sections obtained with Euromex iScope IS.1152-EPL microscopes.

To reveal microcracks and improve the accuracy of their measurements, the specimens were immersed in a 1% aqueous–ethanolic solution of methylene blue.

Table 1

Geometric characteristics of the investigated specimens

Parameter	Estelite Asteria	Estelite Posterior
Number of specimens	5	5
Mass , г	1,14 ±0,01	1,36±0,01
Diameter , мм	8,9±0,01	9,0±0,01
Height , мм	9,75±0,01	10,15±0,01
Cross-sectional area , м²	$6{,}218 \times 10^{-5}$	$6{,}3585 \times 10^{-5}$

The cylindrical specimens were placed between the compression platens of a PMM-125 hydraulic press, and the load was gradually increased until specimen failure occurred. Observation of the compression loading process showed that the force–deformation relationship remained linear, while failure occurred almost instantaneously, which is consistent with the findings of other authors for materials of similar composition [10, 11, 17, 18].

The maximum load, expressed in newtons (N), recorded immediately before specimen failure was taken as the ultimate load. Following compression loading, a microscopic examination of the fracture surface was performed. The crack network identified on the surface of the metallographic section, as well as the width and length of the cracks, was evaluated.

Results

The results of the conducted tests demonstrated differences in the ability of the investigated materials to resist compressive loading. The Estelite Posterior specimens exhibited a higher load-bearing capacity and withstood a maximum load that was 3 kN higher than the corresponding value for the Estelite Asteria specimens. In relative terms, the maximum load for Estelite Posterior was approximately 17.7% higher, while its compressive strength exceeded that of Estelite Asteria by approximately 15%.

Microscopic examination of the fracture surfaces of the failed specimens was performed at ×100 magnification using a Euromex iScope IS.1152-EPL microscope. Fragments of the fractured materials were immersed in a 1% aqueous–ethanolic solution of methylene blue, dried, and embedded in epoxy resin in special molds to obtain cubic specimens (Fig. 2).

Fig. 2. Fixation of material fragments in epoxy resin

From the samples described above, microsections were prepared for microscopic examination. The analysis established that compression loading results in the formation of microcracks in the structure of both investigated materials, characterized by distinct linear structural defects. As the cracks propagate, they become filled with fracture debris originating from the crack walls. Figure 3 shows an example of such a microcrack.

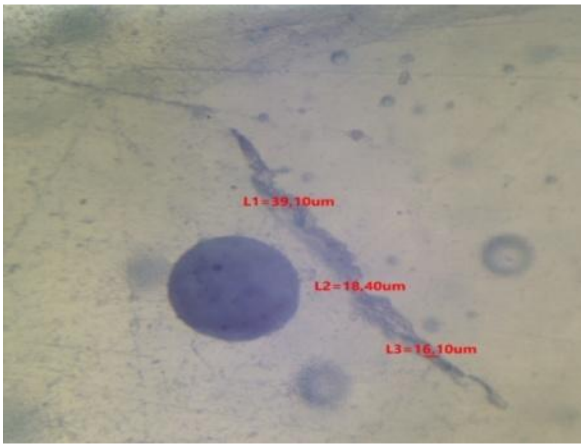

Fig. 3. Crack in Estelite Asteria material after compression loading, ×100

The identified crack propagates in the vicinity of bubble-like defects that formed in the material during its manufacturing process, but without directly interacting with them. This phenomenon may be explained based on the findings reported in [20]. It is likely that the stress fields formed around the bubble and the crack tip have the same sign, resulting in the formation of a potential barrier around the defect that prevents the crack from propagating directly toward the bubble [1, 9, 16, 25]. Under such conditions, the energetically most favorable crack propagation path is located at a certain distance from the defect.

Fig. 4 presents the results of measurements of crack opening width performed using a Euromex iScope IS.1152-EPL optical microscope. Statistical analysis of the results obtained for the Estelite Asteria specimens showed that the mean crack opening width was 24.50 μm.

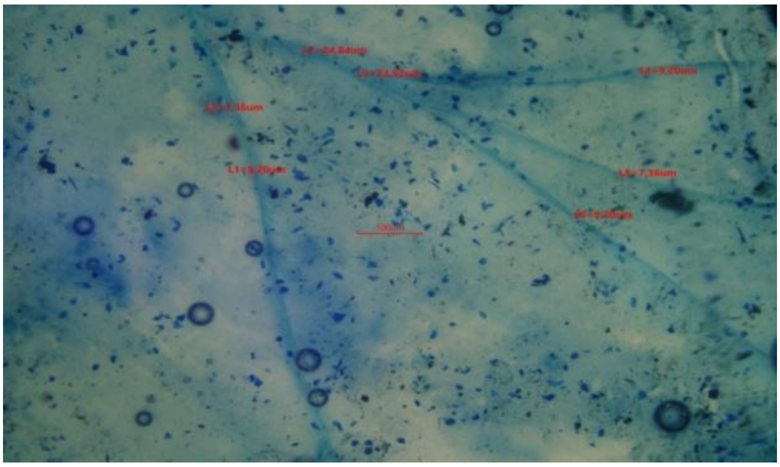

Fig. 4. Defects in Estelite Posterior material after compression loading, ×100

Fig. 4 shows a characteristic pattern of the initiation and subsequent development of a microcrack system. Initial crack formation is observed in the upper left corner of the micrograph, followed by crack branching and a subsequent increase in the number, length, and opening width of the cracks. As the magnitude of the applied load increases, the intensity of crack formation increases, resulting in the development of an extensive microcrack network (Fig. 5), the majority of which propagates along the boundaries of the structural blocks of the material.

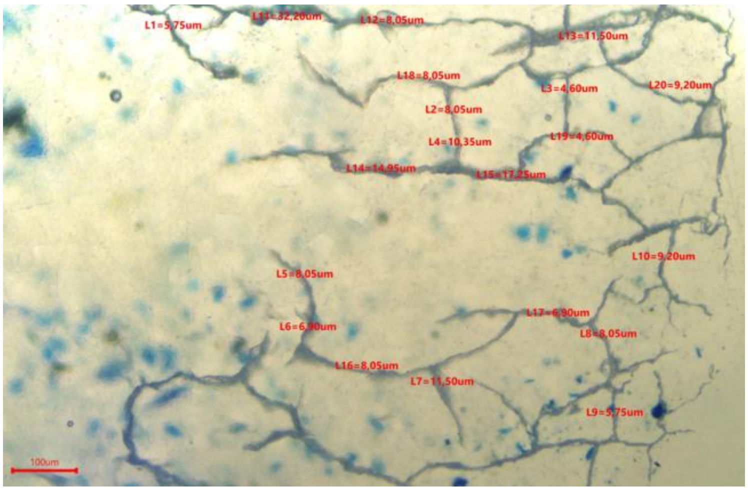

Fig. 5. Surface of a metallographic section of a fractured composite material specimen containing 50% Estelite Posterior and 50% Estelite Asteria, ×100

At this stage, the material is in a state of quasi-equilibrium and retains temporary structural integrity due to the presence of regions not affected by the microcracking process. Relaxation of internal stresses is accompanied by energy consumption for the initiation of new cracks, as well as for their subsequent propagation, which manifests itself as an increase in crack length and opening width [19, 24].

The results of measurements of crack opening width in the investigated materials are presented in Table 2.

Table 2

Results of microscopic examination and comparison of the mean crack opening width in Estelite Asteria and Estelite Posterior materials

parameter	Estelite Asteria	Estelite Posterior
Magnification	×100	×100
Mean crack width , мкм	**24,50**	**13,01**
Absolute difference , мкм	—	**11,49**
Reduction , %	—	**46,9**

Thus, the mean crack opening width in Estelite Posterior was 11.49 μm, or 46.9%, lower than that observed in Estelite Asteria.

Figure 5 shows the results of measuring the width of individual cracks on the metallographic section after failure of the material obtained by mixing 50% Estelite Posterior and 50% Estelite Asteria. The resulting dataset makes it possible to estimate the mean microcrack width in the investigated material during the degradation process.

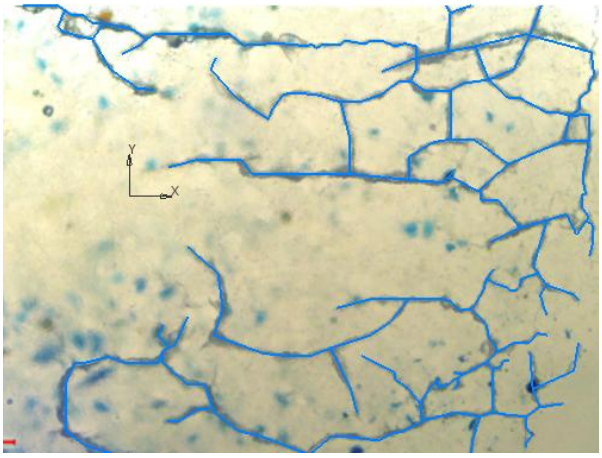

Fig. 6. Surface of a metallographic section of a composite material consisting of a mixture of 50% Estelite Posterior and 50% Estelite Asteria, with approximation lines applied to the microcracks using SOLIDWORKS software, ×100

After the approximation lines have been applied to the microcrack network, it becomes possible to measure the lengths of individual crack segments and the total length of all visible cracks intersecting the plane of the metallographic section.

Measurement of the total microcrack length within the plane of the metallographic section (Fig. 6), taking the actual scale into account, yielded approximately 5.5 mm per 1 mm². It is at approximately this defect density that failure of the material consisting of a mixture of 50% Estelite Posterior and 50% Estelite Asteria occurs.

Discussion

The results obtained demonstrated differences in the mechanical and structural behavior of the investigated dental composite materials. The data from the microscopic analysis of the fracture behavior and morphological features of crack formation provided an important complement to the results of the mechanical tests.

According to the results of the microscopic examination, the mean crack opening width in the Estelite Asteria specimens was 24.50 μm, whereas for Estelite Posterior this value was 13.01 μm, i.e., approximately 1.9 times lower. The absolute difference between the mean crack opening widths was 11.49 μm, while the relative reduction in this parameter for Estelite Posterior was 46.9%. Thus, the higher mechanical strength of Estelite Posterior under compression testing was accompanied by a smaller crack opening width after destructive loading.

The observed relationship may be associated with the specific features of structural damage initiation and development in the investigated materials. Under mechanical loading, stresses are redistributed between the polymer matrix and the inorganic filler. Localized stress concentrations may lead to the formation of microdefects, which, with a further increase in load, can transform into microcracks and propagate through the material, contributing to the formation of a fracture zone.

The nature and propagation path of cracks are determined by a combination of structural and mechanical factors, including the properties of the polymer matrix, the concentration, size, and morphology of the filler particles, as well as the strength of the interfacial interaction between the matrix and the filler. Differences in the structure and characteristics of the filler phase may therefore be one of the factors responsible for the differences in the mechanical behavior of the investigated composite materials.

At the same time, crack opening width cannot be regarded as an independent absolute criterion of material strength. Its informative value can only be assessed in conjunction with the results of mechanical tests and an analysis of fracture behavior. Within the framework of the present study, a comprehensive comparison of the obtained parameters revealed a consistent trend: the Estelite Posterior specimens exhibited a higher compressive strength and a smaller mean crack opening width compared with Estelite Asteria. This may indicate greater structural resistance of Estelite Posterior to crack development and opening under the conditions of the experiment.

Nevertheless, laboratory compression tests cannot fully reproduce the complex mechanical, physical, and chemical factors that determine the performance of dental restorations in the oral cavity. The service performance of composite materials may be affected by the nature and frequency of cyclic loading, temperature fluctuations, water sorption, polymerization shrinkage, the nature of adhesive interactions with dental tissues, and the characteristics of occlusal contacts.

Therefore, the results obtained should be interpreted as a characterization of the structural and mechanical behavior of the investigated materials under the specified laboratory conditions. They confirm the appropriateness of a comprehensive approach to the evaluation of dental composite materials, combining the results of mechanical testing with microscopic examination of fracture behavior and crack morphology on the surfaces of specimens after failure.

Prospects for further research

Further research should focus on investigating the mechanical and structural behavior of the materials under repeated cyclic loading, which will make it possible to assess their fatigue strength and damage accumulation characteristics.

An important area of further research is the performance of thermocyclic tests followed by an assessment of changes in the mechanical properties, structural state, and crack formation behavior of the investigated materials.

A promising direction is to perform quantitative morphometric analysis of microcracks, including the determination of their number, length, opening width, and distribution pattern. In addition, investigation of the morphology of fracture surfaces using scanning electron microscopy would be appropriate, as this would allow the mechanisms of crack initiation and propagation to be established in greater detail.

Conclusions

1. A comparative assessment of the mechanical and microstructural characteristics of the dental composite materials Estelite Asteria and Estelite Posterior was performed based on the results of compression loading tests.
2. Microscopic examination of the fracture surfaces of the specimens at ×100 magnification established that the mean crack opening width for Estelite Asteria was 24.50 μm, whereas for Estelite Posterior it was 13.01 μm. Thus, this parameter for Estelite Posterior was 11.49 μm, or 46.9%, lower than for Estelite Asteria.
3. The higher compressive strength values of Estelite Posterior were accompanied by a smaller mean crack opening width, which may indicate less pronounced structural degradation of the material in the fracture zone under the conditions of the conducted test.
4. The combined use of mechanical testing and microscopic analysis of fracture surfaces is an appropriate approach for assessing the structural and mechanical resistance of modern dental composite materials and determining the specific features of their fracture behavior.

References

1.Aminoroaya, A., Neisiany, R. E., Khorasani, S. N., Panahi, P., Das, O., Madry, H., Cucchiarini, M., & Ramakrishna, S. (2020). A review of dental composites: Methods of characterizations. *ACS Biomaterials Science & Engineering, 6*(7), 3713–3744. https://doi.org/10.1021/acsbiomaterials.0c00051

2.Aminoroaya, A., Neisiany, R. E., Khorasani, S. N., Panahi, P., Das, O., Madry, H., Cucchiarini, M., & Ramakrishna, S. (2021). A review of dental composites: Challenges, chemistry aspects, filler influences, and future insights. *Composites Part B: Engineering, 216*, 108852. https://doi.org/10.1016/j.compositesb.2021.108852

3.Cho, K., Rajan, G., Farrar, P., Prentice, L., & Prusty, B. G. (2022). Dental resin composites: A review on materials to product realizations. *Composites Part B: Engineering, 230*, 109495. https://doi.org/10.1016/j.compositesb.2021.109495

4.Elfakhri, F., Alkahtani, R., Li, C., & Khaliq, J. (2022). Influence of filler characteristics on the performance of dental composites: A comprehensive review. *Ceramics International, 48*(19), 27280–27294. https://doi.org/10.1016/j.ceramint.2022.06.314

5.Yadav, R., Lee, H., Lee, J.-H., Singh, R. K., & others. (2023). A comprehensive review: Physical, mechanical, and tribological characterization of dental resin composite materials. *Tribology International, 179*, 108102. https://doi.org/10.1016/j.triboint.2022.108102

6.Suryawanshi, A., & Behera, N. (2022). Dental composite resin: A review of major mechanical properties, measurements and its influencing factors. *Materialwissenschaft und Werkstofftechnik, 53*(5), 617–635. https://doi.org/10.1002/mawe.202100326

7.Habib, E., Wang, R., Wang, Y., Zhu, M., & Zhu, X. X. (2016). Inorganic fillers for dental resin composites: Present and future. *ACS Biomaterials Science & Engineering, 2*(1), 1–11. https://doi.org/10.1021/acsbiomaterials.5b00401

8.Randolph, L. D., Palin, W. M., Leloup, G., & Leprince, J. G. (2016). Filler characteristics of modern dental resin composites and their influence on physico-mechanical properties. *Dental Materials, 32*(12), 1586–1599. https://doi.org/10.1016/j.dental.2016.09.034

9.de Araújo-Neto, V. G., Sebold, M., de Castro, E. F., Feitosa, V. P., & Giannini, M. (2021). Evaluation of physico-mechanical properties and filler particles characterization of conventional, bulk-fill, and bioactive resin-based composites. *Journal of the Mechanical Behavior of Biomedical Materials, 115*, 104288. https://doi.org/10.1016/j.jmbbm.2020.104288

10.Gornig, D. C., Maletz, R., Ottl, P., & Warkentin, M. (2022). Influence of artificial aging: Mechanical and physicochemical properties of dental composites under static and dynamic compression. *Clinical Oral Investigations, 26*(2), 1491–1504. https://doi.org/10.1007/s00784-021-04122-0

11.Wendler, M., Stenger, A., Ripper, J., Priewich, E., Belli, R., & Lohbauer, U. (2021). Mechanical degradation of contemporary CAD/CAM resin composite materials after water ageing. *Dental Materials, 37*(7), 1156–1167. https://doi.org/10.1016/j.dental.2021.04.002

12.Hirokane, E., Takamizawa, T., Tamura, T., Shibasaki, S., Tsujimoto, A., Barkmeier, W. W., Latta, M. A., & Miyazaki, M. (2021). Handling and mechanical properties of low-viscosity bulk-fill resin composites. *Operative Dentistry, 46*(5), E185–E198. https://doi.org/10.2341/20-253-L

13.Sulaiman, T. A., Suliman, A. A., Mohamed, E. A., Rodgers, B., Altak, A., & Johnston, W. M. (2022). Mechanical properties of bisacryl-, composite-, and ceramic-resin restorative materials. *Operative Dentistry, 47*(1), 97–106. https://doi.org/10.2341/20-191-L

14.Ling, L., Lai, T., & Malyala, R. (2022). Fracture toughness and brittleness of novel CAD/CAM resin composite block. *Dental Materials, 38*(12), e308–e317. https://doi.org/10.1016/j.dental.2022.11.012

15.Varghese, J. T., Cho, K., Raju, P., Farrar, P., Prentice, L., & Prusty, B. G. (2023). Effect of silane coupling agent and concentration on fracture toughness and water sorption behaviour of fibre-reinforced dental composites. *Dental Materials, 39*(4), 362–371. https://doi.org/10.1016/j.dental.2023.03.002

16.Tohidkhah, S., Jin, J., Zhang, A., Aregawi, W., Morvaridi-Farimani, R., Daisey, E. E., Zhang, L., & Fok, A. S. L. (2024). Post-failure analysis of model resin-composite restorations subjected to different chemomechanical challenges. *Dental Materials, 40*(6), 889–896. https://doi.org/10.1016/j.dental.2024.04.005

17.Ning, K., Yang, F., Bronkhorst, E., Ruben, J., Nogueira, L., Haugen, H., Loomans, B., & Leeuwenburgh, S. (2023). Fatigue behaviour of a self-healing dental composite. *Dental Materials, 39*(10), 913–921. https://doi.org/10.1016/j.dental.2023.08.172

18.Lima, V. P., Machado, J. B., Zhang, Y., Loomans, B. A. C., & Moraes, R. R. (2022). Laboratory methods to simulate the mechanical degradation of resin composite restorations. *Dental Materials, 38*(1), 214–229. https://doi.org/10.1016/j.dental.2021.12.006

19.Alshali, R. Z., Salim, N. A., Satterthwaite, J. D., Silikas, N., & Watts, D. C. (2021). Effects of alternatively used thermal treatments on the mechanical and fracture behavior of dental resin composites with varying filler content. *Journal of the Mechanical Behavior of Biomedical Materials, 117*, 104424. https://doi.org/10.1016/j.jmbbm.2021.104424

20.Algamaiah, H., Silikas, N., & Watts, D. C. (2021). Polymerization shrinkage and shrinkage stress development in ultra-rapid photo-polymerized bulk fill resin composites. *Dental Materials, 37*(4), 559–567. https://doi.org/10.1016/j.dental.2021.02.012

21.Aregawi, W. A., & Fok, A. S. L. (2021). Shrinkage stress and cuspal deflection in MOD restorations: Analytical solutions and design guidelines. *Dental Materials, 37*(5), 783–795. https://doi.org/10.1016/j.dental.2021.02.003

22.Taylor, R., Fuentealba, R., Brackett, W. W., & Roberts, H. W. (2021). 24-hour polymerization shrinkage of resin composite core materials. *Journal of Esthetic and Restorative Dentistry, 33*(5), 775–785. https://doi.org/10.1111/jerd.12788

23.Zhang, S., Wang, X., Yang, J., Chen, H., & Jiang, X. (2023). Micromechanical interlocking structure at the filler/resin interface for dental composites: A review. *International Journal of Oral Science, 15*, 21. https://doi.org/10.1038/s41368-023-00226-3

24.Feng, D., He, X., Dong, S., Yang, Z., Zhang, L., & Zhu, S. (2024). Study on the polymerization shrinkage and mechanical-physical properties of dental resin composite modified by polyurethane dimethacrylate and glass flake fillers. ***Journal of Dentistry, 151***, 105426. https://doi.org/10.1016/j.jdent.2024.105426

25.Ren, Z., Chen, H., Wang, R., & Zhu, M. (2024). Comparative assessments of dental resin composites: A focus on dense microhybrid materials. *ACS Biomaterials Science & Engineering, 10*(6). https://doi.org/10.1021/acsbiomaterials.4c00403

Савуляк В.І., Вітавський М. О.Перлова А.В. , Король А.П. Мікроскопічні дослідження процесів руйнування стоматологічних композиційних матеріалів

У статті розглянуто проблеми міцності композиційних матеріалів стоматологічного призначення, зокрема їхньої стійкості до стискання. Цей вид навантаження є переважаючим для фронтальних та бокових жувальних зубів людини. Розуміння механізмів виникнення та розвитку внутрішніх напружень у матеріалах, що застосовуються для реставраційних робіт, має важливе значення для обґрунтованого вибору матеріалів та подальшого вдосконалення їхніх властивостей. Для експериментів використовували композиційні стоматологічні матеріали Estelite Asteria та Estelite Posterior виробництва Tokuyama Dental. Розглянуто методику виготовлення зразків для навантаження стисканням, проведено дослідження з фіксацією граничних зусиль та напружень. Зруйновані зразки розглянуті на предмет визначення виду руйнування. Встановлено, що практично відсутня пластична складова під час процесу деформування, а залежність навантаження – деформація є квазіклінійною. З метою подальшого дослідження уламки матеріалів фіксували в епоксидній смолі, після чого виготовляли кубічні зразки. На їх основі готували мікрошліфи для детального дослідження механізмів накопичення пошкоджень, формування та розвитку мікротріщин у структурі матеріалу. Виявлено, що механізми руйнування та конфігурація мікротріщин залежать від розмірів неорганічних наповнювачів композитів. Показано, що лавиноподібна втрата цілісності виробу з композиційних матеріалів відбувається при досягненні певної щільності мікротріщин (сумарна довжина тріщин на одиницю площі). При цьому розміри фрагментів, обрамлених тріщинами, змінюються в достатньо вузьких межах. Виявлено, що процес заповнення тріщин продуктами руйнування та середовища функціонування вимагає подальших досліджень.

Ключові слова: композиційні матеріали, Estelite Asteria, Estelite Posterior, навантаження стисканням, міцність, структура, мікротріщини, мікроскопічне дослідження.

ISSN 2079-1372 Problems of Tribology, V. 31, No 3/121-2026, 123-130

Problems of Tribology
Website: http://tribology.khnu.km.ua/index.php/ProbTrib
E-mail: tribosenator@gmail.com

DOI: https://doi.org/10.31891/2079-1372-2026-121-3-123-130

Tribological Characteristics of Pulse-Anodized Layers on Aluminum

V. Hvozdetskyi[1] 0000-0002-2956-5182 , D. Yaremchuk[2] 0009-0006-8575-5657

[1] *Karpenko Physico-Mechanical Institute of the National Academy of Sciences of Ukraine, Ukraine*
[2] *Ukrainian National Forestry University, Ukraine*
E-mail: gvosdetcki@gmail.com

Received: 22 July 2026: Revised 25 August 2026: Accept: 20 September 2026

Abstract

This study develops advanced electrochemical synthesis methods for high-performance hard anodic coatings on Al-Cu-Mg alloy (AA2024/D16) substrates. The research systematically investigates the synergistic effects of chemical electrolyte modification via hydrogen peroxide or ozone additions, high-voltage pulse hard anodizing (PHA) modes, and post-synthetic thermal treatments on the coating kinetics and phase composition. It was established that lowering the electrolyte temperature to -5 °C suppresses acid-induced chemical surface dissolution, promoting the steady growth of a dense monohydrated boehmite phase ($Al_2O_3 \cdot H_2O$) with significantly enhanced microhardness. Conversely, elevating the synthesis temperature above 0 °C triggers a structural phase transition toward a trihydrated gibbsite phase ($Al_2O_3 \cdot 3H_2O$). Tribological evaluations under dry sliding and boundary lubrication conditions (mineral and synthetic oils) revealed a unique self-lubricating mechanism: the lower-hardness gibbsite phase undergoes mechanical shearing during sliding contact and forms a continuous, self-replenishing tribo-transfer solid lubricant film on both steel and ceramic counterfaces. Furthermore, a post-synthetic thermal treatment within 100–400 °C followed by hydrothermal boiling induces target matrix dehydration, doubling the coating's abrasive wear resistance and providing a 5- to 10-fold wear reduction relative to the untreated AA2024 aluminum substrate. The pulse modulation effectively mitigates local thermal concentrations within the pore channels, enabling optimal tribomechanical responses under diverse wear modes. Objective: To enhance the durability of aluminum alloys using surface engineering methods. Research methodology: A novel approach involving pulse-mode anodizing was employed to form a surface layer on the aluminum alloy; the physicochemical properties and wear resistance of this layer under friction conditions were investigated. Scientific novelty: Synthesis conditions and electrolyte composition were determined for forming an anodized layer with a specific phase composition. Practical significance: Pulse-mode anodizing and heat treatment ensure improved wear resistance of the aluminum alloy.

Keywords: hard anodizing; aluminum alloys; boehmite; gibbsite; thermal treatment; tribo-transfer film; boundary lubrication, friction.

Introduction: Problem Statement and Signifigance

Aluminum and its alloys are extensively utilized across diverse industrial sectors for modern equipment manufacturing. They serve as critical structural materials in aerospace and aviation vehicles, automotive engineering, rail and maritime transport, and general machinery. However, their inherently low wear resistance and poor tribological performance severely restrict wider industrial application. Currently, the deployment of aluminum alloys has become essential for unmanned aerial vehicle (UAV) manufacturing. The rapid advancement of UAV technologies demands lightweight aluminum alloys (such as Al-Mg, Al-Cu-Mg, and Al-Si series) for critical components, including internal combustion engine elements, gimbal suspension mounting systems, transmission components, and gearbox housings. From a military perspective, drones operate under extreme environmental conditions, such as sandstorms, marine salt fog, and severe engine thermal loads. Conventional anodization techniques fail to provide sufficient protection against abrasive wear and fragmentation impacts. From a civilian standpoint, extending the operational lifespan and reducing structural weight by replacing steel components with surface-hardened aluminum significantly improves payload capacity and flight endurance. To enhance the physical, mechanical, and tribological properties of structural aluminum materials, high-voltage pulse

Copyright © 2026 V. Hvozdetskyi, D. Yaremchuk. This is an open access article distributed under the Creative Commons Attribution License, which permits unrestricted use, distribution, and reproduction in any medium, provided the original work is properly cited.

hard anodization (PHA) is widely adopted. Nevertheless, conventional pulse anodization exhibits significant drawbacks, including a low growth rate of theoxide/hydroxide layer, insufficient hardness, and suboptimal wear resistance. To improve the functional performance of the anodized layers, this study proposes modifying the sulfuric acid electrolyte with hydrogen peroxide H_2O_2 combined with post-synthetic thermal treatment of the formed anodic oxide layer.

Literature review

Pulse Hard Anodizing (PHA) and Self-Lubricating Tribo-Films. Conventional direct current (DC) anodizing frequently fails under extreme sliding conditions due to local thermal concentration inside the structural pores, which leads to macro-defects and micro-cracking. To eliminate this issue, Pulse Hard Anodizing (PHA) has emerged as a frontline technological breakthrough [1 - 5]. Current publications demonstrate that pulse current modulations provide a crucial "cooling relaxation time" during the off-period of the pulse cycle. This effectively mitigates spatial heat accumulation at the pore base, facilitating the uniform synthesis of a less-defective oxide matrix over extended processing periods. From a tribological standpoint, recent boundary lubrication and dry sliding investigations (published in Wear and Coatings) indicate a shifting paradigm: high hardness is no longer the sole requirement for wear mitigation. Researchers have discovered that when a hydrated phase like gibbsite participates in oscillatory sliding contact against steel or ceramic counterfaces, it undergoes controlled mechanical shearing [6 - 8]. This process leads to the deposition of a stable tribo-transfer film (solid lubricant) within the contact interface. This dynamic interfacial film undergoes continuous renewal, dramatically lowering the wear rate even when working under boundary lubrication with mineral or advanced synthetic oils [8 - 12].

Aim of the Research

The aim of this work is to establish the mechanisms governing parameter variations and to optimize the high-voltage pulse anodization process during the synthesis of hard anodic oxide layers on an AD0 aluminum alloy as a baseline material.

Materials and Methods

Flat specimens with dimensions of 20 × 20 × 5 mm were prepared from AA2024 alloy. Prior to the anodization process, the specimens underwent a multi-step surface pretreatment: *Degreasing:* Immersed in an aqueous suspension of CaO + MgO to remove organic contaminants. Rinsing: Washed sequentially in cold and warm tap water. *Desmutting:* Immersed for 30 s in an aqueous solution of nitric acid 400 g/L HNO_3 to remove intermetallic smuts. *Final Rinsing:* Thoroughly rinsed in distilled water and dried. Anodization Setup and Electrochemical Modes. The oxide layers were synthesized using custom-designed electrochemical equipment (Fig. 1a). A 20 wt % aqueous solution of sulfuric acid H_2SO_4 prepared with distilled water served as the base electrolyte. To investigate the effect of temperature conditions, the electrolyte temperature in the setup was maintained within the range of -5°C to +5°C with an accuracy of ±0.1°C. The total duration of the anodization process was 60 min for all experiments. Anodization was performed in two distinct electrical modes (Fig. 1b): Steady-State (Direct Current) Mode (II): Conducted at a stabilized current density of 5 A/dm^2 with a constant voltage of V = 60 V. High-Voltage Pulse Mode (I–III): Executed in cycles consisting of three steps:

Step I (Pulse Initiation): High-voltage pulse stage with V = 140 V and an instantaneous current density of I = 1.4 A/dm^2.

Step II (Main Working Period): Base anodization stage with V = 40 V and I = 0.4 A/dm$_2$.

Step III (Pulse Pause): Off-period where both voltage V and current I were reduced to zero.

Troughout the pulse cycling, the effective average current density was maintained at 5 A/dm^2 via a specialized control unit.

Electrolyte Modification and Process Intensification. To accelerate the layer growth rate and enhance the mechanical performance (hardness and wear resistance) of the coatings, the baseline sulfuric acid electrolyte was modified using two approaches: *Chemical modification:* Addition of hydrogen peroxide H_2O_2 in concentrations of 30, 50, 70, and 100 ml/l. Ozone gas sparging: Continuous bubbling of an ozone-air mixture through the electrolyte at a constant ozone flow rate of 5 mg/min/L.

Microstructural and Physical Characterization. The microstructure, surface morphology, and elemental composition of the synthesized oxide layers and deposited coatings were analyzed using: Optical Microscopy Neophot 22 metallographic microscope, Scanning Electron Microscopy (SEM) Carl Zeiss EVO-40XVP system operated in high-vacuum mode. Energy-Dispersive X-ray Spectroscopy (EDS): INCA Energy 350 microanalysis system coupled with the SEM for elemental profiling. X-ray Diffraction (XRD**):** DRON-3 diffractometer to determine the phase composition of the oxide scales.

Tribological Testing. The mechanical and functional performance of the synthesized layers was evaluated through comprehensive tribological testing according to standardized methods. The wear resistance was characterized under the following contact conditions: Three-body abrasive wear: Testing with loose/unfixed abrasive particles. Two-body abrasive wear: Testing against fixed abrasive media. Oscillatory sliding wear

(Fretting/Reciprocating): Evaluated under dry friction (unlubricated) conditions as well as in the presence of various industrial lubricants.

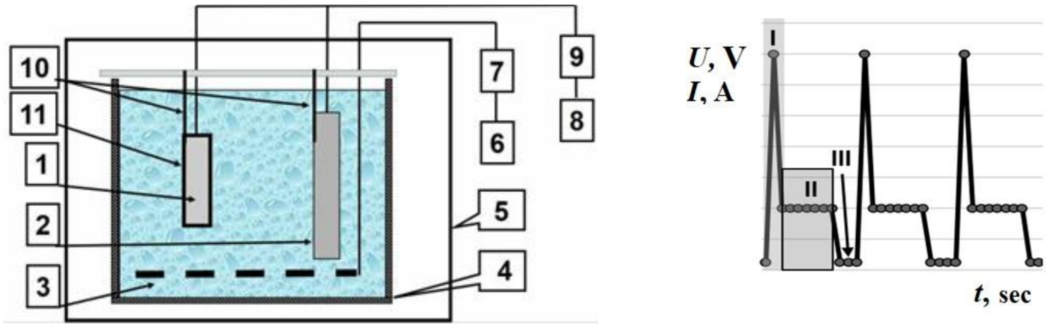

a *b*

Fig. 1. Schematic representation of the experimental setup and electrical parameters: (a**) Schematic diagram of the custom pulse anodization equipment: *1*—specimen (anode); *2*—counter-electrode (cathode); *3*—gas sparger (bubbler); *4*—electrolyte tank 20 wt.% H_2SO_4 solution); *5*—thermal stabilization chamber (operational range from -4 °C to +8 °C ; *6*—air compressor; *7*—flow control unit for the compressor and sparger; *8*—power supply (maintaining an average current density of 5 A/dm2; *9*—pulse modulation and power control unit; *10*—electrode and specimen fixture; *11*—synthesized anodic oxide layer. (**b**) Schematic profile of voltage U and current I variations over time t during the high-voltage pulse anodization cycle**

Results and Discussion

Microstructure and Morphological Features of the Anodic Layers

The synthesized anodic oxide layers characteristically consist of a thin, dense inner barrier layer 10—20 nm in thickness and a porous outer layer with fine, vertically oriented pores extending to the surface (Fig. 2). The highly packed hexagonal columnar cells, each containing a cylindrical pore channel at its center, are composed of heavily hydrated aluminum oxide $Al_2O_3 \cdot nH_2O$. The hydration degree (the number of water molecules, n highly depends on the electrochemical synthesis mode and varies from 1 to 3. Specifically, for the layers formed in the sulfuric acid electrolyte, the structural parameters of the hexagonal cells do not exceed 50 nm, the pore diameters are limited to approximately 25 nm, and the barrier layer thickness ranges within 10-30 nm.

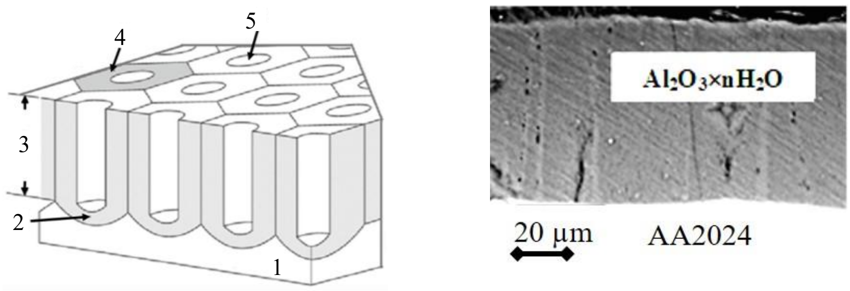

a *b*

Fig. 2 Morphological model of the anodic film formation: (a**) Schematic diagram of pore development: *1*—aluminum substrate, *2*—barrier layer, *3*—barrier layer thickness, *4*—porous anodic layer, *5*—pore channel; (**b**) Cross-sectional structural model of the hexagonal cellular oxide matrix**

Effect of Electrolyte Composition and Oxidation Mechanisms

Experimental data revealed that the addition of hydrogen peroxide H_2O_2 to the baseline electrolyte, as well as ozone O_3 gas sparging, significantly increases both the total thickness and the microhardness of the synthesized anodic coatings. By increasing the H_2O_2 concentration in the sulfuric acid bath from 0 to 70 mL/L, the coating thickness expanded by 33%, growing from approximately (60 to 100 mum (Fig. 3a). Concurrently, the coating microhardness enhanced by 25%, rising from 400 to 500 $HV_{0.3}$. (Fig. 3b). The most pronounced peak in mechanical performance was achieved at an H_2O_2 content of 30 mL/L, where the abrasive wear resistance of the pulse-anodized layer improved by 23%, as evidenced by the lowest mass loss values (Fig. 3b). The simultaneous growth of coating thickness and microhardness during hard anodization (HA) with H_2O_2 modification or O_3 sparging can be attributed to the altered kinetics of oxygen species transport. The introduction of these powerful oxidizing agents enriches the pore channels with active oxygen ions according to the following decomposition and ionization pathways: : ($H_2O_2 \rightarrow 2H^{+2} + 2O^{-2}$, або $O_3 \rightarrow O_2 + O^{-}$). The elevated concentration of highly reactive oxygen ions promotes a structural transition within the aluminum hydroxide/oxide matrix. It drives the dehydration process, reducing the number of chemically bound water molecules in the film from three to one $Al_2O_3 \cdot 3H_2O$ (Gibbsite/Bayerite)→ $Al_2O_3 \cdot H_2O$ (Boehmit). This partial dehydration yields a more compact, dense, and crystalline bohmite-like or low-hydrated alumina structure, which directly accounts for the drastic improvement in hardness and abrasive wear resistance.

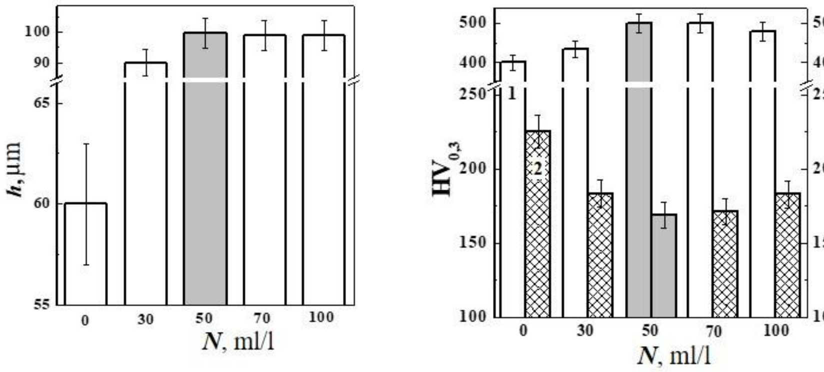

a *b*

Fig. 3. Influence of the hydrogen peroxide concentration n in the electrolyte (at a fixed synthesis duration of 60 min on the coating properties: (a) **Anodic layer thickness h;** (b) **Layer microhardness $HV_{0.3}$ (*1*) and mass loss W during standardized abrasive wear resistance tests (*2*)**

Post-Synthetic Thermal Treatment of Anodic Layers

Post-synthetic thermal treatment of the anodized layers induced further dehydration of the oxide matrix, driving a significant reduction in the chemically bound water molecules from three to one $n = 3 \rightarrow 1$. Specifically, as the heat treatment temperature was elevated up to 400 C, the coating microhardness enhanced from the initial 400 HV0.3 and stabilized at approximately 650 $HV_{0.3}$. Concurrently, this structural alteration led to a nearly 2.5-fold increase in abrasive wear resistance (Fig. 4).

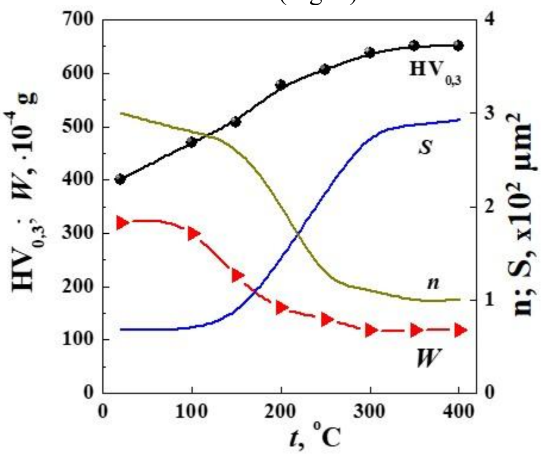

Fig. 4. Influence of the thermal treatment temperature T on the water molecule content n within the aluminum hydroxide matrix, coating microhardness $HV_{0.3}$, mass loss W during standardized abrasive wear tests, and the wear track cross-sectional area S after frictional wear testing.

Comparative Analysis of Steady-State and Pulse Hard Anodization Kinetic Features

The kinetics of the anodization process played a decisive role in determining the final coating properties. It was established that regardless of the electrochemical mode applied (steady-state direct current or high-voltage pulse mode), increasing the synthesis duration led to a substantial improvement in both the coating microhardness (Fig. 5a) and the corresponding abrasive wear resistance of the AA2024 (D16) aluminum alloy substrate (Fig. 5b).

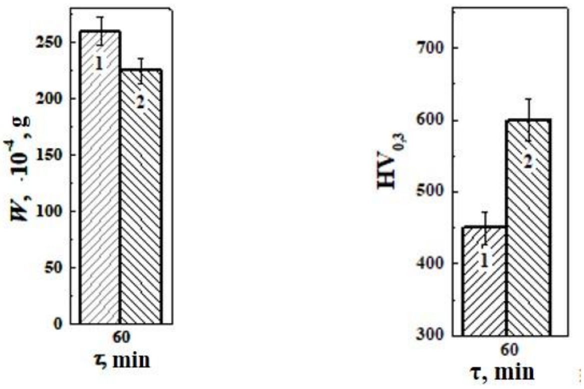

a *b*

Fig. 5. Comparative effect of steady-state (1) and high-voltage pulse (2) anodization modes as a function of processing time on: (a) **microhardness $HV_{0.3}$;** (b) **mass loss W of the anodized AA2024 (D16) aluminum alloy specimens during standardized abrasive wear resistance testing.**

Notably, the positive correlation between the synthesis duration and these functional parameters was significantly more pronounced when the high-voltage pulse mode was employed. The pulse modulation effectively mitigated local thermal concentrations within the pore channels, enabling the steady growth of a denser, less defective, and more wear-resistant crystalline oxide structure over extended treatment times compared to the conventional steady-state method.

Effect of Electrolyte Temperature on the Thickness, Phase Composition, and Tribological Behavior of the Coatings

It was established that conducting the anodization process at a lower electrolyte temperature -5ºC promotes the synthesis of oxide layers with enhanced microhardness due to the suppressed rate of chemical dissolution. Conversely, elevating the electrolyte temperature from -5 C to +5 C accelerated the dissolution processes, which led to a simultaneous reduction in both the total coating thickness (Fig. 6a) and its microhardness (Fig. 6b). X-ray diffraction and phase analysis revealed that coatings synthesized at lower temperatures 0 ºC and -5 ºC were dominated by the boehmite phase $Al_2O_3•H_2O$, containing a single chemically bound water molecule. As the electrolyte temperature was increased to +5 ºC, a phase transition phase coexistence was observed, with the dominant phase shifting toward gibbsite $Al_2O_3•3H_2O$, which locks three water molecules into its crystal lattice. For both the steady-state (1) and high-voltage pulse (2) hard anodization modes, decreasing the electrolyte temperature from +5 ºC to -5 ºC yielded an increase in the final coating thickness h (Fig. 6a). Specifically, the coating thickness increased by 12% for the steady-state mode and by 23% for the pulse mode under condition (II). This temperature-dependent behavior of the coating thickness is governed by the competitive kinetics between electrochemical oxide synthesis and chemical dissolution by the acid electrolyte. Theoretically, an increase in electrolyte temperature intensifies ionic transport, which should accelerate oxide growth. However, it simultaneously accelerates the aggressive surface dissolution of the formed anodic layer, leading to its thinning. Therefore, the observed thickness profiles reflect the synergistic interplay between accelerated electrochemical synthesis and the aggressive acid-induced dissolution that becomes dominant at temperatures above 0 ºC. The results demonstrated that the pulse-anodized layer featuring the monohydrate boehmite structure $Al_2O_3•H_2O$, synthesized at -5 ºC, exhibited the highest microhardness $HV_{0.3}$ and the maximum abrasive wear resistance 1/W (Fig. 6b). On the contrary, the coating containing the trihydrate gibbsite structure $Al_2O_3•3H_2O$, synthesized at +5 ºC, demonstrated the highest frictional wear resistance 1/S during dry sliding interaction against a steel ball counterface. Notably, an identical performance trend was maintained when evaluating the tribological pair with a ceramic ball counterface, proving that the chemical structure of the oxide layer dictates its tribomechanical response under different wear modes.

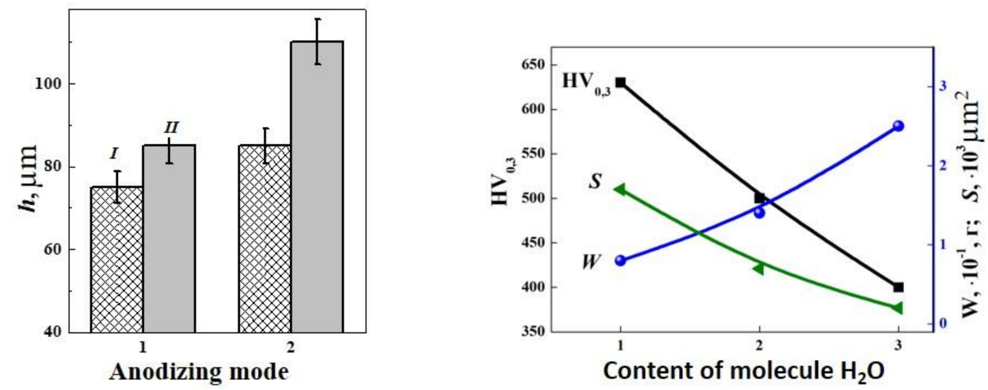

a b

Fig. 6. Effect of electrolyte temperature during a 60-min hard anodization process under steady-state (1) and high-voltage pulse (2) modes: (a) coating thickness h obtained at +5 oC (I) and -5 oC (II); (b) correlation between the water molecule content (n) within the anodic matrix and its microhardness HV0.3, abrasive wear resistance 1/W, and frictional wear resistance 1/S

Tribological Behavior under Boundary Lubrication and the Tribo-Transfer Mechanism

The distinct variations in the microhardness and abrasive wear resistance of the pulse hard anodized layers (PHAL) as a function of the chemically bound water content are closely related to their dehydration profiles and structural transitions. To evaluate this performance, the sliding wear tracks of the anodic layers synthesized via steady-state and high-voltage pulse modes at an electrolyte temperature of -5 ºC were compared against a steel ball counterface under diverse lubrication regimes.

The experimental data revealed that under all tested conditions—including dry sliding, boundary lubrication with mineral oil (I-20), and lubrication with synthetic oil (EDGE 5W-30)—the PHAL specimens consistently exhibited the lowest volumetric wear (Fig. 7). Depending on the specific friction pair and the operational parameters of the oscillatory sliding, the wear resistance of the coatings synthesized in the pulse mode increased by a factor of 2 to 19 compared to the untreated AA2024 aluminum alloy substrate, and by 1.4 to 5.8 times relative to the coatings formed under conventional steady-state direct current. Surface morphology analysis indicated that the steel counterface caused negligible abrasive wear to the anodized layer. Instead, it primarily induced the smoothing of initial machining asperities (Fig. 8). During this process, the outer hydrated oxide layer $Al_2O_3 \cdot nH_2O$ was mechanically sheared and transferred, acting as a solid lubricant film deposited onto the contacting surfaces of either the steel or ceramic ball counterfaces.

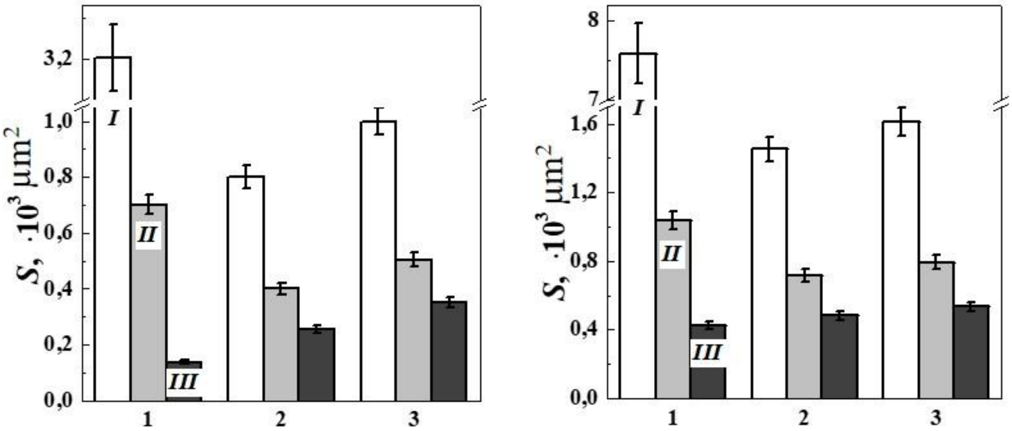

Fig. 7. Frictional wear profiles of the AA2024 alloy substrate without coating (I), with a steady-state anodic coating (II), and with a high-voltage pulse anodic coating (III) under oscillatory sliding conditions against steel (a) and ceramic (b) ball counterfaces tested: (1) without lubrication (dry sliding); (2) under mineral oil (I-20) lubrication; (3) under synthetic oil (EDGE 5W-30) lubrication.

.

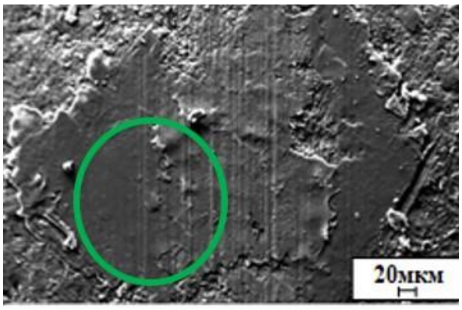

Element	Weight %	Atomic %
O	1.22	4.12
Al	0.43	0.87
Cr	1.74	1.80
Fe	96.61	93.22
Total	100.00	

Fig. 8. Tribotransfer gibbsite film and its corresponding energy-dispersive X-ray spectroscopy (EDS) elemental analysis on the wear scar surface of the ceramic ball counterface

Discussion of the Structural-Tribological Synthesis Mechanisms

Energy-dispersive X-ray spectroscopy (EDS) confirmed the formation of a continuous gibbsite-rich tribo-film on the friction surfaces of both the steel and ceramic counterfaces. This evidence suggests that a dynamic, self-lubricating interfacial film forms directly within the contact zone. Instead of undergoing work-hardening or severe delamination during cyclic sliding, this film undergoes continuous tribochemical renewal and replenishment.

In summary, the abrasive wear resistance and overall tribological behavior of the anodized layers are heavily dictated by the specific hydration state (the number of chemically bound water molecules) within the oxide matrix:

- The boehmite phase $Al_2O_3 \cdot H_2O$ provides the coatings with high microhardness and superior resistance to harsh abrasive scratching.

- The gibbsite phase $Al_2O_3 \cdot 3H_2O$ provides excellent self-lubricating capability, optimizing the friction coefficient and mitigating wear during sliding contact.

Crucially, the concentration of chemically bound water molecules in the aluminum hydroxide matrix $Al_2O_3 \cdot nH_2O$ can be precisely tailored from n = 1 (boehmite) to n = 3 (gibbsite) via three independent processing routes:

- Chemical modification**:** Modulating the electrolyte composition by introducing H_2O_2 in concentrations ranging from 10 to 50 mL/L.

- Thermal control during synthesis**:** Adjusting the electrolyte operational temperature within the range of -5 °C to +5 °C.

- Post-synthetic thermal treatment**:** Subjecting the synthesized anodic coatings to controlled heat treatment within a temperature range of 100 °C to 300 °C.

Conclusions

A novel electrolyte modification method for synthesizing hard anodic coatings (HACs) on commercially pure aluminum **(**AA2024**)** was developed. The approach involves introducing 3–5% hydrogen peroxide H_2O_2 into a base electrolyte of a 20% aqueous sulfuric acid H_2SO_4 solution or systematically purging the bath with ozone O_3. Implementing this oxidizing method effectively enhanced the coating growth kinetics and structural density, resulting in a 50–60% increase in total coating thickness**, a** 40–50% enhancement in microhardness**, a** 15% improvement in abrasive wear resistance**,** and a 30% reduction in wear volume when operating within a sliding friction pair against a bearing steel ball counterface.

A comprehensive post-synthetic thermal treatment protocol for the developed anodic layers was proposed. The process consists of controlled thermal exposure within a 100–400 °C range, followed by subsequent sealing via hydrothermal boiling in distilled water. This specific post-treatment sequence stimulates target dehydration and phase transition, driving the formation of a dense boehmite phase $Al_2O_3 \bullet H_2O$ within the oxide matrix. Consequently, this phase stabilization doubled the abrasive wear resistance of the coatings and provided a 5- to 10-fold increase in wear resistance compared to the untreated AA2024 (D16) aluminum alloy benchmarks.

A high-voltage pulse hard anodizing (PHA) technique was developed to actively regulate the crystal structure of the anodic matrix, enabling the precise synthesis of either a single-phase oxide or a multi-phase structural mixture. The phase distribution is dynamically controlled by adjusting the electrolyte operating temperature within a -5 °C to +10 °C range**.** Within this system:

The monohydrated boehmite phase yields maximum coating microhardness and superior resistance to abrasive scratching.

The trihydrated gibbsite phase $Al_2O_3 \bullet 3H_2O$ provides exceptional self-lubricating tribological behavior. This is due to the dynamic formation and continuous replenishment of a highly stable gibbsite-rich tribo-transfer film directly within the contact zone when sliding against steel or ceramic counterfaces.

The coatings synthesized via this PHA method demonstrated a 15–20% higher thickness and a 1.5- to 3-fold higher wear resistance than those produced via conventional steady-state direct current modes, while outperforming the untreated AA2024 (D16) substrate by 2.5 to 8 times**.**

References

1.Student, M., Pohrelyuk, I., Padgurskas, J., Rukuiža, R., Hvozdets'kyi, V., Zadorozhna, K., Veselivska, H., Student, O., & Tkachuk, O. (2023). Abrasive wear resistance and tribological characteristics of pulsed hard anodized layers on aluminum alloy 1011 in tribocontact with steel and ceramics in various lubricants. *Coatings, 13*(11), 1883. https://doi.org/10.3390/coatings13111883

2.Guo, F., Cao, Y., Wang, K., Zhang, P., Cui, Y., Hu, Z., & Xie, Z. (2022). Effect of the anodizing temperature on microstructure and tribological properties of 6061 aluminum alloy anodic oxide films. *Coatings, 12*(3), 314. https://doi.org/10.3390/coatings12030314

3.Ofoegbu, S. U., Fernandes, F. A. O., & Pereira, A. B. (2020). The sealing step in aluminum anodizing: A focus on sustainable strategies for enhancing both energy efficiency and corrosion resistance. *Coatings, 10*(3), 226. https://doi.org/10.3390/coatings10030226

4.Behzadifar, J., Najafi, Y., & Nazarizade, B. (2026). Synergistic effects of hard anodizing parameters on the microstructural, mechanical, and tribological properties of 6061 aluminum alloy. *Scientific Reports, 16*, 5021. https://doi.org/10.1038/s41598-026-35825-7

5.Costenaro, H., Lanzutti, A., Fedrizzi, L., Terada, M., de Melo, H. G., & Olivier, M. G. (2017). Corrosion resistance of 2524 Al alloy anodized in tartaric-sulphuric acid at different voltages and protected with a TEOS-GPTMS hybrid sol-gel coating. *Surface and Coatings Technology, 324*, 438–450. https://doi.org/10.1016/j.surfcoat.2017.05.090

6.Yu, M., Dong, H., Shi, H., Xiong, L., He, C., Liu, J., & Li, S. (2019). Effects of graphene oxide-filled sol-gel sealing on the corrosion resistance and paint adhesion of anodized aluminum. *Applied Surface Science, 479*, 105–113. https://doi.org/10.1016/j.apsusc.2019.02.005

7.Kim, M., Yoo, H., & Choi, J. (2017). Non-nickel-based sealing of anodic porous aluminum oxide in $NaAlO_2$. *Surface and Coatings Technology, 310*, 106–112. https://doi.org/10.1016/j.surfcoat.2016.11.100

8.Conroy, M., Soltis, J. A., Wittman, R. S., Smith, F. N., Chatterjee, S., Zhang, X., Ilton, E. S., & Buck, E. C. (2017). Importance of interlayer H bonding structure to the stability of layered minerals. *Scientific Reports, 7*, 13274. https://doi.org/10.1038/s41598-017-13452-7

9.Bai, B., Bai, H., Zhang, L., & Huang, W. (2018). Catalytic activity of γ-AlOOH (001) surface in syngas conversion: Probing into the mechanism of carbon chain growth. *Applied Surface Science, 455*, 123–131. https://doi.org/10.1016/j.apsusc.2018.05.174

10. Tregubenko, V. Y., Udras, I. E., & Belyi, A. S. (2017). Preparation of mesoporous γ-Al_2O_3 from aluminum hydroxide peptized with organic acids. *Russian Journal of Applied Chemistry, 90*(12), 1961–1968. https://doi.org/10.1134/S1070427217120102

11. Student, M. M., Pohrelyuk, I. M., Hvozdetskyi, V. M., Veselivska, H. H., Zadorozhna, Kh. R., Mardarevych, R. S., & Dzioba, Yu. V. (2021). Influence of the composition of electrolyte for hard anodizing of aluminum on the characteristics of oxide layer. *Materials Science, 57*(2), 240–247. https://doi.org/10.1007/s11003-021-00538-x

12. Student, M. M., Pohrelyuk, I. M., Chumalo, H. V., & Hvozdetskyi, V. M. (2021). Improvement of the functional characteristics of coatings obtained by the method of hard anodizing of aluminum alloys. *Materials Science, 56*(6), 820–829. https://doi.org/10.1007/s11003-021-00500-x

Гвоздецький В., Яремчук Д. Трибологічні характеристики імпульсно-анодованих шарів на алюмінії

У дослідженні розроблено передові електрохімічні методи синтезу високоефективних твердих анодних покриттів на підкладках з комерційно чистого алюмінію (AA1050/AD0) та сплаву Al-Cu-Mg (AA2024/D16). Систематично встановлено синергетичний вплив хімічної модифікації електроліту шляхом додавання перекису водню або озону, режимів високовольтного імпульсного твердого анодування (PHA) та постсинтетичної термічної обробки на кінетику покриття та фазовий склад. Встановлено, що зниження температури електроліту до -5 °C пригнічує індуковане кислотою хімічне розчинення поверхні, сприяючи стабільному росту щільної моногідратованої фази беміту ($Al_2O_3 \cdot H_2O$) зі значно підвищеною мікротвердістю. Навпаки, підвищення температури синтезу вище 0 °C індукує структурний фазовий перехід до тригідратованої фази гібситу ($Al_2O_3 \cdot 3H_2O$). Трибологічні дослідження в умовах сухого тертя та граничного змащування (мінеральні та синтетичні оливи) виявили унікальний механізм самозмащування: фаза гібситу з низькою твердістю зазнає механічного зсуву під час тертя та утворює безперервну, самовідновлювальну плівку твердого мастила, що транспортується між трибоелементами як на сталевих, так і на керамічних контактних поверхнях. Крім того, постсинтетична термічна обробка при 100–400°C з подальшим гідротермальним кип'ятінням викликає дегідратацію цільової матриці, подвоюючи зносостійкість покриття та забезпечуючи 5-10-кратне зниження зносу порівняно з необробленою алюмінієвою підкладкою AA2024. Імпульсна модуляція ефективно зменшує локалізовані теплові концентрації в порах, забезпечуючи оптимальні трибомеханічні характеристики за різних умов досліджень.

Ключові слова: тверде анодування; алюмінієві сплави; беміт; гібсит; термічна обробка; триботрансферна плівка; граничне змащення, тертя.